Fall 1987

ROCKET-BORNE LOW ENERGY ION MEASUREMENTS IN SPACE

CRAIG JAMES POLLOCK
University of New Hampshire, Durham

Order Number 8800187

Rocket-borne low energy ion measurements in space

Pollock, Craig James, Ph.D.
University of New Hampshire, 1987

U·M·I
300 N. Zeeb Rd.
Ann Arbor, MI 48106

ROCKET-BORNE
LOW ENERGY ION MEASUREMENTS IN SPACE

BY

CRAIG JAMES POLLOCK

BA, SIENA COLLEGE, 1980

DISSERTATION

Submitted to the University of New Hampshire
in Partial Fulfillment of
the Requirements for the Degree of

Doctor of Philosophy

in

Physics

September, 1987

This dissertation has been examined and approved.

Roger L. Arnoldy, Dissertation Director
Professor of Physics

Robert E. Houston
Professor of Physics

Richard L. Kaufmann
Professor of Physics

Martin A. Lee
Research Associate Professor of Physics

Harvey Shepard
Professor of Physics

May 27, 1987

I DEDICATE THIS WORK
WITH LOVE AND GRATITUDE
TO MY FAMILY:

To NANCY,
who has carried the load
and given me
encouragement and strength

To JAMES,
who gives me daily joy

To MY PARENTS,
who have always
nurtured so lovingly

To TERRY

To HAL

To PENNY

To DORIS

To BRIAN

and

To MARK,
who we all remember
so fondly.

ACKNOWLEDGEMENTS

A project such as the one described in this dissertation represents not only a program of scientific research which has been the effort of a team of individuals, but also, more importantly, a process of education and training for me, the student. For this reason, the individuals named in the paragraph below deserve acknowledgement, not only for their roles in bringing this program of research to fruition, but also for their roles as my teachers. Each of them has recognized this aspect of the working relationship and has demonstrated (with occasional human lapses) patience and a pedagogic attitude in the conduct of day to day buisiness.

First and foremost, Roger Arnoldy has provided me with the opportunity to pursue this program of research. He has always taken the time to discuss troubling aspects of the research and has often provided reassurance in the face of setbacks or doubt. His patience has been unabating. In line with his interest in these types of experiments, Professor Richard Kaufmann has provided many insights and helpful suggestions regarding the physical processes occurring in association with beam-plasma injections. The guys in the lab, including Hank Dolben, Ralph Varney and Mark Widholm, have provided the technical support and training in areas of both hardware and software which are essential to the conduct of any program of experimental research in physics. These three, together with Marc Lessard, have provided a stimulating and responsive collegial environment in which to work. Tom Moore's guidance in the area of instrument development and his role in making the calibration facility at NASA's Marshall Space Flight Center available for our use have been important to the early portions of this work. In the machine shop, Arthur Anderson provided many helpful ideas regarding the mechanical design of the HEEPS

instruments. His skill and attention to detail in machining the parts are greatly appreciated. Sherry Palmer's efforts and patience in providing illustrative materials, have been an important element in determining the form of this work and are also greatly appreciated.

Finally, the collaboration with Robert Erlandson has been a very rewarding and fruitful one. His contributions to the experiment itself (under the sponsorship of Professor L. J. Cahill, Jr.) were crucial. Further, his tenacious efforts to understand the plasma systems under study have been laudable and could provide good example to any student of science.

This research was carried out with funding provided by NASA grant #NAG-612.

TABLE OF CONTENTS

(continued)

TABLE OF CONTENTS (continued)

List Of Tables

Section 1

Section 2

List Of Figures

Introduction

Section 1

Section 2

Appendix A

Appendix B

ABSTRACT

A capped hemisphere electrostatic analyzer has been developed for the purpose of performing detailed studies of charged particle distributions in space from sounding rocket platforms. This instrument employs micro channel plate detectors in conjunction with a linear resistive anode to carry out angular imaging, by resistive charge division, of particle arrivals. Two such instruments, capable of supplying 64 x 32 angle-energy positive ion distributions every ~1 second were flown on two separate high latitude sounding rockets in February, 1985, from Sondre Stromfjord, Greenland. One of these two rockets featured an active ion beam experiment whereby 200 eV/q Ar^+ ions were injected into the ionospheric plasma from a separated sub payload in broad (~60° FWHM) beams directed alternately either parallel to or perpendicular to the geomagnetic field. Ion fluxes associated with beam operations were observed on the main payload out to a main/sub payload separation distance of nearly 1 km. Several distinct ion populations are identified, based on their energy/pitch angle characteristics and the existence of ion fluxes at unexpected energies and pitch angles is demonstrated and discussed in light of current understanding of these types of beam-plasma systems. The ion flux signatures of parallel versus perpendicular beam injections are compared and contrasted.

INTRODUCTION

Among the various states of matter is the plasma state which exists at temperatures higher than those of neutral gas. Transition from the gaseous to the plasma state follows melting and boiling in the series of physical phase changes which accompanies increasing temperature. This is accomplished through the ionization of gaseous atoms and molecules, normally by high velocity particles or energetic photons. A plasma differs from a neutral gas in that the atoms are broken into mobile, charged ions (positive) and electrons (negative). Transition to the plasma state is characterized most notably by the onset of long range electromagnetc interactions between the constituent charged particles. The coupling of electomagnetic and particle kinetic effects yields systems of extremely diverse and sometimes bizarre phenomenology. Examples of such include the violent explosions on the surface of the sun which are known as solar flares and are children of the hot, dense and strongly magnetized plasma near the solar surface. Closer to home, another visible example of plasma phenomena in space is provided by the aurora borealis (and aurora australis), also known as the northern lights, which result from the excitation of neutral atmospheric atoms and molecules by energetic electrons precipitating from the near-Earth region of outer space known as the Earth's magnetosphere. The auroral display is, in fact, a characteristic of the interface between the relatively dense neutral (unionized) terrestrial atmosphere and the large plasma system which is the Earth's magnetosphere. The altitude at which auroral light emission intensities maximize is that altitude at which the transition from neutral atmosphere to magnetized plasma takes place, roughly 100 kilometers (km) above sea level. In Figure I-1, is shown a schematic picture of the Earth's magnetosphere. This illustration is a cross-section in the plane defined by the Earth's magnetic dipole and the center of the sun. On the scale of this figure, the sun would be located about 60 feet to

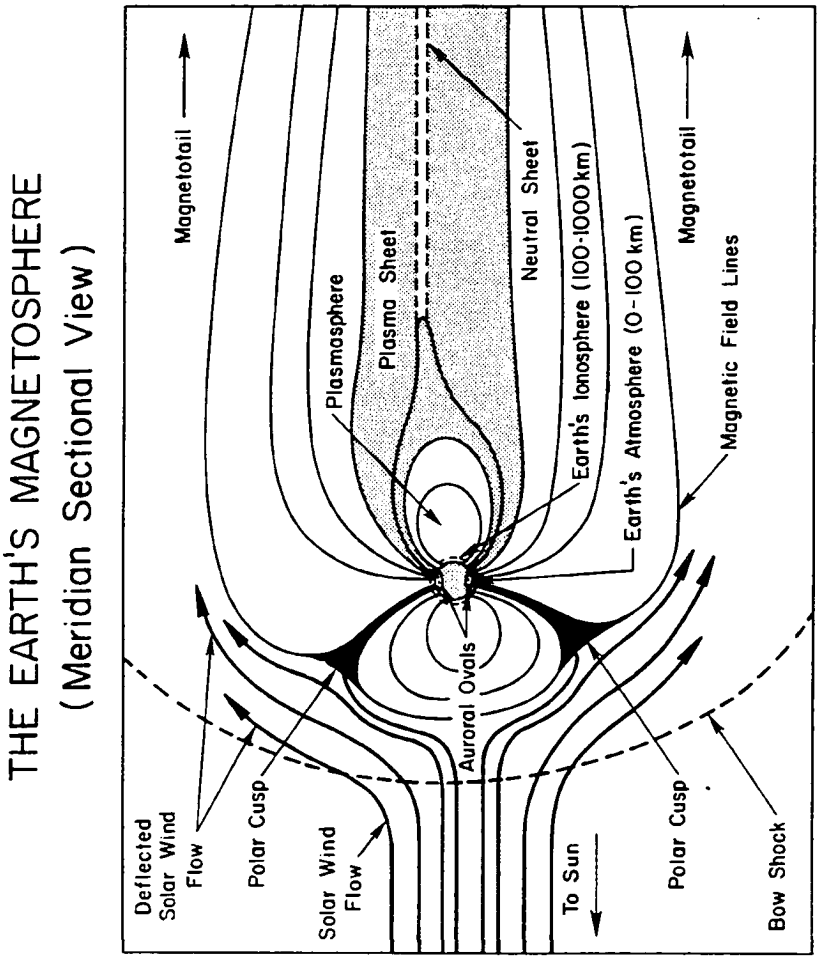

Figure I-1

the left. The general tendency of this magnetospheric system is for hotter, more tenuous plasma at large geocentric distances and cooler, more dense plasma closer to the Earth with, again, transition to cool, neutral gaseous atmosphere at roughly 100 km altitude.

To understand the shape that the Earth's magnetosphere takes in space, one must understand that this is a plasma system existing *inside* a plasma system. The system which contains our own magnetosphere is associated with the sun and is called the heliosphere. Specifically, the heliosphere is a large (contains the entire solar system) diffuse (~10 particles per cubic centimeter at position of Earth), magnetized (~ 5 gamma at the position of Earth) plasma which is expanding and blowing past the the Earth at a variable speed which, at the position of the Earth, is typically around 400 km per second. This 'Solar Wind' is the sun's corona undergoing radial expansion under the influence primarily of hydromagnetic pressure gradients. Thus, the shape of the Earth's magnetosphere, as shown in Figure I-1, results from the ramming of the magnetized solar wind plasma against and past the magnetized terrestrial plasma. The resulting magnetospheric cavity is blunted on the sunward side, forming the 'bow shock' and elongated on the anti-sunward side, forming the 'magnetospheric tail'.

The solar wind flow is characterized by turbulence and variability, which is communicated to the inner magnetosphere through a variety of means, including global magnetospheric compression and expansion in the face of varying solar wind ram pressure, plasma wave excitation and direct entry of solar wind particles into the magenetosphere (generally thought to be the exception, rather than the rule with regard to the magnetospheric energy budget). A result of this intimate communication of solar wind variablity into the magnetosphere is that the magnetospheric plasma itself is characterized by a large degree of turbulence and variability. In addition, as is evident in Figure I-1, the magnetosphere is characterized by a high degree of structure, with plasma parameters varying over several orders of magnitude throughout the system. It must be emphasized that diversity and concentrated forms of free energy characterize this system. Boundary

layers in particular, that is, the more or less thin layers which separate the regions shown in Figure I-1, are characterized by various plasma drifts and instabilities associated with the changes in plasma properties across such layers. It can be seen by referring to that figure, that the Earth's auroral zones themselves occur at the confluence of two boundary layers. One of these, known as the plasma sheet boundary layer, separates the magnetospheric plasma sheet from the magnetospheric tail lobes, while the other is, as mentioned above, the boundary between the magnetosphere itself and the neutral gaseous atmosphere lying below.

Most of what is now known about the near-Earth regions of outer space is known by virtue of our recently developed capability to go there. That is, due to our ability to launch manned and unmanned spacecraft which can carry out detailed measurements of the parameters and processes characteristic of these regions. In the 30 year history of successful space flight, humans have sent probes to nearly all of the other planets, have personally travelled to the Earth's moon and have spent hundreds of thousands of hours carrying out observations and experiments in near earth orbit. We have sent spacecraft to hover out in the solar wind in front of the Earth's magnetospheric bow shock, routinely monitoring solar wind properties and have placed many scientific satellites, weather satellites, communications and other satellites, designed for darker purposes, in a wide variety of Earth orbits. Recently, workers from many nations have collaboated to send a small fleet of heavily instrumented spacecraft to carry out an investigative rendezvous with the comet Halley. Our active exploration of and experimentation in the near-Earth regions of outer space has dramatically increased, not only our understanding of this complex medium, but also our understanding of the subject of plasma physics in general and has vastly furthered our technological capabilities in a wide ranging number of areas which find practical application for purposes far removed from those of space exploration.

The research reported in this thesis, which was funded by the United States National Aeronautics and Space Administration (NASA), represents a very small part of the

large scale effort described above. Specifically, we have employed sub-orbital sounding rocket technology to gain access to the region of the ionospheric plasma between ~100 and 400 km altitude for the purpose of carrying out active ionospheric plasma physics experiments. Such ionospheric plasma physics experimentation has the distinct advantage of the absence of nearby containing walls characteristic of the vacuum chambers in which Earth-bound plasma physics experiments must be performed, providing an anechoic environment for the conduct of the experiments. The experiments that we have conducted have potential bearing on subjects ranging from natural magnetospheric phenomena to the technology of controlled thermonuclear fusion.

SECTION 1: NEW INSTRUMENTATION

Introduction to Electrostatic Analyzers

The use of electrostatic analyzers for the measurement of intermediate energy charged particle fluxes in space is common among experimenters in space physics. Figure 1-1 illustrates the operation concept of such an instrument. In this 2-dimensional illustration, a positively charged ion is shown entering the region between two curved conducting plates (the analyzer) from the right. These plates are held at different electric potentials, setting up an electrostatic field

$$\mathbf{E} \approx -\frac{V_2 - V_1}{R_2 - R_1}\hat{\mathbf{r}} \qquad \text{Eq. 1-1}$$

in the region between the plates through which the particle passes. This field exerts a force

$$\mathbf{F} = q\mathbf{E} \approx -q\frac{V_2 - V_1}{R_2 - R_1}\hat{\mathbf{r}} \qquad \text{Eq. 1-2}$$

on the particle while it is between the plates. Now, in order for this particle to move through the analyzer to the electron multiplier where it is detected, it must move approximately on a circle of radius R_0. A centripetal force given by

$$\mathbf{F}_c \cong -\frac{mv^2}{R_0}\hat{\mathbf{r}}, \qquad \text{Eq. 1-3}$$

which is supplied by the imposed electric field, is required to keep this massive particle on the given circular trajectory. The fact that a particle makes it between the plates to the detector means that the centripetal force required is equal to the applied electrostatic force. Setting the right hand sides of Eqs. 1-2 and 1-3 equal to each other and re-arranging, we find:

$$\varepsilon \equiv \frac{mv^2}{2q} \approx \left\{\frac{R_0}{R_2 - R_1}\right\} \times \left\{\frac{V_2 - V_1}{2}\right\}. \qquad \text{Eq. 1-4}$$

ELECTROSTATIC ANALYZER OPERATION

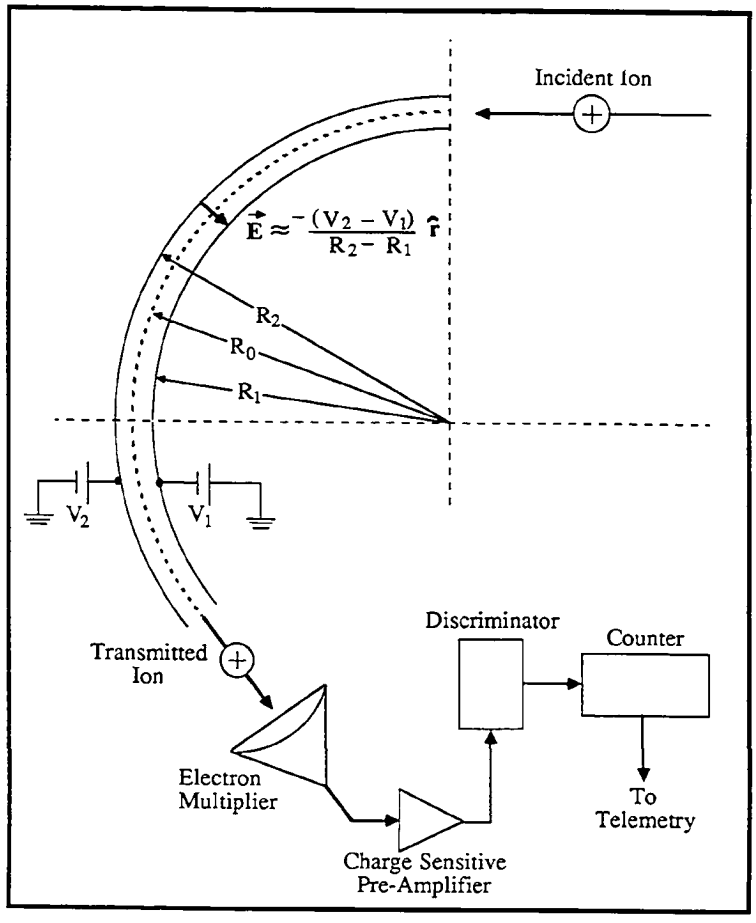

Figure 1-1

Thus, on the left we have a measure of the particle's kinetic energy per unit charge, defined in the remainder of this work as the quanty "ε", and on the right, all quantities which are known and controlled by the experimenter. If the condition implicit in Eq. 1-4 is not satisfied, the particle will collide with one of the two analyzer plates, never reaching the detector and no event will be recorded.

The basic scheme commonly employed in space involves pre-programming the instrument to periodically step through a sequence of voltage states, each state being characterized by a unique potential difference applied across the analyzer plates. While the instrument dwells at a given state, the events at the detector are accumulated in a counter. Before changing states, the counter is read out, giving an event rate for the given state. This corresponds, as described above, to an event rate for a given energy per charge. If the program sequence provides for n unique states and the program repetition period is τ, then the instrument provides an n point energy spectrum at the characteristic period τ.

An example of the raw data obtained in such a manner is shown in Figure 1-2. The top trace (A) in this figure shows a voltage state monitor signal, indicative of the analyzer energy state and the bottom trace (B) shows the values read from the event counter. One can see that, in this case, the instrument steps through a 32 step sequence every ~410 ms. Also, in this case, the event counter is read out and reset 32 times during each 410 ms interval. The data in Figure 1-2 is interpreted in light of the facts that:

1) Selected particle energy per charge is given as a function of time as being proportional to the signal level in trace A.

2) Event rate at a given energy state is given as a function of time as being proportional to the signal level in trace B.

The most meaningful physical quantity that can be rigorously derived from this data is the *differential directional particle flux*

$$J' \equiv \frac{dN}{dA \cdot d\Omega \cdot d\varepsilon \cdot dt}, \qquad \text{Eq. 1-5}$$

which is derived from the data as

TYPICAL ELECTROSTATIC ANALYZER DATA SEGMENT

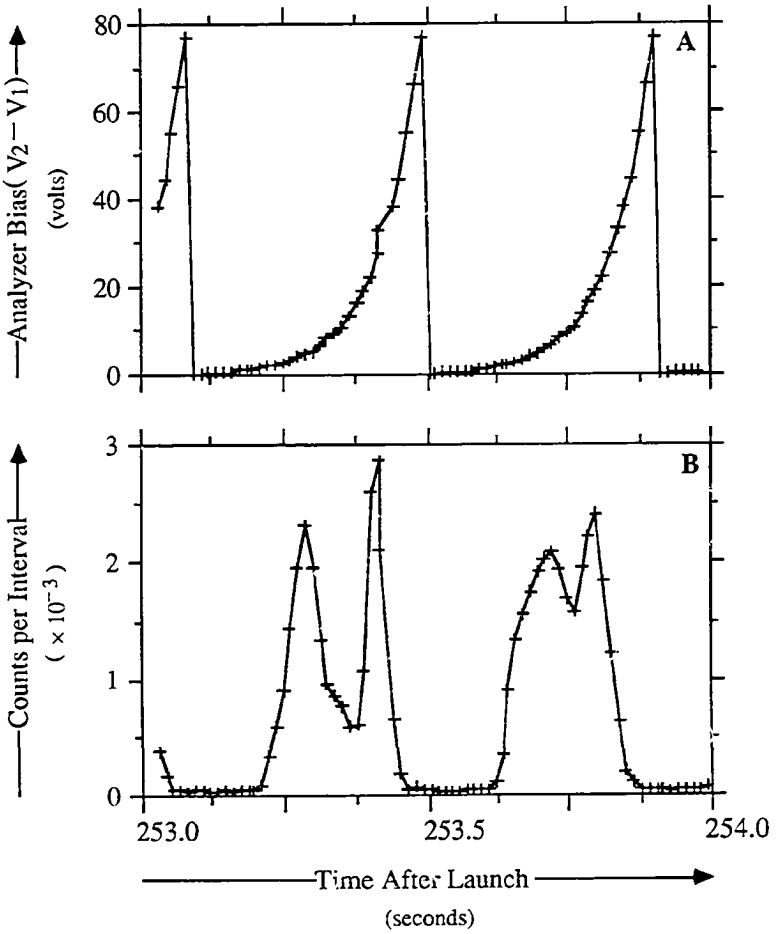

Figure 1-2

$$J' = \frac{C}{(\tau G_0 \varepsilon)}, \qquad \text{Eq. 1-6}$$

where C and ε are provided as particle events count and energy per charge in the data stream, τ is the time during which C events were accumulated and G_0 is the energy independent geometry factor, which characterizes the sensitivity of the instrument. The differential directional flux, J', represents the number of particles per unit area-(solid angle)-time-(energy per charge) to cross an areal element (dA) from directions within the element of solid angle $d\Omega$ centered on the normal to dA (r) and characterized by energies per charge within an interval $d(\varepsilon)$, centered on ε. Conventional units on J' are given as [# / (cm^2-sr-sec-keV)]. With the above units on J', the appropriate units on G_0 are [cm^2-sr-keV/keV]. The relationship between the data and the derived differential directional flux, particularly with regard to the energy independent geometry factor, will be discussed in more detail in subsequent subsections.

One can sometimes push things a bit further and assume or determine (by independent means) a mass number and a charge state (Z) for the particles exciting events in an electrostatic analyzer. Under such assumptions (or with such knowledge) a quantity much more closely related to common theoretical descriptions of the plasma state, namely, the single particle distribution function (f(v)) may be derived from the data. This is possible due to a physical relationship between the differential directional flux (J') and f(v). The single particle distribution function, f(v), represents the number of particles in the spatial volume element d^3r, centered at a given location in space which have velocities within the velocity volume element d^3v, centered on the velocity v, divided by the product $d^3r \times d^3v$. The relationship between J' and f(v) may be expressed through the equation

$$f(\mathbf{v}) = \frac{m^2}{2ZE} J', \qquad \text{Eq. 1-7}$$

where m is the species mass, Z is the charge state and E is the particle energy. This equation is general for nonrelativistic particles and derives from the physical relationship

between the.quantities involved. In practice, it is convenient to use a form of Eq. 1-7 which involves conventional units on both sides. In particular,

$$f(v) = \frac{0.545\ m^2}{Z^2 \varepsilon} J', \qquad \text{Eq. 1-8}$$

where f is given in $sec^3/meter^6$, m is given in atomic mass units (amu), ε is given in kiloVolts (kV) and J' is given in the conventional units [# / (cm^2-steradian-sec-keV)]. Z is still given as, simply, the species charge state.

Hemispheric Geometry to Incorporate Angular Imaging

In addition to the energy spectrum of charged particle fluxes, it is desirable to determine the angular distribution of these particles in velocity space. That is, for a particle of given mass, an energy spectrum gives the flux (J') as a function of particle speed. We are interested, further, in the dependence of J' on the angular components of particle velocity. In a magnetized plasma, one is interested in how the component of particle velocity ($v_{||}$) parallel to the ambient magnetic field (**B**) compares to the component of particle velocity ($v_{\perp}$) perpendicular to **B**. In addition, the magnetic azimuth of the charged particle velocities is often of significant interest, especially in strongly inhomogeneous plasmas such as those described in Section 2 of this thesis. The magnetic pitch angle (α) and magnetic azimuth (ϕ) of a given charged particle are given as functions of the components of the particle velocity as:

$$\alpha \equiv \arctan\left(\frac{v_{\perp}}{v_{||}}\right), \quad 0° \leq \alpha \leq 180° \qquad \text{Eq. (1-9A)}$$

$$\phi \equiv \arctan\left(\frac{v_y}{v_x}\right), \quad 0° \leq \phi \leq 360° \qquad \text{Eq. (1-9B)}$$

where $v_{\perp}^2 \equiv v_x^2 + v_y^2$. The distribution of particle fluxes with pitch angle and magnetic azimuth can have important implications regarding the physical state of the plasma.

The analyzer shown in Figure 1-1 is mono-directional, in that particles are transmitted to the detector only if they arrive from directions near the direction toward which the entrance aperture faces. If one is to determine the distribution of particles as a function of direction in velocity space with such an instrument, one must either deploy a number of such instruments, each looking in a different direction or move a single instrument so as to vary the look direction with time. The most common approach utilizes both techniques, with several instruments deployed on a spinning spacecraft. The time required to obtain an angular flux spectrum, even with several instruments deployed

on a spinning spacecraft, can easily amount to several seconds on a sounding rocket (longer on a more slowly spinning orbital satellite), often placing serious constraints on the temporal and spatial (due to translational spacecraft motion) resolution obtainable with such systems.

A major improvement over this situation may be achieved through the use of an electrostatic analyzer device which looks in many directions simultaneously and yet is capable of imaging particle events with respect to source direction. An analyzer geometry suitable for this purpose was conceived by Dr. C. Carlson (Carlson et al., 1983) at the University of California at Berkeley and is schematically illustrated in Figure 1-3, which should be considered to be a figure of revolution about the vertical symmetry axis. The configuration shown in Figure 1-3 is referred to in this work as a *capped hemisphere* analyzer design. The analyzer will transmit particles of the appropriate energy per charge (ε) whose velocity vectors lie approximately in the plane perpendicular to the instrument symmetry axis. Furthermore, particles arriving at the (cylindrical) entrance aperture from different azimuths will be transmitted to different points at the (annular) exit aperture. The imaging of particles with respect to arrival azimuth is accomplished through the coupled use of this capped hemisphere analyzer design and a scheme for imaging the spatial location of particle arrivals at the annular exit aperture.

The transmission properties of the capped analyzer were modelled numerically and tested in the laboratory by researchers at the University of California at Berkeley, with the result that they are fairly well catagorized. Referring to Figure 1-3, analyzer design parameters of primary interest are the radii of the the conducting spherical sections, characterized by the quantities

$$R_1, R_2 \text{ and } R_3$$

or, equivalently,

$$R_1, \Delta_1 \text{ and } \Delta_2,$$

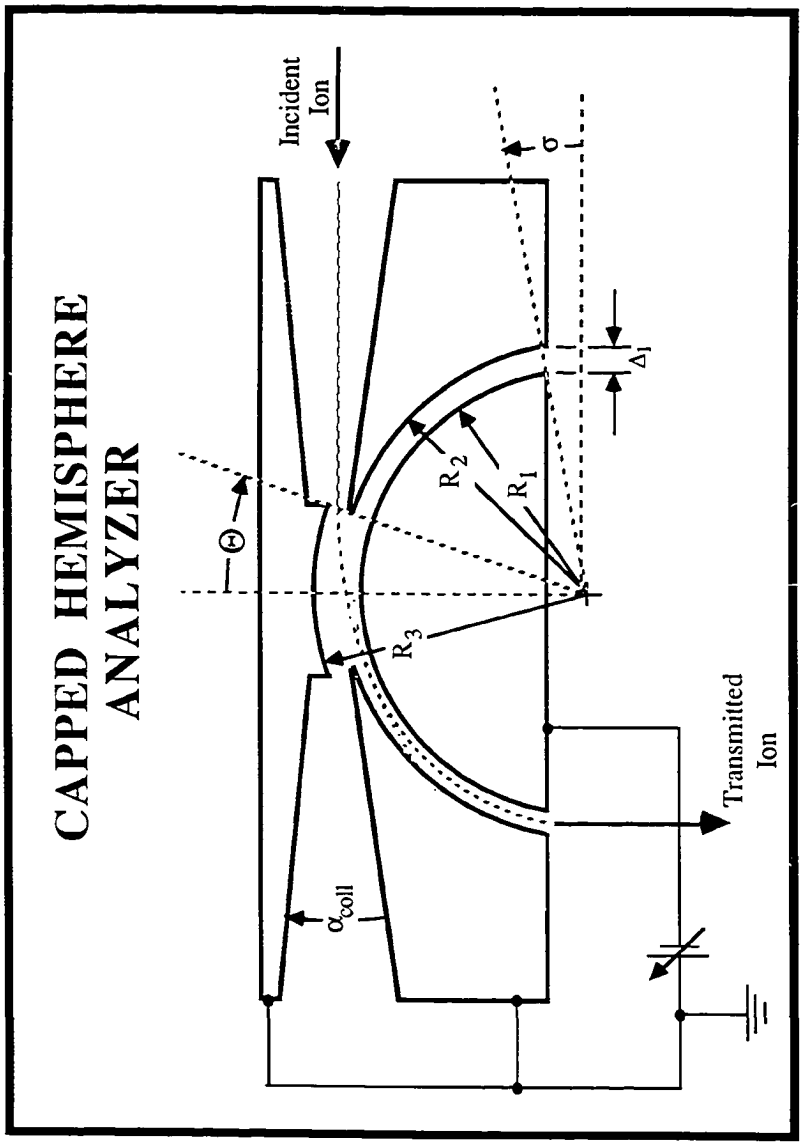

Figure 1-3

where Δ_1 is the inner plate gap ($R_2 - R_1$) and Δ_2 is the outer plate gap ($R_3 - R_2$). In addition, the truncation angles Θ and σ and the collimation angle α_{coll} effect analyzer transmission properties. Figure 1-4, taken from Carlson et al. (1983), illustrates several aspects of capped hemisphere transmission performance, as well as optimized design parameters (Θ and σ) based on the numerical and experimental testing carried out by the Berkeley group. These curves show the instrument geometry factor, the mean of the product of the fractional velocity bandpass ($\Delta v/v$) and the polar angular bandpass ($\Delta\theta$) and the so called analyzer ratio (T_∞ / qV), which represents the ratio of the energy per unit charge for a transmitted incident particle and the voltage applied across the electrodes at R_1 and R_2 as functions of Δ_1.

The geometry factor plotted in Figure 1-4 is normalized to the square of the radius R_1 and is given, as noted above, in units (sr-δ(v)/v), which are based on a velocity bandpass, rather than an energy-per-charge bandpass. The quantity plotted in the figure (G/R_1^2) can be re-expressed in terms of more conventional units (cm^2-sr-kV/kV) by using the relation

$$\frac{dE}{E} = 2\frac{dv}{v}, \qquad \text{Eq. (1-10)}$$

with the result that

$$G_0 = 2R_1^2 \times \left(\frac{G}{R_1^2}\right), \qquad \text{Eq. (1-11)}$$

where G_0 carries the conventional units alluded to above and (G/R_1^2) is given in Figure 1-4. It must be realized that this geometry factor applies to the entire capped hemisphere analyzer and, specifically, incorporates 2π radians of azimuthal sensitivity. The curves in Figure 1-4 have served as primary aids in selecting design criteria for the instruments built at UNH to be flown on NASA rocket flights 29.015 and 35.012.

CAPPED HEMISPHERE DESIGN
& TRANSMISSION PARAMETERS

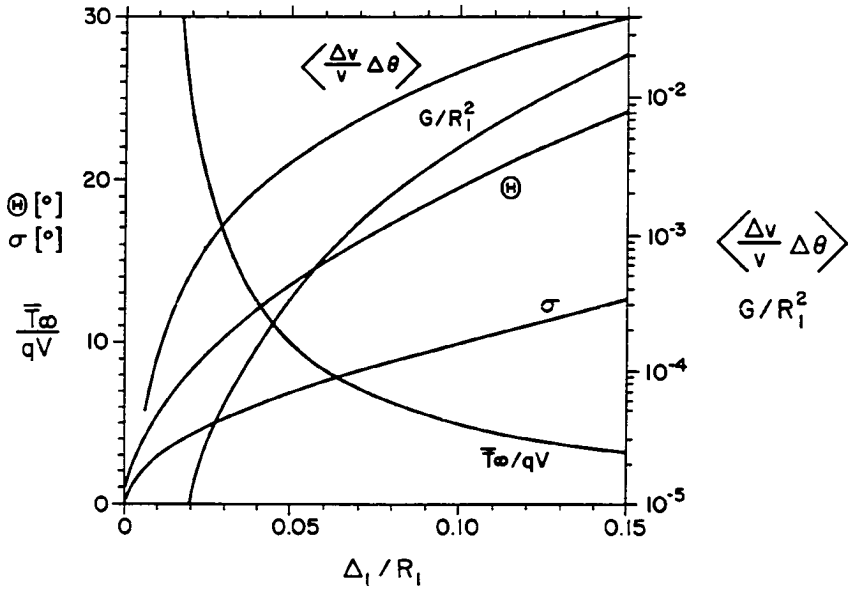

Figure I-4

Spatial Imaging in Focal Plane of Capped Hemisphere Analyzer

A key to the use of the capped hemisphere for angular charged particle imaging rests on imaging the passage of particles through the annular exit aperture of the capped hemisphere analyzer. This imaging can be carried out in essentially 3 steps:

1) Effect Electron multiplication.

2) Pick-up charge burst and distribute to circuit board inputs.

3) Analyze distribution at circuit board inputs and deliver resulting encoded position.

The nature of the systems operative in step 2 dictate the analysis required in step 3.

The Use of MicroChannel Plates.

Electron multiplication is neccesary at the analyzer exit aperture in order to provide charge bursts that are large enough to be evaluated electronically. It is critical that the resulting charge burst retains the localization of the input particle event. A device which is well suited to these purposes is the microchannel plate electron multiplier (MCP), a glass wafer-like array of many thousands of small diameter (~ 10 μm) single channel *continuous dynode lectron multipliers* . The function of a continuous dynode electron multiplier is illustrated in Figure 1-5, reproduced from Wiza (1981). The process of charge multiplication depends on the extraction of electrons from the doped semi-conducting inner channel surface by electron impact with the channel walls. Extracted electrons are accelerated down the tube in the applied electric field, to either be emitted at the output face or, to strike the channel wall, extracting more electrons for the cascade. The electron gain will be given by the mean number of electrons to be extracted from the semi-conducting wall per 'typical' electron impact, raised to the power of the mean number of wall collisions a 'typical' electron suffers in traversing the length of the tube, under the assumtion that all

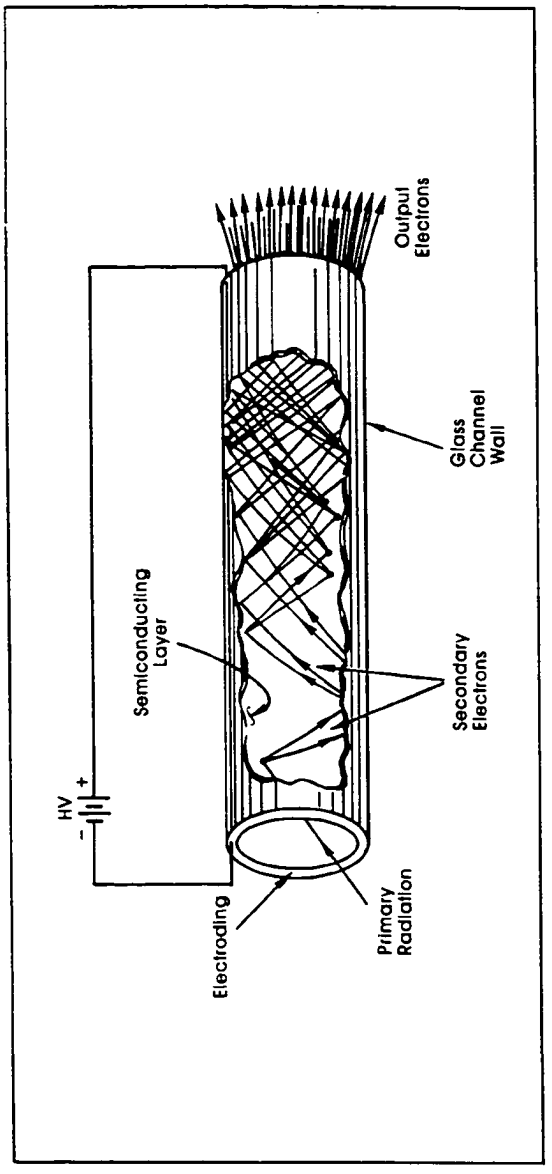

Figure 1-5

electrons emitted by the channel surface either are emitted at the output face or give rise to further electron emission by impacting the tube wall. The high voltage bias applied across the channel serves the purposes of driving the cascade toward the output face and supplying the required electron current.

Figure 1-6, illustrates the appearence of a single MCP in part A, shows, in part B at the right, how a pair of MCP's may be arranged in the stacked *chevron* configuration (see Fig 1-7, below) and, in part C at the lower left, gives a simple schematic indication of the appropriate electrical biasing configuration.

Aside from the drastic differences in physical configuration, the performance characteristics of MCPs have many similarities to those of Channeltron electron multipliers, which are single channel electron multipliers and have been in use in space physics for a long time. Typical gains for single straight channel MCPs are near 10^4 with 1000 Volts applied across the plate. The gain is limited by the onset of a phenomenon known as *ion feedback*, wherein ions in the vicinity of the channel outputs are accelerated toward the input face by the applied field in the channel. These ions produce spurious electron emission due to ion-wall collisions. Introducing tube curvature (Timothy, 1981) inhibits this process, apparently by limiting the typical ion kinetic energy gain and, therefore, the rate of spurious electron emission due to ion-wall collisions. A zeroeth order curvature can be (and is, commonly) introduced to a pair of MCP's stacked in series, by:

1) Using MCPs whose channel axes are not perpendicular to their input and output faces, the angular deviation from perpendicularity being defined as the channel bias angle.

2) In stacking the series pair, rotationally orienting the two MCPs such that their channel axes are coplanar but not parallel, that is, the channel orientations should oppose each other, displaying the shape of a vertical chevron in cross-section, as illustrated in Figure 1-7.

MICRO-CHANNEL PLATES

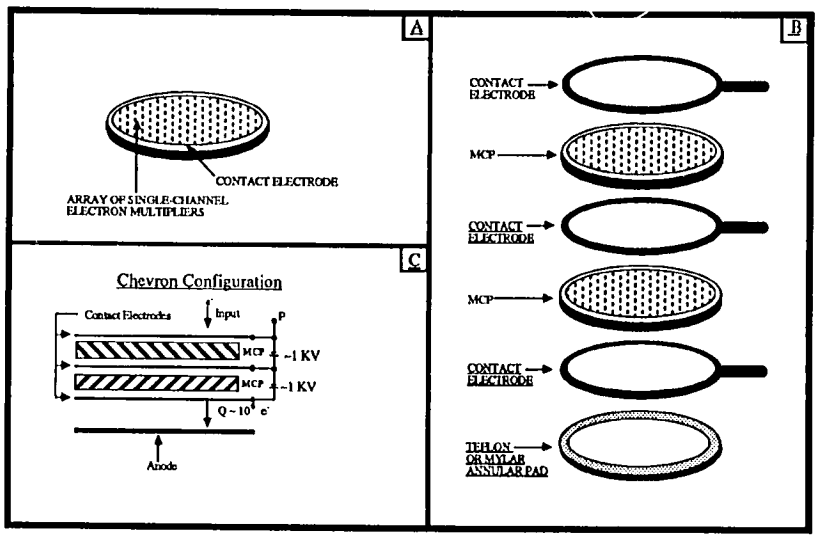

Figure 1-6

Resulting chevron gains are on the order of 10^6 - 10^7, with an applied stack bias of ~ 2000 Volts. Curved channel MCPs are available, offering single plate gains of ~10^6 (Timothy, 1981). These

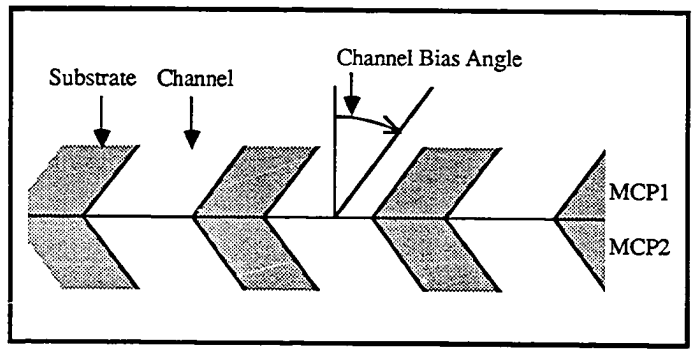

Figure 1-7: CHEVRON CONFIGURATION

curved channel plates are substantially more expensive than pairs of straight channel plates, but the gain achieved has a very high degree of consistency, as demonstrated by emitted pulse hight distributions of (~50% FWHM).

A microchannel plate electron multiplier system transforms a single charged particle or photon at the plate input (analyzer exit aperture) into a burst of ~ 10^6 - 10^7 electrons at the plate output (collecting anode), while retaining spatial localization to as little as 10 microns, a typical inter-channel distance. Such a system suffices easily for the neccesary imaging step 1, listed above.

The second and third imaging tasks listed above involve the scheme for localizing the MCP electron charge burst. Referring again to Figure 1-3, the question remains: 'How can one discriminate between transmitted ions giving rise to MCP charge bursts occuring at various locations along the annular exit aperture?'. Several approaches to answering that question will be listed and briefly dicussed in the following paragraphs. The variety of techniqes applied to this problem is large, so that only a representative sampling of such

will be presented here. It is recommended that the reader consult the noted references for more in depth coverage of the subject.

Choices for Imaging Anode Configuration.

The burst of charge emitted by the MCP system will be deposited on a planar anode placed (generally) parallel and in immediate proximity to the MCP output face. In a very short time, the charge deposition must 'drain' along the conducting anodic surface onto the circuit board pick-ups for electronic analysis. The ability to fabricate anodes whose characteristic 'drainage' patterns depend predictably on the location of a charge burst deposition fills the requirements for step 2 and opens the door to the use of electronic circuit board techniques for recognizing and catagorizing the signatures of charge bursts occurring at various positions on the anode. A number of schemes are available for carrying out either 1 or 2 dimensional imaging of microchannel plate charge burst occurances, with a rough dilineage between so-called discrete anode and transmission line techniques.

Imaging With Discrete Anodes. In the simplest case of imaging with discrete anodes, in the capped hemisphere case, an anode such as that shown in Figure 1-8 would be used. This 12 segment anode has the characteristic that a burst of charge deposited on one of the individual anode segments will 'drain' exclusively through the charge sensitive pre-amplifier associated with that segment, yielding direct correspondence to physical location through the identity of the stimulated amplifier. This approach is very attractive due to its simplicity. Such an anode could be manufactured easily as a printed circuit board with dimensional control of on the order of 0.005", corresponding to an angular measure of less than a degree for a typical system based on 1" diameter MCP's. The major disadvantage to such an approach in rocket-borne space experiments lies in the large quantity of electronic circuitry required to support the discrete anode assembly. The circuitry is simple, corresponding conceptually to the stages in Figure 1-1, below the

DISCRETE

IMAGING ANODE

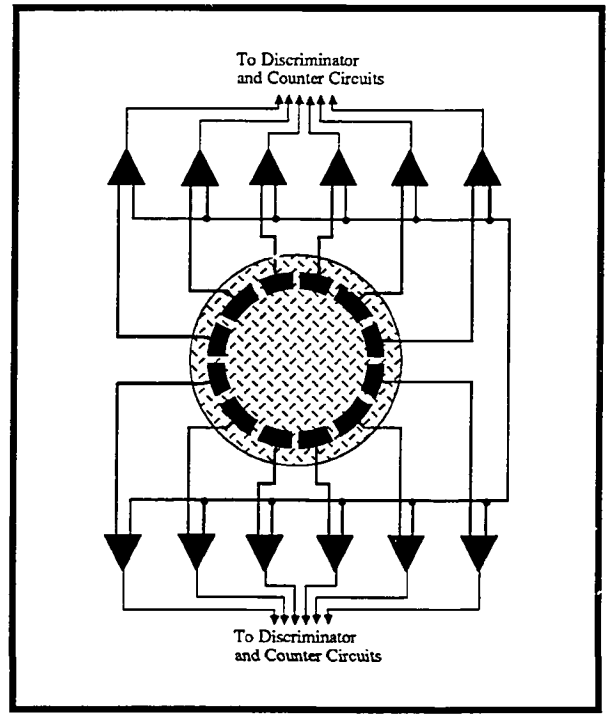

Figure 1-8

electron multiplier stage. The drawback lies in the need for one such circuit for every anode segment. In the case where 71/2 degree angular resolution is required over 360 degrees of space, a total of 48 separate process circuits are required. The cost of these circuits in terms of weight, power and space is very significant.

Schemes have been employed (Timothy, 1985) which serve to reduce the number of electronic process circuits required to service a multiple discrete anode array. These depend upon division of the MCP charge burst among a pair of electrodes, in the one dimensional imaging case, with one electrode defining coarse event location and the other giving fine event location within the identified the coarse grouping. In this way, an array of (a*b) pixels may be supported by only (a + b) separate process circuits.

In addition, there are the so-called *wedge and strip* (Martin, et al., 1981) techniques for imaging the spatial occurance of microchannel plate charge bursts in one or two dimensions. The basic idea in this approach involves deposition of anode electodes which are characterized by uniform variation in cross section along the imaged direction.

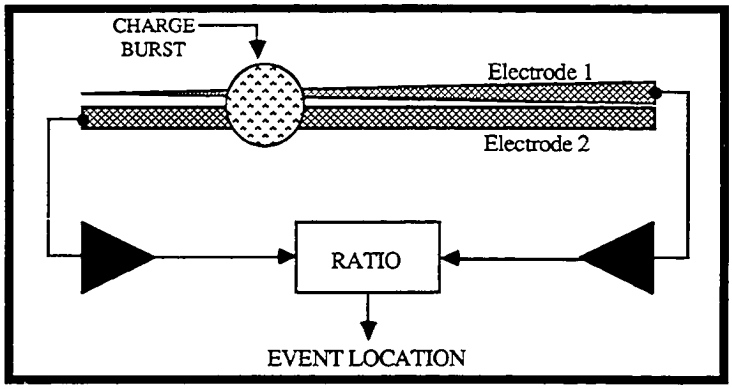

Figure 1-9: Wedge & Strip Event Imaging

A charge burst at a given location will give rise to a pre-amplifier response which varies in the same manner, with postion, as the cross section of the deposited anodic electrode. Since the electron clouds emitted by MCPs vary substantially in magnitude, a pair of electrodes, whose variations in cross section differ must be deposited in close proximity, so that the emitted electron cloud is divided between them. The ratio of the two pre-amplifier responses, then, provides the ratio of conducting cross-sections presented by the two electrodes at the location of the event, which in turn provides the event location through the known electrode geometry. The simple illustration above shows electrodes with linearly varying cross section. These and other techniques have been reviewed by Timothy (1985).

R-C Transmission Line Imaging. So called transmission line imaging is more subtle than discrete anode imaging in the quality of the anodic response to charge injection and, often, in the ensuing analysis required. As a concrete illustration, in the case of one dimensional imaging such as required in capped hemisphere applications an anode such as that shown in part A of Figure 1-10 could be used. This anode consists of a thin planar substrate, such as a piece of fiberglass pc board, onto which a resistive carbon ink has been serigraphically deposited along the annular region shown. In this manner, a uniform resistance (R_0) per unit length along the 'image annulus' is achieved. Grounded metal foil on the back of the substrate provides capacitive coupling to any point on the image annulus so that the strip is also characterized by a uniform capacitance per unit length (C_0). The region between the two electrode contacts A and B at x=0 and x=l, respectively, may then be effectively modelled (see figure 1-10 b) as a uniformly resistive-capacitive transmission line, along which the electrostatic potential V(x,t) obeys the following partial differential equation, which is the so-called *telegraphist's equation* for the case of zero line inductance and zero shunted line conductance:

$$\frac{d^2V}{dx^2} = R_0 C_0 \frac{dV}{dt}, \qquad \text{Eq. (1-12)}$$

RESISTIVE-CAPACITIVE IMAGING ANODE

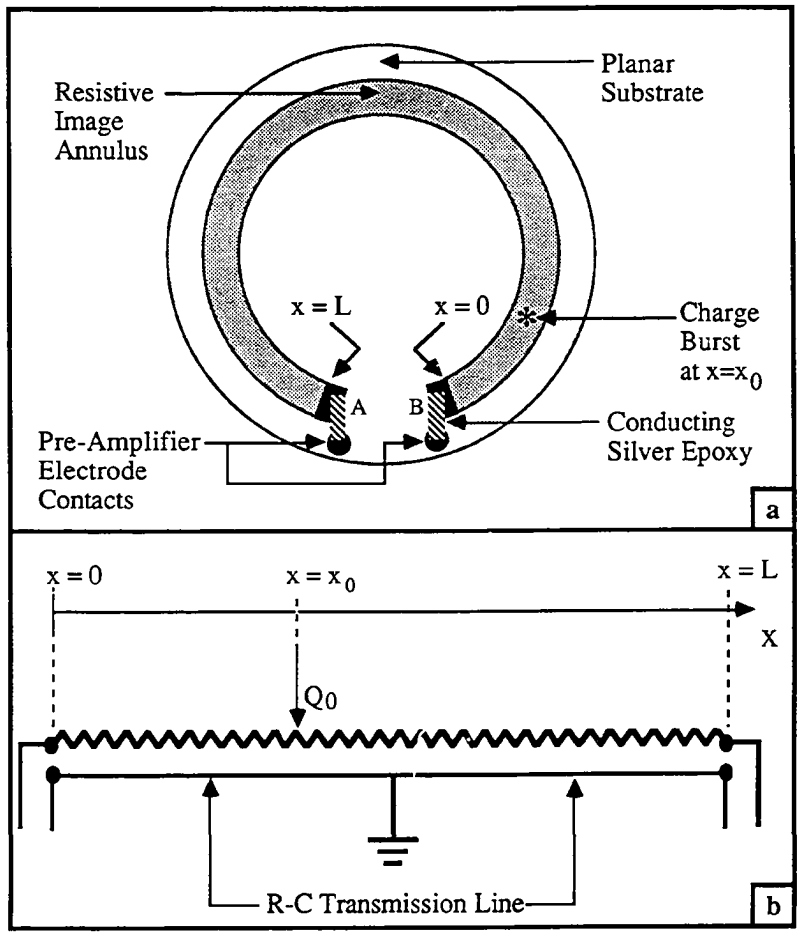

Figure 1-10

where x and t are the spatial coordinate of a point along the strip and the coordinate in time, respectively, V(x,t) is the value of the voltage at (x,t) along the strip, R_0 and C_0 are the resistance and capacitance per unit length along the strip and x_0 is the location of charge injection at the time t = 0. Boundary Conditions at x=0 and x=L are obtained by virtue of the fact that these points are tied to the pre-amplifier inputs, which are effectively held at ground, yielding,

$$1)\ V(x=0,t) = 0, \qquad \text{Eq. (1-13 a)}$$

$$2)\ V(x=L,t) = 0. \qquad \text{Eq. (1-13 b)}$$

In addition, an initial condition may be applied, in the case where the charge injection takes place on a time scale which is short in comparison to the strip diffusion time, given by the quantity $R_0C_0L^2/\pi^2 \approx 70$ nsec, where $R_0C_0L^2$ is the product of the total strip resistance and capacitance. In this case, the charge injection may be considered to be impulsive at t=0. Considering that, in general,

$$V(x,t) = \frac{q(x,t)}{C_0}, \qquad \text{Eq. (1-14)}$$

where q(x,t) is the linear charge density on the strip, we may write:

$$V(x,t=0) = \frac{Q_0\,\delta(x-x_0)}{C_0}, \qquad \text{Eq. (1-15)}$$

where $\delta(x - x_0)$ is the Dirac delta function. This function is defined to be zero at all values of x such that $x \neq x_0$ and to be infinite at x_0. Further, the delta function is defined such that the definite integral of its product with an arbitrary function f(x) is defined to be equal to $f(x_0)$ if the range of integration includes x_0, and to be equal to zero otherwise. Under the above conditions, the solution for V(x,t) may be expressed as (Kalbitzer & Melzer, 1967)

$$V(x,t) = \frac{2Q_0}{C_0L}\sum_{n=1}^{\infty}\sin(nz)\sin(nz_0)\exp\left(\frac{-n^2\pi^2 t}{R_0C_0L^2}\right), \qquad \text{Eq. (1-16)}$$

where $z \equiv \pi x/L$. The current may be obtained at any point as

$$I(x,t) = \frac{-1}{R_0}\frac{dV(x,t)}{dx}$$

$$= \frac{-2\pi Q_0}{R_0 C_0 L^2}\sum_{n=1}^{\infty} n\cos(nz)\sin(nz_0)\exp\left(\frac{-n^2\pi^2 t}{R_0 C_0 L^2}\right). \qquad \text{Eq. (1-17)}$$

The electrostatic potential and the electric current, as computed using the above equations, are shown in Figures 1-11 a&b as a functions of z and of the time, normalized to the time $R_0C_0L^2$. The diffusive nature of the anodic response is apparent in this figure.

It is the above expression (Eq. 1-17) for the electric current on the strip which will yield to analysis to determine the injection location (x_0). There are at least two techniques that one may use for this purpose, which will be referred to as the *'resistive charge division'* and *'charge delay time'* techniques.

Resistive charge division. With a charge sensitive pre-amplifier connected to either end of the strip, the output amplitude of a given amplifier for a given event will be proportional to the total amount of charge delivered to that end of the strip. The signal amplitudes derived at the outputs at x =L and x = 0, then are given by:

$$S_A \propto |q_A| = \int_0^{\infty} dt\ i(x=L,t) \qquad \text{Eq. (1-18)}$$

&

$$S_B \propto |q_B| = \int_0^{\infty} dt\ i(x=0,t). \qquad \text{Eq. (1-19)}$$

With i(x,t) given by equation 1-17, the integrals in equations 1-18 and 1-19 can be carried out and the following expression derived in a straight forward manner:

$$\frac{S_A}{S_A+S_B} = \frac{x_0}{L}, \qquad \text{Eq. (1-20)}$$

where x_0 is the injection point. The determination of the injection point, then is reduced to the measurement of the ratio of the charge delivered to one end of the strip to sum of the charge delivered to the two ends, that is, the total charge injected. These principles may be

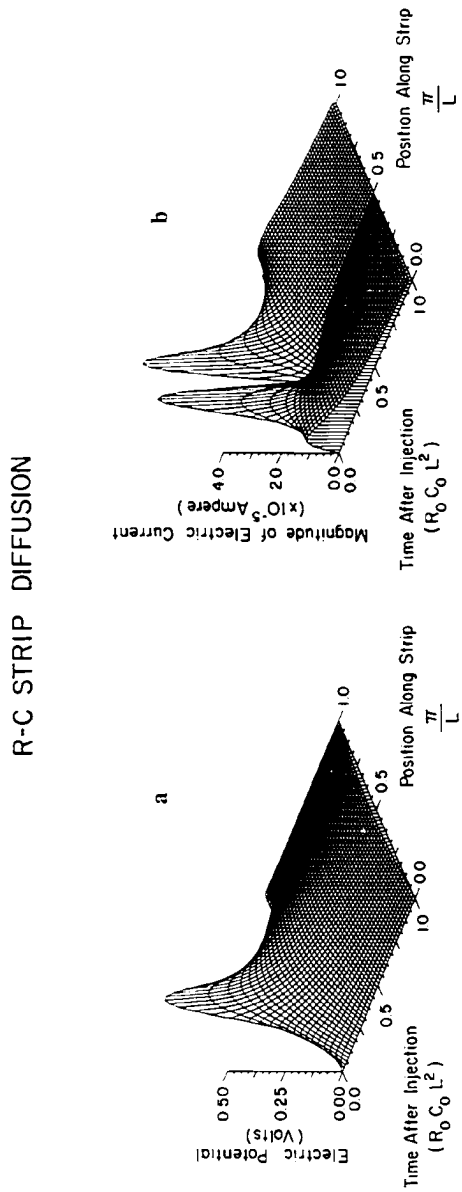

Figure I-11

extended in a straight forward manner to the case of two dimensional imaging on a planar anode.

Charge Delay Time Technique. Again, with a charge sensitive pre-amplifier connected to the ends of the strip, the signals derived at the outputs at either end as functions of time will be given by:

$$S_A(t) \propto \left| \int_0^t dt'\ i(x=L,t') \right| \qquad \text{Eq. (1-21)}$$

&

$$S_B(t) \propto \left| \int_0^t dt'\ i(x=0,t') \right|, \qquad \text{Eq. (1-22)}$$

with the constants of proportionality depending upon the pre-amplifier gains. These functions are shown plotted verses time in Figure 1-12, taking a proportionality constant of unity and using

$$R_0L = 7.0 \times 10^4 \text{ Ohms},$$

$$C_0L = 10 \text{ pF}$$

and

$$Q_0 = 1.0 \times 10^{-12} \text{ Coulombs},$$

which typify the strip parameters and magnitude of charge depositions on the units flown. It can be seen that signal timing is different on the two ends of the strip (provided that injection occured such that $x_0 \neq L/2$). Further, it can be shown that at a given end, the delay time, that is (Elmore, 1948):

$$T_d \equiv \left| \frac{\int_0^\infty dt'\ t'\ i(t')}{\int_0^\infty dt'\ i(t')} \right| \qquad \text{Eq. (1-26)}$$

is a quadratic function of x_0, the injection point. In fact, it can be shown that the difference in delay times at the two ends of the strip can be written as:

R-C
STRIP DYNAMICS

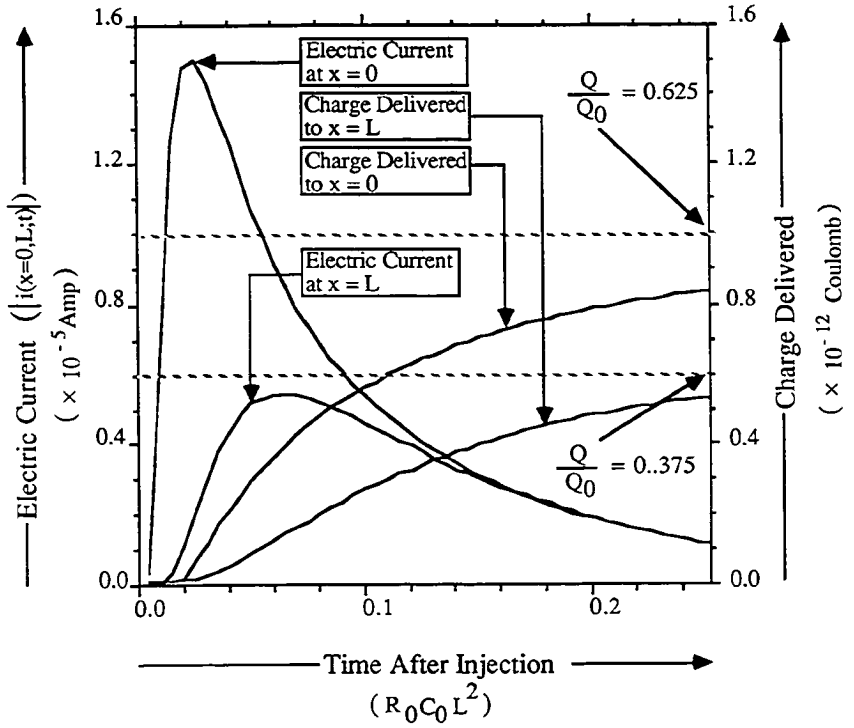

Figure 1-12

$$T_{dA} - T_{dB} = \frac{R_0 C_0 L^2}{6} \left\{ 1 - \frac{2 x_0}{L} \right\}. \qquad \text{Eq. (1-27)}$$

Again, we have a linear relation between a 'measurable' property of the strip outputs and the event location which provides the basis for electronic analysis. I have put the word 'measurable' in quotes because, in fact, the difference between the delay times is not an easily measurable parameter of the output signals. Commonly, the difference in peak times, $T_{pB} - T_{pA}$ is measured. This difference cannot, in general, be shown bear a linear relation to event location but, in practice, it can be close enough to linear to be useful. Exceptions are found in functions of t which are symmetric about the maximum. In such cases, $T_d = T_p$ and the linear relation between the difference in peak times and event location is exact.

One can see from Figure 1-12 that the current transient is quite fast. For the strip simulated in that figure, the technique provides a spatial sensitivity of 1 milli-meter per nano-second. This requires very fast circuitry, analyzing what amounts to the initial stages of charge delivery at the strip ends. To slow the signal down significantly would encroach unacceptably on the maximum analyzable event rate, due to pulse pile-up. Therefore, we chose the resistive charge division technique described above for the HEEPS instruments flown on board NASA flights 29.015 and 35.012.

Specific Instrument Construction

Overview

In this section we will describe, in some detail, the scheme by which the concepts discussed in the previous subsections were implemented in the construction and operation of one prototype and two flight HEEPS instruments. The electronics involved were all designed by Mark Widholm, who closely supervised most aspects of the development of these instruments.

The two major components of a HEEPS instrument system are the HEEPS Front End (HFE) and the HEEPS Electronics (HE). The HFE includes the electrostatic analyzer, the MCP assembly, anode and Pre-amp, as well as a high a voltage diode board which delivers MCP high voltage bias levels. This assembly must be deployed in flight, to immerse the electrostatic analyzer entrance aperture in the sampled plasma. The HE includes the HEEPS Logic board (W-37), high voltage (W-2-A-1) and low voltage (W-1-2) power supplies, the analyzer Sweep Reference Generator (W-38) and Sweep Generator (W-8N), as well as a HFE deployment monitor (on W-37) and input power filtration (W-20). The W-numbers identify these boards with schematics on file at the University of New Hampshire.

The HFE and HE are connected through a Cannon Connector #DBM-13W-3P(S)-NMB, where the P (S) is used to specify the male (female) part, and a spliced high voltage jumper along which high voltage MCP bias was transmitted. The HE provides low voltage power for running the HFE pre-amps, the sweeping analyzer electrode bias (0 to -76 Volts) and the jumpered MCP bias. The HFE, in turn, supplies event signals **A** and **B** from the two pre-amplifiers at the ends of the anode strip. Somewhat more detailed descriptions of various instrument components follow.

Analyzers

The prototype analyzer and those built for the 29.015 and 35.012 instruments were machined from aluminum by machinists in the Physics Department machine shop at the University of New Hampshire. The design parameters of greatest interest are tabulated below in Table 1-1. Refer to Figure 1-3 for interpretation of these parameters.

	R_1	R_2	R_3	$\Delta V/R_1$	σ	Θ	α_{coll}
PROTO	0.426"	0.458"	0.495"	0.075	9°	17°	12°
29.015	0.426"	0.478"	0.535"	0.12	9°	21°	12°
35.012	0.426"	0.478"	0.535"	0.12	9°	21°	12°

Table 1-1: HEEPS analyzer parameters (flight and prototype instruments).

Referring to Figure 1-4, the above capped hemisphere parameters *predict* analyzer ratios of 6 and 4, respectively, for the prototype and flight instruments, and geometry factors of

$$G_0 \cong 3.5 \times 10^{-3}\ \text{cm}^2\text{-sr-keV/keV} \quad \text{(prototype)} \qquad \text{Eq. (1-28)}$$

&

$$G_0 \cong 2.3 \times 10^{-2}\ \text{cm}^2\text{-sr-keV/keV} \quad \text{(flight)}. \qquad \text{Eq. (1-29)}$$

These are obtained by applying the prescription outlined previously to the values of (G/R_1^2) read from Figure 1-4. The procedures and results of calibrations of HEEPS units built at UNH can be found in the following subsection.

The analyzers themselves were constructed from three pieces, referred to as the inner, center and outer electrodes, supplying the conducting surfaces at R_1, R_2 and R_3, respectively. These analyzer electrodes are the construction focus and the most massive parts of the HFE. Other parts of the HFE, such as the MCP assembly, the anode and the preamp assembly fasten directly to the center electrode of the analyzer set.

The inner electrode was mounted concentrically within the center electrode. It was neccesary to structurally mate the inner and center electrodes, retain their mutual electrical

HEEPS ELECTRODE SUPPORT

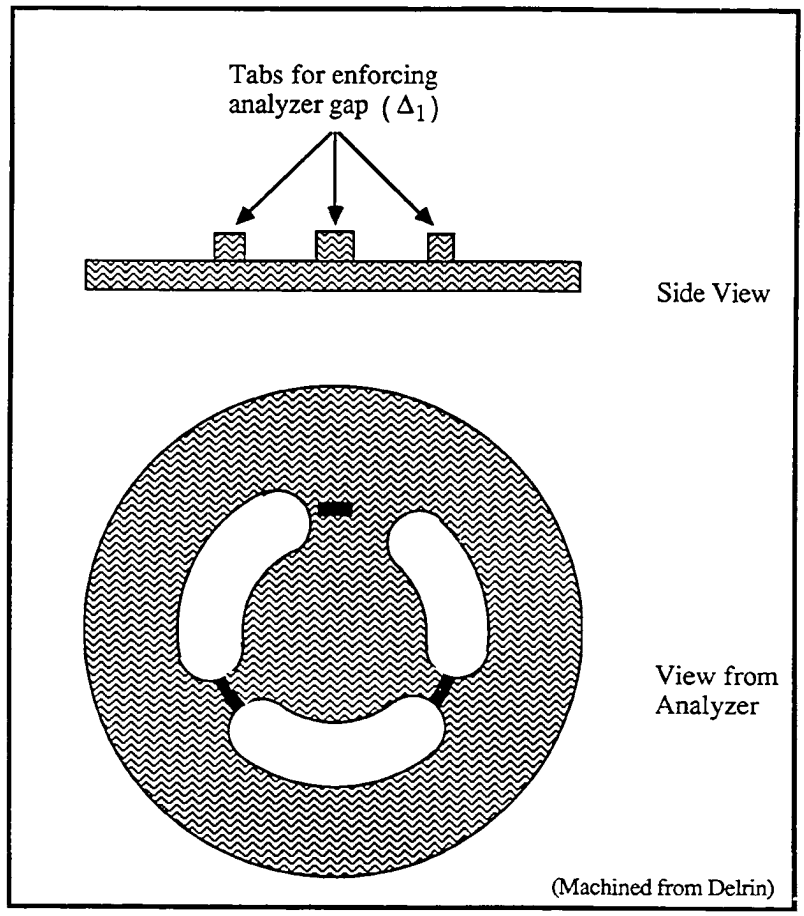

Figure 1-13

isolation and enforce the correct analyzer plate gap (Δ_1) in order to achieve nominal analyzer performance. These tasks were accomplished through the use of a machined delrin electrode support, which is shown in Figure 1-13, on the previous page. This support fastened to the bottom of the center electrode along a 1.36" dia. bolt circle and to the bottom of the inner electrode along a concentric 0.40" dia. bolt circle. The electrode support provided stable mounting of the inner electrode while retaining large angular access for particles at the analyzer exit aperture to the MCP input face. The analyzer plate gap (Δ_1) between the inner and center electrodes was enforced by the electrode support at the three places where delrin bridges the annular aperture with protrusions which extend into the gap, as illustrated in Figure 1-14, below, and which were hand fitted upon manufacture by Arthur Anderson in the Physics Department Machine Shop at UNH. This arrangement imposed three blind spots on the image annulus, the largest of the three being located in the

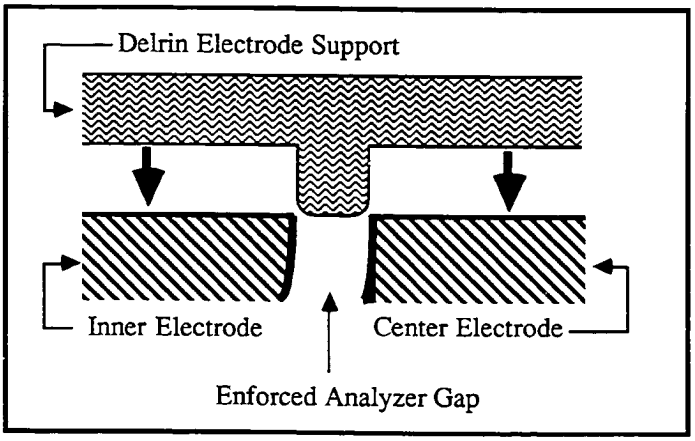

Figure 1-14: Enforcement of Analyzer Plate Gap (Δ_1).

vicinity of the resistive strip ends, where nominal imaging quality is expected to be poorest. This is due to the fact that the one dimensional diffusion model breaks down for locations on the strip such that the distance to a strip end is on the order of the width of the strip.

The other analyzer gap (Δ_2, see Figure 1-15, below) was enforced by standing the outer (*topcap*) electrode off the center electrode with three cylindrical (0.188" diameter) aluminum standoffs located near the outer edge and spaced every 120 degrees. Machine screws passed through these stand-offs, fastening the outer (*topcap*) electrode to the center electrode, with which it was electrically common. Figure 1-15 sketches this and several other assembly features of the HFE. The *topcap* stand-offs were placed complimentarily to the blind spots in the delrin electrode support so that no additional blind space was created.

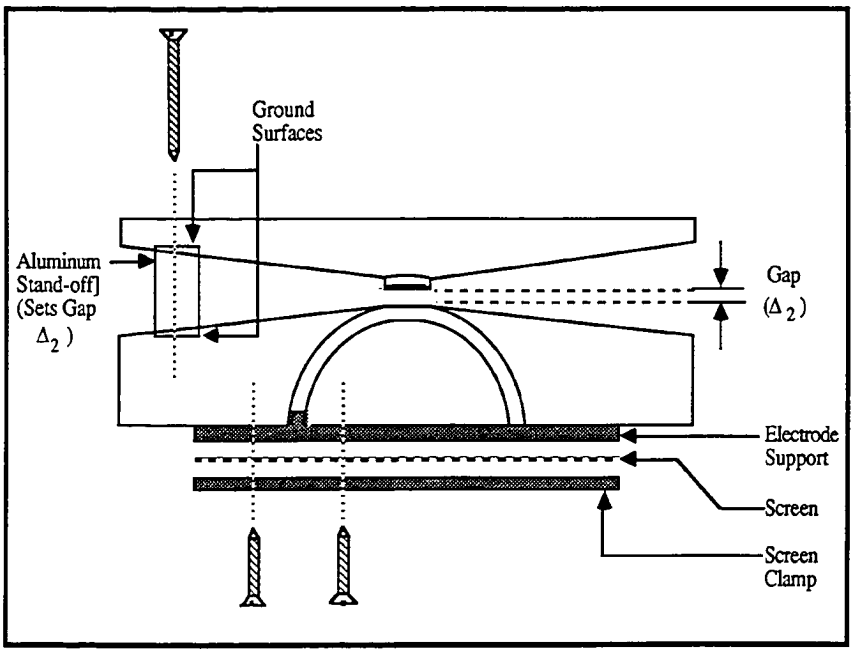

Figure 1-15: HEEPS Analyzer Assembly.

As indicated in the analyzer assembly diagram above, a fine mesh screen was placed immediately below the analyzer exit aperture. Particles passing through the analyzer must pass through the screen before striking the MCP stack input face. No significant reduction in instrument sensitivity was imposed by the screen, as it was

characterized by a transmission ratio of greater than 90%. This conducting screen was held near ground potential, effectively shielding the space between the analyzer electrodes from the input face of the MCP assembly, immediately below, which was held at nearly 2000 Volts negativeby the MCP high voltage supply. Some uncertainty exists with regard to the electrical state of the screen during flight. It is known that it was held either at ground or at +0.7 volts and thought to have been held at ground. Which configuration existed has substantial bearing on the interpretation of the lowest energy (< 1 eV/q) particle fluxes measured during the two flights. One of the major reasons for thinking that the screen was held at ground is that the in-flight data commonly show large event rates at the lowest energy steps, where particles with energies per charge of substantially less than 0.5 Volts are thought to have been selected. If the screen was held at +0.7 Volts, only selected particles with energies per charge greater than 0.7 Volts could have passed through the screen and onto the analyzer input face.

It turned out to be difficult to achieve a 'symmetric' electrostatic bias configuration for the HEEPS analyzers, so we decided to bias them assymetrically, with negative bias applied to the inner electrode and with the outer and center electrodes held at chassis ground, as shown in Figure 1-3. This introduces a systematic error to the nominal energy measurement, in that an incident ion must fall through an electrostatic potential gradient to get onto a nominally selected trajectory. Assymetric biasing tends to reduce the effective analyzer ratio because the selected particle gains energy upon analyzer entry and is *subsequently* selected. The energy responses of the flight instruments were calibrated with particle sources of known energy per charge, so that the error alluded to above is not a factor in the interpretation of the data obtained with these instruments. Coaxial cable was run behind the largest blind spot in the delrin electrode support, along a groove milled into the bottom of the center electrode, to provide the sweeping analyzer bias signal. The cable shield was grounded with a press fit against the center electrode by the delrin electrode support, as is illustrated below in Figure 1-16. The center conductor was soldered to a

brass screw turned into a hole tapped in the bottom of the inner analyzer electrode. This arrangement provided sure bias contact and excellent strain relief.

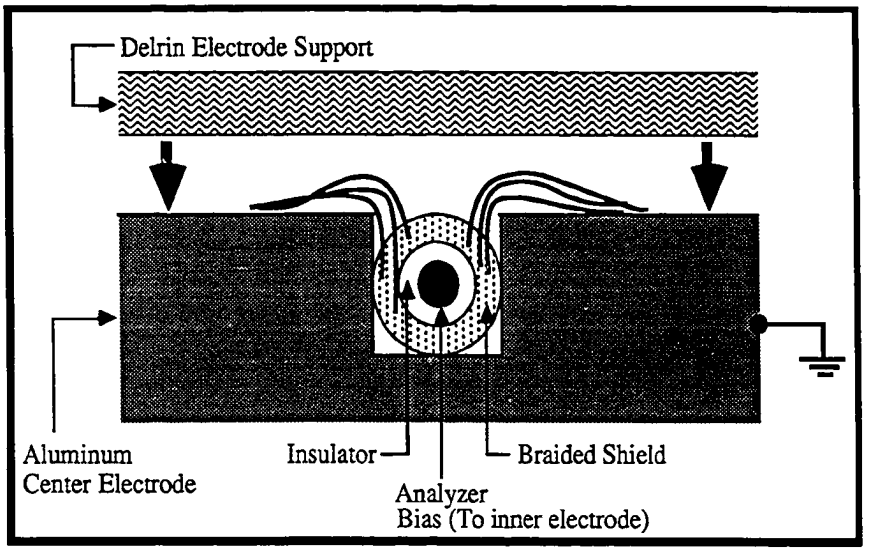

Figure 1-16: Analyzer Sweep Bias Delivery and Cable Shield Grounding With Press Fit to Center Electrode.

MCP Assemblies

The MCPs used in the HEEPS experiments built at UNH were manufactured and marketed by Varian Image Tube Division, Palo Alto California. The models used were Varian model #VUW-8916 ES. The nominal specifications for this model MCP are shown below in Table 1-2. This information was provided by Varian and is standard for this model MCP. The 'ES' designation stands for 'Engineering Sample', which is the lowest quality line that Varian sells.

	Thickness	Diameter	Channel Spacing	Channel Bias	Electron Gain @ 1000 V	Strip Current @ 1000 V
Varian MCP #VUW 8916-ES	0.021"	0.984"	15 μm	11°	Not Specified (typ ~10^4)	Not Specified (typ ~16μA)

Table 1-2: MicroChannel Plate Parameters.

The quality of these units was suitable for our purposes. The pulse height distributions (PHD) of output charge bursts from *chevron* assemblies constructed from these MCPs have not been what we had hoped, however. Several researchers (Timothy, 1974; Timothy & Bybee, 1975) have reported PHDs for *chevron* assemblies which are characterized by full widths at half maximum (FWHM) of on the order of 100 percent, while, at UNH, we have not been able to obtain such distinctive peaks in the *chevron* MCP assemblies. The data in Figure 1-17, on the following page, show two crude PHDs obtained in the laboratory at UNH, illustrating the gain performance of the stack under two different MCP stack bias configurations. It can be seen from this figure that the PHDs are quite broad (~200%). The reasons for this poor performance comparison are not known, although, in my opinion, two actions may yield significant improvement in the *chevron* performance obtained at UNH. First, improvement of handling and storage environment would be helpful, as there has been no practice of storage under dry nitrogen atmosphere, and little control of air quality in the lab, where these devices are handled. Second, it is possible that introducing a potential drop of on the order of a couple of hundred volts between the output face of the input MCP and the input face of the output MCP would tighten up the PHDs. Imposing such a potential drop would accelerate electrons emitted from the first MCP onto the input face of the second MCP, inhibiting the lateral spreading of the charge burst between the plates. This would tend to give lower the average gain, but also to tighten up the PHD. This second approach has not been investigated in the laboratory at UNH.

TYPICAL CHEVRON
PULSE HEIGHT DISTRIBUTIONS

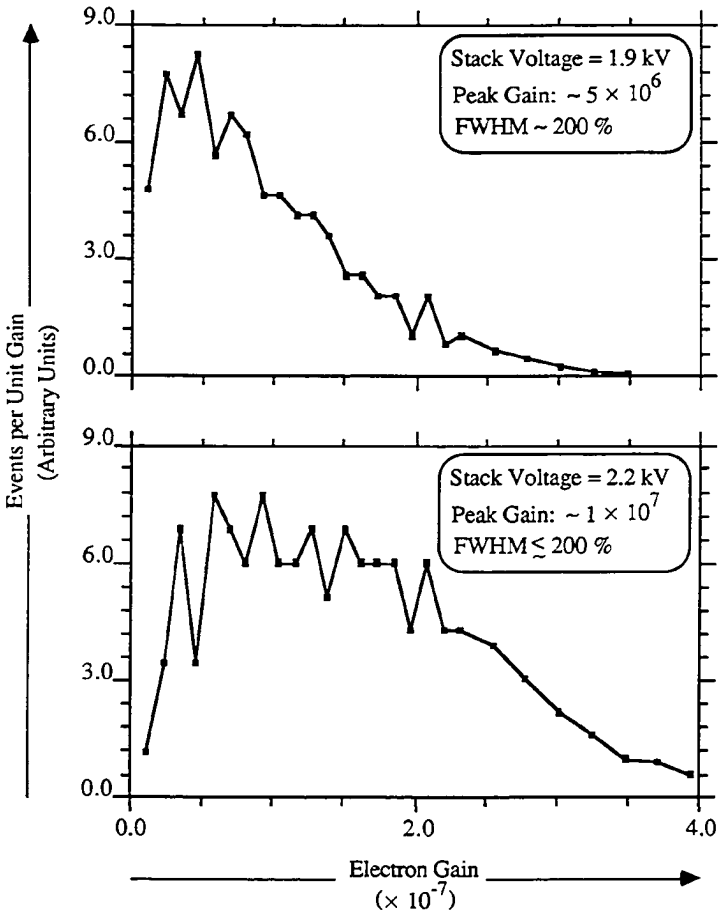

Figure 1-17

The MCP stack was mounted in a concentric circular MCP holder machined from delrin.

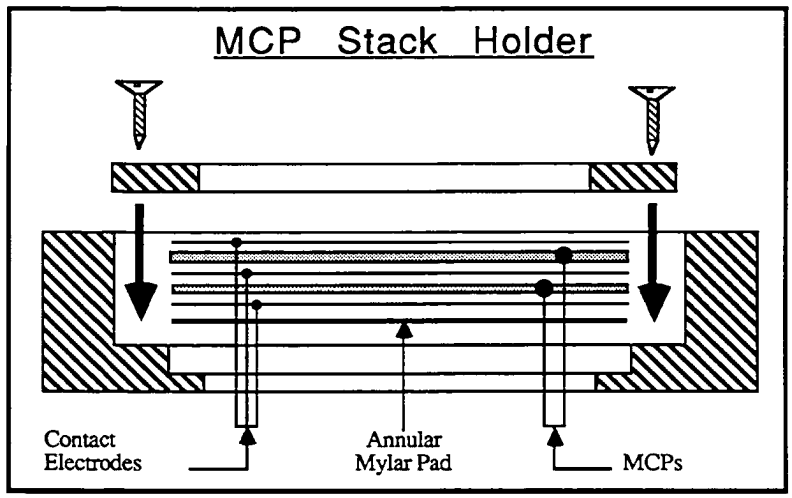

Figure 1-18

This unit, sketched in Figure 1-18, above, provides secure housing for the stack and strain relief for three high voltage bias connections to the MCP contact electrodes. It mounts to the center electrode in such a way that the MCP input face was parallel and in immediate proximity (separation = 0.195") to the analyzer output face. The stack was laid down in a cylindrical cradle milled into the delrin holder and an annular cover was laid down over that and fastened with nylon flathead screws turned into tapped holes in the holder. The spacing was arranged so that the annular mylar pad (~ 0.01" thick) was under slight compression when the system was assembled. This provided a good measure of shock mounting, facilitating survival of the rigors of launch and deployment.

High voltage bias was delivered to the HEEPS Front End (HFE) along one spliced line at –1860 Volts. The high voltage diode chain shown in Figure 1-19, below, served to

enforce zeroeth order voltage division across the MCPs, although the voltage characteristics of the circuit were undoubtedly determined by the resistive MCPs. This diode chain was mounted on a small circular printed circuit board and located inside the HFE, but not as part of the MCP/Anode/Pre-amp stack. It's phyical location within the HFE is shown in Figure 1-22.

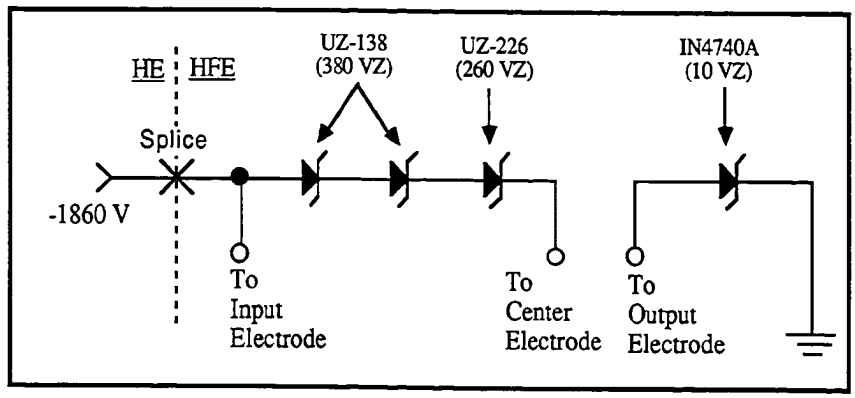

Figure 1-19: Delivery of high voltage bias from the HEEPS Electronics (HE) to the HEEPS Front End (HFE).

Anodes

The resistive-capacitive anode used in all three instruments was described in principle earlier and is well represented in by the sketch in Figure 1-10. The strip was manufactured by Clarostat Mfg. Co., Dover N. H., at a nominal cost to the University of New Hampshire. The carbonised polymer resistive ink (Clarostat's recipe) was applied serigraphically onto a 0.025" thick woven glass laminate (Universal Oil Procucts Co., Norplex Div.'s G-30). Data supplied by Clarostat engineers and displayed in Figure1-20 illustrate the linear resistive properties of the two strips flown in HEEPS units. The strip resistance is charaterized by reasonably good (<3% deviation) linearity over most of the angular range for both strips flown. Nine such resistive-capacitive strips were supplied by Clarostat; the best two having been flown and one committed to the prototype instrument.

HEEPS RESISTIVE ANODE PROPERTIES

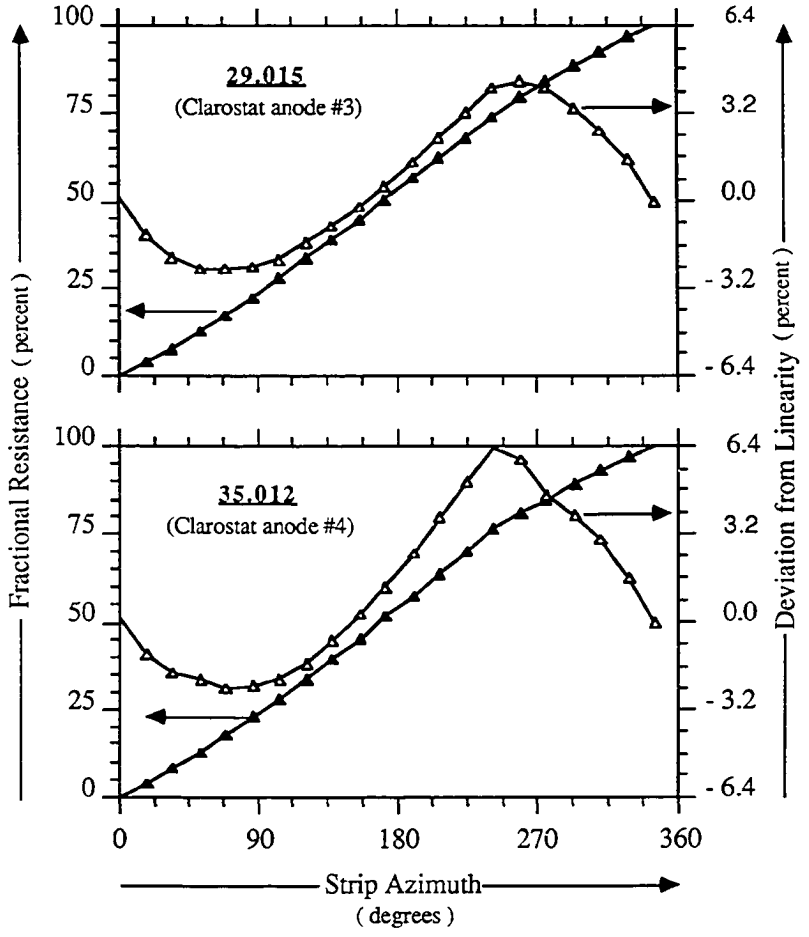

Figure 1-20

The total resistance and capacitance on these strips is typically 70 kΩ and 10 pf, respectively, yeilding a typical strip time constant of ~70 nsec.

The anode was cut into the circular shape shown in Figure 1-10 and mounted directly against the MCP holder with three nylon screws which passed through clearance holes in the MCP holder and fastened into tapped holes in the bottom surface of the center analyzer electrode along a 1.522" dia. bolt circle. In this manner, the anode was located and oriented very close (0.060" separation) and parallel to the MCP stack output face. Terminal stakes were mounted on the non-strip side of the anode and the signals a & b were taken from these directly to the pre-amplifier inputs, less than 1/2" away.

Pre-Amplifiers

Two charge sensitive pre-amplifiers (schematically shown in Figure 1-21), were mounted directly underneath the anode and provided mono-polar output voltage pulses whose timing was determined by the circuit parameters (in the limit of fast strip diffusion) alone and whose amplitude was proportional the amount of charge delivered to the given input ('a' or 'b'). The charge (q) delivered to, say, the 'a' input causes a voltage ($V_1 = q/C_1$) to be developed across C1. Since the input 'a' is held at ground by IC1, and the charge injection at 'a' is negative (MCP electrons), the voltage developed across C1 appears as a positive signal at the IC1 output (pin 6). The time scale for delivery of charge to input 'a' is short compared to the time scale for drainage through R1, so the charge delivery to 'a' may modelled as being roughly impulsive, leaving the signal growth at pin 6 to be limited by the IC1 performance parameters. The voltage at the IC1 output appears across R3, driving a current onto the input node (pin 2) of IC3. The charge accumulated on this node will drain across R5 on the R5*C5 time scale, giving rise to the output voltage pulse (A) at IC3, pin 6. The gain of the second stage for the 'a' ('b') side is given by the ratio R5/R3 (R4/R6).

HEEPS
PRE-AMPLIFIERS

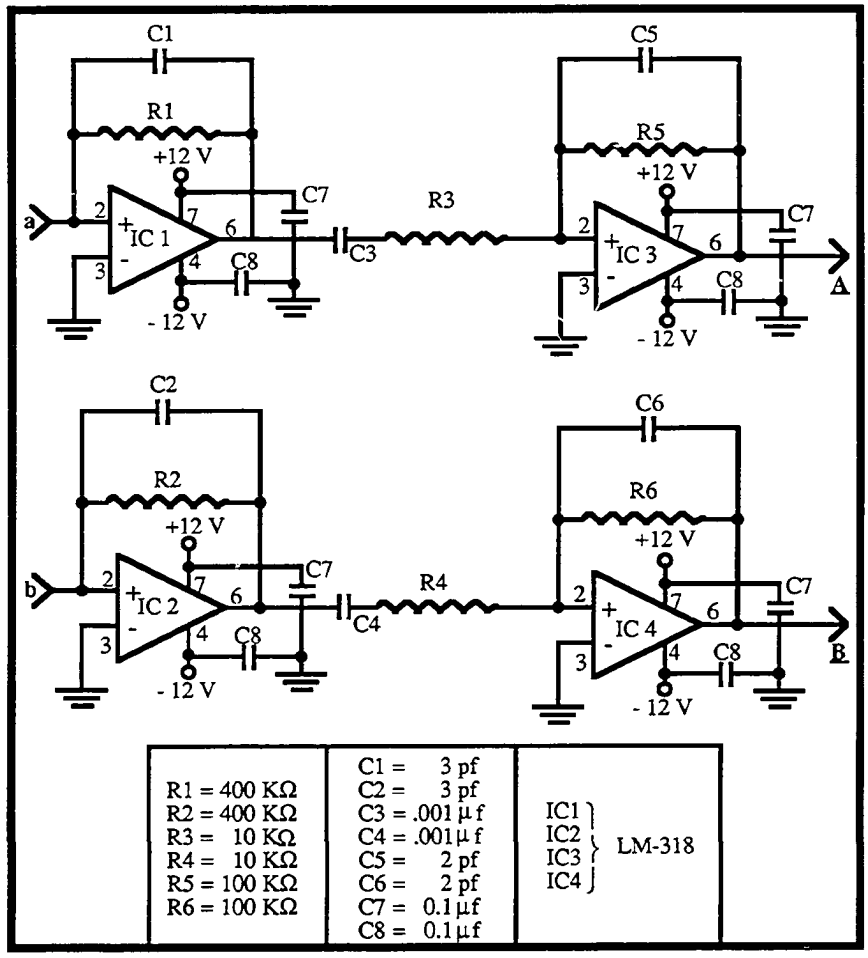

Figure 1-21

This pre-amplifier pair was built on a circular (1.75" dia.) printed circuit board, with the component side foiled (as much as possible) with ground plane. The pre-amplifier circuit board was stood off of the anode on .375" long nylon stand-offs, with the component side of the board facing away from the stack components previously described. Signals from the anode were fed into eyelets on the pre-amplifier board. The signals **A** and **B** (pre-amp outputs) were taken from the pre-amplifier board, out of the HFE along two shielded coaxial cables and delivered to the **A** and **B** inputs of the HEEPS Logic Board.

HFE Superstructure

The entire HEEPS Front End is illustrated in Figure 1-22. The HFE was held together by spanning the center analyzer electrode, a bulkhead wall and an end cap with a cylindrical aluminum cover which provided rigidity to the entire unit. The aluminum cover was composed of two half-cylinders, so that access to the inside of the HFE could be achieved while maintaining structural rigidity. These pieces were all machined from aluminum at UNH. The end cap included a mounting bracket to which a swinging deployment arm (aluminum U-channel) was attached. This arm shrouded the cable bundle which carried the signals exchanged between the HFE and HE units.

HEEPS Logic

The signals **A** and **B**, taken from the HFE, are brought to inputs on the HEEPS Logic Board (W-37) along two shielded coaxial cables. Figure 1-23 shows, in crude block diagram form, the main elements of the logic circuit. This board features linear signal conditioning in the stages preceeding ADC input, which is not shown in the block diagram. These linear stages provide 'tweaking' facilities including offset, balance and range adjustment potentiometers ('pots'). The offset adjustment permits nulling of accumulated DC offsets in the linear operational amplifiers (LM-318) on the pre-amplifier

HEEPS FRONT END (HFE)

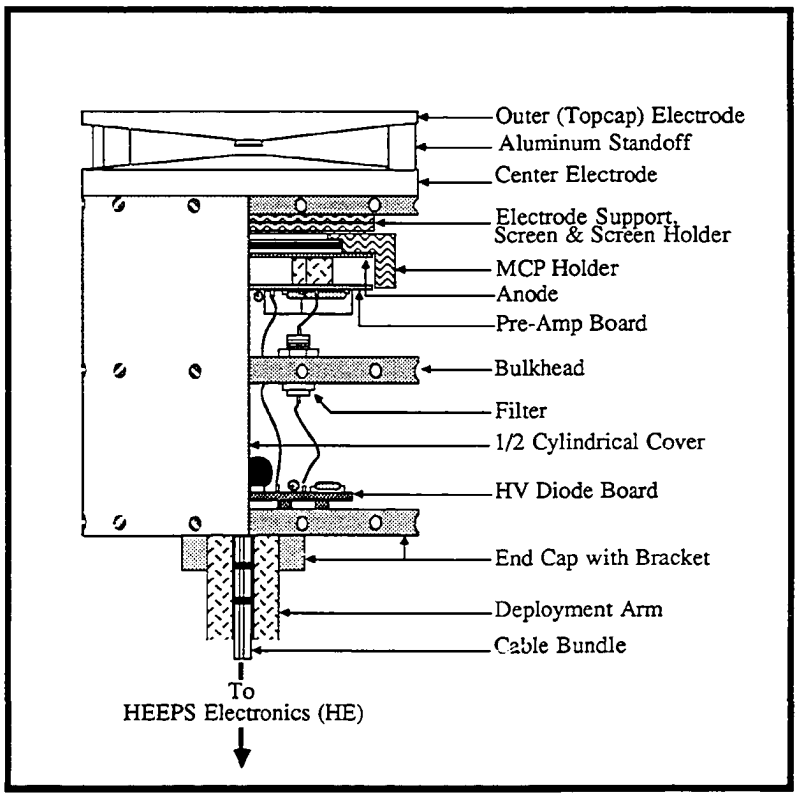

Figure 1-22

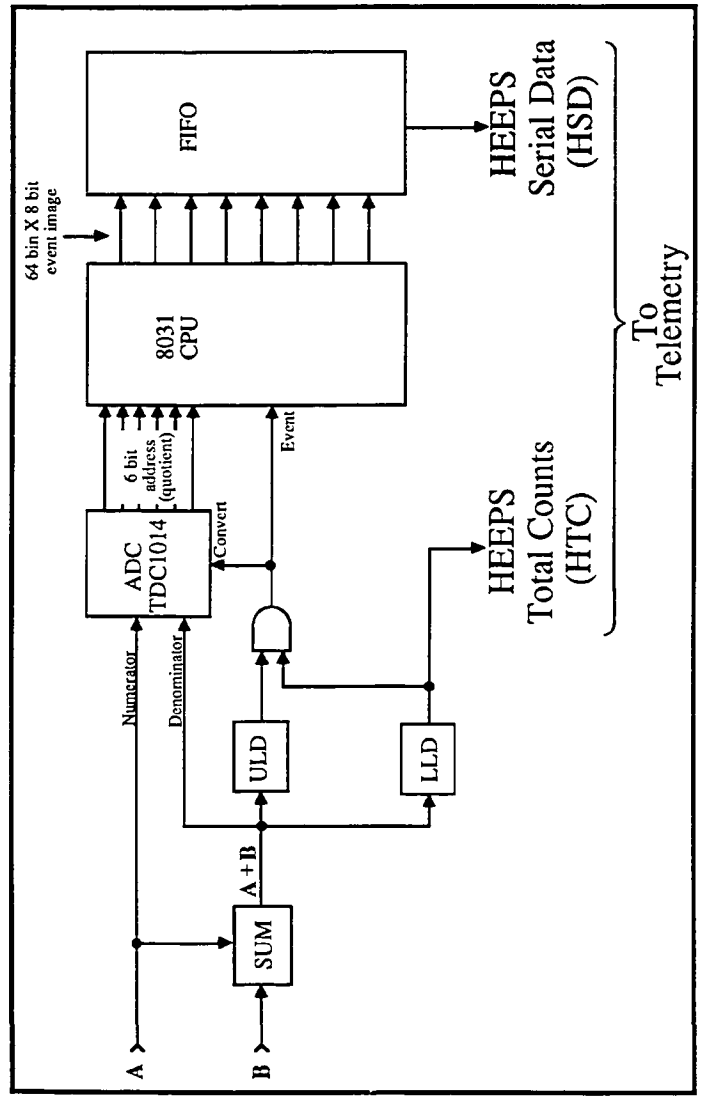

Figure 1-23

and logic boards. The balance and range adjustments enable variations in signal gains such that the quotient (Q) evaluated by the ADC is given by the expression:

$$Q = \frac{k_1 A}{A + k_2 B},$$

where the parameters k_2 and k_1 are determined by the balance and range adjustments, respectively. These adjustments allow inbalances in the linear amplification stages between the resistive strip and the ADC inputs to be compensated for. The balance and range pots were set iteratively with the HFE in the vacuum chamber and under particle bombardment from fixed and known directions.

The six-bit (TDC1014) analog to digital converter (ADC) takes the signal k_1A as input, and the signal $(A + k_2B)$ as reference and delivers the quotient as a six bit (0 - 63) address to the 8031 microprocessor, which increments the counts in the given address location by one. These counts are accumulated as sixty four 8-bit words in the 8031 1 k-byte RAM for the duration of an energy step dwell, after which the 64-bin x 8-bit spectrum is passed to the FIFO (first in-first out) data buffer for storage and read out to telemetry as serial data. The transient nature of the input and reference signals to the ADC requires good temporal synchronization of the two signals and timely delivery of a convert command signal to the ADC. The use of the TDC1014 ADC, with its fast (~25 nsec) conversion on command, allows the use of a transient reference signal, eliminating the need for retention of the pulse amplitude or for evaluation of the quotient prior to ADC analysis.

All events for which the denominator exceeds a lower threshold are counted in the HEEPS Total Counts (HTC) signal, while only those events for which the denominator falls between the lower and an upper threshold are accepted for ADC analysis. This is because the TDC1014 requires a reference signal which falls within a given voltage range. Specifcally, the performance specification of ±1/4 LSB linearity is given for reference

voltages of between 0.8 -1.2 Volts. It is this aspect of the logic board performance which would benefit from narrower pulse height distributions out of the MCP assembly.

The short term storage of the bin spectrum in the 8031 (while other signals are available immediately for telemetry interrogation) means that the serial angular image data lags other data in the telemetry stream by the energy step dwell time, which was ~12.8 ms in the case of flight 29.015 and twice that in the case of flight 35.012. The 8031 is an 8-bit processor. Therefore, the bin spectrum is composed of 8-bit words, giving a maximum event rate of 256 per bin between readouts before the bin count wraps around. The telemetry system on both flights 29.015 and 35.012 were based on a 10-bit word, so that every word of HEEPS serial data contains two garbage bits which must be properly masked upon post-flight analysis.

The telemetry data rate from NASA flight 29.015 was 400 k-bits per second, while the data rate from the 35.012 TM system was half that at 200 k-bits per second. The placement of the HEEPS and aspect magnetometer data within the telemetry data stream is shown in the paragraph structure diagram in Figure 1-24, for the case of flight 29.015, while the same information for flight 35.012 is shown in Figure 1-25.

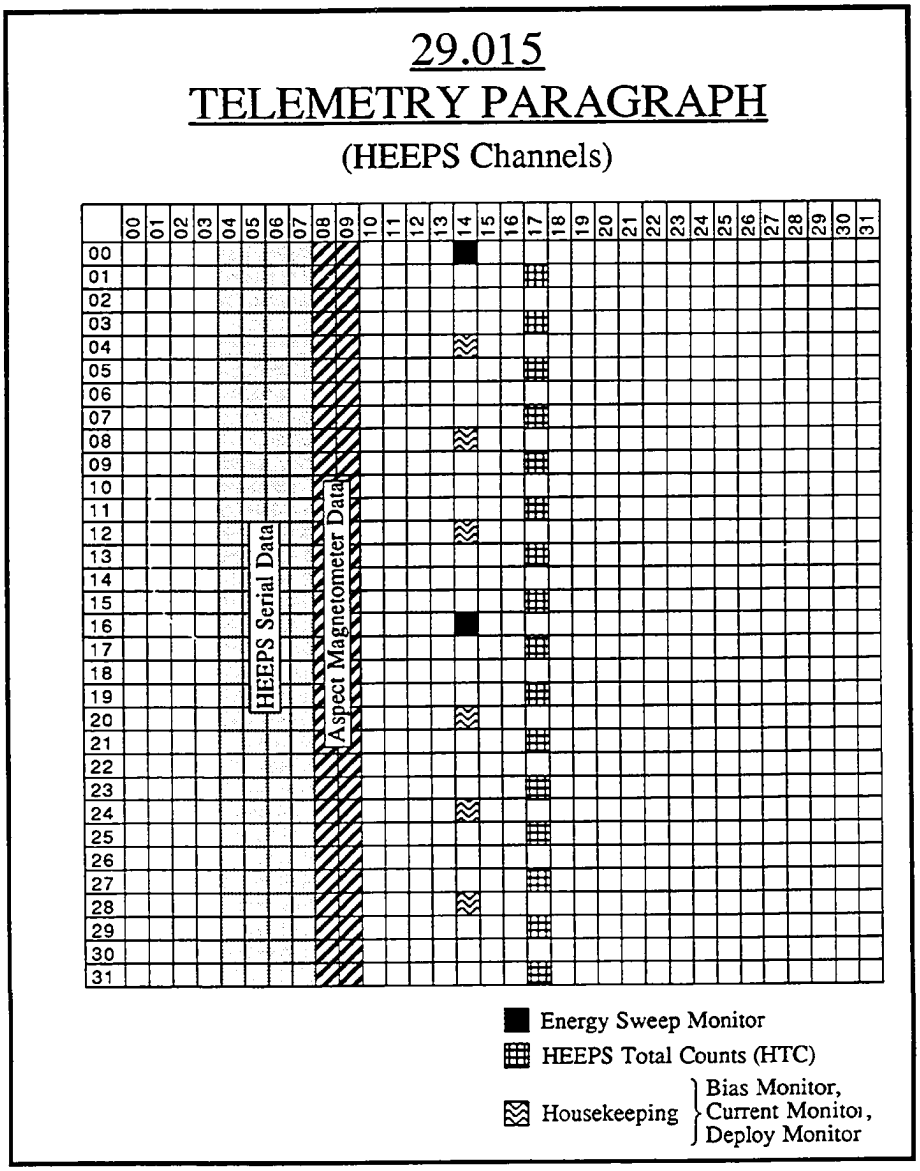

Figure 1-24

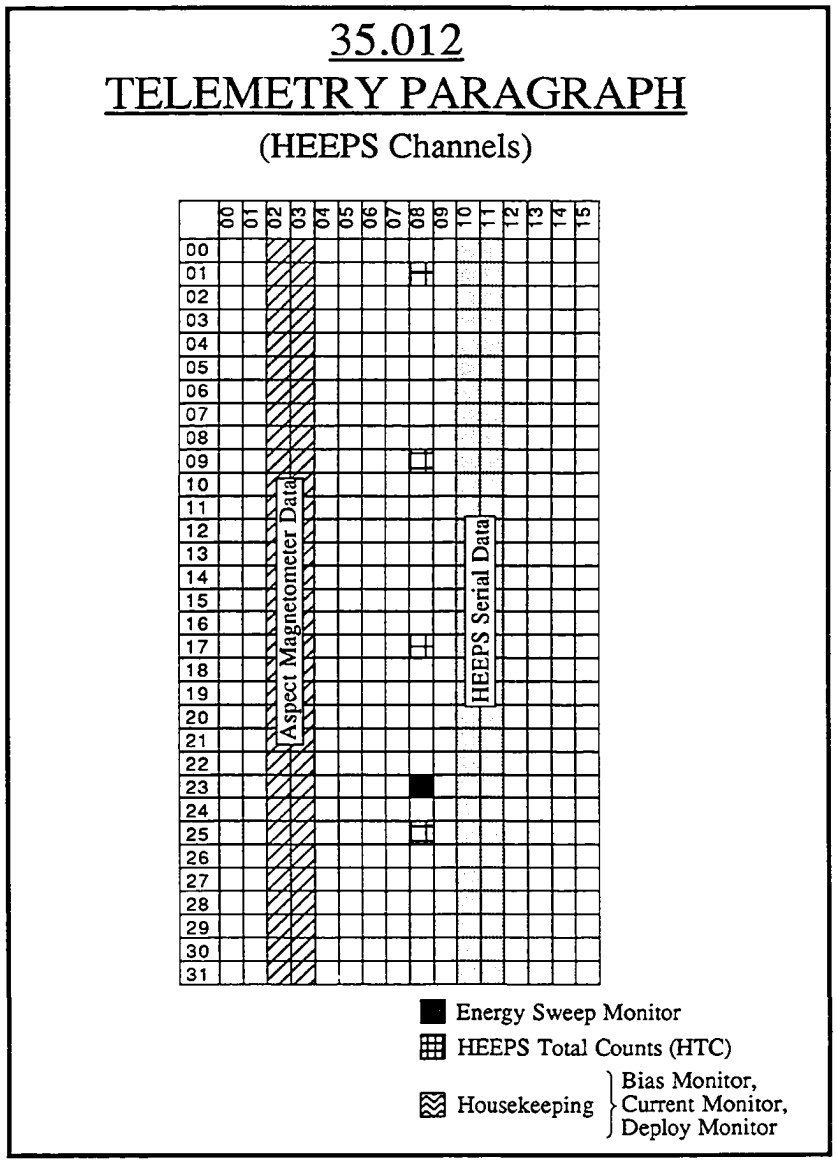

Figure 1-25

Instrument Calibration Procedures

The theoretical aspects of the performance of an instrument such as HEEPS provides a basis for understanding the relationship between the instrument response and the particle flux environment in which it operates. However, laboratory calibration is necessary in order to derive quantitative flux measurements from the in-flight data. The information that one can derive from the operation of a properly calibrated electrostatic analyzer deployed in a plasma environment consists of the magnitude of the differential directional particle flux (J') as a function of the particle energy per unit charge (ε) and motional direction. For an instrument such as HEEPS, the calibration should provide the answers to the following questions:

1) What is the probable energy per charge (ε_j) associated with particle events recorded in energy selection state j and what is the probable uncertainty ($(\delta\varepsilon)_j$) in the energy per charge?

2) What is the probable source direction (θ_i,ϕ_i), with respect to a coordinate system fixed in the instrument (see Figure 1-31), associated with a particle event recorded in angular imaging bin i and what is the probable uncertainty ($(\delta\theta)_i,(\delta\phi)_i$) in the source direction?

3) What is the probable magnitude of the differential directional flux ($J'_{i,j}$) of charged particles associated with a recorded event rate ($C_{i,j}$) in angular imaging bin i and energy selection state j and what is the probable uncertainty ($(\delta J')_{i,j}$) in this flux magnitude?

Given the answers to these questions and instrument data in the form $C_{i,j}$ for various i and j, then the functional values

$$J'(\theta_i,\phi_i,\varepsilon_j),$$

where θ_i and ϕ_i define the look direction for the i^{th} bin, and associated uncertainties follow.

Energy Calibration

Calibration of the energy response of the HEEPS instruments flown on flights 29.015 and 35.012 was carried out in the laboratory at The University of New Hampshire during the summer and fall of 1984. The objectives of these calibrations were two-fold:

1) To determine the energy per unit charge for particles to which the instrument is most sensitive as a function of the applied analyzer bias voltage.

2) To determine the FWHM of the transmission vs ε curve as a function of center energy per charge (ε).

The experimental arrangement for these measurements, which were carried out under high vacuum, is shown in Figure 1-26. Ions produced near the hot, positively biased gun anode are accelerated toward the grounded conducting cathode. Some of these ions pass through a small hole in the cathode and arrive at the HEEPS entrance aperture with an energy per charge:

$$\varepsilon_g = V_g,$$

where V_g is the bias applied to the hot filament. Typically, the analyzer plate bias (V_p) is held fixed while the gun bias (V_g) is varied and event rate data is recorded as a function of gun bias. The data generated from such an experiment is shown in Figure 1-27, where the normalized event rate is plotted versus gun bias for a fixed analyser plate bias of 18.8 volts. In this case the energy per charge at maximum transmission is

$$\varepsilon_0 = 80 \text{ Volts}$$

and the FWHM of the transmission curve is given as

$$\text{FWHM} = (14 \text{ V} \div \varepsilon_0) \times 100\% = 18\ \%.$$

In Figures 1-28 & 1-29, the center selected energy (ε_0) is plotted versus the analyzer plate bias for the 29.015 and 35.012 HEEPS units, respectively. The selected

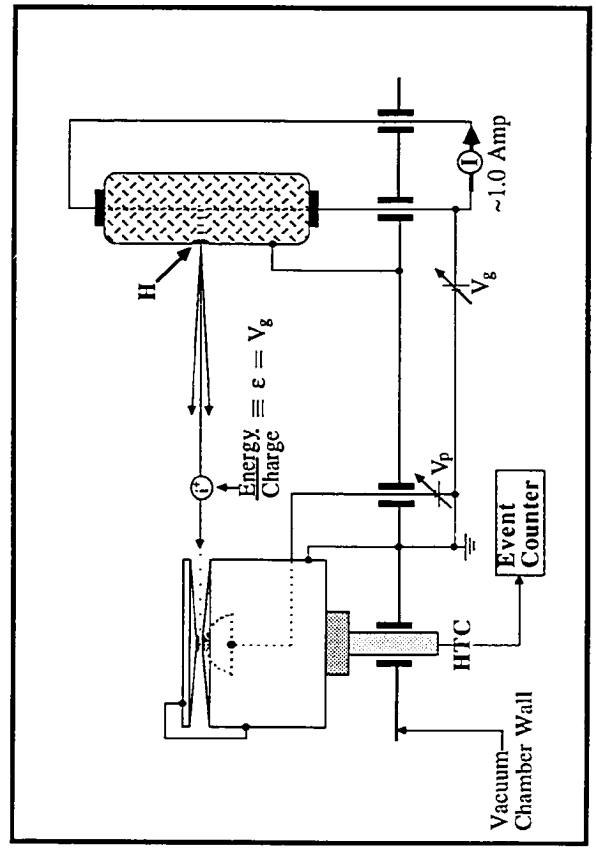

Figure 1-26

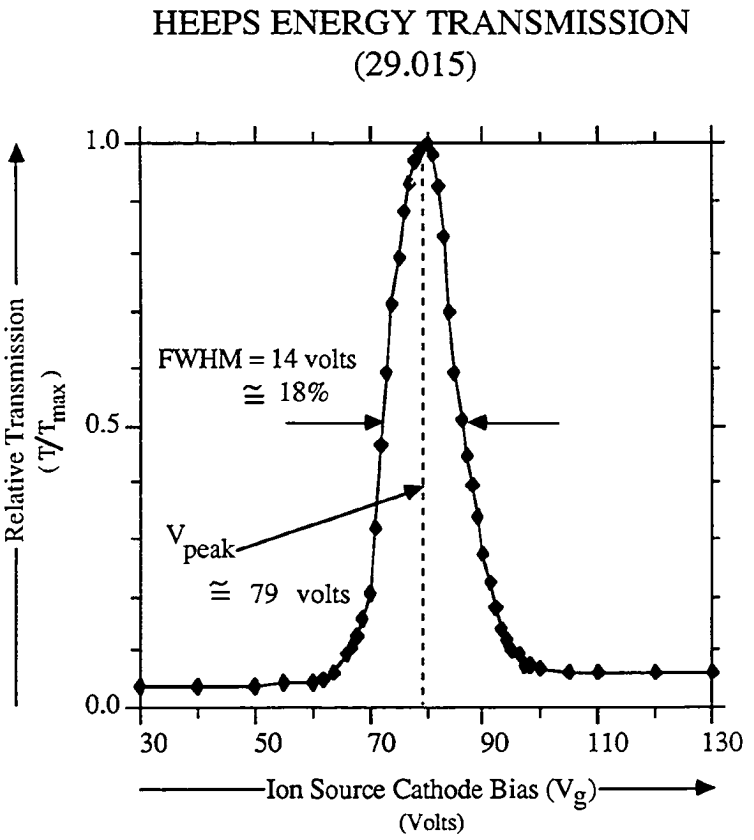

Figure 1-27

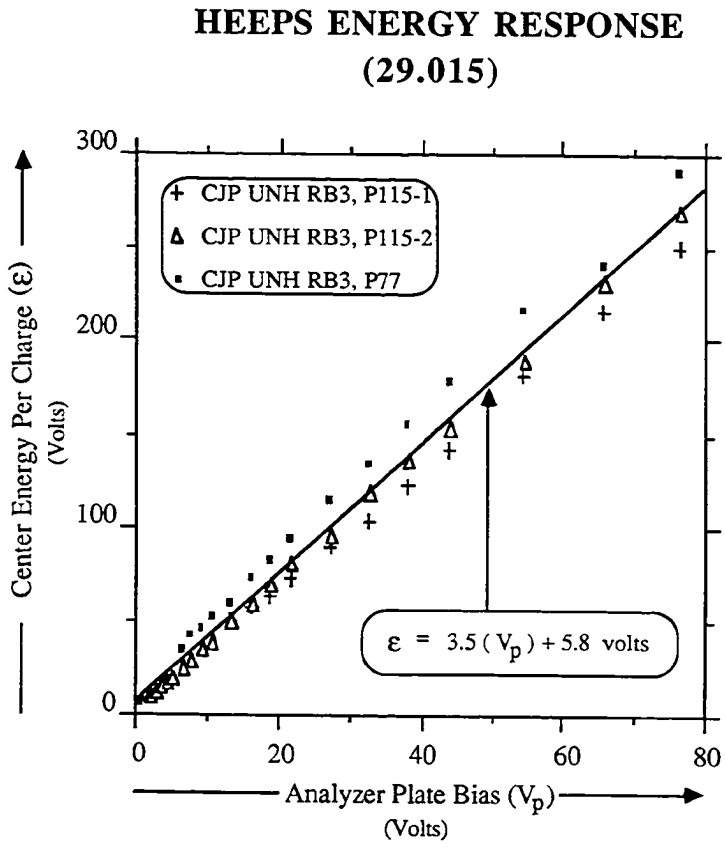

Figure 1-28

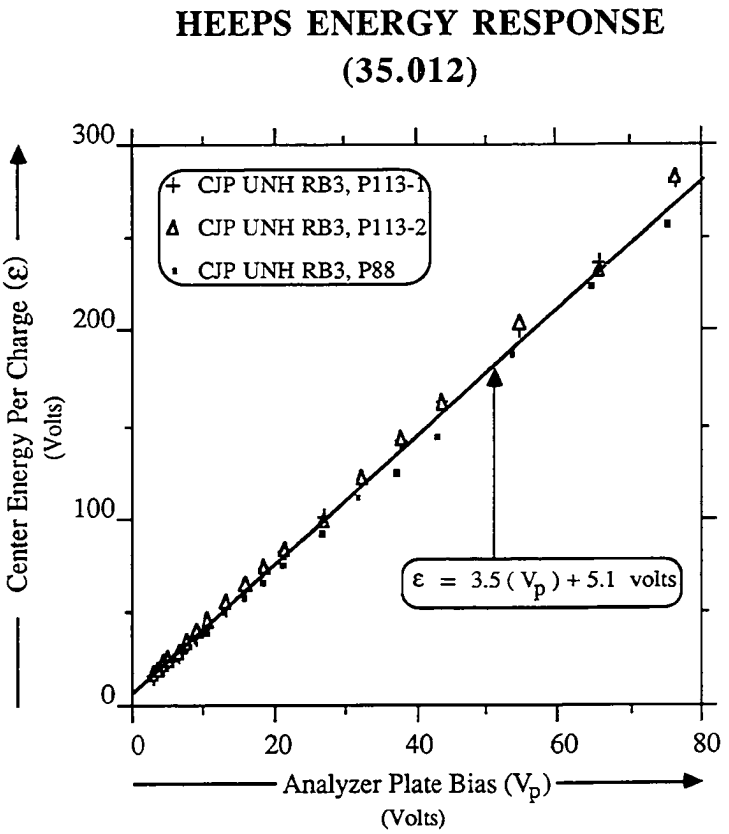

Figure 1-29

energy is a nearly linear function of plate bias. Linear regression analyses on these data yield the following equations:

$$\varepsilon = 3.5\,V_p + 5.8 \text{ Volts} \quad (29.015) \qquad \text{Eq. (1-31)}$$

$$\varepsilon = 3.5\,V_p + 5.1 \text{ Volts} \quad (35.012). \qquad \text{Eq. (1-32)}$$

The fact that these regression results give non-zero intercepts is not understood. One does not expect that, with zero plate bias applied to the analyzer, 5 eV particles would be selected. Rather, it is expected that in the limit of zero analyzer bias, zero energy particles would be selected. In the analysis of the in-flight data, it is assumed that these offsets are artifacts of the calibration experiments, although no plausible explanation of their presence has been concieved.

For the purpose of analyzing the in-flight data, it is convenient to use the functional dependence of the selected energy per charge upon energy sweep step number. This dependence is roughly exponential and may be derived from the energy calibration data, since it was the flight power supplies which provided the analyzer bias during the calibration experiments, and the step number was included in the recorded calibration data. Table 1-3 gives the values of the selected energy per charge for the 32 HEEPS energy steps for the two flights 29.015 and 35.012, under the assumption that the regression intercepts alluded to above are invalid artifacts. The values in this table are those used in the in-flight data analysis.

Figure 1-30 shows the FWHM of the transmission vs gun bias curve plotted versus and as a percentage of center transmission energy per charge (ε_0). It can be seen from Figure 1-30 that the two instruments flown had energy per charge bandpass widths of 16 to 18 percent with the mean of all the measurements being closer to 16%.

Some comments are appropriate with regard to the energy response of these instruments:

1) The 29.015 and 35.012 HEEPS instruments were built to identical specifications. Their energy response characteristics should reflect this uniformity.

Selected Energy Per Charge (HEEPS Flight Units)

	Selected Energy per Charge (Volts)	
Energy Step	Flight 29.015	Flight 35.012
0	0.2	0.4
1	0.2	0.4
2	0.2	0.4
3	0.7	0.4
4	1.1	0.9
5	1.7	1.5
6	2.4	2.2
7	3.2	3.1
8	4.1	4.1
9	5.3	5.2
10	6.6	6.2
11	8.1	8.1
12	9.9	10
13	12	12
14	15	15
15	18	18
16	21	21
17	25	25
18	30	30
19	36	36
20	43	42
21	51	50
22	60	59
23	72	70
24	85	83
25	100	97
26	119	115
27	140	135
28	166	159
29	196	187
30	231	220
31	273	258

Table 1-3

HEEPS ENERGY PASSBAND

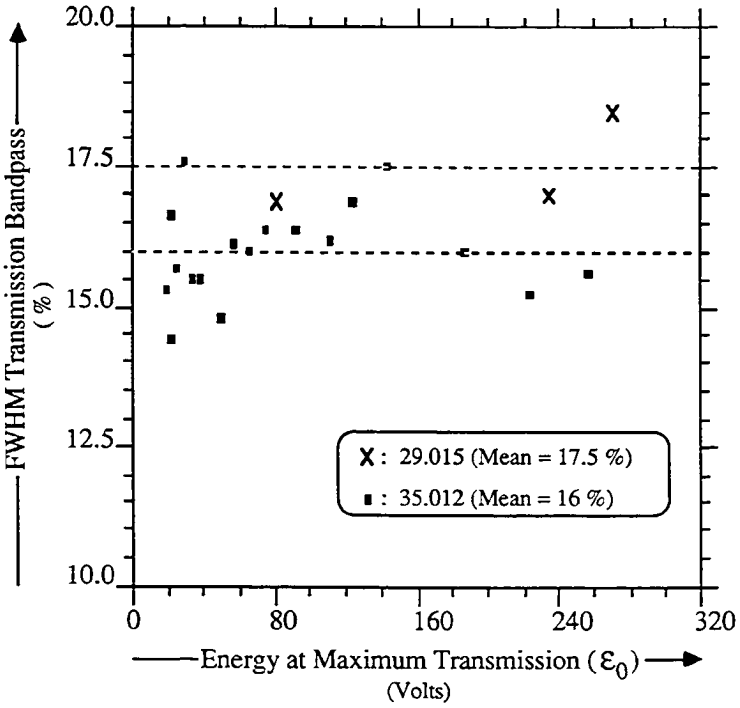

Figure 1-30

1) The 29.015 and 35.012 HEEPS instruments were built to identical specifications. Their energy response characteristics should reflect this uniformity. Indeed, the response curves shown in Figures 1-28 and 1-29 are identical to within the estimated errors in the linear parameters. This does not hold for the bandwidths shown in Figure 1-30, although only three data points are shown in that figure in the case of the 29.015 instrument.

2) The energy response of a capped hemisphere analyzer depends on the polar incidence angle, θ (See Figure 1-31). The measurements described above were carried out with an effective point source located near $\theta = 90°$, but with no controlled variation in polar angle incorporated. Measurements carried out at the Marshall Space Flight Center Low Energy Ion Facility (LEIF) and described in a subsequent subsection of this thesis show, however, that the center selected energy, ε_0, varies by ~20% over the range of polar angles for which the transmission is appreciable (see Figure 1-40)).

3) The scatter in the measurements shown in Figures 1-28 & 1-29 is not only significant, but is systematic as well, with data collected at different times tending to fall along distinct lines. The source of this variation is unknown, but it is plausable that it is due to differences in polar incidence angle, which was not tightly controlled during these calibrations.

Azimuthal Angular Calibration

As with the energy calibrations, the HEEPS azimuthal angular calibrations were carried out in the laboratory at the University of New Hampshire during the summer and fall of 1984. The experimental apparatus used to carry out these angular calibrations was quite similar to that used for the energy calibrations (Figure 1-26), and is illustrated in Figure 1-32. Notable differences in the apparatus are the calibrated rotational vacuum

HEEPS
ENTRANCE APERTURE

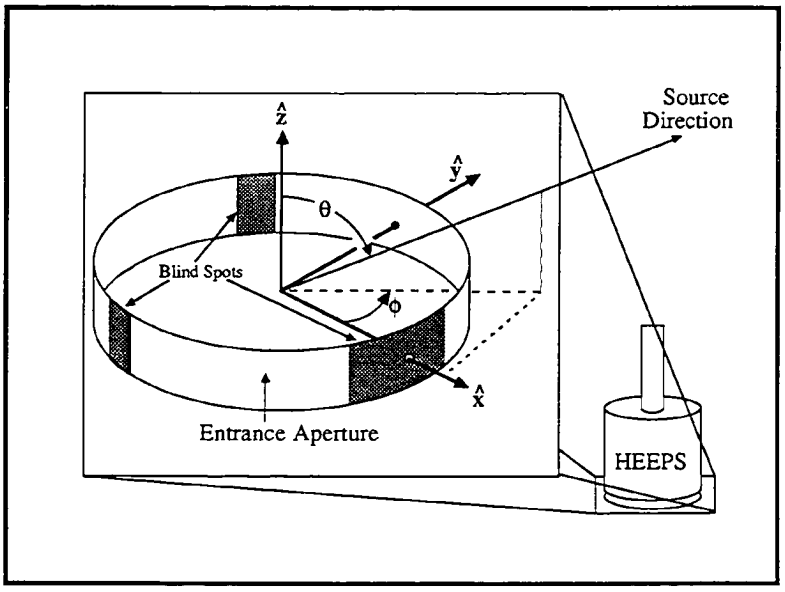

Figure 1-31

AZIMUTHAL ANGULAR CALIBRATION

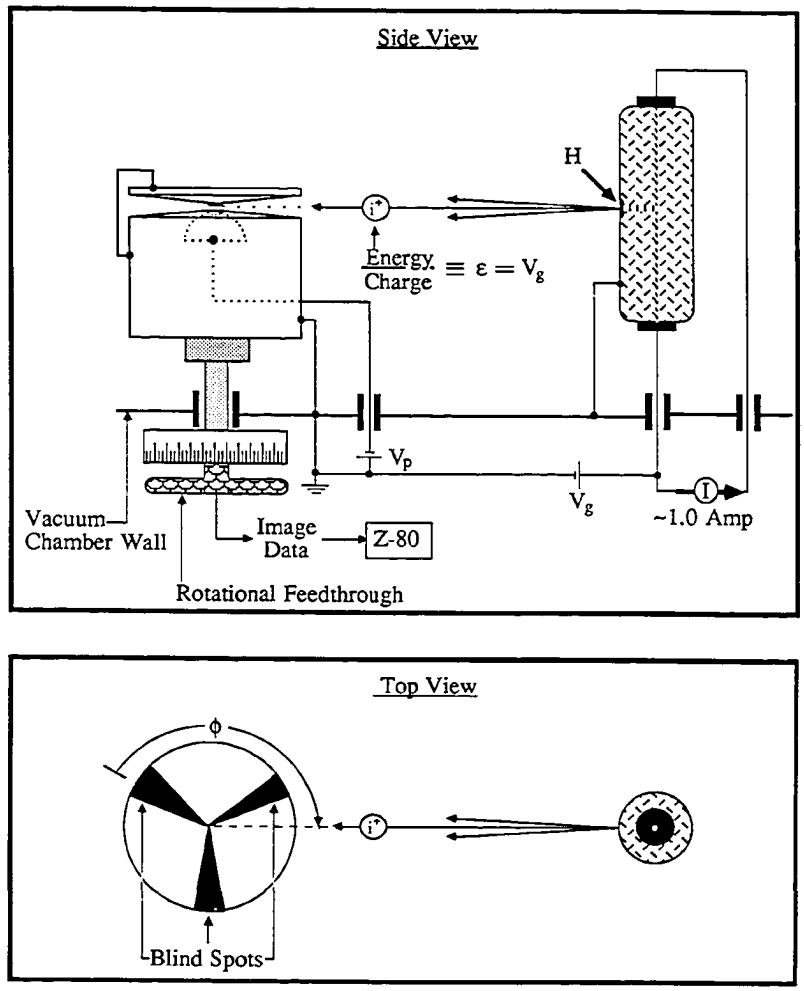

Figure 1-32

feedthrough and the collection and storage of HEEPS image data in the case of the azimuthal angular calibrations. The objectives of these measurements were:

1) To determine the relative instrument sensitivity as a function of particle source azimuth (ϕ, see Figure 1-31) in the vicinity of the three instrument blind spots.

2) To determine the probable source azimuth (ϕ_i) for particles exciting events in angular imaging bin i.

3) To determine a measure of the uncertainty in source azimuth ($(\delta\phi)_i$) for particles exciting events in angular imaging bin i.

The determination of the relative instrument sensitivity in the vicinity of the blind spots was accomplished by recording the total instrument event rate as a function of source azimuth (ϕ) while holding all other source parameters constant. Plots of the resulting relative sensitivity vs azimuth angle are shown in Figures 1-33 & 1-34 for the instruments flown on flights 29.015 and 35.012, respectively. This information can be used in two ways. First, it can go into the characterization of the absolute instrument sensitivity which will be discussed in a subsequent subsection. Secondly, the calibration of the angular imaging required hours of instrument operation, during which time the particle source could not be relied upon to maintain a constant flux. As described below, the angular sensitivity data was used to weight the angular imaging data in order to obtain meaningful results.

In the case of the azimuthal angular imaging calibration, the calibration data was obtained in the following manner: The HEEPS instrument was mounted on the rotational vacuum feedthrough and rotated about its symmetry axis 'z', so that the hot anode particle source was located at a small azimuth with respect to the detector coordinate system (see Figure 1-32). The source azimuth (ϕ) was recorded as read from the vernier scale attached to the vacuum feedthrough. While the instrument was bombarded by particles from the source, a 64 bin ($0 \leq i \leq 63$) angular event image was accumulated for a fixed period of time and subsequently stored on magnetic disc. The HEEPS instrument was then rotated 2

HEEPS BLIND SPOTS (29.015)

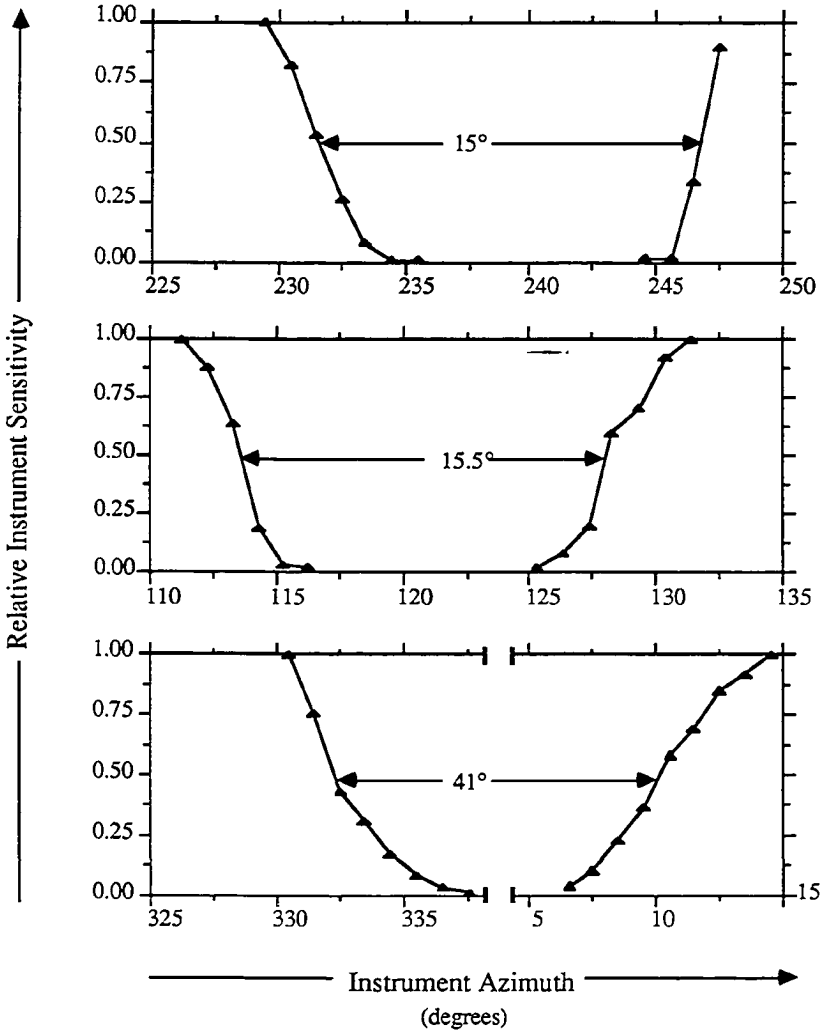

Figure 1-33

HEEPS BLIND SPOTS (35.012)

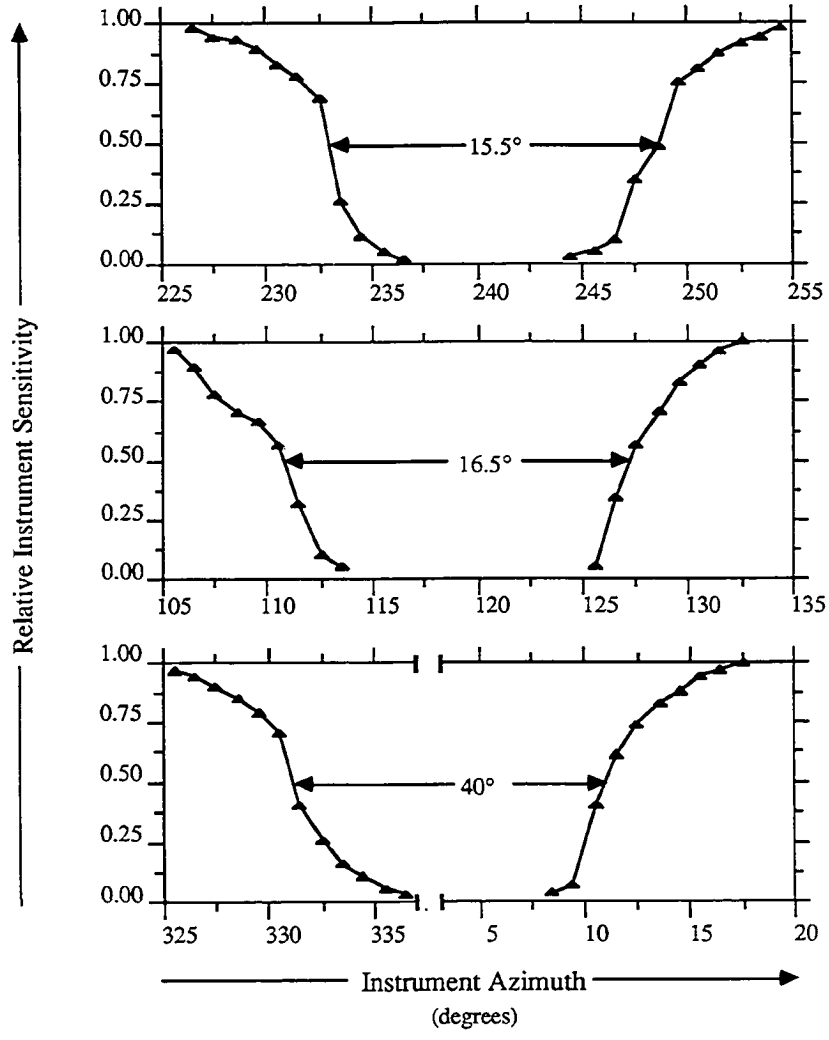

Figure 1-34

degrees, incrementing the source azimuth by that amount and a new angular event image was recorded and stored. This process was repeated, collecting data every 2 degrees, until the entire sensitive azimuthal range of the instrument had been covered. The above procedure provided a data matrix

$$C[h,i],$$

which represents the number of events recorded in bin i while the source was located at detector azimuth

$$\phi_h \equiv 2 \times h \quad (0 \leq h \leq 179), \qquad \text{Eq. (1-33)}$$

where h is an azimuthal index.

The reduction of this calibration data involves the definition of a probability

$$P[h,i]$$

that a particle event in a given bin (i) originated from a source at a corresponding detector azimuth (ϕ_h). This probability is given as

$$P[h,i] = \frac{(C[h,i] \times W[h])}{\sum_h (C[h,i] \times W[h])}, \qquad \text{Eq. (1-34)}$$

where W[h] is a weighting function and is equal to the relative instrument sensitivity at the azimuth ϕ_h. In cases where this sensitivity is less than 0.05, we define:

$$W[h],$$

$$C[h,i],$$

$$P[h,i] \equiv 0. \qquad \text{Eq. (1-35)}$$

Figures 1-35 & 1-36 show grey scale displays of P[h,i], as derived from laboratory calibration data, versus ϕ_h and i for the HEEPS instruments flown on 29.015 and 35.012, respectively. The zeroeth order linearity of these instruments as well as distortion of imaging quality in the vicinity of the blind spots (near 120 and 240 degrees) and strip ends (near 0 and 360 degrees) is apparent in these figures.

In addition, moments of P[h,i] may be taken over h, in order to identify a probable source direction and associated uncertainty with a given bin (i). Specifically,

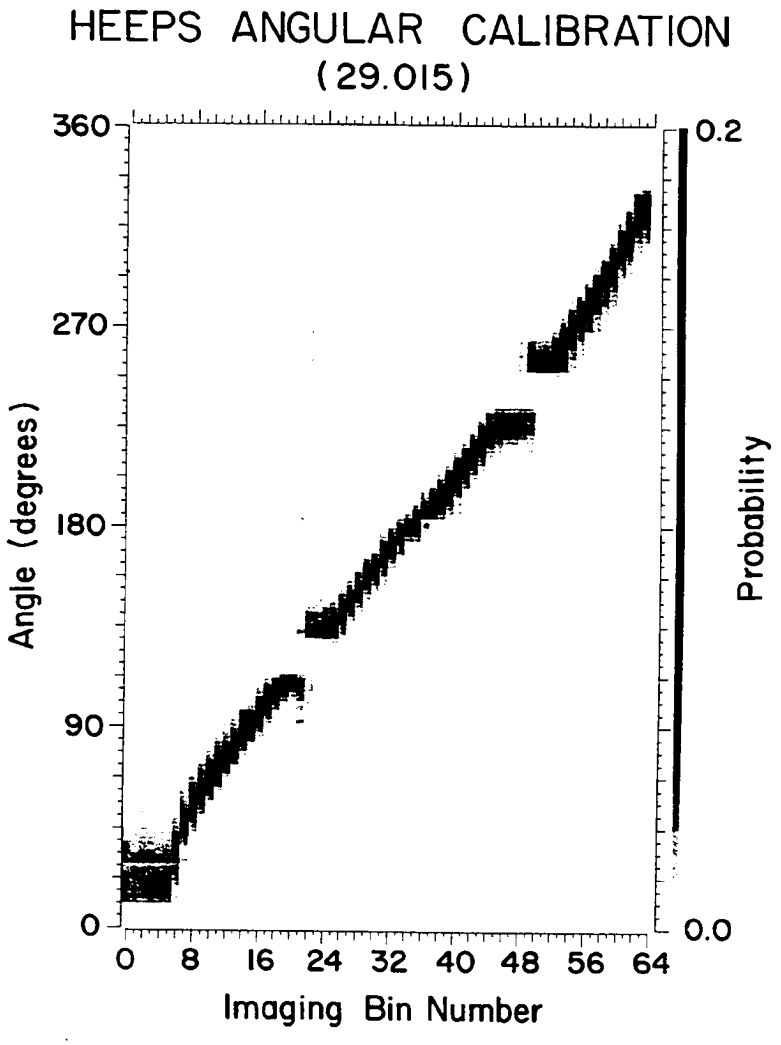

Figure 1-35

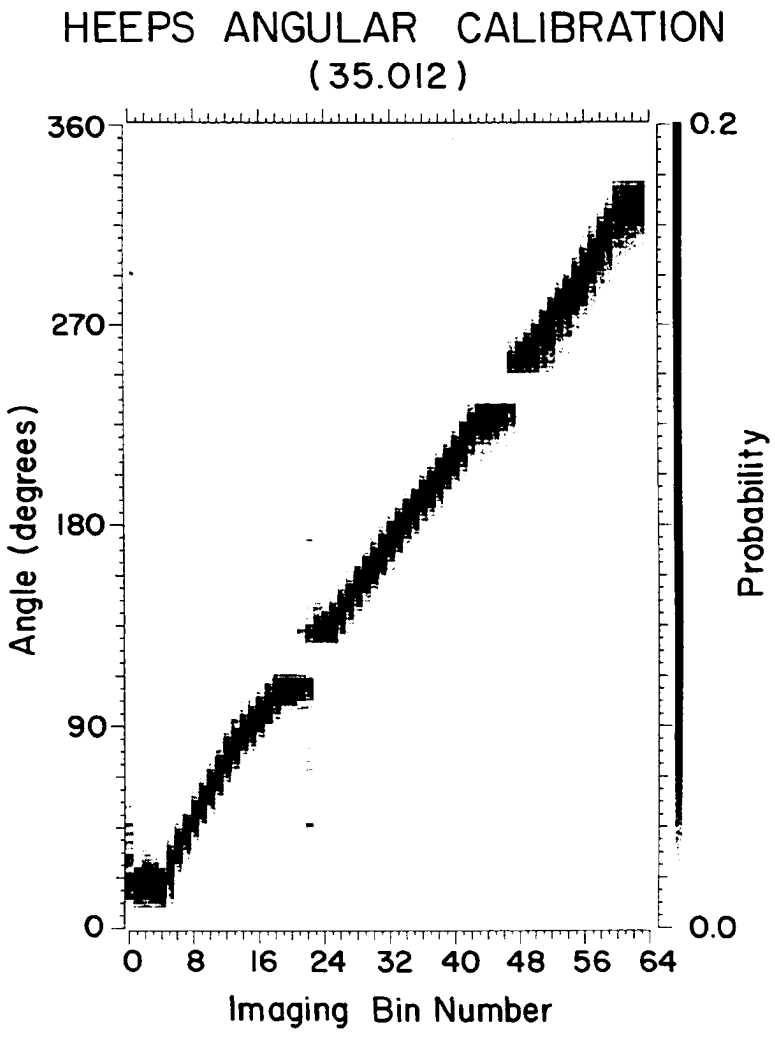

Figure 1-36

$$\phi_i \equiv \frac{\sum_h' (\phi[h] \times P[h,i])}{\sum_h' P[h,i]} \qquad \text{Eq. (1-36)}$$

and

$$(\delta\phi)_i \equiv \sqrt{\frac{\sum_h' \{(\phi[h] - \phi_i)^2 \times P[h,i]\}}{\sum_h P[h,i]}}, \qquad \text{Eq. (1-37)}$$

are defined, where the prime on the summation symbols indicates that only a subrange of h is included in those sums. This subranging is incorporated in order to minimize the distortion of these statistical moments by instrument dark events which are not associated with the particle source and yet are distributed in small numbers throughout the calibration data sets. The moments were computed over an azimuthal subrange 66 degrees wide and centered on preliminary mean values of $\phi[i]$ computed without subranging. The results are shown in Figures 1-37 & 1-38 for the 29.015 and 35.012 instruments, respectively. These figures summarize the angular imaging characteristics of the two instruments. It can be seen that the response is roughly linear, with uncertainties which are typically 7°, but which range down to nearly 3° and up to more than more than 15° in the vicinity of the blind spots.

It should be emphasized that it is expected that this imaging quality will be degraded in a significant but poorly understood manner at high instrument count rates. This is due to problems involving pulse pile up resulting from the finite (several μsec) duration of the analog signals and due, also, to poor ADC performance in the face of small amplitude reference pulses which become more common as event rates increase.

HEEPS ANGULAR IMAGING (29.015)

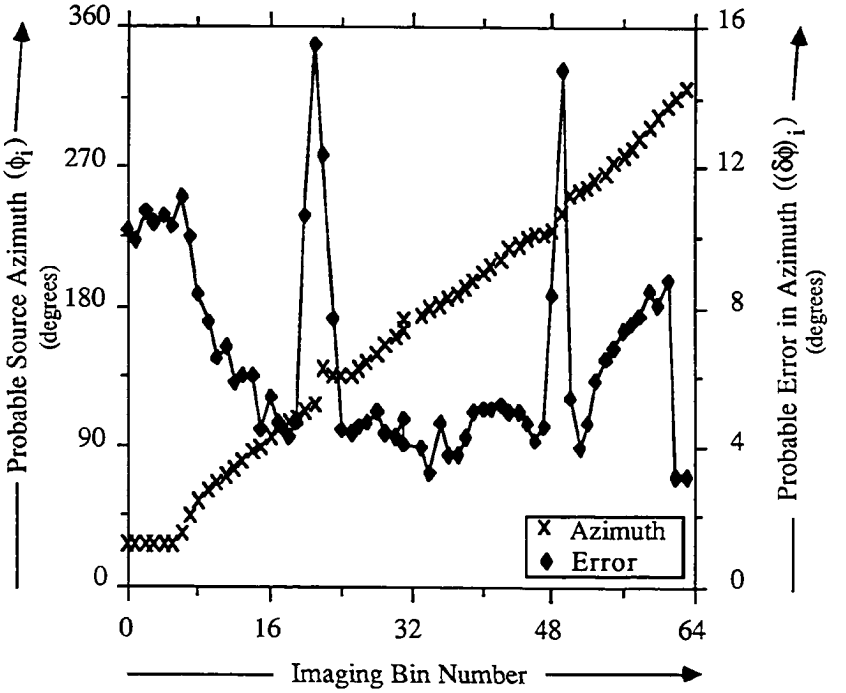

Figure 1-37

HEEPS
ANGULAR IMAGING
(35.012)

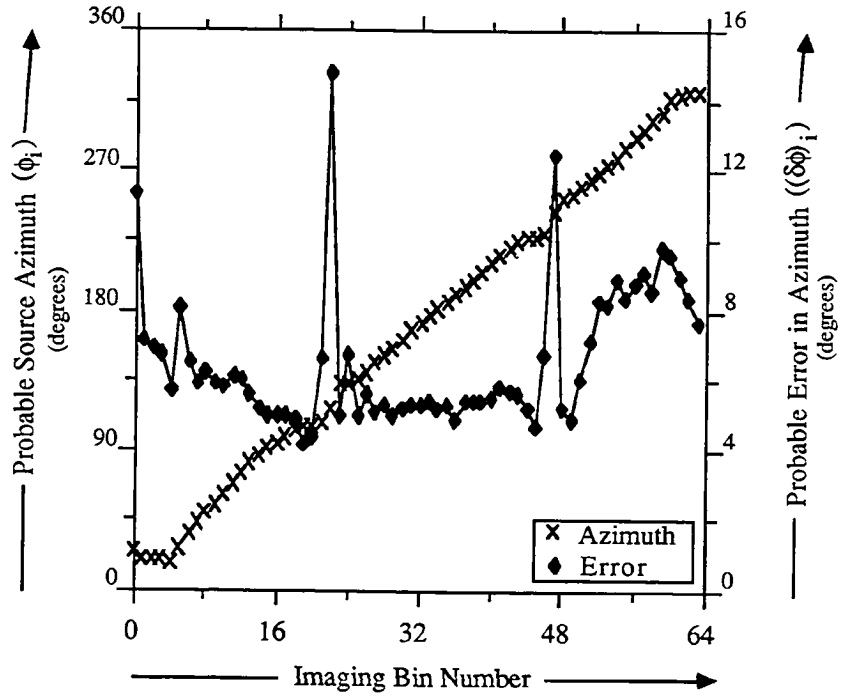

Figure 1-38

Calibration of Instrument Sensitivity

The quantity which is conventionally used to characterize the sensitivity of an electrostatic analyzer is referred to as the energy-independent geometry factor, is denoted by the symbol

$$G_0$$

and carries the units

$$Cm^2\text{-Sr-keV/keV}.$$

This geometry factor provides the relationship between the instrument count rate and the differential directional particle flux emanating from the direction $\mathbf{r}$, through the equation

$$J'(\mathbf{r}, \varepsilon_j) = \frac{C_j}{\varepsilon_j \times G_0}, \qquad \text{Eq. (1-38)}$$

where

- $J'(\mathbf{r},\varepsilon_j)$ is the differential directional flux of particles at the instrument entrance aperture, emanating from within $\delta\Omega$, centered on $\mathbf{r}$ and with energies per charge within $\delta\varepsilon$, centered on ε.
- $\mathbf{r}$ is the unit vector at the entrance aperture pointing toward the probable particle source direction,
- ε_j is the probable particle energy associated with the instrument energy selection state j

and

- C_j is the event rate recorded in the instrument energy selection state j.

In this context, G_0 may be thought of as the product:

$$G_0 = (\delta A)(\delta\Omega)(\delta\varepsilon/\varepsilon), \qquad \text{Eq. (1-39)}$$

where

- δA is the effective area of the entrance aperture,
- $\delta\Omega$ is the angular field of view of the instrument

and

$-\delta\varepsilon/\varepsilon$ is the fractional energy bandpass of the instrument.

The correctness of the relationship between J' and C_j expressed in equation 1-38 depends critically on the constancy of J' over δA, $\delta\Omega$ and $\delta\varepsilon$. This equation actually provides the average of J' over δA, $\delta\Omega$ and $\delta\varepsilon$. In the case of an instrument such as HEEPS, J' varies substantially over the instrument field of view, which spans roughly 300 degrees in azimuth. For any given angular imaging bin, however, the constancy of J' over the field of view is much more reasonable. The approach, then, will be to determine a geometry factor (G_{0i}) associated with each angular imaging bin and determine J' through the equation

$$J'(r_i, \varepsilon_j) = \frac{C_{i,j}}{\varepsilon_j \times G_{0i}}, \qquad \text{Eq. (1-40)}$$

where the subscript i refers to a given angular imaging bin.

Calibration of the instrument sensitivity was carried out using NASA's Low Energy Ion Facility (LEIF) (Biddle et al., 1983) at the George C. Marshall Space Flight Center (MSFC) in Huntsville, Alabama during the summer of 1984. Due to instrumental difficulties, the instruments flown on NASA flights 29.015 and 35.012 could not be used during these experiments. Instead, a prototype instrument was calibrated and the results scaled as described below.

The primary differences between calibration facilities available at UNH and those available at MSFC were:

1) The LEIF featured a broad beam particle source whose absolute integrated particle flux was stable, could be periodically monitored and, therfore, was known.

2) The LEIF also featured a 3-axis angular positioning table for instrument mounting so that the angular position of the instrument being calibrated could be varied arbitrarilly and known to within less than 1°.

These features were utilized in order to determine the effective area (δA) for a given typical angular imaging bin, as well as the quantity

$$\langle \sin(\theta)\, \delta\theta\, \delta\varepsilon \rangle,$$

which is the mean value of the product of the contribution of the polar angle (θ, see Fig 1-31) to the angular bandpass ($\delta\Omega$) and the bandpass in energy per charge. This quantity is grouped in this manner, because the polar bandpass is dependant upon particle energy and, likewise, the particle energy bandpass is dependent upon the polar angle of the source.

The determination of δA basically involves exposing the instrument to a known particle flux having the following characteristics:

1) The particle energy per charge (ε) is that energy per charge to which the instrument is most sensitive in the given energy selection state.

2) The spread in energy per charge of the incident particles is small compared to the energy band pass of the instrument.

3) The direction of the source with respect to the instrument coordinate system is that direction to which the instrument is most sensitive for the angular imaging bin under calibration.

4) The incident particles are monodirectional at the entrance aperture, compared to the angular acceptance width of the bin under calibration.

These conditions ensure that virtually all particles incident at the effective entrance aperture will be transmitted to the detector. It should be noted that these conditions do not ensure that all such particles will be recorded as events in the bin under calibration. This is so because some particles will be recorded in other bins and some particles won't be recorded at all due to the inefficiency of the detection system (mcp-anode-electronics) at the analyzer exit aperture. For this reason, δA is really a measure of the product of the detection efficiency and the area of that portion of the entrance aperture effective for the bin under calibration. However, we will refer to δA simply as the entrance aperture area.

Under the conditions noted above, data was collected at various incident flux intensities. The data recorded at each flux level included the incident integrated ion flux (ions/cm^2-sec), the count rate in bins where it was appreciable and the total instrument count rate. Figure 1-39 shows the total instrument count rate plotted versus incident integrated ion flux. The circled data points reflect data recorded on June 26,1984 while the squared points reflect data recorded on June 27. Unfortunately, problems with instrument performance were encountered on June 27 and we couldn't get the count rate above ~59 kHz, as is evident in the figure. The nature of the problems encountered on the 27th of June is not understood. The best indication we have is that, as shown in Figure 1-39, the instrument would not count events faster than 59 kHz, no matter how intense the bombardment source became. It appears that some kind of saturation problem set in, but we have been unable to come up with a specific characteristic of the instrument which would account for this saturation. Unfortunately, we were not able to repeat the experiment before flight. For this reason, and because of the fact that these prototype calibration results had to be scaled, as described below, to the case of the flight instruments, the calibration of the absolute instrument sensitivity must be considered as the weak link in all of the HEEPS calibration work to have been carried out. However, comparison of the results with expectations based on other sources of information (as also described below) gives reason for some confidence regarding the quality of our conclusions regarding the absolute sensitivity of the flight HEEPS instruments. In any case it is important that more quantitative sensitivity calibrations be carried out on these types of instruments in the future, if they are to receive the extensive use that we now anticipate.

The solid straight line shown in Figure 1-39 has a slope (S) of 1.4×10^{-2} cm^2. The curved line is of the form

$$y = \frac{S\,x}{1 + S\,x\,\tau}, \qquad \text{Eq. (1-41)}$$

where

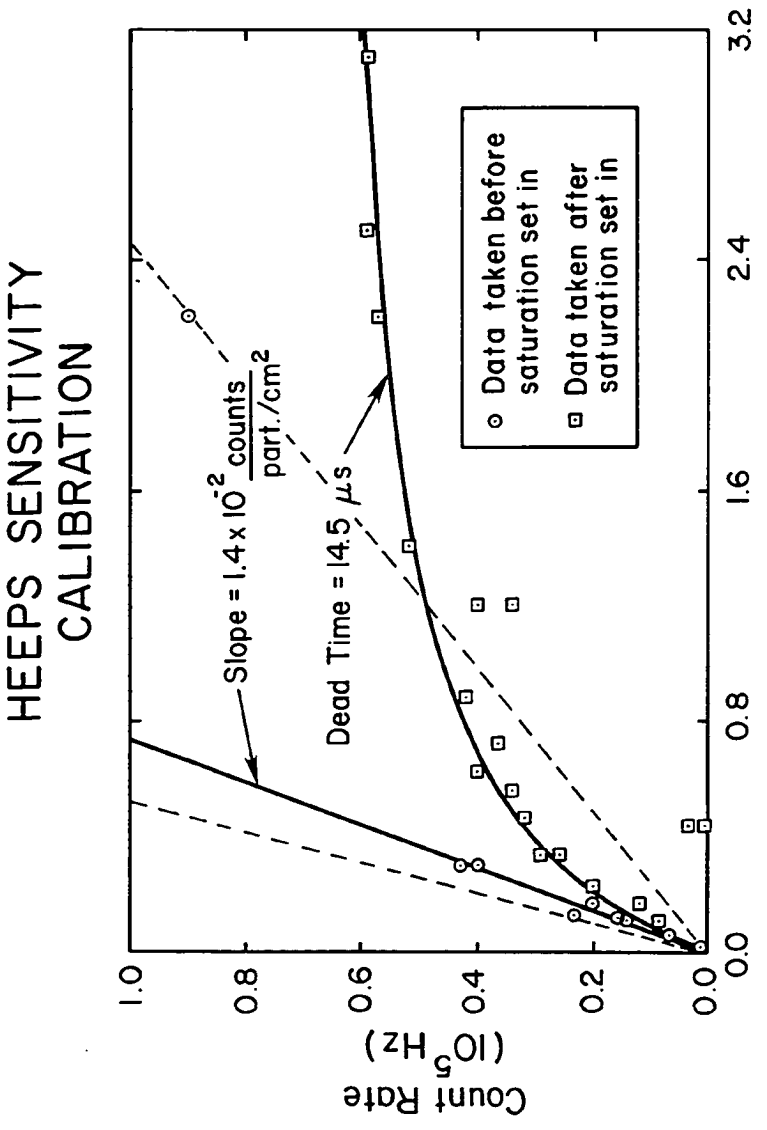

Figure 1-39

$$S = 1.4 \times 10^{-2}\,\mathrm{cm}^2 \qquad \text{Eq. (1-42)}$$

and

$$\tau = 14.5\ \mu\mathrm{sec.} \qquad \text{Eq. (1-43)}$$

This type of curve accurately models a non-paralyzably saturated counting system (Evans, 1955) which would perform linearly in the absence of saturation, but which is subject to a dead-time given by τ (see the following subsection). We will adopt the slope S as the primary result of the measurements, although it must be regarded as being highly uncertain owing to the erratic instrument performance described above. It is reasonable to bracket the measurements with the dashed lines shown in Figure 1-39, however, and say that the slope is given by

$$S = \left(1.4\ {}^{+0.3}_{-1.0}\right) \times 10^{-2}\ \mathrm{cm}^2. \qquad \text{Eq. (1-44)}$$

To get the value (δA) that we are seeking, we must multiply this slope by the fraction of the total instrument counts that went into the bin under calibration. This fraction ranged between 25% and 38% and averaged 34% for all the data recorded, so that we have,

$$\delta A = \left(4.8\ {}^{+1.0}_{-3.4}\right) \times 10^{-3}\ \mathrm{cm}^2. \qquad \text{Eq. (1-45)}$$

With regard to the determination of the width of the polar angular response ($\delta\theta$) (see Figure 1-31) and the fractional energy bandpass ($\delta\varepsilon/\varepsilon$), these quantities must not be considered independently since the polar response depends upon particle energy and the energy response depends on the polar angle of particle incidence. If the instrument is exposed to a constant flux of particles at various energies and from different polar source angles, then a relative sensitivity $g_j(\theta,\varepsilon)$ may be defined such that

$$g_j(\theta,\varepsilon) \equiv \frac{C_j(\theta,\varepsilon)}{C_j(\theta_0,\varepsilon_j)} \leq 1, \qquad \text{Eq. (1-46)}$$

where

- $C(\theta,\varepsilon)$ is the instrument count rate,

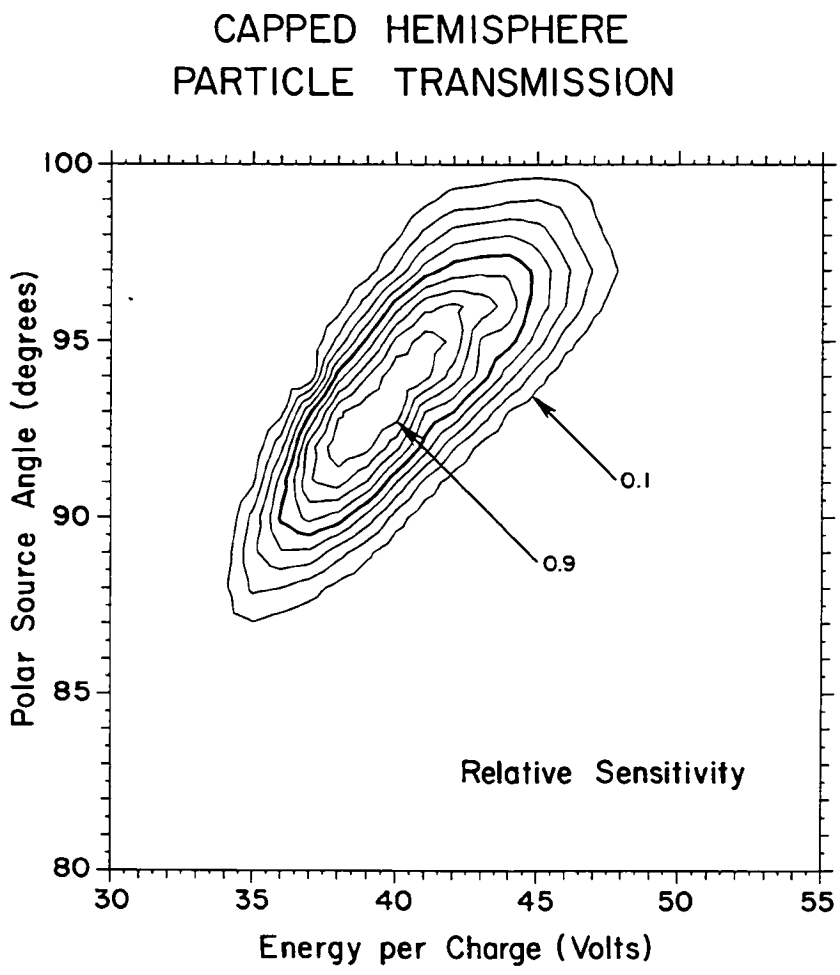

Figure 1-40

- ε and θ are the energy per charge and instrument polar source angle, respectively for incoming particles

and

- ε_j and θ_0 are the energy per charge and instrument polar source angle for which C_j is a maximum.

Count rate data was collected at various ε and θ and normalized to the maximum count rate (recorded at ε_j and θ_0). The resulting $g_j(\theta,\varepsilon)$ is shown plotted in contours versus ε and θ in Fig 1-40. This figure reveals much about the transmission properties of the capped hemisphere analyzer. The reader should note first that the polar source angle of maximum sensitivity is not 90°, but is near 93°. Secondly, particles incident from polar angles greater than 90° are transmitted with higher energies than those incident from polar angles less than 90°. This is to be expected, since particles incident from polar angles less than 90° require greater deflection in the electrostatic field to bring them onto the detector.

Using the data shown in Figure 1-40, and approximating

$$\sin(\theta) \sim 1, \qquad \text{Eq. (1-47)}$$

the quantity $\langle \sin(\theta)\, \delta\theta\, \delta\varepsilon \rangle$ may be estimated as the area enclosed by the $g_j(\theta,\varepsilon) = 0.5$ contour or, alternatively, as the volume under the surface represented by the contours in Figure 1-40. Each of these methods gives a value within 3% of

$$\langle \sin(\theta)\, \delta\theta\, \delta\varepsilon \rangle = 7.2 \times 10^{-4} \text{ radian-keV}. \qquad \text{Eq. (1-48)}$$

Taking $\varepsilon_j = 0.04$ keV (see Figure 1-40) yeilds

$$\frac{\langle \sin(\theta)\, \delta\theta\, \delta\varepsilon_j \rangle}{\varepsilon_j} \equiv 1.8 \times 10^{-2} \frac{\text{radian - keV}}{\text{keV}}. \qquad \text{Eq. (1-49)}$$

Also, taking twice the rms imaging deviation for the azimuthal bandpass from the azimuthal angular calibration (Figures 1-37 & 1-38), we get:

$$\delta\phi \equiv \frac{2 \times (6.7°) \times 2\pi}{360°} = 0.23 \text{ radians}. \qquad \text{Eq. (1-50)}$$

Combining the above results yeilds:

$$G_{0,i} \cong \delta A\, \delta\phi\, \langle \sin(\theta)\, \delta\theta\, \delta\varepsilon/\varepsilon \rangle$$

$$= \{(4.8\ ^{+1.0}_{-3.4}) \times 10^{-3}\ \text{cm}^2\} \times \{0.23\ \text{rad}\} \times \{1.8 \times 10^{-2}\ \text{rad-keV/keV}\}$$

$$= (2.0\ ^{+.41}_{-1.4}) \times 10^{-5}\ \text{cm}^2\text{-ster-keV/keV} \quad \text{(prototype)} . \qquad \text{Eq. (1-51)}$$

This result applies to bin 42 on the prototype instrument under calibration at MSFC. The instruments flown on board NASA flights 29.015 and 35.012 had analyzer plate gaps which were larger than the calibrated prototype instrument, although the analyzers were geometrically similar to the prototype and identical to each other. The larger gaps imply a larger effective area as well as larger energy and polar angular bandpasses for the flight instruments. Taking this result to be typical of the bins for the prototype instrument, a typical bin geometry factor for the flight instruments may be estimated by scaling according to the curve in Figure 1-4, which was produced by numerical methods by the Berkeley group (Carlson et al., 1983). This scaling leads to the result:

$$G_{0,i} = \left[(2.0\ ^{+.41}_{-1.4}) \times 10^{-5}\right] \times \frac{23}{3.5}\ \text{cm}^2\text{-ster-keV/keV}$$

$$= (1.3\ ^{+.27}_{-.92})\ \ 10^{-4}\ \ \text{cm}^2\text{-ster-keV/keV} \quad \text{(per bin, flight)} . \qquad \text{Eq. (1-52)}$$

Summing over all bins gives values ranging from 12% to 44% of the total instrument geometry factor predicted based on Carlson's numerical computations. The difference can, in large part, be attributed to the inefficiency of the detector/counting systems, which was not incorporated in Carlson's work.

Comparison may also be made between these numbers and a 'back-of-the-envelope' method of calculating electrostatic analyzer geometry factors, which is given by

$$G_0 \sim \frac{A_1 A_2}{L^2} \times \frac{\Delta\varepsilon}{\varepsilon} \cong 2 \times 10^{-2}\ \text{cm}^2\text{-ster-keV/keV}. \qquad \text{Eq. (1-53)}$$

This result applies to the entire instrument. Here A_1, A_2 and L are the areas of the entrance and exit apertures and the path length of a selected particle through the analyzer, respectively. The above estimate was obtained using flight instrument parameters and a

fractional energy pass band of 20% and compares well with Carlson's numerical result, which is given for these analyzer parameters by Equation 1-29.

The bin geometry factor given by Equation 1-52 was adopted as the average bin geometry factor for the two flight instruments. Relative variations in sensitivity of the imaging bins was accounted for in the in-flight data analysis by accumulating in flight bin distributions over long time periods, including many rocket spins and in the absence of apparently anisotropic particle fluxes, so that the average distribution of events in bin space should be isotropic. Relative bin sensitivities were then taken as being proportional to the resulting counts in the given bin. The results are shown in Figure 1-41. These data were used in the in-flight data analysis, as described in Appendix B.

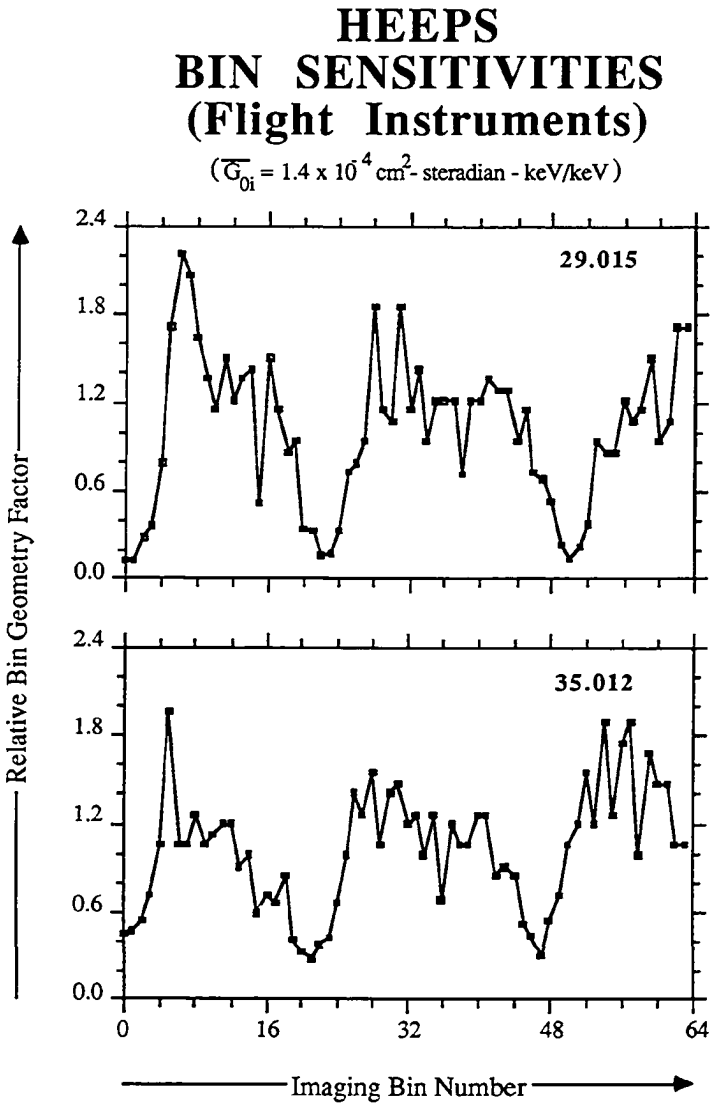

Figure 1-41

Flight Peformance

Purpose and Scope

It is the purpose of this section to present some of the aspects of instrument performance characteristics which affect the interpretation of the in flight data. Although both the 29.015 and 35.012 instruments produced nominal performance throughout their flights, saturation effects produced by high event rates had significant impact on both instruments. These saturation effects evidenced themselves in three ways:

1) Counter Wrap-around,
2) Dead-time Saturation of Counting Systems and
3) Distortion of angular imaging.

In some cases, these effects are well understood and, therefore, reasonably easily taken into account in the data analysis, while in others, this is not the case. In this section, these saturation problems will be discussed in a general way, with most reference to details of the performance of the individual instruments deferred to later sections.

Instrument Saturation

Counter Wrap-Around. The simplest difficulty encountered at high count rates occurs when the event counter wraps through zero. A ten bit counter will count as high as $2^{10} - 1 = 1023$. If more than 1023 events are recorded between counter resets, the counter will wrap through zero, like the odometer on a car at 10^5 miles. In this case, the event rate becomes a multivalued function of the instrument count rate, calling for often assumptive interpretation of the data and reducing its value. The count rate (C_w) at which counter wrap-around sets in depends upon the number of bits in the counter and the data accumulation period (τ) as follows:

$$C_w = \frac{(2^n - 1)}{\tau}. \qquad \text{Eq. (1-54)}$$

For the HEEPS Total Counts (HTC) signal, the instruments on both rockets used 10 bit counters. The accumulation period for (HTC) was 1.6 ms in the case of flight 29.015 and 6.4 ms in the case of flight 35.012. This yields:

$$C_w = \frac{1023}{1.6 \times 10^{-3}\,\text{sec}} = 640\ \text{Khz} \qquad (29.015) \qquad \text{Eq. (1-55)}$$

$$C_w = \frac{1023}{6.4 \times 10^{-3}\,\text{sec}} = 160\ \text{Khz} \qquad (35.012). \qquad \text{Eq. (1-56)}$$

Due to non-paralyzable saturation of the HTC signal, discussed in the next subsection, the maximum count rate that was attainable by either instrument was on the order of 300 kHz. Comparison with equations 1-55 & 1-56, above, allows the conclusion that counter wrap-around was a problem on flight 35.012, but not on flight 29.015.

Dead Time Saturation of Counting Systems. An event counting system typically requires a finite time to register an event occurence. Thus, typically, for some time period following the occurence of a counted event, the counting system is insensitive to subsequent incident particles. This time period is referred to as the instrument dead time. The existence of a dead time associated with counting systems leads to systematic counting errors at high event rates.

In many cases, instrument dead time effects can be modelled, resulting in retrieval of data quality. Of critical significance with regard to instrument performance under saturated (high event rate) conditions is the question of whether the instrument is *paralyzably* or *non-paralyzably* dead following a recorded event. With reference to the time lines shown in Figure 1-42, the zero of time (t) corresponds to the occurence of a counted event, following which the instrument is insensitive until $t = \rho$. That is, no events will be recorded during this period. Events incident after time $t = \rho$ will be recorded with normal instrument efficiency, unless the instrument suffers from paralyzable dead time saturation. In that case, again with reference to the time lines in Figure 1-42, the occurence of an

SATURATION TIME LINES

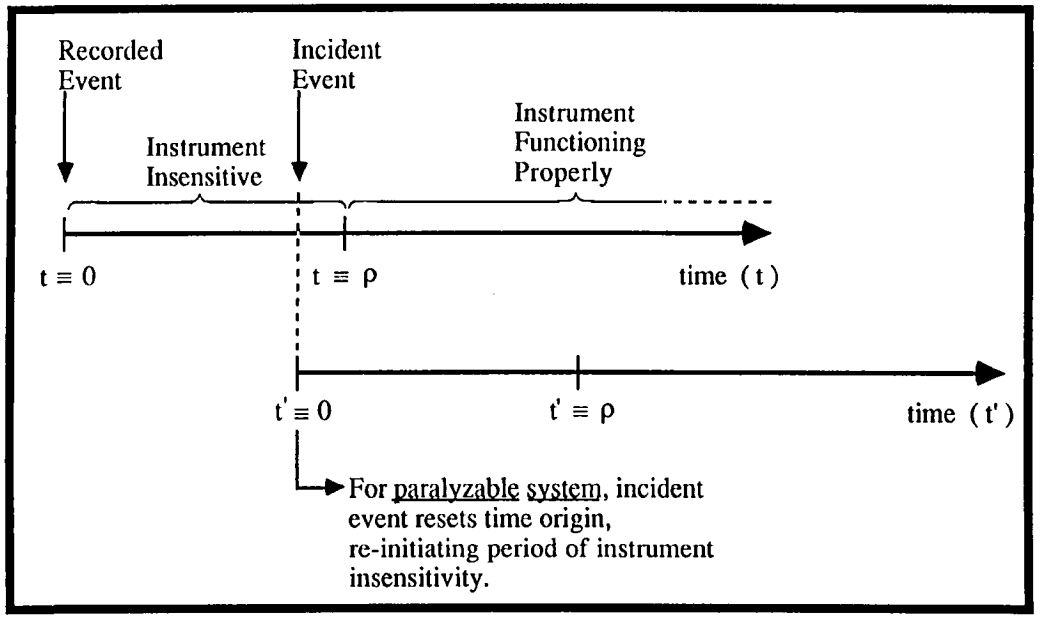

Figure 1-42

incident event during the period ($0 \leq t \leq \rho$) will cause the origin of time to be reset, re-initiating the period of instrument insensitivity.

The behavior of systems subject to dead time saturation effects may be accurately modelled by resorting to the use of Poisson counting statistics which give the distribution of event intervals as

$$dP(\tau) = N \exp(-N\tau)\, d\tau, \qquad \text{Eq. (1-57)}$$

where $dP(\tau)$ is the probability that the interval from any instant in time until an incident particle event will be equal to τ, given that the mean value of the interval is N^{-1}. The expectation value for the instrument count rate is given as the inverse of the mean interval between recorded events. That is,

$$n(N) = \langle \tau_r \rangle^{-1}, \qquad \text{Eq. (1-58)}$$

where n(N) is the instrument count rate and τ_r is the interval between recorded events. The quantity $\langle \tau_r \rangle$ may be calculated according to

$$\langle \tau_r \rangle = \int dP(\tau)\, \varepsilon(\tau)\, \tau, \qquad \text{Eq. (1-59)}$$

where $dP(\tau)$ is given by the Poisson distribution and $\varepsilon(\tau)$ is the instrument sensitivity as a function of time (τ) following a recorded event. In the present context, $\varepsilon(\tau)$ is taken to be a step-like function, whose value is 0 or 1, depending upon whether the instrument is 'dead' or 'live'. Applying this formulation results in the relations given by Evans (1955):

$$n = \frac{N}{1 + N\rho} \qquad \text{(nonparalyzable)}$$

$$n = N \exp(-N\rho) \qquad \text{(paralyzable)},$$

for the saturation performance of ideally paralyzable and nonparalyzable counting systems. Furthermore, it can be shown, through a straight forward application of equation 1-58, that in the case where an instrument is characterized by a sequence of paralyzable (τ_p) and nonparalyzable (τ_{np}) dead times, the resulting instrument count rate (n) will be given as a function of the event rate (N) by:

$$n = \frac{N \exp(-N\rho_p)}{1 + N\rho_{np}}. \qquad \text{Eq. (1-62)}$$

This result is independent of the order in which the two paralyzable intervals occur and is valid so long as they are consecutive and don't overlap. Figure (1-43) illustrates these points, showing n plotted verses N for the paralyzable and nonparalyzable cases, as well as for an intermediate case, illustrating the application of equation 1-62. Since any element of paralyzable behavior in an instrument counting system yields the rolling over of the count rate with increasing event rate, care should be taken to eliminate all paralyzable behavior from such systems.

Figure 1-44 shows two seconds of HEEPS energy sweep moniter (HSwp) and HEEPS Total Counts (HTC) data from NASA flt. 29.015. This data period includes the time when ion beam operations were initiated, with the commencement of operations evident in the data at 122.5 seconds flight time. The 'hard' upper edge on count rates encountered at most energies at ~ 360 kHz which begins at ion beam turn on is a signature characteristic of a non-paralyzably saturated instrument, whose dead time is given as ρ = 2.8×10^{-6} sec. No evidence of paralyzable response in the HTC signal of either flight instrument (29.015 or 35.012) has been noted in the laboratory or flight data..

Saturation of Azimuthal Imaging. The quality of the azimuthal angular imaging critically effects the nominal flux measurement in a capped hemisphere system. If the imaging saturates giving, say, a flat spectrum in bin space, then one can only recover the average flux over the (very wide) instrument field of view. The azimuthal angular imaging calibrations, discussed previously, were carried out at typical total instrument count rates (HTC) of near 3 Khz. Both instruments suffered in-flight background event levels of greater than 3 Khz. During 29.015 ion beam events, saturation of the azimuthal angular imaging was common. In addition, both flight instruments commonly suffered saturating event rates when measuring the thermal ionospheric plasma.

DEAD TIME SATURATION CURVES

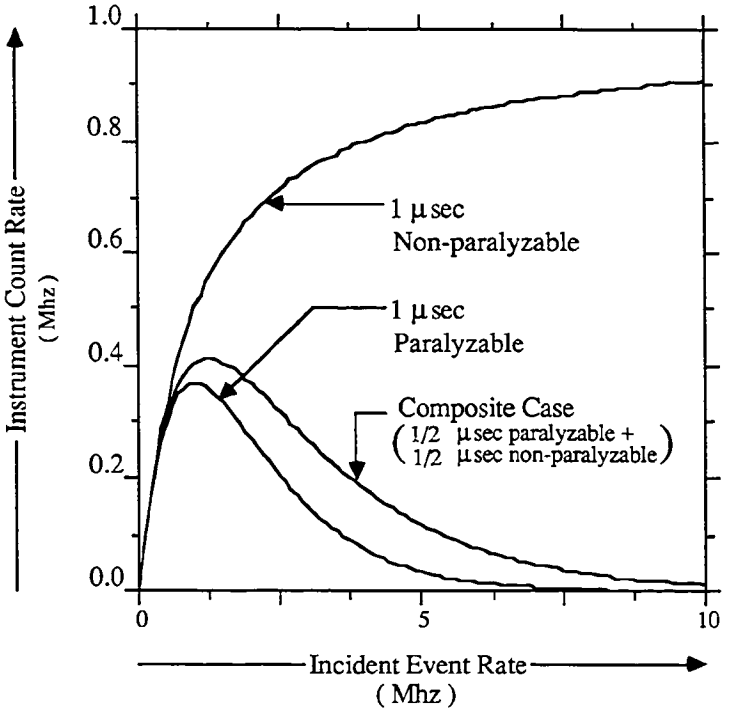

Figure 1-43

NON-PARALYZABLE SATURATION OF HEEPS TOTAL COUNTS

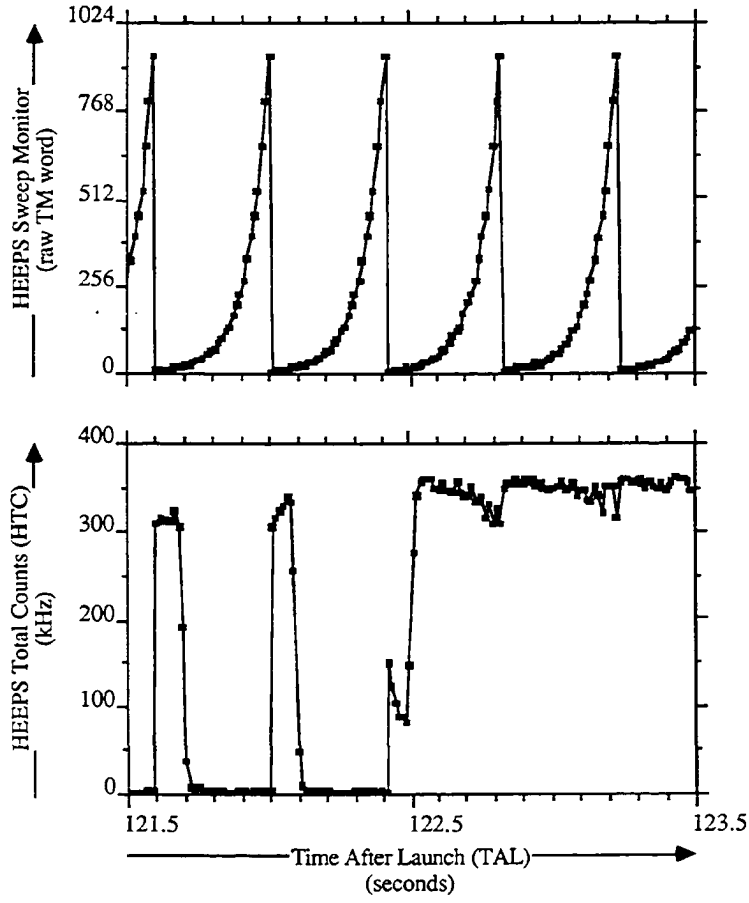

Figure 1-44

The imaging system has potential sources of saturation, virtually along the entire analysis path. A nonparalyzable dead time of on the order of 10 μsec is enforced by the 8031 event processing loop. This can be expected to effect the integrated imaged event rate, but not the quality of the imaging. The linear circuitry associated with the pre-amplifier and the linear stages of the Heeps Logic Board have time constants which are typically a couple of micro-seconds. As event rates become such that typical event intervals approach these time scales, pulse pile up occurs. In this case, the interpretation of the event data depends not only on the quality of a given event, but also on the recent event history of the instrument. Effects of pulse pile up are expected to become significant at HTC rates of >100 kHz. Finally, the microchannel plate systems are expected to undergo gain degradation at event rates such that the resulting emitted electron current density approaches the ambient strip current density carried by the MCP's. A 'figure of merit' advocated by the manufacturer is that the emitted electron current density should not exceed 10 % of the ambient strip current density. The resulting inferred tolerable event flux for the MCP assemblies flown is roughly 10 kHz / mm^2. The data indicate that this limit was routinely exceeded in flight, but no evidence of the paralyzable behavior that would result in the HTC signal has been noted.

Figure 1-45 shows in flight HEEPS ion data collected aboard flight 29.015 during the third perpendicular ion beam event. At the top, segments of the energy sweep (HSwp) data and the corresponding HTC, event rate indicate two seperate peaks in the event rate. Directly associated with each data point in the HTC signal, a 64 bin azimuthal angular spectrum is available. Four of these spectra have been selected and displayed in the bottom half of the figure to illustrate, qualitatively, the dependence of HEEPS in flight imaging performance on the HTC rate. The letters A through D in the figure associate a given HTC point with the appropriate azimuthal imaging spectrum below. In conjunction with increasing (HTC) rates, progressing from points A through D, the azimuthal image not only changes in shape, but varies strongly in integrated intensity. The changes in shape

HEEPS
ANGULAR IMAGING
(29.015, IN FLIGHT)

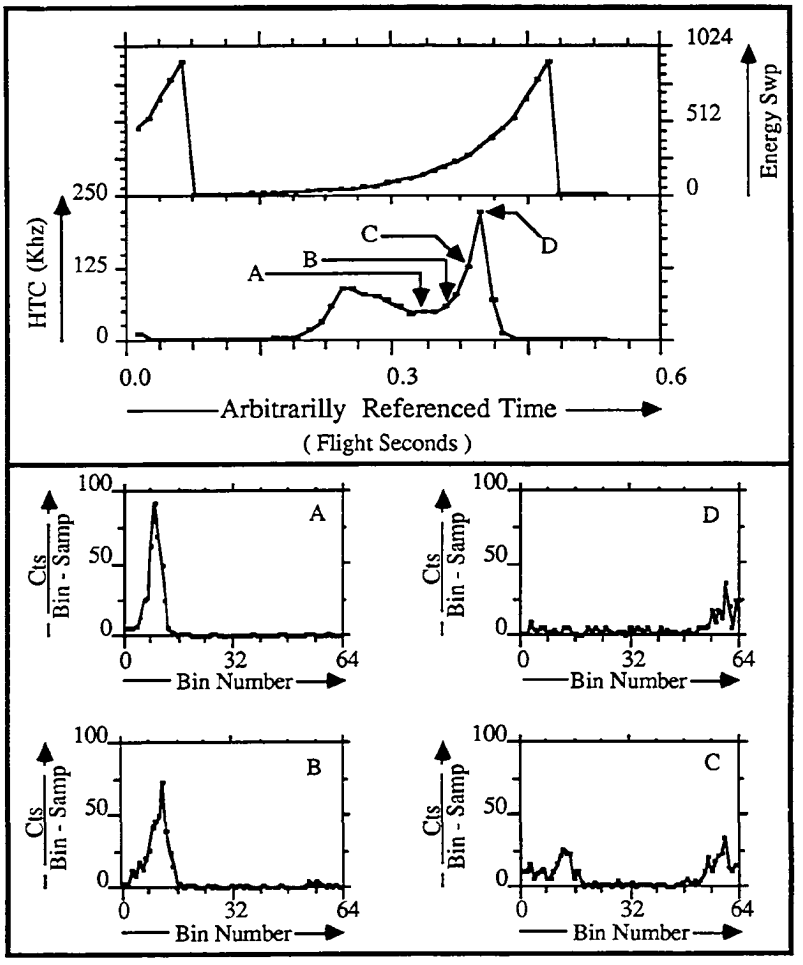

Figure 1-45

could be due to real flux changes, but the decrease in the integrated intensity with increasing HTC rates is certainly a saturation effect.

The dependence of HEEPS' integrated imaged event rate on the HTC rate is illustrated more quantitatively in Figure 1-46. This figure shows the sum of the counts in the imaging bins in kHz, plotted verses the HTC rate, also in kHz. The plotted points were derived using 40 seconds of data, amounting to over 3000 angular images. The linear regime at HTC rates under 50 Khz and the subsequent saturation of the imaging response is apparent in the figure. The smooth curve drawn through the data indicates the response of a counting system which is subject to a sequence of 2.5 μsec paralyzable and 10 μsec nonparalyzable dead times. Such a model for the behavior illustrated in Figure 1-46 has limited applicability, except that a ~10 μsec nonparalyzable saturation contribution is a reasonable expectation of the circuit parameters on the Heeps Logic Board. In any case, the model approximates the data over the much of the range of HTC. The linear imaging regime, defined in this context as less than 50 Khz, is characterized by an imaging efficiency, with respect to HTC, of around 0.5. This can be explained as due to the fact that imaged events were gated by upper and lower level voltage discriminators, while HTC discriminated only against events below the lower threshold, although pre-flight threshold measurements indicated that a higher linear imaging efficiency should have been obtained.

SATURATION OF ANGULAR IMAGING (29.015 HEEPS, IN FLIGHT)

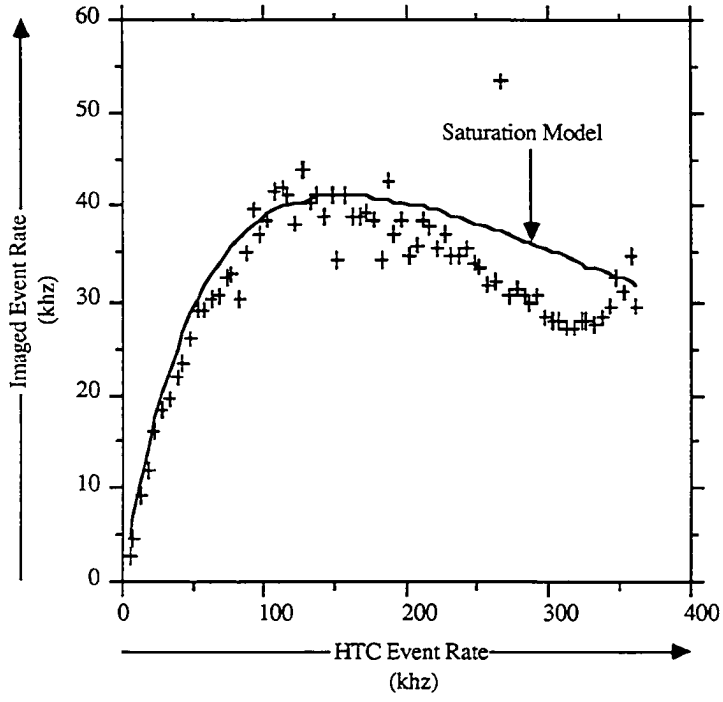

Figure 1-46

SECTION 2: NASA FLIGHT 29.015 (AN ACTIVE EXPERIMENT)

Review of Ion Beam Physics

Introduction.

For years, various plasma physics researchers have been interested in the characteristics of the collisionless interaction between streaming charged particle beams and magnetic fields. This is due not only to the similarity of such systems with naturally occuring beams in magnetized space plasmas, but also to their potential applications in the fields of confined plasma heating (Humphries, 1980; Ott et al., 1977) and spacecraft charge neutralization (Cohen et al., 1982; Olsen, 1981a, 1981b, 1985; Schmidt et al., 1986). For homogeneous field geometries, the interesting physical effects which are operative in such systems arise from two distinct causes:

1) In the case where the charged particle streaming has a component transverse to the magnetic field, charge separation can take place, due to the nature of Lorentz force

$$\mathbf{F}_L = q\frac{\mathbf{v} \times \mathbf{B}}{c}, \qquad \text{Eq. 2-1}$$

exerted by the magnetic field (**B**) on the streaming charged particles, and to the disparity in the masses (m) of the ions and electrons in the stream.

2) In the case where there are both streaming and non-streaming charged particle components present, plasma wave instabilities may arise due to electrostatic and electromagnetic coupling between these components.

If, in addition, magnetic field inhomogeneities exist, charge separation may take place due to charged particle gradient and curvature drifts (Chen, 1974), which are inversly proportional to the species charge and, therefore, oppositely directed for electrons and ions.

An example of early efforts at understanding the physics of such systems in the context of space plasmas is provided by the works of Chapman & Ferraro (1931, 1932, 1933), wherin the nature of the interaction between the earth's dipole magnetic field and clouds of charged particles, thought to be emitted by the sun and moving through interplanetary space at roughly 1000 km-sec^{-1}, was considered. The formation of a space charge dominated transition layer (the *Ferraro Layer*, or *magnetopause*) due to inertial charge separation between solar wind ions and electrons and the compression of the dayside geomagnetic field due to currents flowing in this thin layer were primary results of these works.

In his theory of the formation of the solar system, Alfven (1954) proposed that there exists a *critical velocity* transverse to ambient magnetic field lines for any given neutral atomic species, above which rapid ionization takes place due to some (unspecified) collective process. Alfven's idea was that neutral matter falling toward the sun became ionized and tied to interplanetary magnetic field lines when its velocity exceeded the species *critical velocity*, given by

$$v_c = \sqrt{\frac{2e\Phi}{m}}, \qquad \text{Eq. 2-2}$$

where m and Φ are the species mass and 1st ionization potential, respectively, and e is the magnitude of the electron charge. More recently, a specific mechanism for this collective ionization process has been proposed (McBride et al., 1972), which involves a hybrid plasma instability (the modified two stream instability) resulting from the relative cross (magnetic) field streaming between newly created ions and electrons which, due to their smaller mass, are more tightly tied to the field lines. McBride et al. envisioned the growth of electrostatic ($\mathbf{k} \times \mathbf{B} = \mathbf{0}$) waves which heat the electrons parallel to $\mathbf{B}$. In turn, the heated electrons provide more ionization through binary collisons, feeding back positively on the process and providing the possibility of collective discharge. Such a collective process could well be operative in cometary environments and in the modern heliosphere, into which neutral interstellar gas drifts and becomes photo-ionized by solar UV radiation.

In the Earth's magnetosphere, the occurance of ion beams streaming along the field lines in the geomagnetic tail (Eastman et al., 1985) and above the auroral zone (Yau et al., 1985) have been well documented. In the magnetospheric tail, these beams have been most commonly observed in the plasma sheet boundary layer, which separates the region of the central plasma sheet, characterized by relatively warm (1 keV) and dense (~1/cc) plasma from the north and south tail lobe regions, which are characterized by cooler, more diffuse (~0.05/cc) plasma. The genesis and evolution of these beams are outstanding problems in the field of space plasma physics.

Recently, at lower terrestrial altitudes, diffuse beams of positive ions with large pitch angles ($90° \leq \alpha \leq 120°$) have been observed from earth orbiting satellite (Klumpar, 1979; Sharp et al., 1977; Shelley et al., 1976) and sounding rocket platforms (Whalen, et al., 1978; Yau et al., 1983). These beams have been dubbed *ion conics* because of the conical shape of their distribution functions in velocity space. The questions of how these beams are created and of their stability against the growth of plasma wave modes have recently received a great deal of attention among space physicists.

In the field of confined plasma heating, relative streaming between various charged species is known to give rise to a number of plasma wave instabilities, which in turn may provide the heating sought in the creation of a controlled thermonuclear reaction. In such cases, the heating of the reaction plasma ultimately derives from the streaming energy of the injected plasma.

With regard to spacecraft charge neutralization, the aquisition of excess positive charge by spacecraft operating in magnetospheric environments has been known to interfere with the measurement of low energy (thermal) positive ion fluxes due to the inability of these particles to reach the spacecraft. It has been proposed (Chappel et al., 1987) that in some cases this problem obscures most of the plasma in a given region, leading to erroneous conclusions regarding the nature and source of the plasma. This charging results from the emission of large photo-electron fluxes by the spacecraft when it

is illuminated by the sun. When this emission exceeds the electron flux that can be provided by the ambient thermal plasma, the craft charges up, preventing the continued net loss of electrons. It has been proposed that this problem may be overcome by the active emission of a beam of positive ions by a beam generator on board the spacecraft. In this way, an equilibrium could be obtained, such that the spacecraft floating potential is close to the potential of the plasma in which it is immersed and very low energy ions would have unimpeded access to the sampling instrumentation.

Finally, again in the field of space physics, electron beams have been used in attempts to probe distant regions of the magnetosphere. In the series of Echo experiments carried out jointly among researchers at the University of Minnesota and the University of New Hampshire, among others (Arnoldy et al., 1985 and references therein), energetic (10 - 40 keV) electron beams have been emitted from sounding rocket platforms in such a manner that, if the beams maintain their integrity and if the field lines onto which they are injected are closed in the opposite hemisphere, the electrons in the beam will be reflected at the opposited hemisphere, to return to and be detectable in the vicinity of the beam-emitting payload. Charging of the beam-emitting payload would prevent the escape of the electron beam, so that the emission of positive ions from the same payload, for the purpose of payload charge neutralization, has received consideration among the researchers involved.

Some Theoretical Works

Motivated by experiments of Wetstone, Ehrlich and Finkelstein (Wetstone et al., 1960), who found that low density plasmas fired into bent coil magnetic fields were effectively guided by the field lines and that high density plasmas moved along straight paths, across field lines, G. Schmidt (1960) considered the motion of plasmas injected into vacuum along curved magnetic field lines, according to the *guiding center approximation.* In the cylindrical magnetic geometry illustrated in Figure 2-1, Schmidt found that electric currents in the +z direction result from gradient and curvature guiding center drifts along $\pm z$

TANGENTIAL PLASMA INJECTION

(After Schmidt, 1960)

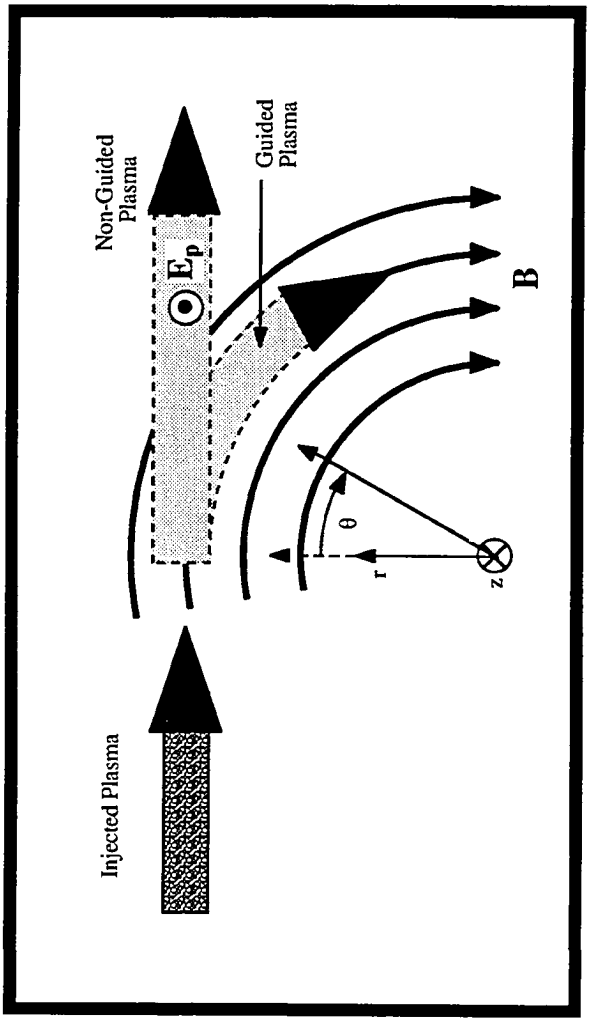

Figure 2-1

for ions and electrons, respectively, giving rise to charge separation and a polarization electric field, $\mathbf{E}_p$, which points in the -z direction and increases with time. The time rate of change of the **E** field gives rise, in turn, to a polarization drift in the ±z direction:

$$v_{dp} = \frac{\pm 1}{\omega_c B} \frac{d\mathbf{E}}{dt}, \qquad \text{Eq. 2-3}$$

for ions and electrons, respectively, which detracts from the gradient and curvature drift currents and, therefore, from **E**. The axial electric field combines with the azimuthal (applied) magnetic field to provide a radial $\mathbf{E} \times \mathbf{B}$ drift which is the same for electrons and ions. It is this drift which produces the deviation from guided plasma motion. Schmidt found that the beam propagation was controlled by the beam dielectric constant:

$$\varepsilon_d = 1 + \frac{4\pi mnc^2}{B^2}$$

$$= 1 + \frac{c^2}{V_A^2}, \qquad \text{Eq. 2-4}$$

where m is the plasma ion mass, n is the plasma density, B is the magnetic induction intensity, V_A is the Alfven speed and c is the speed of light in a vacuum (3×10^{10} cm-sec^{-1}). Specifically, for large ε_d the plasma was found to move along a straight line path, while for small ε_d (~1) the plasma was effectively guided by the magnetic field. This result expresss the idea that, to the degree that a plasma beam can electrically polarize, it can propagate inertially by virtue of its own polarization. A diffuse beam essentially does not carry the requisite charge to set up the polarization field and is guided by **B**.

A number of authors (Peter & Rostoker, 1982; Treuman et al, 1983; Treuman & Häusler, 1984) have investigated the transverse injection of plasma streams into regions of magnetic field by the use of the two fluid plasma equations. The work of Treuman et al. represents a comprehensive and somewhat detailed review of the subject. In these works, a number of different physical scenarios have been distinguished, based on:

1) The dimension of the beam (R_b) transverse to both the ambient magnetic field (B_0) and the direction of initial beam velocity (u_0), as compared to the beam ion gyroradius (r_{gb}), with broad beams characterized by $R_b \gg r_{gb}$ and narrow beams characterized by $R_b \leq r_{gb}$,

2) The density of the beam plasma (n_b), as compared to the density of any background plasma and

3) the speed (u_0) of the incident beam as compared to the local Alfven speed (V_A) and the ambient electron thermal speed (v_{te}), with distinction drawn between slow ($u_0 < V_A, v_{te}$) and fast ($u_0 > V_A, v_{te}$) beams.

A relatively simple case which illustrates some of the basic effects involved, and is similar to that considered by Chapman & Ferraro is that of a broad plasma beam, composed of both positive and negative charged particles, incident upon a region of purely transverse magnetic field. With reference to Figure 2-2a, adapted from Longmire (1963), a beam of equally massive, but oppositely charged particles is incident from the left (-x direction) upon a vacuum induction field in the z (out of the page) direction, which is characterized by an asymtotic ($x=+\infty$) intensity of B_0. All quantities are invarient with respect to y. It can be seen that the positive and negative particles are deflected in opposite directions by the Lorentz force associated with **B**, giving rise to an electric current density (**J**) in the (-y) direction. This current is responsible for the ramping up of the magnetic field in the boundary region of the system. Longmire (1963) has presented the solution of this problem for the field and fluid paramaters as functions of x, in the steady state, for the cases of both equal (Figure 2-2a) and unequal (Figure 2-2b) particle masses. In both cases, the beam fails to penetrate the field region and is reflected back toward the left. The primary differences between the two cases are:

1) In the equal mass case, the boundary layer thickness is on the order of the ion gyro-radius, while in the unequal mass (ions and electrons) case, the boundary

PLASMA IMPINGING ON MAGNETIC FIELD REGION

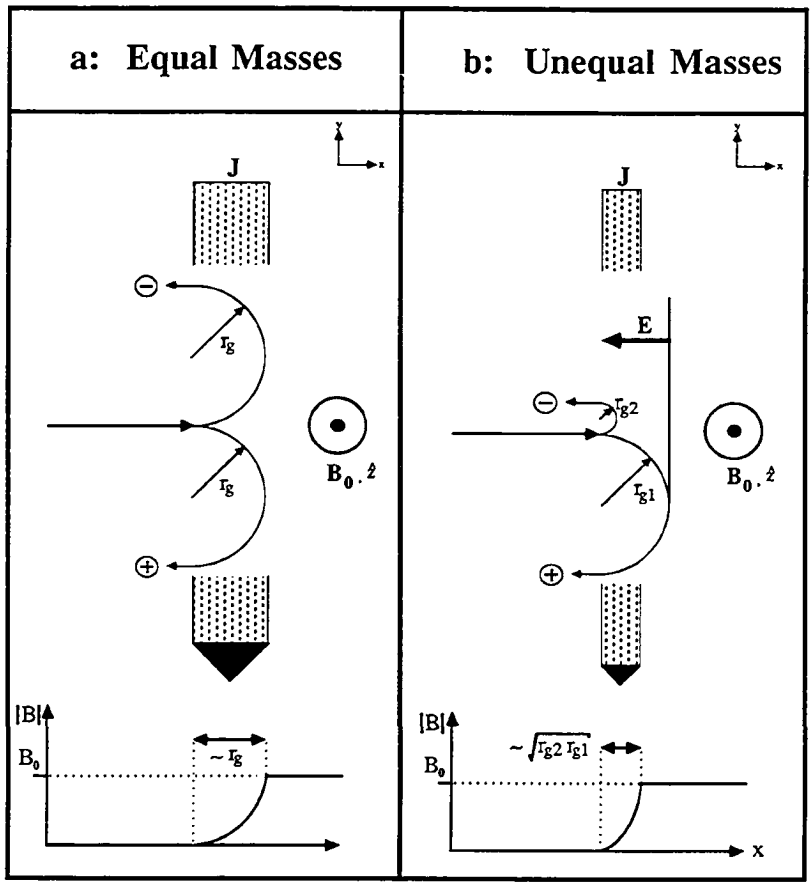

Figure 2-2

layer is thinner, being on the order of the geometric mean of the gyro-radii of the two species.

2) There is no electric field in the equal mass case, whereas in unequal mass case, charge separation, owing to the deeper penetration of the more massive ions gives rise to an electric field directed toward the left. It is found that, in this case, both the electric and magnetic fields strongly influence the electron dynamics, while the ions are influenced primarily by the retarding electric field. The electrons drift in the y direction, along the boundary layer, in the crossed electric and magnetic fields and become the major carriers of the current J.

A situation which corresponds closely to many experimental and naturally occurring phonomena is illustrated in Figure 2-3, below

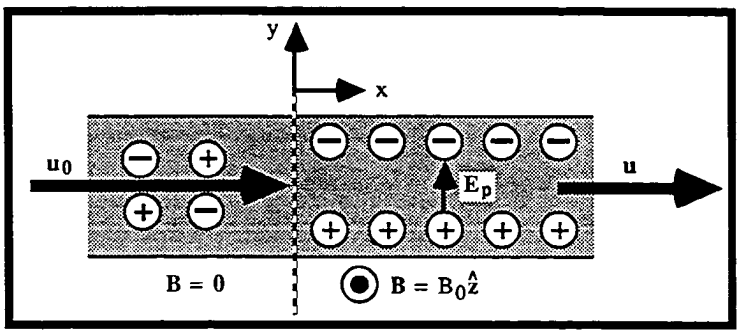

Figure 2-3: Penetration of narrow plasma beam into transverse magnetic field,by virtue of electric beam polarization.

This sketch illustrates the electric polarization of a narrow plasma beam, which enables it to penetrate into a transverse vacuum magnetic field. In cases such as this, the boundedness of the beam in the y-direction provides for the establishment of the electric polarization field, due to the oppositely directed Larmor gyration of the electrons and ions in the beam. These charges undergo separation in the y direction, until further separation is prevented by the polarization electric field. Peter & Rostoker (1982) have modelled this type of system, finding that the narrow beam penetrates the plasma, drifting in the crossed polarization

electric and magnetic fields. Using simple arguments, they show that the plasma velocity across field lines is given by:

$$u_x = u_{x0}(1 - \frac{1}{\varepsilon}), \qquad \text{Eq. 2-5}$$

where, again, ε is the beam plasma dielectric constant, given by equation 2-4, above, and u_{x0} is the incident plasma velocity. Peter & Rostoker go on to derive this result as an average over spatial oscillations of the beam drift velocity, through a rigorous application of the two-fluid plasma equations. Both the electrons and ions participate in the drift, so that the beam carries no electric current as it propagates through the magnetic field. The results of Peter & Rostoker's work is reminiscent of that of Schmidt, alluded to above, in that the ability of the plasma beam to penetrate across magnetic field lines depends upon its capacity to set up and maintain a transverse electric polarization field in which the beam plasma undergoes an $\mathbf{E} \times \mathbf{B}$ drift.

The presence of a background plasma presents an additional factor to be taken into account in considering the capacity of a beam plasma to penetrate a magnetic field. Such a background plasma provides mobile charge carriers which may have the capacity to short out, not only the beam polarization electric field (illustrated in Figure 2-3 above), which would permit beam propagation, but also the longitudinal electric field (illustrated in Figure 2-2b), which would prevent such propagation in the first place. The presence of a background plasma was taken into account in the work of Treumann et al (1983), where they outline a simple derivation of the result that:

$$u_x = u_{x0}\left(1 - \frac{1}{2\left\{1 + \frac{V_{Ap}^2}{V_{Ab}^2}\right\}} \right) = u_{x0}\left(1 - \frac{1}{2\left\{1 + \frac{n_b m_b}{n_p m_p}\right\}} \right), \qquad \text{Eq. 2-6}$$

where u_x is the beam plasma penetration velocity and V_{Ab} (V_{Ap}), n_b (n_p) and m_b (m_p) are the Alfven velocity, particle density and particle mass for the beam (background) plasma, respectively. This result predicts that beam plasmas characterized by large mass densities will propagate through the ambient magnetized plasma relatively unimpeded, while small

mass density beams may be slowed by as much as 50% in the magnetized background plasma.

It should be emphasized that, by penetration into the plasma, we mean penetration to depths on the order of the ion Larmor radius, as contrasted to beam reflection on a length scale of the electon-ion hybrid Larmor radius, such as would take place for the broad beam case discussed by Longmire, and described above. These two length scales are highly disparate. The Larmor radius of a 200 eV Argon ion in a 0.5 gauss field is 258 meters, while the hybrid Larmor radius based on the same Argon ion and an electron moving with the same velocity is less than 1 meter. It is the possibility of propagation in the range of length scales between these two extremes which has been addressed in the works cited above.

Previously Reported Rocket-Borne Results

Several rocket-borne heavy ion beam injection experiments had been carried out before the launch of NASA flight 29.015. Major results obtained from these experiments and reported in the literature will be briefly reviewed here in order to provide a context for the presentation of the positive ion data that we have obtained aboard flight 29.015.

Porcupine. Easily the most ambitious single project to have been carried out to date has been the Porcupine campaign, which was a collaboration between researchers in the Federal Republic of Germany, France, the Soviet Union and the United States. Two sounding rocket payloads were launched in March, 1979, during this campaign, each of which featured multiple ejectable sub payloads (See report by Hausler et al (1986) and references therein for a complete summary of the experiments and results of the Porcupine campaign.). One of the subpayloads in each of the two flights contained a Xenon ion beam generator which produced a ~4 amp Xe^+ ion beam at ~200 eV/q which opened into a half-angle of ~30°. The sub payload containing the ion beam generator was deployed at a large angle of ~60° to the magnetic field lines from the instrumented main payload and other sub

payloads which carried plasma diagnostic instrumentation. In this manner, the spinning (~3-4 Hz) source sub payload periodically 'illuminated' the other payloads with its beam in a lighthouse fashion as it moved away at several (3-4) meters per second. Several major results of these experiments are as follows:

1) Based on measured bipolar magnetic field perturbations, observed every time the beam passed over the main payload, the beam was found to be carrying most of its 4 Ampere beam current across magnetic field lines after it had propagated more than several meters from the source. This is in stark contrast to the idea that a polarization electric field is allowing beam propagation across field lines. In such a case, the beam electrons would travel with the ions and the beam would be current neutralized. Closer than several meters to the ion beam source, the stripping of the beam electrons by the geomagnetic field is incomplete, so that ions and electrons move together and carry no current. The current, therfore, builds up over a length scale of several meters.

2) Also based on magnetic measurements, electric currents are seen to be flowing out of the beam, along magnetic field lines, in regions where the beam current has built up to its full strength. These currents are assumed to be carried by ionospheric electrons flowing into the beam, and to be complimented by electron currents flowing into the beam (electrons flowing out) in the vicinity of the beam-emitting sub payload.

3) Electric field measurements carried out on board a University of California at Berkeley sub payload at separation distances greater than 100 meters from the beam source indicate that an electric field (E_{pol}) in the direction of an expected beam polarization electric field existed within the beam, but at an intensity which was reduced by a large fraction from that expected based on the polarization drift model of beam propagation (ie: Peter & Rostoker, 1982, see above). Further, an electric field (E_{ret}) outside the beam was observed to be oppositely directed to that inside

the beam, indicating a return plasma flow ($\mathbf{u}_{ret}$) outside the beam, as illustrated in Figure 2-4, below.

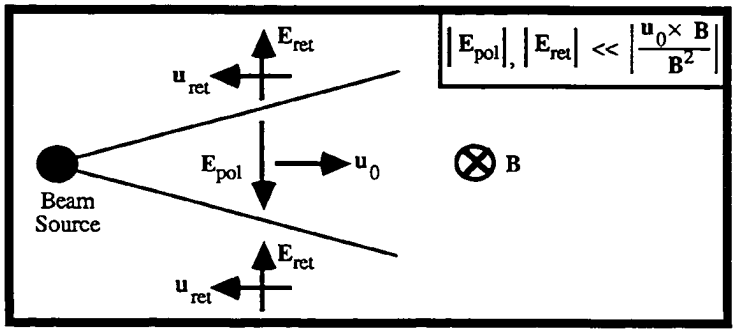

Figure (2-4): Electric fields in the vicinity of Porcupine Xe^{+} beam, as measured at the University of California sub payload.

Direct particle measurements were carried out during the Porcupine flights by the use of wide field of view Retarding Potential Analyzers (RPA), which provide integral particle flux measurements over the RPA field of view. In the case of electrons, the RPA looked up the field line and generally supported the pitcure of electrons flowing along field lines into the beam. Further, by combining the RPA measurements with payload potential measurements, the energy of these electrons was estimated to be above 2 eV. In the case of the ions, consistent maxima in the ion flux were observed when the RPA viewed in the direction of the source, evidencing direct observation of beam ions. By combining measurement of these fluxes with Langmuir probe electron density measurements and assuming $n_e = n_i$, the beam ion velocity was estimated. Based on such estimates, it was suggested that at separations of greater than 150 meters (after the beam density had fallen below the background ionospheric density), the beam began to be slowed in its transverse motion through the ionospheric plasma. This is consistent with predictions based on models of the transverse beam injection process, produced by theoretical researchers (Peter & Rostoker, 1982 and Treumann et. al., 1983).

The Porcupine flights were very well instrumented for making plasma wave observations, with the main payload and 2 of the four sub payloads equipped for such observations. Both low and high frequency waves were commonly observed during Xe^+ injections (Kintner & Kelley 1981; Lebreton et al., 1983; Pottelette et al., 1984). A detailed discussion of these wave observations or the possible responsible instabilities is beyond, not only the scope of this work, but also the expertise of this author. It is sufficient to note that significant plasma wave power was consistently observed in association with beam injection, that these waves were often highly structured in both frequency and configuration space and that wave structure was often highly correlated with structure in other measured parameters such as charged particle density and Xe^+ source payload spin phase. One of the more striking aspects of the observed wave fields included harmonic emissions at multiples of the H^+ cyclotron frequency. These emissions extended at least to the 20^{th} but, notably, were weak or absent at the 1^{st} through 3^{rd} H^+ cyclotron harmonics. In addition, broad band waves in the 0 - 16 kHz frequency range were observed in regions of large plasma density gradients at the leading edge of the rotating beam (Lebreton et al, 1983). Primary candidates for driving plasma waves in this kind of environment include streaming instabilities associated with the beam ions (Kintner & Kelley, 1983; Roth et al., 1983; Seiler et al., 1976), drift instabilities associated with density gradients on the leading and trailing edges of the beam (Potellette et al., 1984) and current instabilities associated with electrons flowing into and out of the beam along magnetic field lines.

ARCS 1. Flight 29.015 itself is often referred to as ARCS-3, for Auroral Rocket for Controlled Studies-3 and, as this name indicates, was the third such experiment to be undertaken in collaboration by the University of New Hampshire and other institutions. The first of these experiments, NASA flight 29.014, (Kaufmann et al., 1985; 1987; Moore et al., 1982, 1983; Walker et al., 1980 a,b and Walker,1986) was flown from Poker Flat Research Range in Fairbanks, Alaska in January of 1980 and was a joint project of the

Universities of New Hampshire and Minnesota, Cornell University and the Naval Research Laboratory. This rocket payload carried a single beam generator which nominally produced a 100 mA Ar^+ beam , which opened into a ~30° half-angle cone and which was operated several times on the downleg of the flight. As in the case of ARCS-2, the beam was ejected from an ionization chamber which was maintained at +60 V with respect to the rocket ground. This is in contrast to the beam on flight 29.015 (ARCS-3), where the beams were produced in chambers maintained at ~ +200 V with respect to rocket ground. ARCS-1 differed from the following two ARCS experiments in that the ion beam operated from on board the main payload, there being no separable sub payload associated with the experiment. ARCS-1 had no instrumentation with which to measure the beam ions, as the only positive ion particle detectors on board were Ion Drift Detectors (IDD) which were cylindrical electrostatic analyzers operating in the range 0.5 - 5.0 eV/q. In addition to the IDDs, two fast Pulsed Langmuir Probes (Holmes & Szuszcewicz, 1975), one of which was capable of following large shifts in payload potential, AC and DC electric field experiments, a $\delta n/n$ wave experiment and octospheric electrostatic analyzers, capable of measuring electrons in the energy range 0.08 - 25 keV, made up the diagnostic instrument package on flight 29.014.

The major result of the analysis of the data obtained during this flight to have been reported so far involves the effects of ion beam operation on the background electron populations (Moore et al., 1982; Kaufmann et al., 1985). Specifically, anomolous superthermal (<1 keV) electron populations were observed at the beam-emitting payload in coincidence with ion beam operation. Strangely, these electrons were observed to be isotropic in pitch angle at energies above ~300 eV/q and to fill only the downgoing ($0 \leq \alpha \leq 90$) hemisphere for electron energies below ~300 eV/q. An explanation of the presence of these electrons which was first put forward by Moore et al. (1982) and elaborated on by Kaufmann et al. (1985) involves the interruption of an electric current system on anomolously resistive magnetic field lines connected to the beam-emitting rocket payload.

This current system may have been a pre-existing system associated with a weak auroral arc to which the rocket was magnetically connected during much of its downleg flight, or it may have been associated with the closure of the 100 mA current carried away from the payload by the beam ions. In any case, with reference to the anomolous resistivity mechanism put forward in the works of Rowland et al. (1981, a, b) and Rowland and Palmadesso (1983), large amplitude and broad band low frequency waves observed during gun operations are thought to have impeded electric currents flowing upward along the magnetic field lines by trapping the low energy current carrying electrons. This results in the establishment of a parallel electric field which directly accelerates electrons already energetic enough to avoid trapping. These same waves then scatter the accelerated electrons in pitch angle, producing isotropy in the downgoing hemisphere. The pitch angle scattering takes place through an anomolous Doppler resonance which is given by the satisfaction of the following relationship between the parallel electron velocity ($v_{||}$), the electron cyclotron frequency (Ω_{ge}), the parallel wave number ($k_{||}$) and the wave frequency (ω):

$$v_{||} = \frac{\omega \pm \Omega_{ge}}{k_{||}}, \qquad \text{Eq. 2-7}$$

or, for the low frequency waves under discussion here ($\omega \leq 10$ kHz $<< \Omega_{ge} \approx 10^7$ Hz), the resonance condition is given as:

$$v_{||} = \frac{\pm \Omega_{ge}}{k_{||}}. \qquad \text{Eq. 2-8}$$

For electrons with pitch angles near 90°, this condition cannot be satisfied. Kaufmann et al. (1985) have argued that electrons with energies greater than about 300 eV interact directly with waves whose perpendicular wavelength is comparable with the electron gyro-radius, or:

$$k_{\perp}\rho_e \approx 1. \qquad \text{Eq. 2-9}$$

This represents a finite gyroradius effect and will allow electrons with gyro-radii larger than the smallest perpendicular ion fluctuation wavelength present to scatter through 90° to

become an upcoming electron which can then participate in the anomolous Doppler scattering expressed in the resonance condition embodied in Eq. 2-8. Based on these arguments and the fact that superthermal electrons observed on board flight 29.015 are isotropic in both hemispheres only for electrons above ~300 eV, Kaufmann et al. place a lower cutoff of 1 to 1.5 meters for the perpendicular wavelengths of the scattering ion waves in the system.

In addition to the effects of gun operations on the local electrons, described above, solid evidence of transient payload charging at the initiation of beam operations was consistently observed in both the detected thermal ions (Moore et al., 1983) and in the electron current collecting pulsed Langmuir probe (Kaufmann et al., 1987). Peaks in the thermal ion count rates, normally seen at a Volt or two (eV/q) move off (above) the 5 volt scale for some 40 ms at the beginning of the gun pulses, indicating a transient negative payload excursion of at least ~5 Volts for that duration. Additionally, the pulsed Langmuir probe was seen to collect a saturated ion current, which was independent of the applied probe sweep voltage for, again, some 40 ms following the initiation of a given beam operation. As in the case of the thermal ion observations, a negative voltage excursion of greater than ~5 Volts is inferred from this observation.

ARCS-2. NASA flight 36.001, flown in November, of 1982, also from Poker Flat, Alaska, featured a separable sub payload from which two ion beam generators operated. This experiment was very similar in most respects to the ARCS-3 (NASA flight 29.015) experiment, with only a few important differences. Very little has been published regarding this ion beam experiment, with the exception of the paper (Moore et al., 1983) presented by T. E. Moore at the ESA Symoposium on Active Experiments in Space in May, 1983. They presented evidence of highly structured DC electric fields in the immediate vicinity of the beam emitting sub payload, which were strongly influenced by the release of ACS gas into the plasma. In addition, they presented data showing enhanced wave fields which were broadband and without structure in frequency while the beam

emitting sub payload was attached to the diagnostic payload and which were narrowly banded and centered in frequency near the ambient lower hybrid resonance frequency when the two payloads were unattached. Beam-related positive ions were observed on the diagnostic payload during both attached and unattached beam operations, although no details of the distribution of these ions in phase space have been presented.

Objectives, Experimental Approach and Flight Overview

Description of Goals

In the previous subsection, we discussed some of the theoretical and experimental work which preceeded NASA flight 29.015 in trying to discern the details of the interaction between plasma beams and the background plasmas and magnetic fields into which these beams flow. It should be apparent from that discussion that, although much progress has been made, many questions remain to be answered.

In the first place, no experiment carried out in space to date had properly addressed the question of the measurement of the detailed distribution of positive ions in phase space in the vicinity of a beam emitting souce. A knowledge of the distribution of beam ions as a function of energy, directional motion and position with respect to the beam source provides direct knowledge of the propagation of the beam through the magnetized plasma. Furthermore, knowledge of the distribution of ambient ions as a function of the same parameters could provide a measure of the degree of coupling between the beam ions and the background ions, in addition to important clues as to the nature of that coupling. Primary goals of this experiment, then, were to provide such detailed ion measurements and to distinguish between the various measured ion species on the basis of particle mass. The ability to distinguish between particles of different masses would provide the basis for distinguishing between characteristics of the beam particles (Ar^+: m =40 amu) and those of the ambient (typically O^+: m = 16 amu) background plasma.

Secondly, we were interested in providing comprehensive diagnostics of the plasma environment on and near the geomagnetic field line which connected to the beam source, as a function of distance from that source. The reader may recall that the geometry of the Porcupine experiments was such that all diagnostics were carried out at locations which were separated from the plasma source roughly across magnetic field lines, while the

ARCS-1 (NASA flight 29.014) experiments featured no separable payloads, so that all measurements were carried out from on board the beam emitting rocket payload. Thus, no measurements had been carried out at points separated from the beam source in a direction along the geomagnetic field line through the source. This is a very important region of space with respect to these type of experiments, however, due to the facts that dense field aligned currents may be flowing in this region to provide current continuity at the beam source 'node' and that, in this region, observations of the beam particles themselves may be carried out after they have performed one or more full gyrations, and represent the characteristics of the beam in a state of advanced evolution.

Payload Instrumentation

As mentioned above, NASA flight 29.015 included the reflight of the 36.001 main payload, which had been recovered after flight in November, 1982 and which received some modification before reflight. The experiment description given in this and the following subsections applies to flight 29.015 and 36.001, except for several important differences, which will be pointed out as the descriptions proceed.

The 29.015 flight package is illustrated in block form in Figure 2-5, which includes a sampling of the vehicle dimensions. The package consisted of the separable sub payload, the main payload instrumentation section, the Pulsed Code Modulation (PCM) telemetry system section, the Atitude Control System (ACS) section and the payload recovery section. The entire package was launched from a rail and powered into space by a 2-stage Terrier-Malemute rocket motor system. Futher description of these various payload sections will be presented in the following paragraphs.

Sub Payload. We will begin our description at the nose, with the separable sub payload, which included all systems associated with the generation of the plasma beams, a single axis aspect magnetometer, a collimated, calibrated auroral photometer, a spherical Langmuir probe and an independent FM-FM telemetry system. With the exception of the

NASA SOUNDING ROCKET 29.015

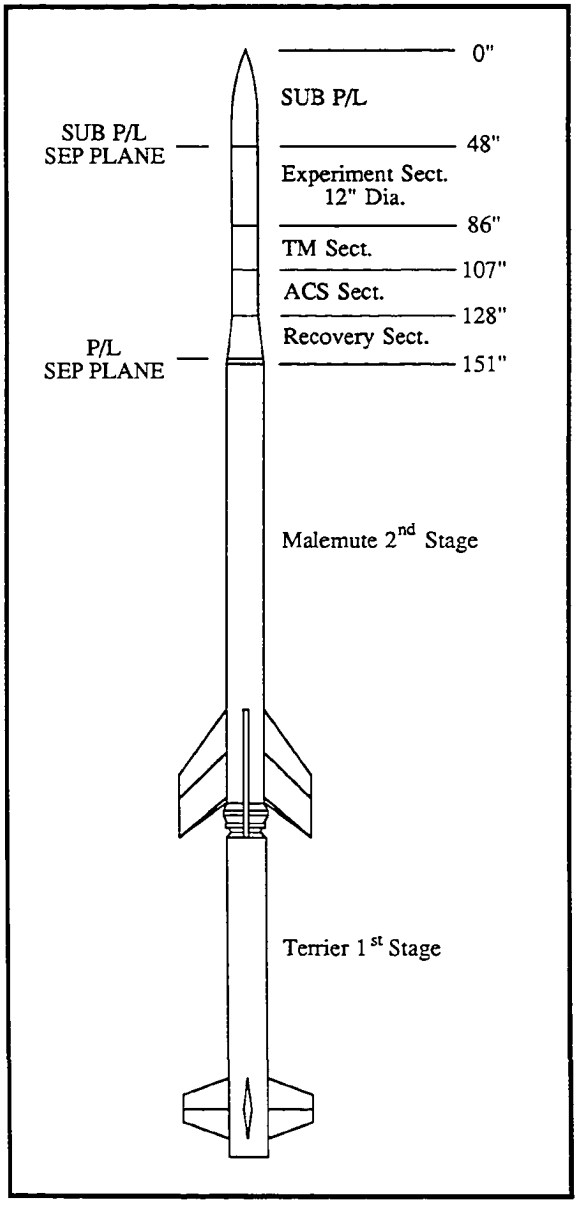

FIGURE 2-5

photometer experiment, which was built and calibrated at UNH, all elements of the sub payload were constructed by R. E. Erlandson and J. Pearson, under the direction of Professor L. J. Cahill at the University of Minnesota. This package was very similar in the cases of flight 36.001 and 29.015, with only three important differences, which will be listed below. The sub payload assembly is schetched in Figure 2-6.

The plasma generation system has been described in full elsewhere (Erlandson, 1984, 1986) and consisted of two beam generators, one pointing anti-parallel and the other perpendicular to the sub payload spin axis. The operation of plasma beam generators such as those flown in these experiments is illustrated in Figure 2-7, taken from Erlandson (1984). With reference to that figure, a flow of neutral Argon gas is introduced to the ionization chamber as shown. The gas atoms are ionized by electrons which are emitted by the hot, current carrying filament. These electrons are energized by virtue of a positive electrostatic potential applied to the cylindrical anode. The probability for ionization by electron impact within the chamber is increased by introducing the axial magnetic field, created by the solenoidal current windings shown. The presence of this (~ 25 Gauss) field increases the ionization probability by inhibiting electron transport from the hot filament to the anode, increasing the residence time of energetic electrons within the chamber. Also by virtue of the positively biased cylindrical anode, the ions produced in the chamber are born in a region of positive potential with respect to subpayload ground and, to the extent that the sub payload remains at the same electric potential as the external plasma, these new ions are produced in a region of positive potential with respect to that plasma. This last is a very important point, since maintaining the sub payload near the plasma potential is not a trivial matter. This will be discussed more fully in a later subsection. The newly created ions are ejected by reason of the electric potential gradient between the chamber interior and the plasma outside, forming a beam whose energy distribution depends on the electrostatic potential distrubution within the chamber, the distribution of locations at which new ions are formed and the nature of any diffusive processes taking place within and near the

29.015 SUB PAYLOAD

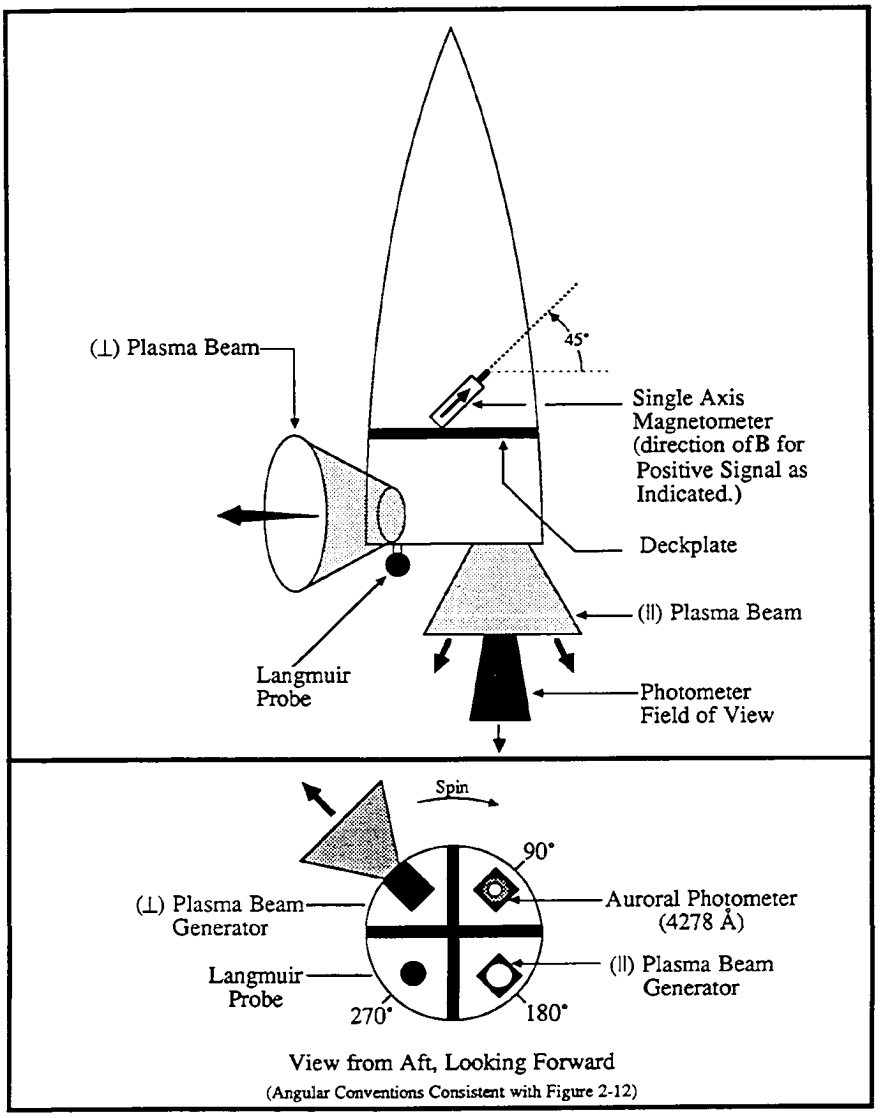

Figure 2-6

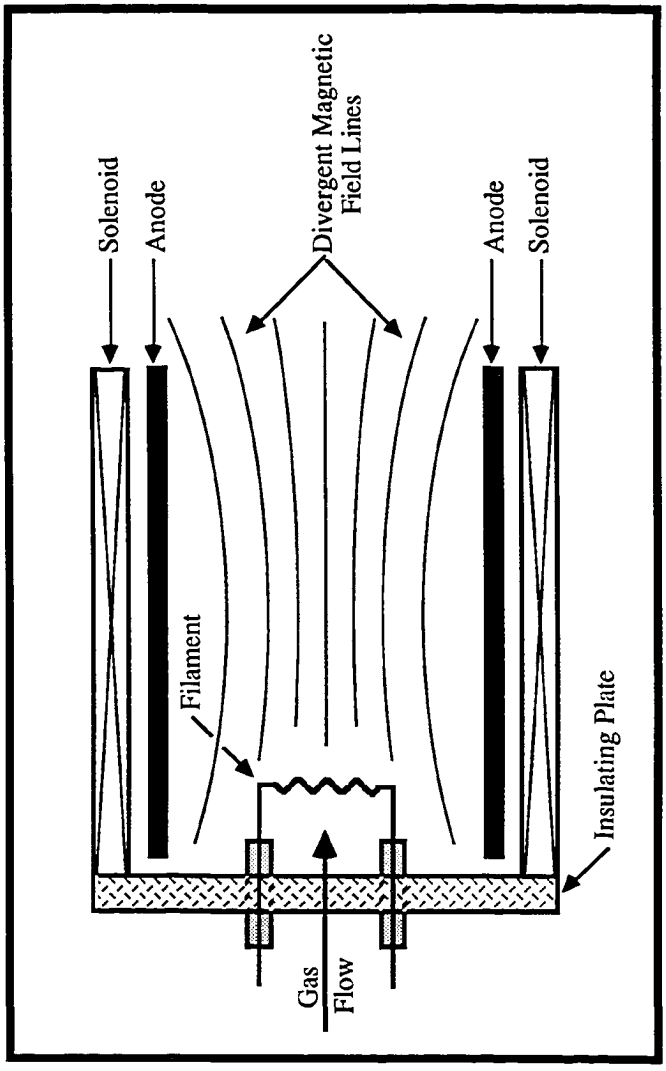

Figure 2-7

ionization chamber. Laboratory measurements of the resulting beam characteristics were performed by C. J. Pollock and R. E. Erlandson at the NASA Wallops Flight Facility in the summer of 1984. In this experiment, a prototype HEEPS electrostatic analyzer was used to measure energy spectra as functions of angle with respect to the beam generator symmetry axis. Figure 2-8 shows a collection of such energy spectra, taken with a 202 Volt bias applied to the generator anode. It can be seen from this data that at large angles the analyzer event rate maximizes in broad peaks near half the anode voltage, while at smaller angles, the distributions are narrower, peaking at energies per charge corresponding more closely to the applied anode bias. These high energy peaks measured near the beam axis show count rates more than 2 orders of magnitude larger than the peak count rates observed at larger angles. Secondary maxima at small angles may be seen at energies per charge of ~300 - 400 Volts (<~ twice the anode voltage). These may be attributed to particles which are doubly ionized within the chamber and then partially recombined before reaching the analyzer. Figure 2-9 shows event rates plotted as functions of angle, using the same data as that used to generate Figure 2-8. The unfilled triangles represent the event rates summed over energies and the filled triangles represent the event rates at the energy of maximum transmission. From this figure, it can be seen that the intense part of the beam had an angular width of ~20 - 30°, depending upon the criteria used. In other measurements (Erlandson, 1984), the beam was found to have a Half Width at Half Maximum (HWHM) of 23°. Figure 2-10 shows the Ar^+ ion beam density (n) plotted as a function of energy, derived from the data taken at a beam angle of 8° and using the relation

$$n = \frac{J}{v}, \qquad \text{Eq. 2-10}$$

where J is the measured integral ion flux and v is the measured ion velocity. This data is not directly comparable to the situation encountered in space, because the laboratory measurements were carried out under extremely reduced flux conditions. The maximum density is seen to occur near 150 eV/q. This figure should be compared with Figure 1 of

ANGULAR VARIATION OF AR^+ ION BEAM ENERGY DISTRIBUTIONS

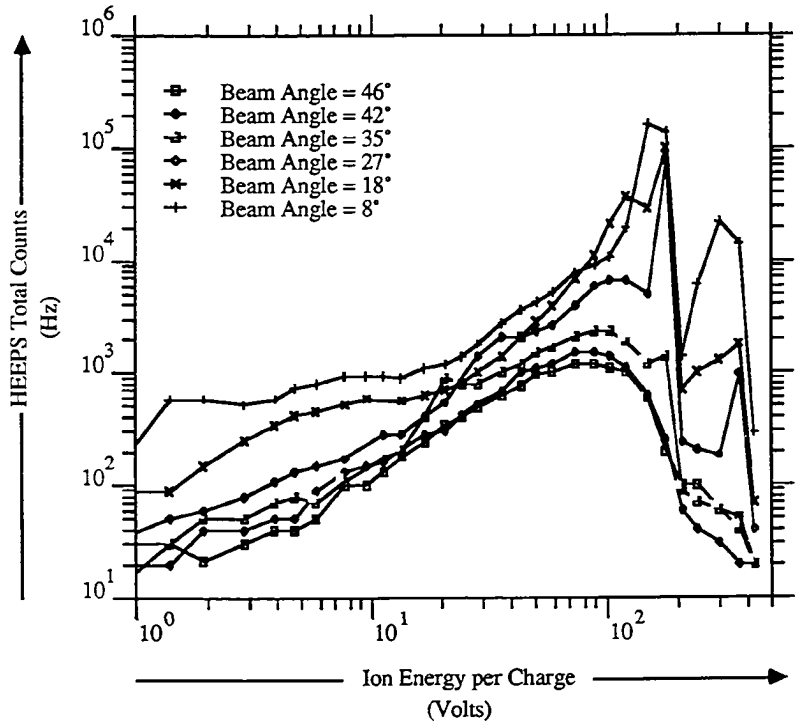

Figure 2-8

ANGULAR AR^+ BEAM FLUX PROFILE (Laboratory Measurements)

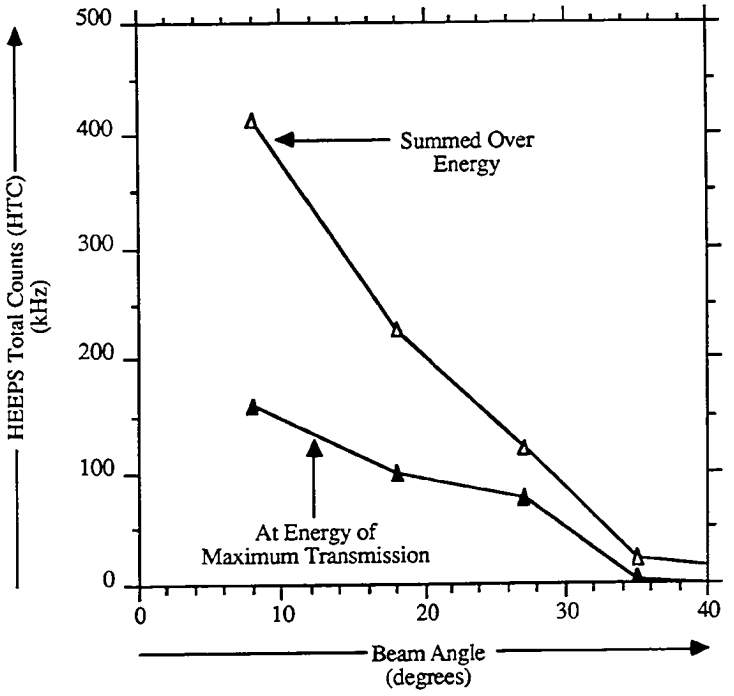

Figure 2-9

ENERGETIC AR^+ BEAM DENSITY PROFILE (Laboratory Measurements)

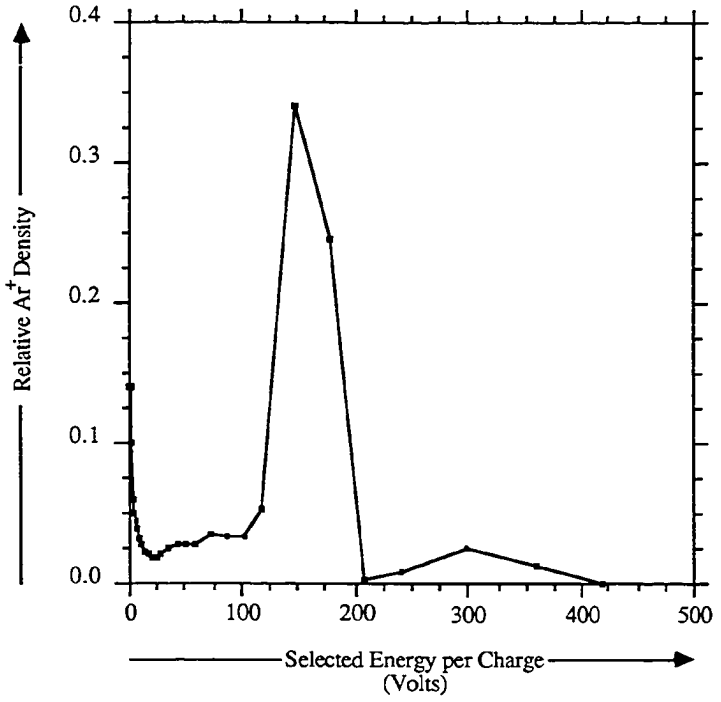

Figure 2-10

Moore et al. (1983), which shows a similar curve, based on data produced by the Hughes Aircraft Corporation, for the case where the anode bias was 60 Volts. These results are quite different, with Figure 1 of Moore et al. (1983) showing the density maximizing at ~ 25 eV/q, less than half of the applied anode bias. It is not easy to reconcile the difference between these two figures, which appear to give such different results in the beam energy distrubutions. Retarding Potential Analyzer (RPA) measurements carried out by Erlandson (1984) indicate energy distributions similar to those shown by Moore et al. It would be worthwhile to carry out more laboratory tests with both electrostatic analyzers and RPA's before flying another beam generator of this type.

The sub payload carried a calibrated photometer which featured an RCA-4441A photomultiplier tube, covered by an interference filter with an ~80 Angstrom (FWHM) bandpass centered at ~4560 Angstroms. This permits passage of λ = 4278 photons emitted in the 1st negative band of molecular nitrogen (N_2), a common constituent of the neutral upper atmosphere. Photon emissions at this wavelength are common in the presence of precipitating energetic auroral electrons (Egeland et al., 1973). This photometer was collimated, with a circular 8° (FWHM) field of view. Calibration of the photometer for absolute sensitivity to incident photon flux was carried out at the University of New Hampshire, with the use of a calibrated standard lamp (EG&G Ortec Model 597-1). The results of these sensitivity calibrations for the 29.015 flight (SN-4) and spare (SN-3) units are shown in Figure 2-11. This figure shows the photon emission intensity in the photometer look direction in units of kilo-Rayleighs, plotted against the voltage output of its logrithmic amplifier, which is the signal telemetered to earth. The Rayleigh is a unit of photometric column emission, with 1 Rayleigh corresponding to an emission of 10^6 photons in all directions from within a column of cross section equal to 1 cm^2.

A 20 cm^2 spherical Langmuir probe was mounted 2.2 cm below the base of the sub payload. This probe featured a sweeped bias which ran from -3 V to +3V, with a 0.27 second sweep period, and was sensitive to ion or electron currents of from 0.1 to 15 μA

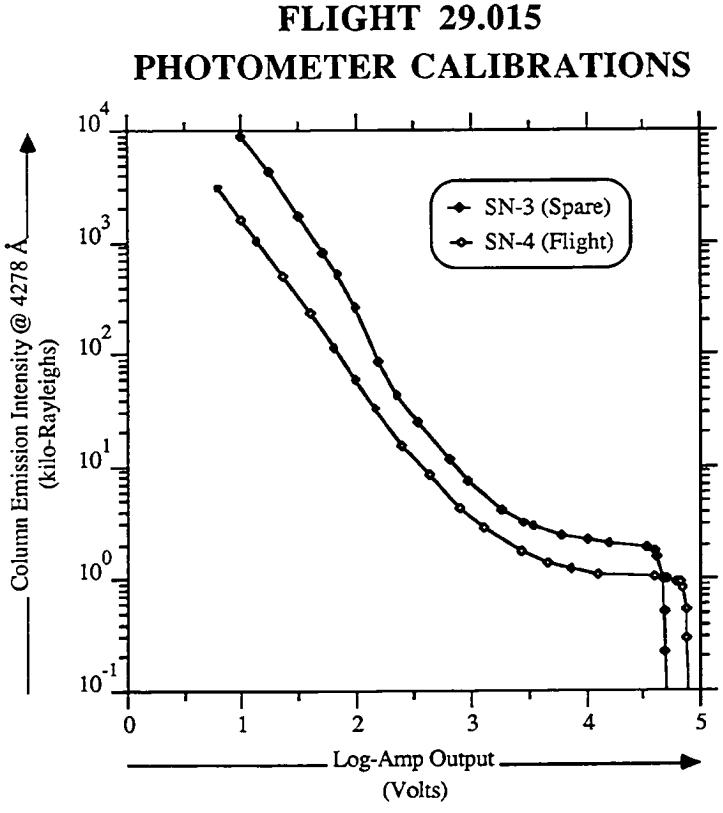

Figure 2-11

(Erlandson, 1986). The close proximity of this probe to the sub payload base (Debeye length ~ 1 cm) limited its usefulness for quantitative plasma diagnostics, however, as will be shown, the probe's performance provides telling evidence with regard to the electrodynamic state of the sub payload during ion beam operations.

Finally, a HeliFlux® (Schonstedt Instrument Company, Reston, Va.) single axis aspect magnetometer was placed in the sub payload for the purpose of monitoring the dynamic stability of the sub payload during its flight. This magnetometer was oriented with its sensitive axis inclined by ~ 45° from the sub payload spin axis. Calibration data provided by the manufacturer yeilds the expression:

$$B = (-0.596\ V + 0.249)\ \text{Gauss} \qquad \text{Eq. 2-11}$$

for the magnetic induction (B) along the magnetometer's sensitive axis, as a function of the output voltage (V), which is telemetered to ground. The signal received from this magnetometer indicates that, indeed, the sub payload flew in a stable spinning trajectory, with a uniform spin period of 0.362 seconds and coned with a half angle of ~1° and a coning period of ~2 seconds.

Differences between the sub payloads flown on the 36.001 (ARCS 2) and the 29.015 (ARCS 3) missions were:

1) The 36.001 sub payload carried no Langmuir probe, such as that described above, which was carried on the 29.015 sub payload.

2) In the case of the 36.001 sub payload, the beam generator which pointed anti-parallel to the sub payload spin axis emitted a He^+ (m = 4 amu) ion beam, while the generator which pointed perpendicular to the spin axis emitted an Ar^+ (m = 40 amu) ion beam. In the case of the 29.015 sub payload, both beam generators emitted Ar^+ ion beams.

3) The beam generators flown on the 36.001 sub payload featured anodes biased at ~ +60 V, while those flown on board 29.015 had anodes biased at +220 V ±10%

and +190 V ±10% (Erlandson, 1986), in the cases of the perpendicular and parallel generators, respectively.

Main Payload. Major elements of the 29.015 main payload included the main payload instrumentation section, which housed the major share of plasma diagnostics, the Pulsed Code Modulation (PCM) telemetry system, which transmitted digital data to the receiving station located at the launch site, the Atitude Control System (ACS), which was used to control the orientation of the payload for purposes of obtaining controlled sub payload ejection geometry and maintaining nominal main payload aspect, and the main payload recovery system section, which included the re-entry parachute and a radio beacon transmitter.

The main payload instrumentation section is illustrated in Figure 2-12, which shows the location and orientation of most of the instruments referred to in the description provided below. Note the four wiring raceways (RW) labelled as the 0°, 90°, 180° and 270° RW. Of particular interest in this figure are the two coordinate systems labelled as 'gyroscope coordinates' and 'magnetometer coordinates', and the relation of the various experiments to them. Particle and field data collected in flight are directly interpreted in terms of one of these two coordinate sets. In turn, as described in Appendix A, the orientation of these systems in a system fixed with respect to Earth is provided either by data from the 3-axis aspect magnetometer or from the 3-axis inertial gyroscope system (not shown).

As mentioned above, the 29.015 and 36.001 main payloads were one in the same, the 36.001 main payload having been recovered after its flight in November, 1982. The single important difference between these two payloads rested in the replacement of the two Ion Drift Detector (IDD) electrostatic analyzers, flown on flight 36.001 with the single HEEPS instrument flown on board flight 29.015. The HEEPS instrument has been

29.015 MAIN PAYLOAD INSTRUMENTATION

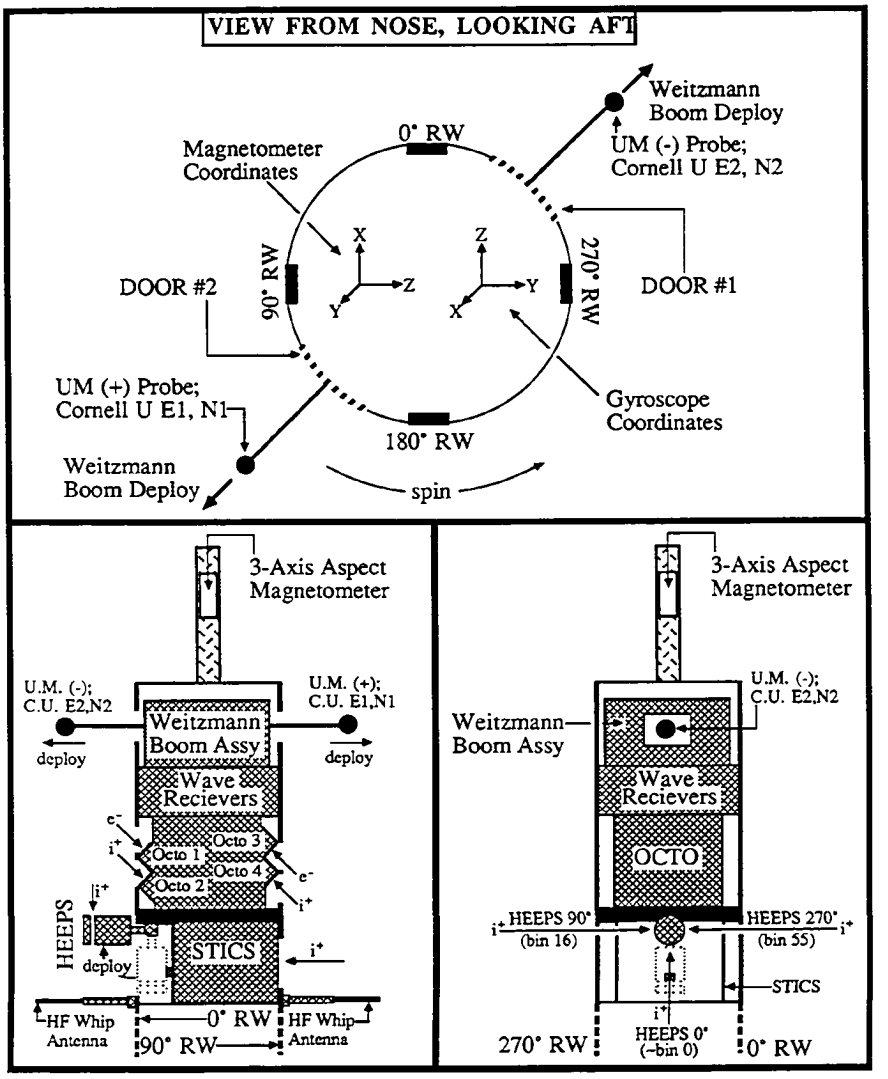

Figure 2-12

described in full in Section 1. All other instrumentation on board the main payload was flown on both the 36.001 and 29.015 payloads.

Supplementing the low energy ion measurements carried out by HEEPS (IDDs) was a SuperThermal Ion Composition Spectrometer (STICS) which consisted of two stages: an electrostatic analyzer operating in the range ~ 0 - 500 eV/q, followed by a magnetic mass spectrometer stage, which was designed to operate in two modes, selecting particles according to their mass per charge into three channels. In the low mass mode, STICS selected particles with (m/q) of ~ 1 (H^+), 4 (He^+) and 16 (O^+), while in the high mass mode, STICS selected particles with (m/q) of 2 (He^{++}), 8 (O^{++}) and ~30 (O_2^+, N_2^+ and NO^+) . This instrument was designed and built at UNH. Unfortunately, due to problems with high voltage arcing in the channeltron electron multiplier circuits, no useful data was obtained with the STICS instruments flown on either ARCS-1 or ARCS-2.

Characterization of the energetic particle environment aboard the ARCS 2 & 3 experiments was provided for by the use of 4 octospheric electrostatic analyzers (OCTO 1-4), two of these (OCTO 1&3) being dedicated to electron measurments and two (OCTO 2&4) dedicated to the measurement of energetic ions. The OCTO analyzers were swept through the energy per charge range 10 eV - 20.7 keV in 32 steps every ~ 6.5 seconds. Additionally, each of these 32 steps was toggled between two values of selected E/q, giving a total of 64 distinct energy states in the ~ 6.5 second sweep. These electrostatic analyzers featured energy independent geometry factors of $1x10^{-3}$ cm^2-ster-keV/keV, 8°x8° fields of view and resolution in energy per charge of ~ 10%. Two octospheres (OCTO 1&2) were oriented with look directions inclined by 45° from the payload spin axis and two (OCTO 3&4) with look directions inclined by 135 degrees from the spin axis,which was, in turn, inclined by 135° from the geomagnetic field, providing full pitch angle coverage from the spinning payload.

In addition to the instrumentation, described above, for measuring charged particle fluxes, both the ARCS 2 and 3 experiments carried a single set of 3 meter (tip to tip)

Weitzmann booms and a pair of high frequency plasma wave antennas. The Weitsmann booms were used to deploy one pair each of cylindrical Langmuir probes and spherical electric potential probes. The signals from the two electric potential probes provided information on the difference in electric potential between the two probes (3 m separation) or between either probe and the rocket skin. This information was processed by several independent recievers to provide measurements of the electric field along the line between the probes in several distinct frequency ranges extending from DC to more than 10 kHz. The Langmuir Probes provided information on the electron density and temperature within the sampled plasma, as well as on fluctuations ($\delta n/n$) in the frequency range from 0 to 10 kHz. In addition to the electric field experiments, a magnetic induction antenna was flown on the main payload. The signals from this antenna were processed by a wave reciever sensitive in the frequency range from 200 Hz to 10 kHz. Finally, a Develco model 7200c three axis magnetometer was mounted at the top of the main payload and has been used for the determination of the orientation of the payload with respect to the ambient geomagnetic field. This magnetometer is sensitive to induction fields in the range from -0.6 to 0.6 Gauss and is certified by the manufacturer to have its axes orthogonal to each other to within 1°. The signal from each axis was transmitted to earth on both FM-FM and PCM telemetry links, with the PCM transmission providing a 14 bit word for each of the 3 axes every 3.2 milli-seconds, yielding an expected achievable measurement sensitivity of ~7 nano-Teslas. Each of the various wave and field experiments listed above were provided by either the Unversity of Minnesota (Professor L. J. Cahill) or by Cornell University (Professor P. M. Kintner). More detailed descriptions of many of these experiments may be found in the work of Erlandson (1986).

Flight Overview.

Geophysical Conditions Surrounding Flight. Nasa flight 29.015, otherwise known as ARCS 3, was launched toward geomagnetic south (geographic

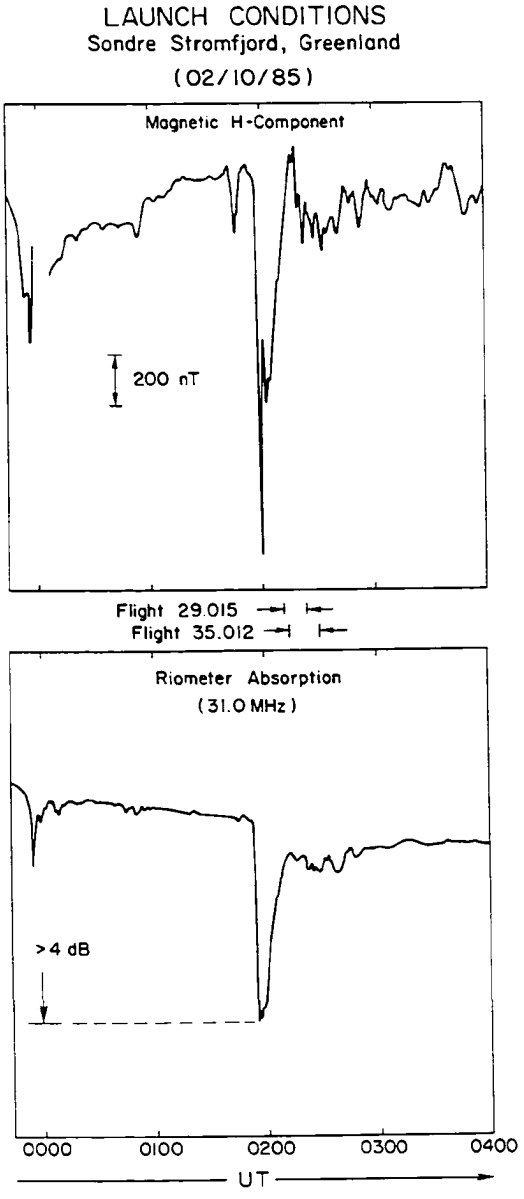

Figure 2-13

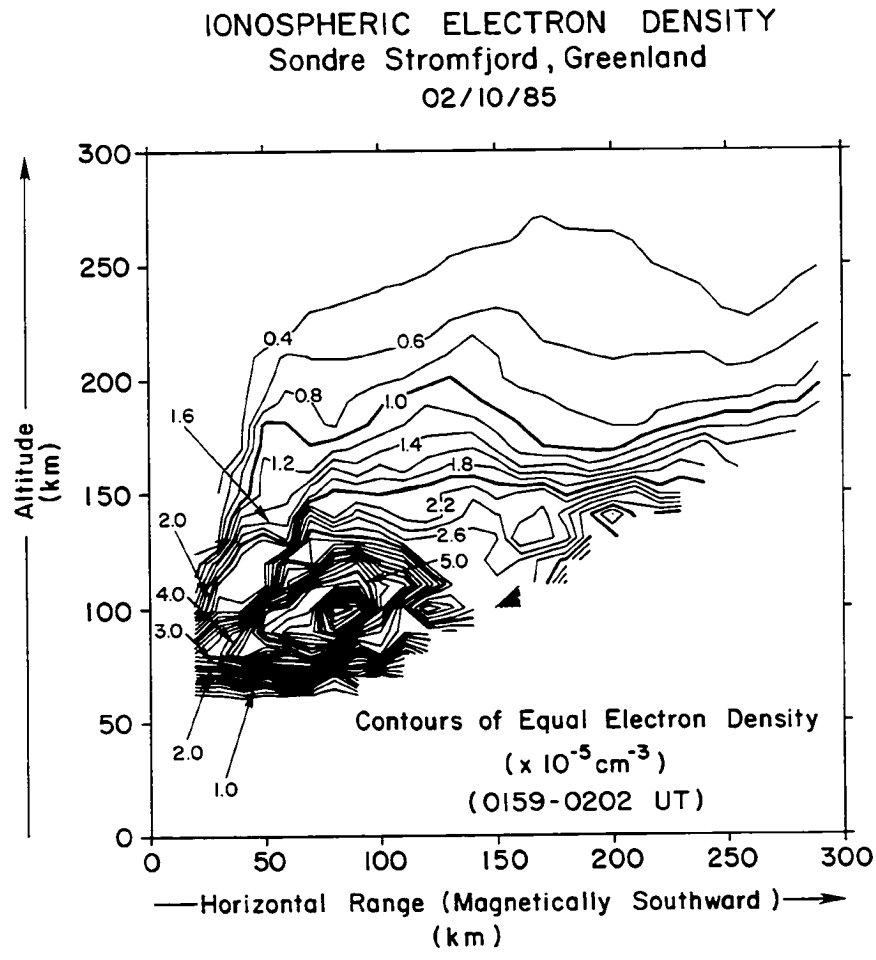

Figure 2-14

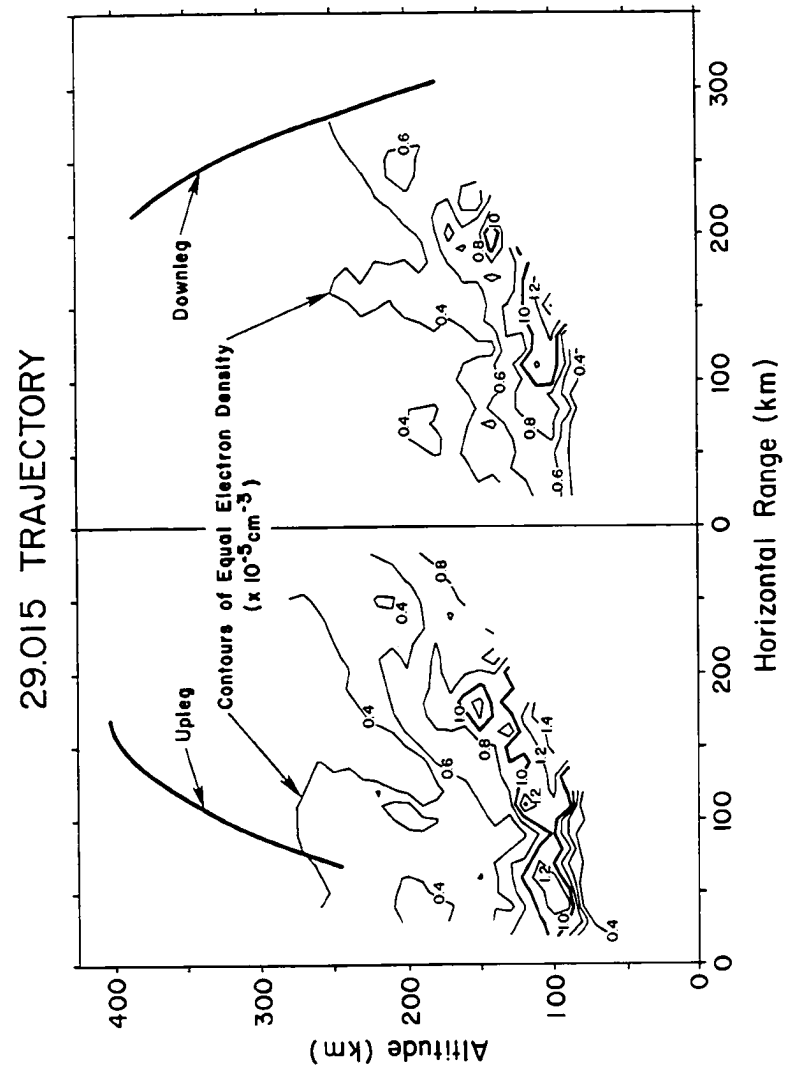

Figure 2-15

southeast) from Sondre Stromfjord, Greenland, at 0211 UT (~ midnight MLT) on 10 February, 1985. At an invarient latitude of 74.1°, Sondre Stromfjord lies well within the region of the nominal geomagnetic polar cap, northward of the statistical auroral oval, as did the entire 29.015 trajectory, which approched the oval from the north. The three hour global index (k_p) of geomagnetic activity was near 4 on the night of February 9-10.

Figure 2-13 shows the recorded magnetic H component as well as the 30 MHz riometer absorption measured near the launch site, plotted verses UT time for several hours near the time of the launch. These data were supplied through the courtesy of Eigil Friis-Christensen (magnetometer) and Peter Stauning (riometer), both of the Danish Meteorological Institute. Shortly before launch, at roughly 0200 UT, an extremely large (> 4 db) increase in the riometer absorption above the launch site indicated the occurence of intense auroral electron precipitation overhead, although this was not verified with visual observations due to the fact that the sky was overcast at the time. In addition, a large (> 1000 nT) negative bay in the magnetic H component accompanied the riometer absorption event at the launch site shortly before launch. This was indicative of a westward electrojet current system flowing in the ionosphere above the launch site at the time. Ionospheric density measurements carried out by members of the Stanford Research Institute (SRI) using the Sondre Stromfjord Incoherent Scatter Radar facility supported the conclusion of intense electron precipitation overhead, showing enhanced densities which reached 7×10^5 cm^{-3} near 100 km altitude at the time of the launch. This is well illustrated in Figure 2-14, which shows contours of equal electron density plotted versus altitude and horizontal range southward from the launch site during the time interval extending from ~0158 to ~0202 UT. However, by the time the 29.015 rocket payload got into space and was making measurements, the riometer absorption had decreased dramatically, as had the overhead ionospheric electron density and the deflection of the horizontal magnetic component (see Figure 2-13). Figure 2-15 shows the trajectory of the 29.015 payload plotted as altitude versus horizontal range and superimposed on contours of equal electron

density as measured with the radar by the SRI researchers during the flight. It can be seen from this figure that the density was much decreased from the peak values of near 10^6 observed immediately prior to launch, indicating locally decreased auroral activity. Stacked plots of measurements made by the Danish Meteorological Institute's Greenland magnetometer chain indicate that the intense westward electrojet had moved southward, beyond the range of the 29.015 payload. Finally, electron measurements carried out from on board NASA flight 35.012, which was in flight from Sondre Stromfjord simultaneously with flight 29.015, indicate minimal electron precipitation activity taking place during the flights. All these facts indicate that, although a large amount of geomagnetic substorm activity was taking place in the vicinity of the Greenland subcontinent, this rocket flew through an ionosphere which was largely quiescent and devoid of auroral activity, with local electron densities being at or below a level of several times 10^4 cm^{-3} throughout most of the flight (see Figure 2-15).

Experiment Plan and Overall Vehicle Performance. Table 2-1 shows a list of the various scheduled flight events, along with the flight times and corresponding altitudes at which these events were executed during the 29.015 experiment. These times and altitudes are accurate to within 1 second and 10 km, respecively. After the powered portion of the flight, the experiment doors (1&2: see Figure 2-12) were released with the use of pyrotechnic explosive devices, allowing them to fall away from the spinning (spin frequency = 2.73 Hz; spin period = 0.366 sec) payload under the influence of centrifugal acceleration. Removal of these doors exposed the experiments to the sampled plasma and provided clearance for the Weitzmann booms, the HF whip antennas and the HEEPS particle experiment, all of which required deployment for proper operation. Having cleared the doors, more pyrotechnic explosives were fired, allowing experiment deployment. The release of the experiment doors and the deployment of experiments were electronically monitered with microswitches, which verified that all these operations were carried out successfully. The HEEPS experiment and the HF whip antennas were equipped with a

29.015
SCHEDULED
FLIGHT EVENTS

Nominal Time of Event (seconds TAL)	Altitude at Nominal Time of Event (km)	Description of Event
0	0	Terrier Ignition
4.4	1.5	Terrier Burnout
8	3.9	Malemute Ignition
29.5	42	Malemute Burnout
54	107	Experiment Doors Separation
55	109	Payload Separation
59	118	ACS Manuever #1 (align with velocity vector)
60	120	Whip Antenna Deployment
60.5	121	E-Field Antenna Deployment
80	163	HEEPS Deployment
110	219	Experiment High Voltage On
111	221	ACS Manuever #2 (align with B-vector, nose down)
122	240	Ion Beam Enable
134	260	Sub Payload Separation
144	275	ACS Manuever #3 (align 135° from B-vector)
194	339	ACS Valve Off
336	406	Apogee
609	58	Experiment High Voltage Off
611	53	ACS Manuever #4 (+90°)
613	48	Experiment Power Off
632*	0	*Estimated Impact

Table 2-1

latch and a spring clamp, respectively, insuring that these devices remained fixed, once successfully deployed. Following successfull instrument deployment, high voltage was enabled on the particle detectors at 110.3 seconds TAL , at an altitude (~ 220 km) which was large enough to minimize the risk of instrument failure due to high voltage corona arcing. This is a critical time for these detectors, due to the fact that at at neutral pressures intermediate between those encountered at sea level and in space, the danger of arcing is at a maximum. Although the ambient neutral pressure at 220 km is easily low enough to safely operate the various HV circuits, outgassing of the materials of which the payload is made tends to keep the pressure higher than the ambient pressure. It is for this reason that great care should be taken in chosing materials out of which to construct these experiments. This is especially true in the immediate vicinity of high voltage circuits. An excellent compilation of experimental data on the outgassing properties of various materials is provided by Campbell et al., 1984.

While the above flight events were being executed, the main and sub payloads remained together, aligned as at launch with their spin axes pointing *upward*, roughly anti-parallel to the ambient magnetic field. The flight plan called for ejection of the sub payload *downward* along the magnetic field line, which required the entire assembly to be flipped over so that the rocket nose pointed down before sub payload ejection could take place. This task was accomplished by the gyroscopically controlled Atitude Control System (ACS), through the use of a high pressure Argon gas jet which fired periodically, selectively applying the required torque to flip the payload assembly over. The ACS system began firing at 111.4 seconds flight time. At roughly 134.4 seconds flight time, the two payloads having been flipped over by the ACS system, the subpayload was ejected downward with a velocity of separation (determined by the turning of a potentiometer) relative to the main payload given by

$$v_{sep} = 2.2 \pm 10\% \text{ meters/second}$$

(Erlandson, 1986). As described in Appendix A, at the time of sub payload separation, the payload spin axes deviated from parallelism with the geomagnetic field by ~7.5°, so that the nominal separation velocity had components both parallel and perpendicular to the field, given by:

$$v_{\parallel} = 2.18 \text{ m / s},$$

$$v_{\perp} = 0.29 \text{ m / s},$$

where the perpendicular component ($v_{\perp}$) of the separation velocity was directed ~14° east of magnetic south. Following sub payload separation, the main payload was again re-oriented by the ACS system, so that its spin axis was aligned at ~135° to the ambient magnetic field, and at a geomagnetic azimuth of ~72° south of east. The sequence of ACS maneuvers and the sub payload separation is illustrated in Figure 2-16.

Prior to the ejection downward of the sub payload, but after the ACS had started to turn the payload pair over, the first ion beam event was initiated shortly after 122 seconds TAL. This was the first of 17 ion beam events (9 ⊥ and 8 ||) to be carried out before the main and sub payloads re-entered the Earth's atmosphere. It lasted for more than 28 seconds, some 11 seconds longer than any of the others, terminating at 150.9 seconds TAL, nearly 17 seconds after sub payload separation. Table 2-2, taken from Erlandson (1986), shows the schedule of ion beam exercises that were carried out from the sub payload, along with indications as to whether the perpendicular (⊥) or (anti) parallel (||) beam was operating and the altitude and line of sight separation between the two payloads at the times of the beginning and end of each exercise. One can see that the beam generators were operated in a periodic cycle in which one generator would be on for roughly 17 seconds, followed by 10 seconds of no beam operations, 17 seconds during which the other generator was on and then 10 more seconds when no beam operated. The single exception to this cycle was the first (⊥) beam exercise which lasted for ~28 seconds. Figure 2-17 illustrates the sequence of ion beam generator operations, along with the relative positions of the main and sub payloads, with repect to the local ambient magnetic

29.015 SUB PAYLOAD DEPLOYMENT GEOMETRY

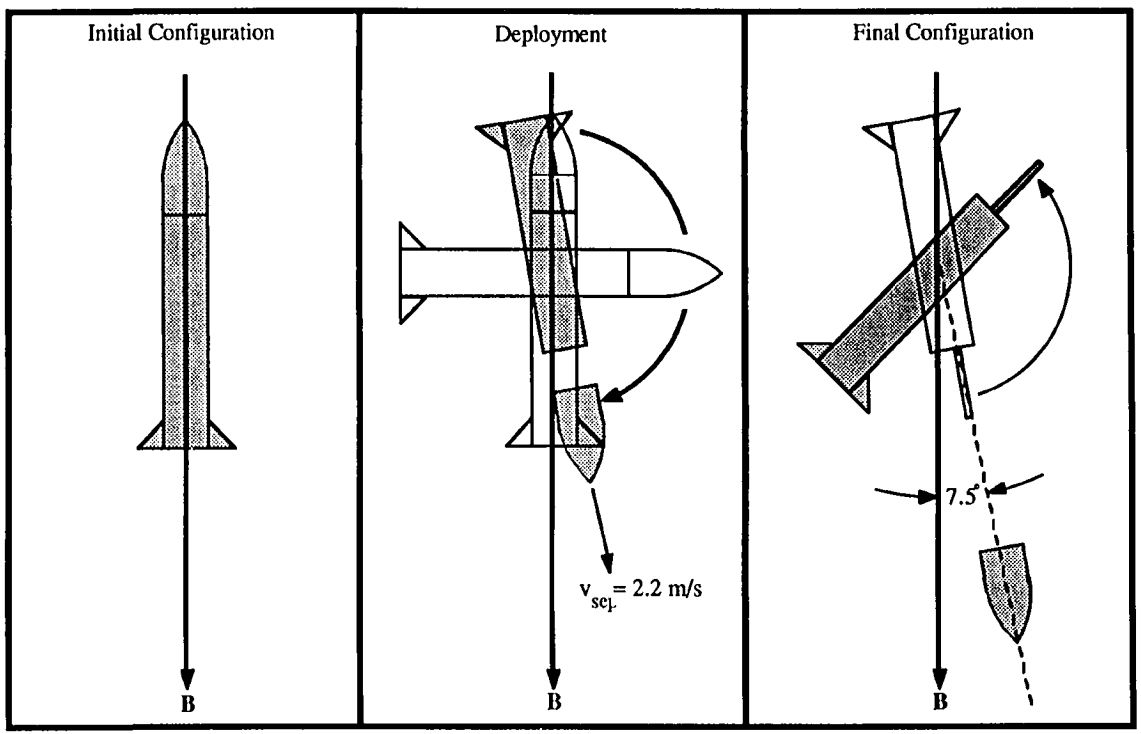

Figure 2-16

ION BEAM GENERATOR OPERATIONS

BEAM GENERATOR	BEAM EVENT	ON - OFF TIME (seconds)	NOMINAL SEPARATION (m)	ALTITUDE (km)
⊥	1	122.6 - 150.9	0 - 36	232 - 281
∥	1	161.5 - 178.6	60 - 97	296 - 318
⊥	2	189.0 - 206.1	120 - 158	330 - 348
∥	2	216.6 - 233.6	181 - 218	358 - 373
⊥	3	244.1 - 261.2	241 - 279	380 - 390
∥	3	271.7 - 288.8	302 - 340	395 - 401
⊥	4	299.2 - 316.4	363 - 400	404 - 406
∥	4	326.8 - 344.0	423 - 461	406 - 404
⊥	5	354.4 - 371.6	484 - 522	401 - 395
∥	5	382.1 - 399.2	545 - 583	390 - 380
⊥	6	409.6 - 426.8	605 - 643	373 - 358
∥	6	437.3 - 454.4	666 - 704	349 - 331
⊥	7	464.9 - 482.1	727 - 765	318 - 295
∥	7	492.6 - 509.8	788 - 826	281 - 252
⊥	8	520.3 - 537.5	849 - 887	235 - 203
∥	8	548.0 - 565.2	909 - 948	180 - 147
⊥	9	575.7 - 592.9	971 -1009	123 - 83

Table 2-2

Nominal
Main-Sub Payload
Separation

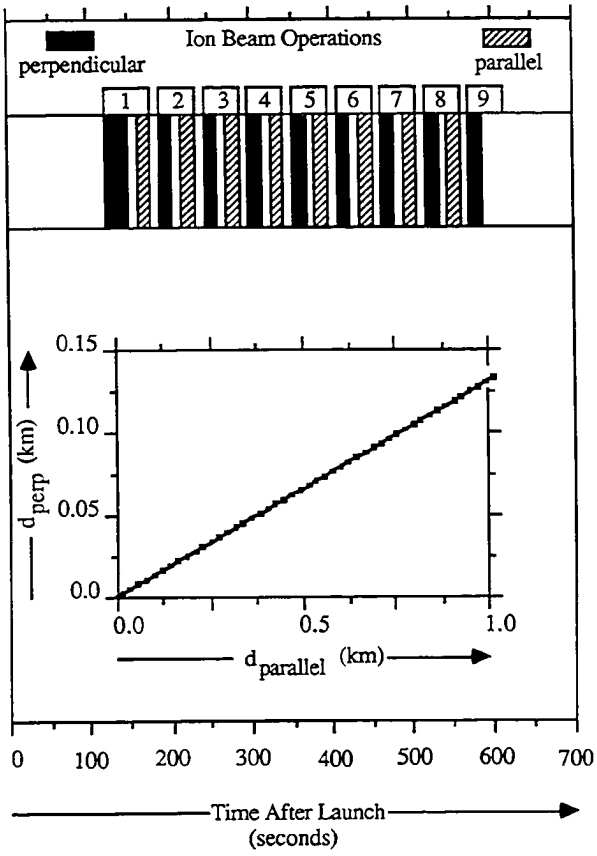

Figure 2-17

field throughout the flight. The perpendicular beam generator fired Ar^+ ions across field lines continuously, as the sub payload spun at 2.73 Hz, sweeping the beam through the ionosphere in a lighthouse fashion. On the other hand, when the parallel beam generator operated, the ion beam was directed upward, along the field line toward the direction of the instrumented main payload and anti parallel to the sub payload spin axis (see Figure 2-6). The picture, then is one in which the two beam generators were operated alternately and repeatedly from the sub payload, while plasma diagnostic measurements were carried out on both paylaods and the two moved apart along and across magnetic field lines until atmospheric re-entry at ~588 seconds TAL. All this, while moving through an ionospheric plasma which was, from all indications, reasonably quiescent, in terms of auroral electron precipitation activity.

The experimental picture in the case of the earlier ARCS 2 experiment was quite similar to that presented above for flight 29.015. Exceptions lie in the differences in payload instrumentation described above in addition to the following facts. First, and probably most importantly, ARCS 2 was flown from Poker Flat Research Range in Fairbanks Alaska, into an active system of auroral arcs (Arnoldy et al., 1986), so that ion beam operations were carried out in a plasma through which large fluxes of energetic electrons flowed into the ionosphere, below. This is important, if for no other reason, because the resulting high electron fluxes largely shrouded any beam-induced elecrtron fluxes (such as those observed on board ARCS-1 (NASA flight 29.014). Finally, in the case of ARCS-2, the sub payload was deployed upward, along the magnetic field line, in contrast to the downward deployment of the 29.015 sub payload, described above.

The performance of the 29.015 experiment vehicle was nominal in all respects. The sequence of scheduled events was carried out successfully without exception and all vehicle systems operated flawlessly throughout the flight. The experiment payload reached an apogee of 406 km 174 km downrange at 320 seconds TAL and re-entered the atmosphere

330 km down range at 588 seconds TAL. The main and sub payloads maintained stable spinning trajectories with small degrees of coning throughout the flight.

Overall Instrument Performance. The quality of the performance of the instrument systems flown on board NASA flight 29.015 was mixed, with reliable performance obtained from some and failure of other instruments occuring. All systems on board the separated sub payload, including the plasma generation systems, the photometer, the Langmuir probe and the single axis magnetometer seem to have given reliable performance throughout the flight. On the main payload, the wave and field instrumentation all operated reliably, with the minor exception that narrow band interference signals originating on the payload appeared consistently in the wave receiver data streams. These signals mostly constituted an annoyance in the analysis of the data, but, more seriously, in some cases prevented the proper operation of automatic gain control (AGC) circuits in the recievers, precluding realization of the intended dynamic range in sensitivity for the affected instruments. Most seriously affected in this manner was a magnetic loop antenna provided by the University of Minnesota (Erlandson, 1986). Of the particle experiments on flight 29.015, the two Octospheres (OCTOs 2 & 4) designed for the measurement of positive ion fluxes and the positive ion HEEPS instrument operated reliably throughout the flight, providing extensive ion observations. Unfortunately, neither of the electron sensitive Octospheres (OCTOs 1 & 3) provided useful data, so that we have no electron observations to report from this flight. Additionally, the positive ion sensitive STICS instrument, which was to provide ion composition information, as well as fast ion spectral data and an additional look direction, failed due to arcing in the high voltage circuits early in the flight so that no ion composition information is available from this experiment.

The failures of the 2 Octospheres and the STICS instrument provide, however, a lesson to be learned. These instruments were all flown previously on the ARCS-2 payload which was recovered after flight. On the ARCS-2 downleg, a timer which should have

turned off high voltage to the particle experiments failed, delaying HV turn-off by ~20 seconds and causing high voltage arcing in the particle detectors during atmospheric re-entry. Subsequent physical inspection of these instruments showed evidence of arcing along non-conducting surfaces. The instruments were cleaned and, in some cases, components were replaced but the instruments themselves were re-flown on flight 29.015, with many of the original components in place. In spite of extensive vacuum testing of these instruments prior to re-flight on the 29.015 payload, sad experience has shown that once an arcing path has been established along or through a piece of material, it is very difficult to get the same piece of material to reliably withstand high voltage application without repeated breakdown. The physical evidence of the failures of the 29.015 particle instruments is not available, as the payload was not recovered the second time after flight over Greenland (although NASA tried), so that we will never know if the high voltage arcs occurred along previously established paths. The possibility that that is the case, however, along with the high cost of the failures in terms of our experimental objectives should be borne in mind and should guide us in the future when considering the re-use of instrumentation which has, lets say, a checkered history, in space or elsewhere.

29.015 POSITIVE ION OBSERVATIONS

INTRODUCTION

The positive ion observations obtained on board flight 29.015 are plentiful, varied and highly structured. We have observations from the 29.015 HEEPS instrument and the two 29.015 ion octospheres, OCTO 2 & OCTO 4. The HEEPS instrument has been described in full in Section 1, while the Ocotspheres have been briefly described in the previous subsection. In general, the fluxes are large at small main-sub payload separations and decrease with time as the two payloads move apart along their respective trajectories.

There are several important central characteristics brought out by these charged particle observations, which may be catagorized as follows:

1) Perpendicular Beam Events

-Strong fluxes of ions are consistently observed near 90° magnetic pitch angle and near energies per charge ($\varepsilon \equiv E/q$) of 90 eV/q, which is roughly 1/2 the expected beam energy of ~ 200 eV/q.

-Strong ion fluxes near 90° magnetic pitch angle are also consistently observed to be distributed at low energies between ~5 and ~50 eV/q.

2) Parallel Beam Operations

-Ions fired antiparallel to **B** are consistently observed at pitch angles near 180 degrees and at energies-per-charge (~200 V) which are nearly equal to the beam generator anode bias (V_a=185 V).

-A population of ions broadly distributed near 90° magnetic pitch angle is consistently observed at the same energy per charge as those antiparallel particles described immediately above.

-During parallel beam events, a population of ions is consistently observed near ninety degrees magnetic pitch angle and broadly distributed near an energy per

charge which is a small fraction of the beam energy. These ions are extremely similar in their energy and pitch angle characteristics to those 90° low energy particles observed, as described above, during perpendicular beam events.

3) Ambient Ions

-From the time that beam operations commenced, until late in the flight, after beam related fluxes had substantially died away, observed particle events characteristic of the cool ionospheric plasma were absent in the HEEPS positive ion data. This, in spite of the fact that all nominal expectations are to observe substantial thermal ionospheric fluxes throughout the flight.

The positive ion data collected by the 29.015 Ion Octospheres generally corroborates the HEEPS ion data, where the two instruments sample common regions of phase space.

ENERGY-TIME OVERVIEW

An overview of the 29.015 HEEPS ion observations in the energy-time domain is presented in Figure 2-18. Here we show the HEEPS instrument count rate, given by the HTC signal, plotted logarithmically versus time in four energy bands (0.2-2.4, 5.3-36, 60-119 and 140-273 eV/q) throughout the flight. In addition, the times and nature ($\perp$ or ||) of ion beam events are indicated directly above the bottom data band. From thermal energies along the top trace through the highest HEEPS energy steps, along the bottom, the effects of the operation of the beam generators are evident in the data. In addition, substantial low energy (< ~2 eV/q) event rates due to thermal ionospheric plasma are observed before initiation of the 1st beam event and again, later in the flight, after evidence of ion beam exercises has diminished, but are absent at intermediate times.

This figure should be considered from the point of view that there are three distinct time frames of physical interest:

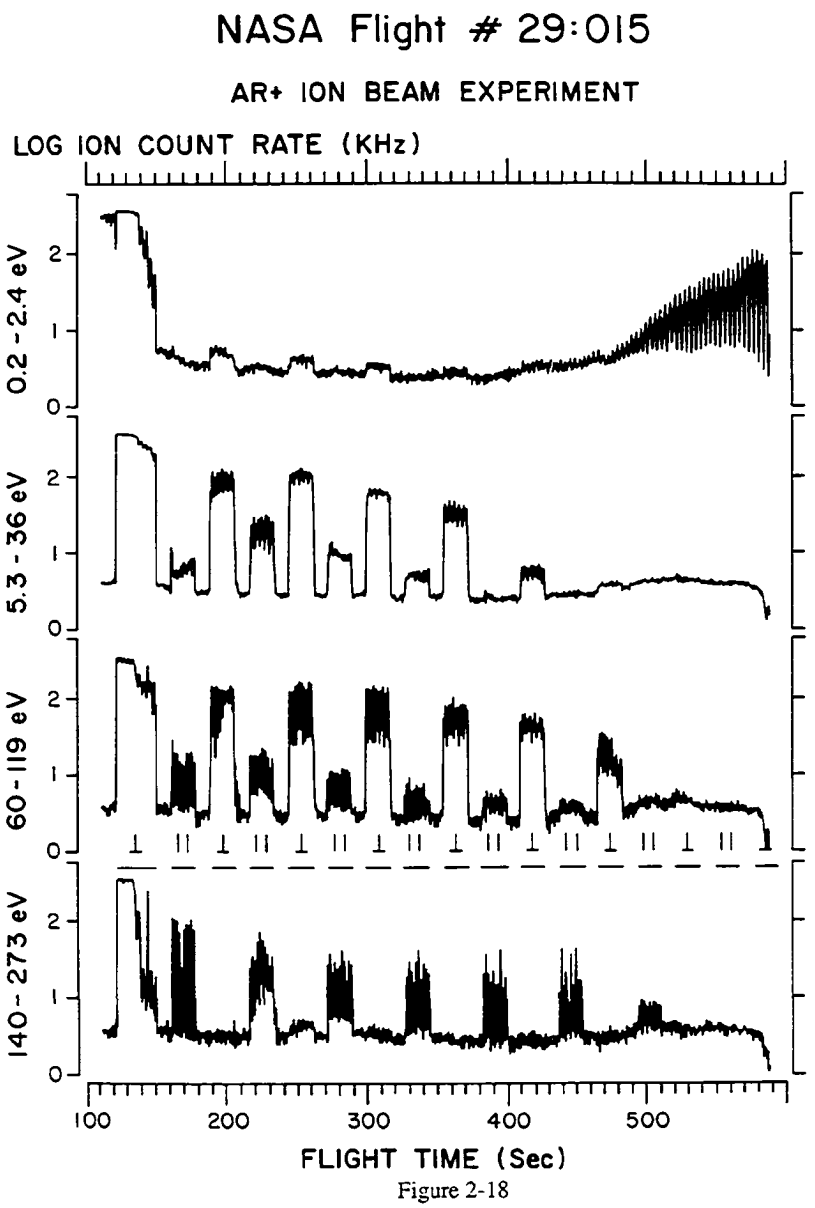

Figure 2-18

1) From high voltage turn-on at ~110 seconds Time After Launch (TAL) until initiation of the 1st perpendicular beam event at 122 seconds TAL. This is an early, if brief, period of observation of natural ionospheric plasma.

2) From the beginning of beam operations until sub payload separation near 134 seconds TAL. This is the period of attached ion beam operations.

3) From the time of sub-payload separation until loss of signal due to atmospheric re-entry at ~588 seconds TAL. This is the period of non-attached ion beam operations.

During time frame (1) and late in time frame (3), the HEEPS positive ion events are largely confined to energies per charge below 2 eV/q. These events are due to particles which constitute the cool (kT ~ a fraction of an eV) ambient ionospheric plasma. Note the near absence of event rates above background in this energy band between ~151 and 470 seconds TAL. The absence of particle events at thermal energies during most of the experiment is surprising and not well understood. We expect to see events in this energy range throughout the flight. We can substantiate this expectation due to the fact that another UNH rocket payload, NASA flight 35.012, was in flight simultaneously in the same region of space. This rocket payload also carried a HEEPS ion analyzer which was designed and built to the same electrical and mechanical specifications as the 29.015 HEEPS instrument. Figure 2-19 shows the event rates recorded by the 35.012 HEEPS instrument as a function of time throughout its flight. It can be seen that substantial thermal event rates were measured throughout the 35.012 experiment, with event rates in this energy band minimizing briefly between ~ 450 and 550 seconds TAL at an altitude of near 800 km, 400 km higher than the apogee of flight 29.015. This is in stark contrast to the case of flight 29.015, were thermal positive ion events were largely absent throughout most of the flight, as described above.

The onset of beam operations near 122.4 seconds TAL is evident as a glitch and a change in the nature of the lowest energy event rates (top trace, Figure 2-18), which become hard saturated for the following ~16 seconds, and as a 'step function to saturation'

HEEPS THERMAL EVENTS
(NASA Flight 35.012)

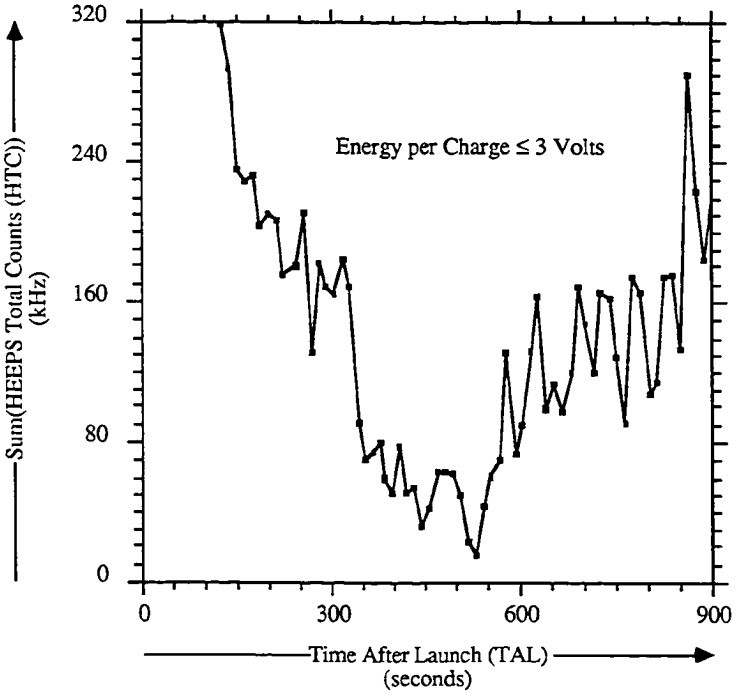

Figure 2-19

in the higher energy channels, which had been quiet before the beam was turned on. During attached ion beam operations, between 122.4 and 134.35 seconds TAL, the HEEPS instrument registered heavily saturated event rates in all 32 energy channels and achieved little useful angular imaging. Shortly after sub payload separation, at 134.35 seconds TAL, the measured fluxes changed, decreasing with time as the two payloads moved apart and becoming more localized between energies of ~5 and ~110 eV/q. Figure 2-20 shows line plots of the HEEPS total count (HTC) rate plotted versus time in four energy bands from 110 seconds to 152 seconds TAL. The data in this figure represent contributions from all pitch angles. The saturated instrument operation in all four energy passbands is apparent between 122 seconds TAL, when beam operations commenced, and 135 seconds TAL, near the time of sub payload separation. Beginning shortly after subpayload separation, the fluxes dropped off significantly at energies per charge lower than ~5 ev/q and higher than ~110 eV/q. Figure 2-20 shows clearly that, although the fluxes below 5 eV/q and above 110 eV/q generally decreased with time after sub payload separation, the decrease was modulated with strong periodic enhancements. Indeed, the lowest energy fluxes did not begin to significantly drop off until fully 4 seconds after separation. The character of the flux drop-off after subpayload separation indicates not only a change in the state of the main payload due to separation, but also, large inhomogeneiies in the immediate vicinity or 'near zone' of the beam-emitting sub-payload. All positive ion fluxes above background disappeared when the 1^{st} ($\perp$) beam event terminated at 150.9 seconds TAL.

During non-attached beam events, substantial fluxes at primarily superthermal (~ 5-220 eV/q) energies were consistently observed. Between beam operations, fluxes above background in all 32 energy channels are generally absent. A comparison between the 66-119 and 140-273 eV/q energy bands in Figure 2-18 shows that the cases of parallel and perpendicular ion beam operations differ markedly at higher energies with regard to the energetics of the observed ion fluxes. Throughout non-attached beam operations, the high

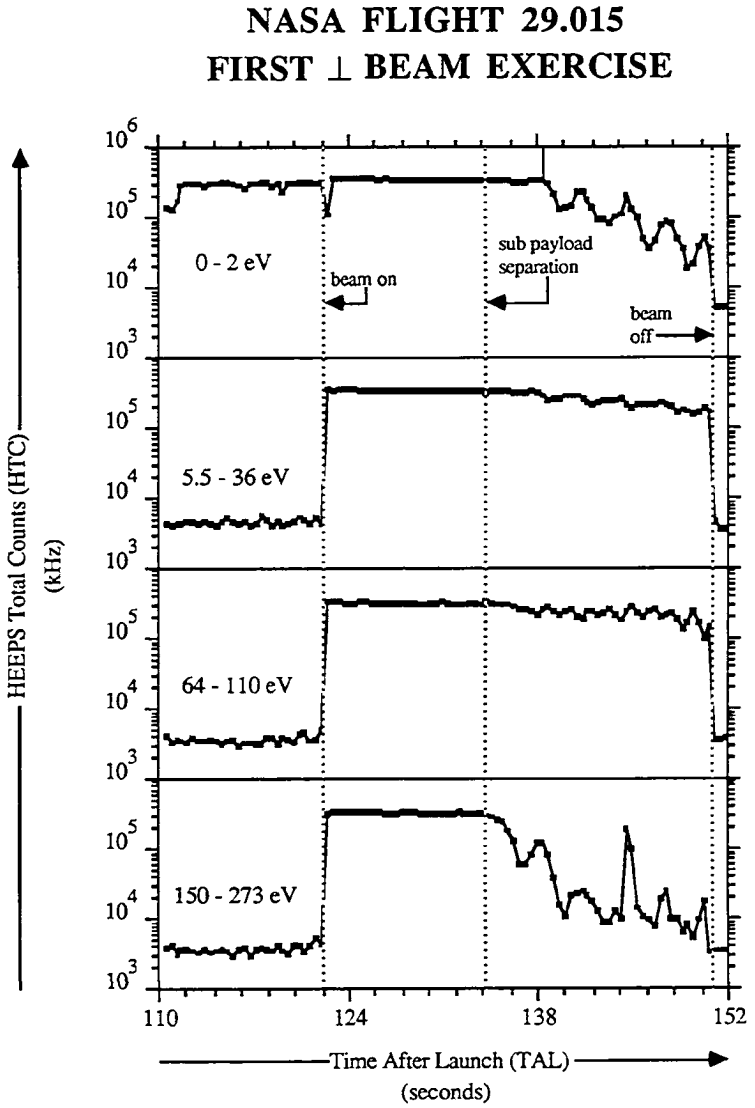

Figure 2-20

energy ion flux cut-off observed during perpendicular ion beam operations (~110 eV/q) is on the order of 1/2 that observed during parallel beam operations (>190 eV/q). Note that little evidence of perpendicular beam operations can be seen in the 140-273 eV/q energy band. This, in spite of the experimental fact that the accelerating voltage applied to the perpendicular generator anode (220 V) was 35 Volts larger than that applied to the parallel generator anode (190 V).

Events occuring in the 5.3-36 eV/q band are observed during both perpendicular and parallel beam operations, although the fluxes in this energy range are stronger and more persistent during perpendicular events than during parallel events. It can be seen that at times, the event rates in this band dominate those in either of the higher energy bands. The dominance of the low energy event rates over those at higher energies is accentuated by the fact that the particle density varies as the count rate over the sqare root of the energy per charge (ε), giving an often strong domination of these low energy particles in terms of particle density.

Late in the flight, evidence of beam operations disappears and fluxes localized to < 2 eV/q re-appear gradually. These low energy fluxes are modulated at a frequency of 0.29 Hz, which represents the beat frequency between the 2.44 Hz energy sweep and the 2.73 Hz rocket spin period. This low energy signature is characteristic of a moderately rammed thermal ionospheric plasma, accelerated to a payload floating at a small ($\approx$1 V) negative potential with respect to the ambient plasma.

The temporal dependence of the measured ion fluxes shows a great deal of periodic structure, as illustrated in parts a, b and c of Figure 2-21, where, in each case, the HEEPS Total Counts (HTC) event rate is plotted against time over the time period of a given beam event. Figure 2-21a shows events near 200 eV/q measured during the 4^{th} $\parallel$ beam event. The strong periodicity in the events at a frequency of 0.6 Hz is the outstanding feature in the data. Figure 2-21b shows the HTC signal plotted versus time for particles in the energy range near 20 eV/q, during the 5^{th} ($\perp$) beam event. In this case also,

PERIODICITIES IN THE HEEPS TOTAL COUNTS (HTC) EVENT RATES

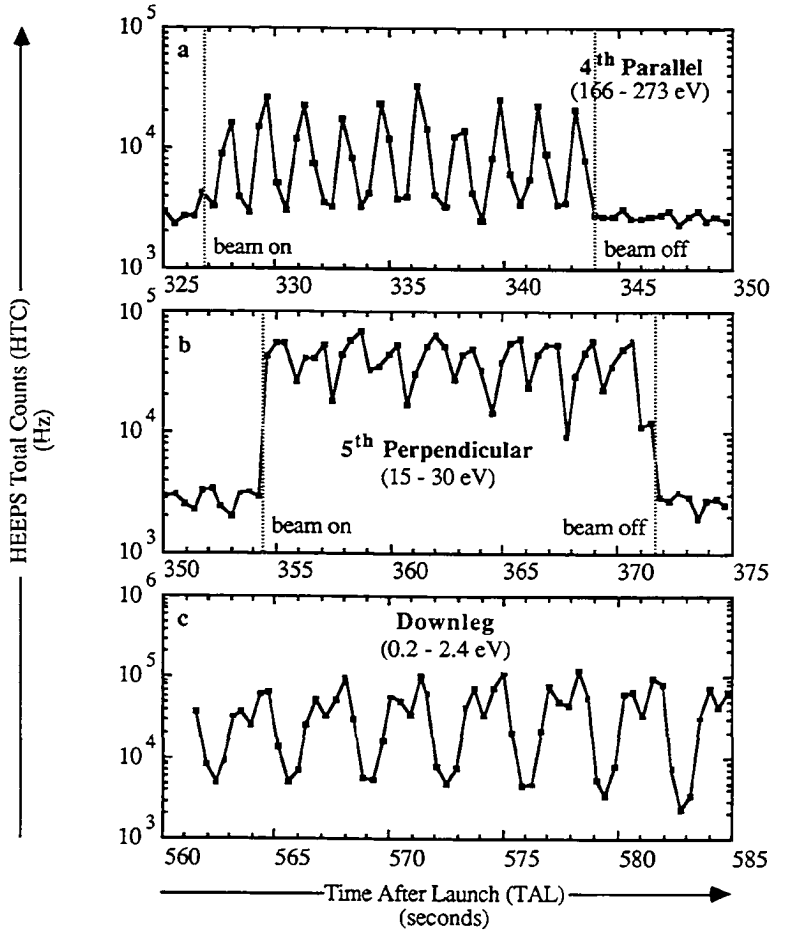

Figure 2-21

strong periodicity is the rule, with repetition frequencies of 0.3 Hz and 0.6 Hz. Again, in Figure 2-21c, HTC events in the thermal energy range are plotted versus time over a 25 second time period right before the payload undergoes atmospheric re-entry. In this case also, as noted above, strong periodicities at 0.29 Hz and 0.58 Hz are evident. In all cases, we have the beating between the 2.44 Hz energy sweep signal and the 2.73 Hz rocket spin. The system beat frequency is given by the difference between these two contributors to be 0.29 Hz. The occurance of a component at twice that, or ~0.58 Hz, is not so readily understood. The important conclusion that can be drawn from the beating periodicities observed in the HEEPS Total Counts data is that the ion fluxes are both anisotropic in space and, as is demonstrated in Figure 2-18, nonuniform in energy. The spatial anisotropy of the measured ion fluxes is found to be highly structured and ordered by the geomagnetic field, as will be demonstrated below.

HEEPS Energy-Pitch Angle Distributions

Appendix B contains a series of figures showing the characteristics of the positive ion flux environment derived from data collected by the 29.015 HEEPS instrument during ($\parallel$) and ($\perp$) ion beam operations. Each of the 16 figures in this appendix shows data collected during a given ion beam injection event and represents an average over some 16 seconds of data, corresponding to ~39 energy-angle distributions. All 16 of these figures have a common format, showing a contour plot in part (a) and two different surface perspectives, in parts (b) & (c), of the differential directional positive ion energy flux plotted against the HEEPS analyzer energy step and the measured particle magnetic pitch angle. Along the left edge of the contour plots a sampling of the selected energy at the given step is provided, while Table 1-3 shows the selected energy associated with each of the 32 steps for this instrument. Appendix B also includes a description of how the values plotted in Figures B-1 through B-16 were derived from the HEEPS data. These values are roughly proportional to the HEEPS angular imaging bin event rate at a given pitch angle

and energy, and are equal to the product of the differential directional particle flux (J') and the energy per charge (ε) at the given energy and magnetic pitch angle. I suggest that the reader peruse this figure set before continuing reading.

Perpendicular Beam Events. Figures B-1 through B-8 show fluxes measured during the 1st through the 8th perpendicular beam events, respectively. In general, the largest fluxes observed during the 29.015 experiment were associated with the perpendicular ion beam injections. These fluxes tended to be seen in two energy ranges: A low energy population seen distributed broadly from ~5 to ~50 eV/q and a higher energy population which was more narrowly distributed in energy near 100 eV/q. Both of these populations are seen to be strongly peaked in magnetic pitch angle, with peak fluxes occuring near a pitch angle of 90°.

As described above, the 1st (⊥) beam event was a mixed case, with sub payload separation occuring during the event. The data shown in Figure B-1 is from the time period *after* separation. The heavily saturated state of the HEEPS instrument is evident in the imaging quality in both energy and pitch angle, although, as can be seen in Figure 2-20, by the end of this event, the two ion populations near 20 and 100 eV/q had become totally dominant.

Figures B-2 through B-5 show the ion energy flux profiles obtained during the 2nd through the 5th perpendicular beam events. The data in these figures were collected over an altitude range extending from 330 km on the upleg, though apogee at 406 km (attained after the 4th ⊥ event) to 395 km on the downleg and over a nominal main-sub payload separation range of from 120 ($d_{\perp}$≈16 m, $d_{\parallel}$≈119 m) to 522 meters ($d_{\perp}$≈68 m, $d_{\parallel}$≈518 m). I group these events together in their presentation because their features are quite similar, differing primarily in degree from one event to the next. As pointed out earlier, the primary features of note in these distributions are the two large flux peaks centered near 90° magnetic pitch angle and at energies per charge near 20 and 100 eV/q, respectively. Also of note in these figures are small peaks in the flux at larger pitch angles. The dominance of the two primary

peaks is unquestionable, however, during these 2nd through 5th beam events. As can be seen by comparing Figures B-6 and B-7, associated with the 6th and 7th (⊥) beam events, with B-2 through B-5 a primary difference is apparent in the absence of the low energy peak near 90°. Careful examination of the data in Figure B-6 reveals the remains of the low energy peak near 90° during the 6th (⊥) event. At the time of this event, the altitude was near 360 km. The main and sub payloads were thought to be separated across field lines by 80 meters and along field lines by some 600 meters. Twice the gyro-radius of a 20 eV/q 90° Ar^+ ion in a 0.6 Gauss field is 135 meters.

The high energy 90° flux peak, on the other hand, remains well defined in these figures, though fluxes in this energy-pitch angle range are decreasing with time and by the time of the 8th perpendicular beam event (Figure B-8), are barely discernable above the background. Events in this energy-pitch angle range were the most persistently observed, being present starting at the 1st (⊥) event and continuing to be so, into the 8th. At the time of the 8th (⊥) beam event, the altitude was near 220 km. The main and sub payloads were thought to be separated across field lines by 110 meters and along field lines by some 860 meters. Twice the gyro-radius of a 100 eV/q Ar+ ion at 90° pitch angle is >300 meters in a 0.6G field, and somewhat larger in the Earth's field which is less than 0.6 Gauss at all altitudes encountered during this experiment.

Notice in Figures B-6 through B-8 that during the late beam events, starting at the 6th, the development of fluxes near 180 degrees pitch angle in the thermal (0 - 2 eV/q) energy range occurs. This can be seen in these (⊥) events as well as in the late parallel events, described below. Of marked interest is the *absence* in these figures of events in this energy range at times between the 1st (⊥) and ~the 6th (||) events. Late in the flight, on the payload downleg, these particles are seen to be ramming upward in the payload frame of reference. Hence, the peaking of fluxes near 180° magnetic pitch angle. Observation of this phenomna gives confidence in the performance of the HEEPS instrument.

Figures 2-22 and 2-23 summarize the characteristics of the energy-pitch angle spectra collected during (⊥) beam injections. Each of these two figures (and Figures 2-24 and 2-25, which show data from (||) beam events) are divided into 8 frames, showing data collected during the 1st through the 8th beam events. Figure 2-22 shows the result of integrating the data shown in Figures B-1through B-8 over pitch angle, showing the variation of energy flux with energy for each of the 8 (⊥) events and shows the development and decay of various features in the energy distributions from one beam event to the next. Another view of the data (Figure 2-23) shows pitch-angle spectra which have been integrated with respect to energy, showing the evolution, from event to event, of the distribution of positive ion flux with magnetic pitch anlge. In the case of Figures 2-22a and 2-23a, integrated ion fluxes measured during the 1st (⊥) event have been divided according to those measured before and after sub payload separation and the two cases are show distinct spectral features. In Figures 2-23f, 2-23g and 2-23h, integrated ion fluxes have been separated according to whether particles in the thermal energy band were included. The enhancements in these distributions at large pitch angles for the cases that include the thermal particles corresponds to the increase in event rates at thermal energies shown in Figures 2-22f, 2-22g and 2-22h. At this time the payload is on the downleg and, in the payload frame of reference, the thermal ions are seen to be flowing upward. Hence the concentration of these particles near 180° magnetic pitch angle.

Parallel Beam Events. As Figures B-1 through B-8 serve to illustrate the features of the distribution of ion energy flux with pitch angle and energy per charge during (⊥) events, in Figures B-9 through B-16, we present the same type of illustrations for the (||) beam events. Again, we consistently observe distinct and repeatable structure in the flux distributions. The huge flux peak just 'glued' into the 273 eV/q - 180° corner in Figure B-9 (1st (||) beam event) can only be interpreted as direct beam particles impinging on the main payload, no more than 97 meters away from the beam source, which is

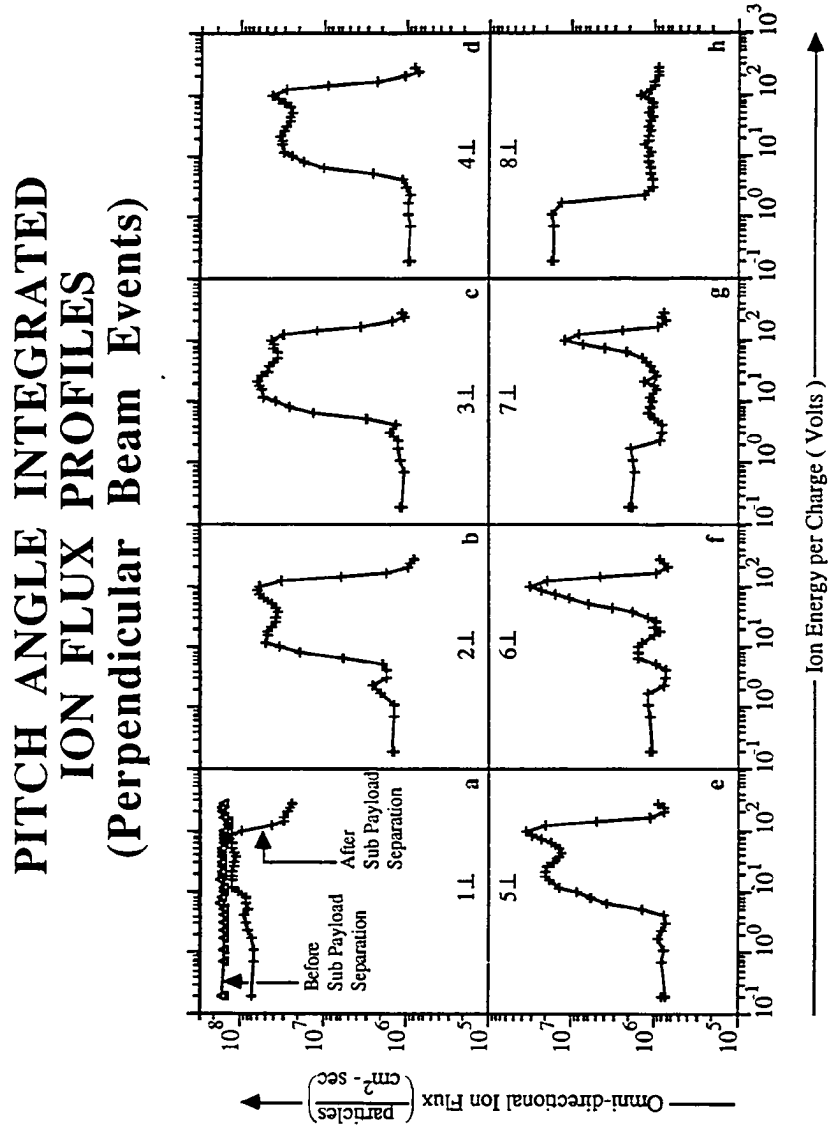

Figure 2-22

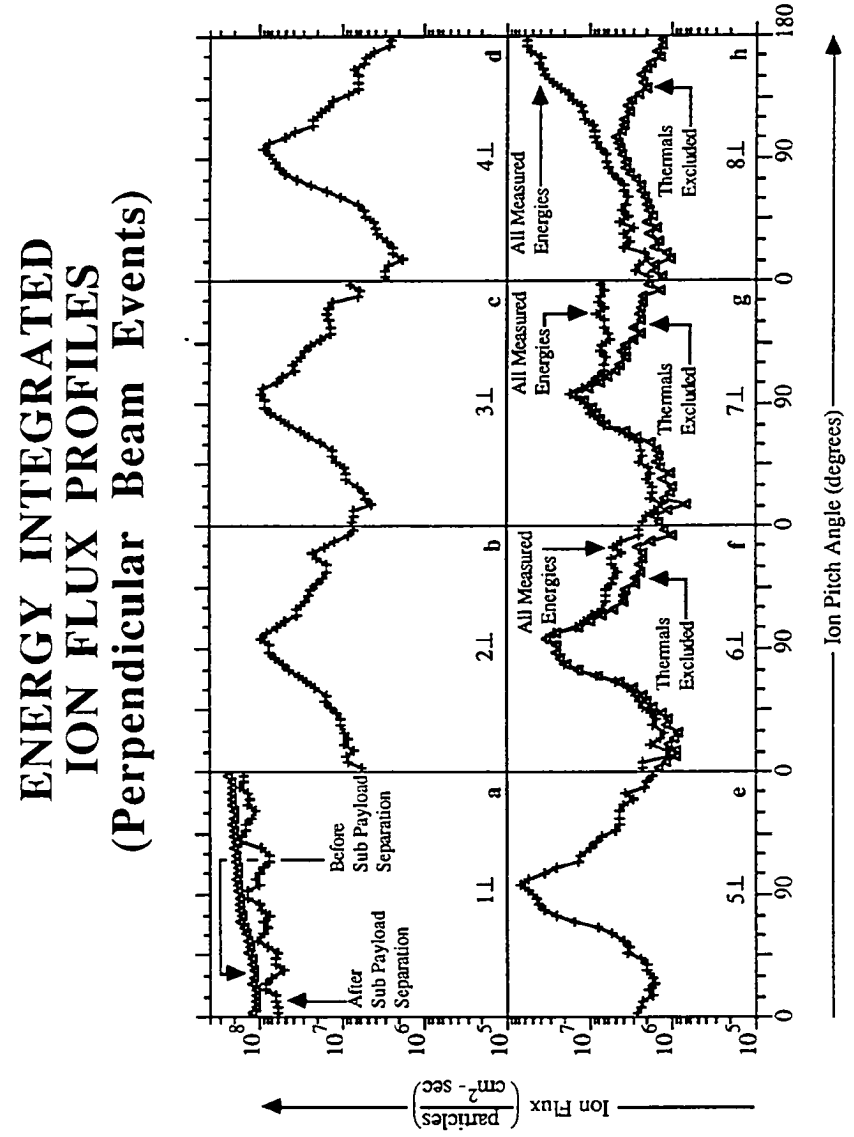

Figure 2-23

directed right toward us, up the field line. The evolution of this peak from event to event (Figs. B-9 through B-14), as time goes on, includes a systematic drift to smaller pitch angles as well as an intensity decrease until it is no longer identifiable, at the time of the 7th (||) event (Figure B-15). The energy of these particles is always near 200 eV/q, in contrast with the high energy particles identified during (⊥) beam events, which were near 100 eV/q. Another distinct population of high energy (~200 eV/q) particles may be identified during (||) beam events 1 through 7 in Figures B-9 through B15. These partciles are distributed somewhat broadly near and above 90 degrees magnetic pitch angle. This group of ions is also very persistent, being still distinctly identifiable through most of the 7th (||) event which ended near 500 seconds TAL.

Figures B-9 through B-12 show another population of positive ions to have been present during the 1st through the 4th (||) beam events (although only marginally during the 1st (||) event), this time at low energies, peaking near 20 eV/q. These ions are seen to be strongly peaked at very nearly, but slightly below 95° magnetic pitch angle. They are extremely similar in their energy-pitch angle characteristics to the low energy ~95° peak observed consistently during the 1st through the 5th (⊥) events. By the time of the 5th (||) beam event, these low energy (~5 < ε < ~50 eV/q) particles near 90° can no longer be distinctly identified in the data during (||) injections.

Figures 2-24 and 2-25 are similar to Figures 2-22 and 2-23 and show spectra for each of the 8 (||) beam operations, which have been integrated over magnetic pitch angle, in the case of Figure 2-24, and energy per charge in Figure 2-25, to give the integrated ion flux as as functions of energy per charge and magnetic pitch angle, respectively. Again, as in the case of the (⊥) events, these two figures give a sense of the evolution of the ion flux distributions with time, from one event to the next. As in Figures 2-23f, 2-23g and 2-23h, particles in Figures 2-25f, 2-25g and 2-25h have been divided so as to separate the contribution of particles in the thermal energy range, which, again, are consistently

PITCH ANGLE INTEGRATED ION FLUX PROFILES (Parallel Beam Events)

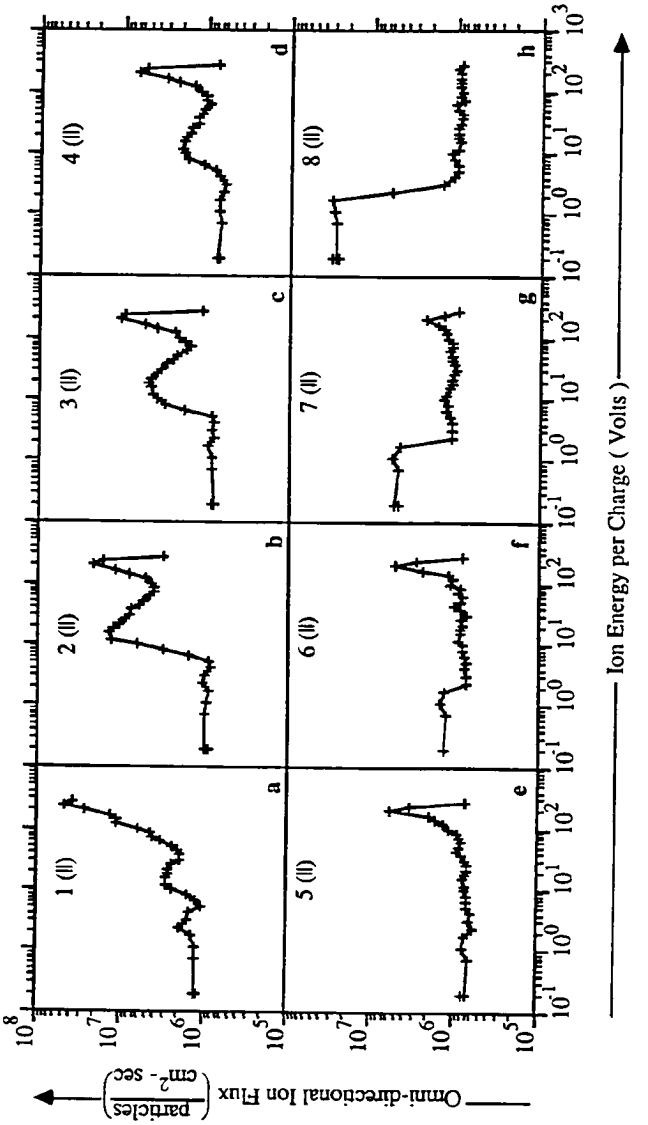

Figure 2-24

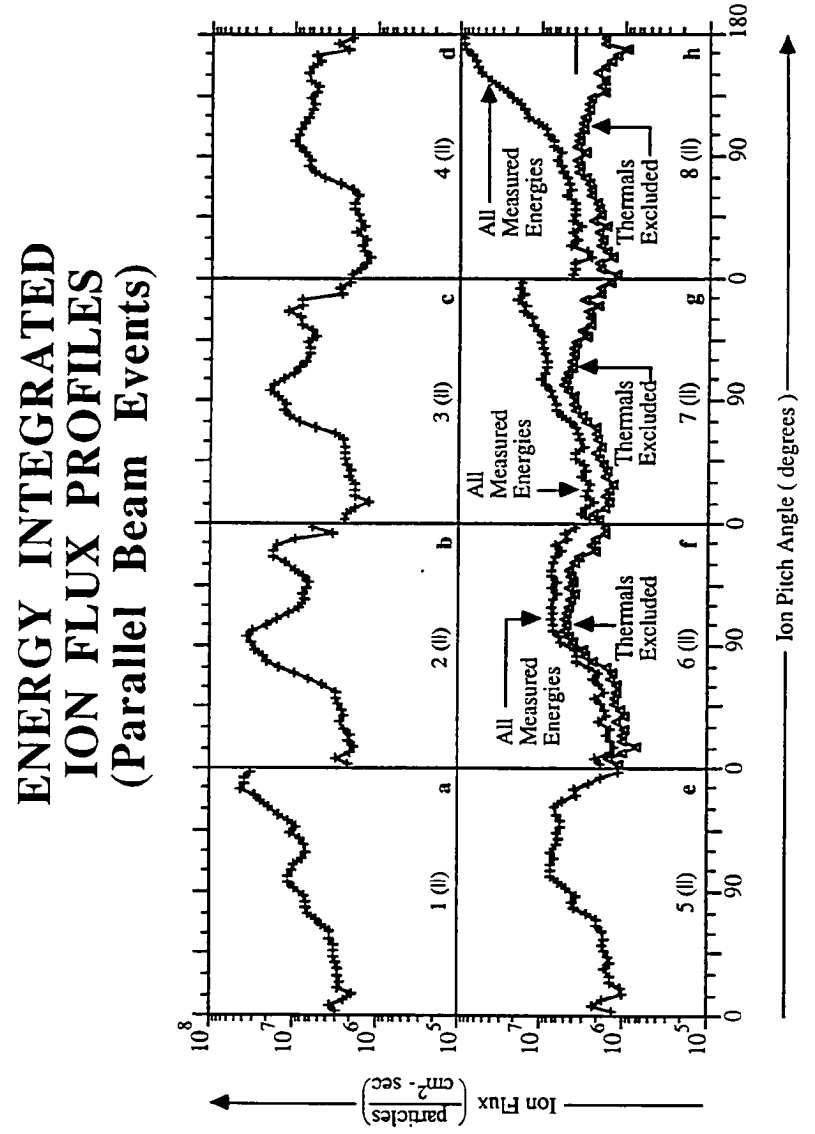

Figure 2-25

bunched at large pitch angles. Note with reference to Figure 2-24 that the 20 eV/q flux does not vary monotonically in time, but maximizes during the 2nd (||) event.

Summary (Pitch Angles): In order to further summarize the characteristics of these ion pitch angle distributions, we have computed the mean pitch angle and the RMS deviation in pitch angle over several distinct subranges of pitch angle and energy per charge for each of the first 16 ion beam events. We show the results of this analysis in Figure 2-26 which contains four parts, each showing the calculated mean pitch angle plotted against time, with the error bars providing the measure of the RMS deviation; that is, the width of the peaks in pitch angle. The results plotted in each part were obtained by including particles in the textually noted energy per charge range and in the range of pitch angles implied by the labelling of the given vertical axis. This information gives an estimate of the location and width (in pitch angle) of four of the five (no thermals analyzed here) major distinct energy flux peaks evident in the distributions shown in Figures B-1 through B-16. The mean pitch angle of the ~20 eV/q peak (Figure 2-26a), which appears during both ($\perp$) and (||) events, is consistently near 95° for events where the peak is strong. This is also true of the ~100 eV/q peak (Figure 2-26b), which appears only during ($\perp$) events. The ~ 200 eV/q particles seen near 90° (Figure 2-26c) during (||) events appear at pitch angles which are consistently more upgoing that either of the two transverse lower energy populations. In Addition, there is a small, persistent trend toward larger pitch angles from event to event from the 2nd through the 6th (||) events. A similar trend in the opposite sense may be seen in the mean value of the pitch angle measured at large pitch angles ($135° \leq \alpha \leq 180°$) in the ~ 200 eV/q energy range (Figure 2-26d) during (||) beam events. In this case, the mean value is seen to move from 164° during the 1st (||) event down nearly to 150 degrees during the 6th (||) event. This downward trend is understated by Figure 2-26, since the peak flux is obviously located much more closely to 180 degrees than 165 degrees (see Figure B-9) during the 1st (||) event, although, 150 - 155° is a good estimate of the location of the high energy peak at large pitch angles during the 6th (||) event

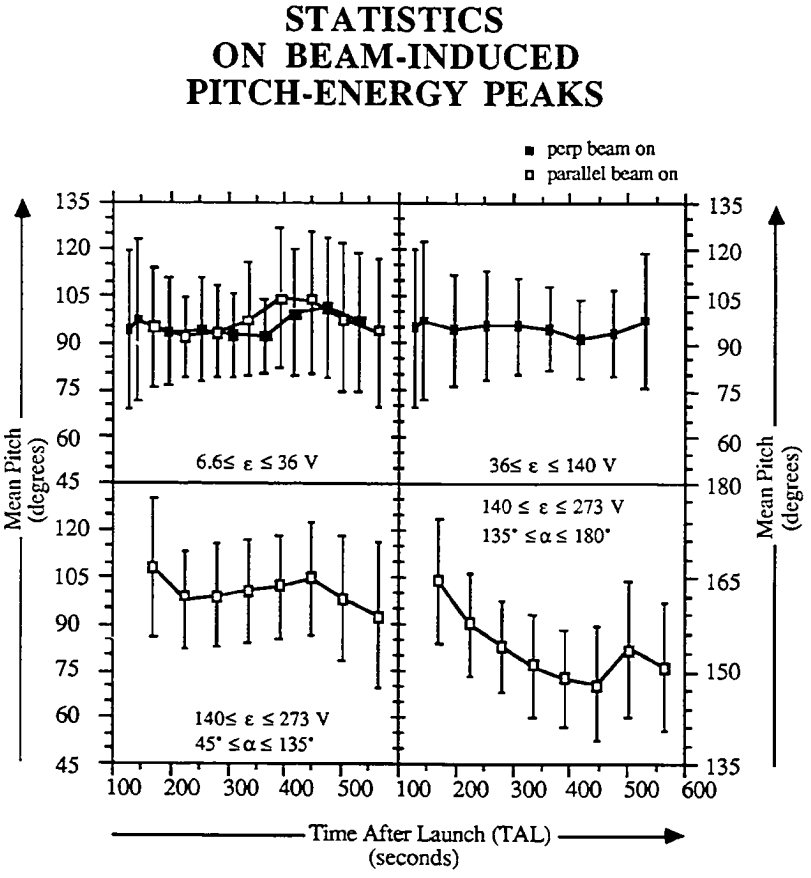

Figure 2-26

(see Fig. B-5). This understatement results from the calculation of the mean over a finite range of pitch angle which, by definition is bounded above and below.

HEEPS Azimuth Observations

It is clear that structure exists in the azimuthal distribution of positive ion fluxes during beam injection events. As examples of this, Figures 2-27 and 2-28 show plots of the differential directional positive ion energy flux measured during the 3rd (||) and 7th (⊥) events, in much the same format as used in Figures B-1 through B-16. In these cases, particle magnetic pitch angle (α) has been replaced by the geomagnetic azimuth (ϕ), which is defined in this work to be zero for particles moving toward geomagnetic east and to increase toward the geomagnetic south, such that $0^\circ \leq \phi \leq 360^\circ$. These two figures illustrate the azimuth-energy dependence of fluxes averaged over pitch angles, running from 45° to 135°. They provide information on the azimuthal dependence of the 20 eV/q, 90° and the 200 eV/q, > 90° peaks of the the 3rd (||) and the 100 eV/q, 90° peak of the 7th (⊥) events, respectively. Not apparent in these figures is the fact that the HEEPS analyzer was very insensitive to particles moving toward the geomagnetic north near and slightly above 90° magnetic pitch angle. Nevertheless, that absence of sensitivity probably does not entirely account for the very large disparity in fluxes observed between the northern and southern azimuthal magnetic hemispheres seen in the data. There is marked variation in the azimuthal flux structure with energy, evident in the 3rd (||) fluxes shown in Figure 2-27. Figure 2-28 shows that the particles near 100 eV/q and 95° magnetic pitch angle observed during the 7th (⊥) beam event (recall Figure B-7) were strongly peaked in geomagnetic azimuth, with peak fluxes moving toward the geomagnetic south-southeast. This figure has been chosen to demonstrate the azimuthal flux structure, naturally, because it serves as the best example of this structure in the data. As in the case of the energy-pitch distributions (Fig B-1 through B-16), the angular distributions became more strongly peaked as beam related fluxes grew less saturating (weaker).

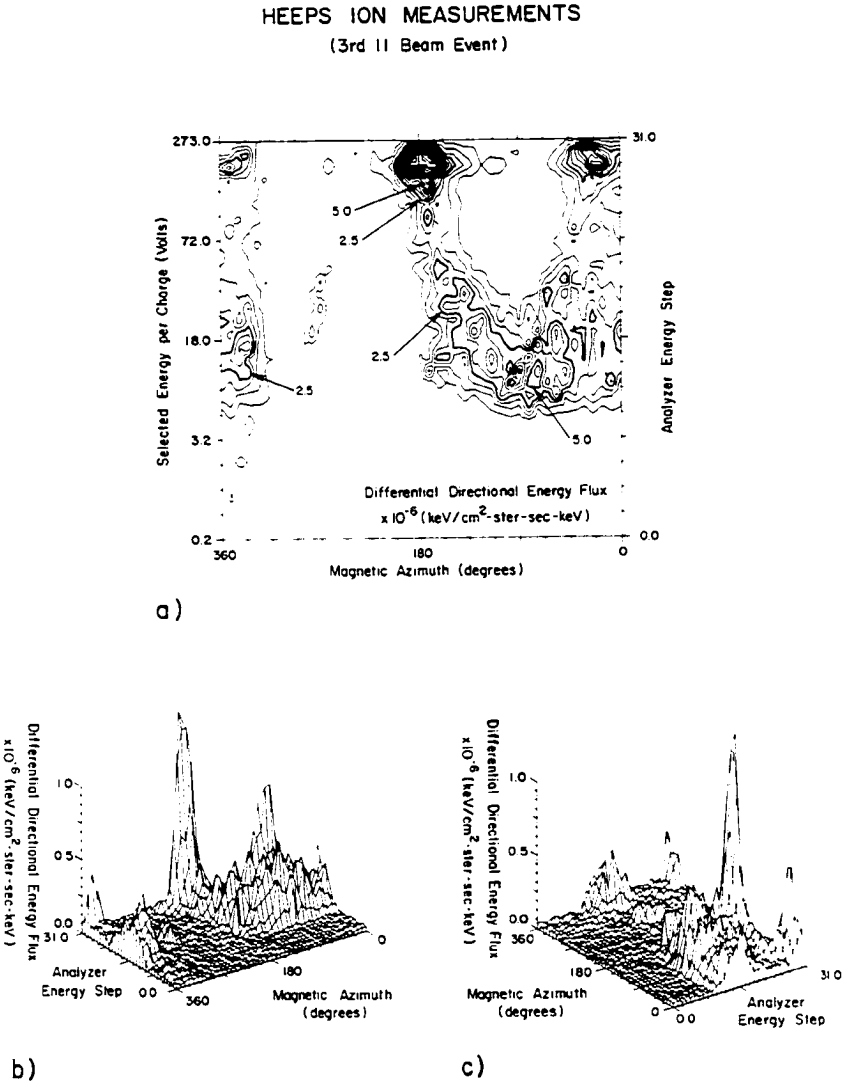

Figure 2-27

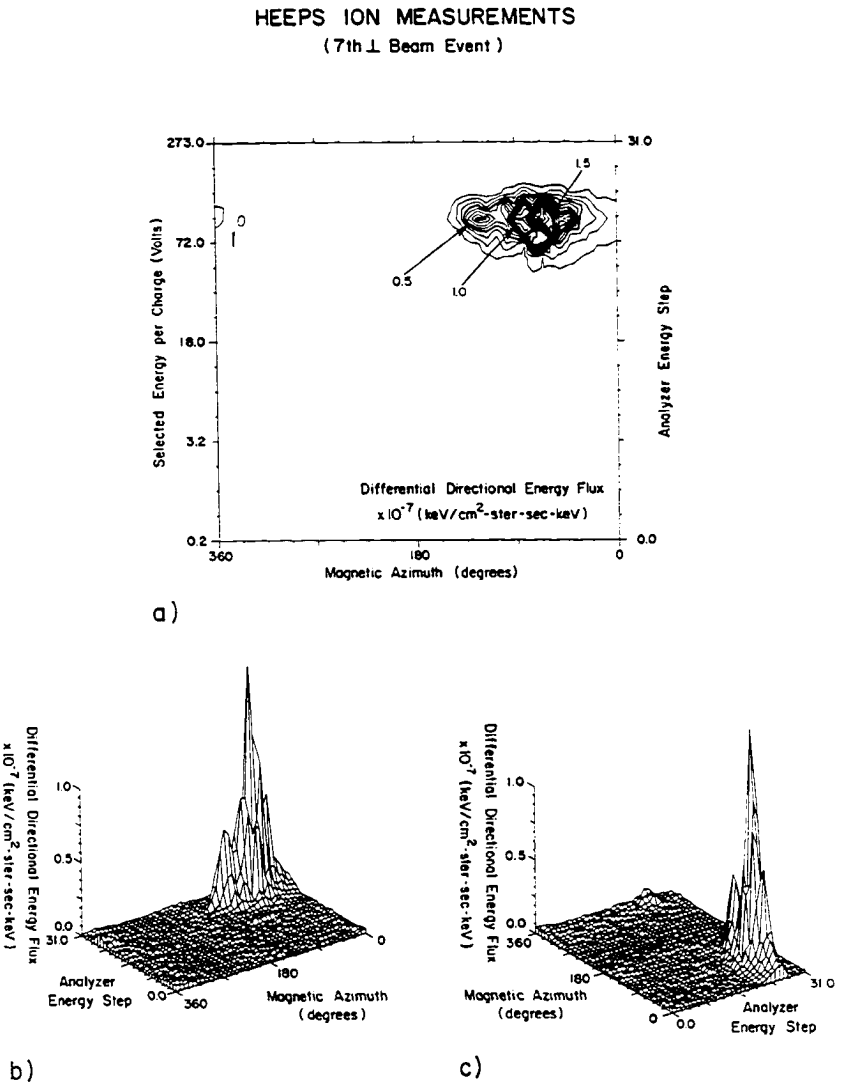

Figure 2-28

Octosphere Ion Observations.

As described earlier in this section, the 29.015 main experiment payload featured four octospheric electrostatic analyzers, of which two (OCTO 1 & 3) were dedicated to electron measurements and two (OCTO 2 & 4) were dedicated to positive ion measurements. We will be presenting positive ion data from OCTOs 2 & 4 in this subsection. By virtue of the orientation of the main payload spin axis and the placement of the instruments (see Fig.2-12), OCTO 2 was sensitive to ions in the pitch angle range from 0° to 90°, while OCTO 4 was sensitive to ions in the range 90° to 180°. Only the bottom 7 energy steps in the 64-step sweep were useful for viewing ions associated with beam operations on this experiment, the others extending upward in energy from 280 eV/q. As was also mentioned earlier in this section, there were actually only 32 sequential energy steps with each of these toggling between two discrete selection states, so that a total of 64 distinct energy bands were covered. The energy per charge associated with each of the eight lowest energy bands are listed in table 2-3, below.

STEP #	0	1	2	3	4	5	6	7
SELECTED E/q (Volts)	10	14	26	46	125	162	219	280

Table 2-3: Lowest eight energies selected by Octosphere electrostatic analyzers.

Figures 2-29 through 2-31 show data obtained on board the main payload during the 2nd (||), 3rd (⊥) and 6th (⊥) beam events, respectively. These three figures show data pertaining to Octosphere positive ion measurements, arranged in a common format. Along the bottom trace and the one directly above it are shown the magnetic pitch angle (in degrees) and the event rate (in counts per sample), respectively, associated with OCTO 2, while along the top trace and the one directly below it are the pitch angle and event rate associated with OCTO 4. The sample rate of these two instruments was 625 Hz, so that full scale on the event rate signals corresponds to octosphere count rates of 640 kHz. At

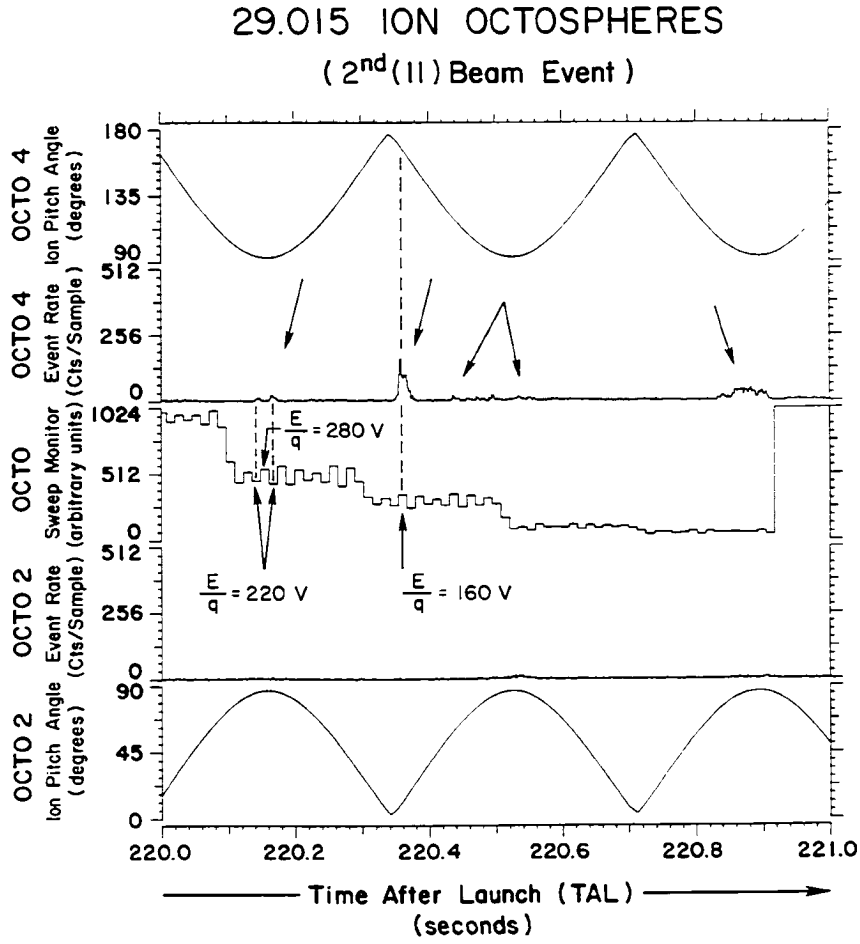

Figure 2-29

the center of each figure, we have shown data from the OCTO energy sweep monitor, which is indicative of the current energy selection state of the analyzer, although, as can be seen by inspection of the figure, this data is of limited usefulness at the lowest couple of steps.

During the 2nd (||) beam event (Figure 2-29), OCTO 2 measured moderately large (60 kHz) event rates near 165° magnetic pitch angle and an energy per charge of ~160 eV/q. These are the same particles which contribute to the the ~200 eV/q peak near 180° magnetic pitch angle seen in the HEEPS energy-pitch angle spectra during the 1st 6 (||) beam injections. Note the marked absence of events on either of the two neighboring toggles, showing the absence of particles in this pitch angle range at energies per charge near 125 Volts. Also apparent in this figure are small amplitude responses seen by the OCTO 2 instrument near 90° magnetic pitch angle and at 220 eV/q and below, with the largest event rates near 90° occuring in the 10 and 14 eV/q energy channels. These lowest energy ions at ~10 eV/q correspond to the low energy 90° degree ions observed in more detail with the HEEPS imaging analyzer.

Figure 2-30 shows similar data collected during the 3rd (⊥) beam event. Small amplitude response can be seen in the in the OCTO 2 instrument near 90° magnetic pitch angle and in the 125 eV/q energy channel. These are the ~100 eV/q, 90° particles commonly observed by HEEPS during (⊥) beam events. However, the dominant response in this figure is seen in the low energy channels near 90°. Just as the two pitch angle traces pass through 90°, the energy step changes, so this is not as clear as it might be, but there is some indication of modulation of these low energy fluxes with the sweep toggle, favoring the lowest energy channels and indicating that these ion fluxes peak below 46 eV/q. These particles are the same as the low energy (~20 eV/q) ions observed near 90° with the HEEPS analyzer. As in the case of the HEEPS measurements, the event rates at low energies are seen to dominate those near 100 eV/q, although the domination is stronger in the OCTO data than in the HEEPS data.

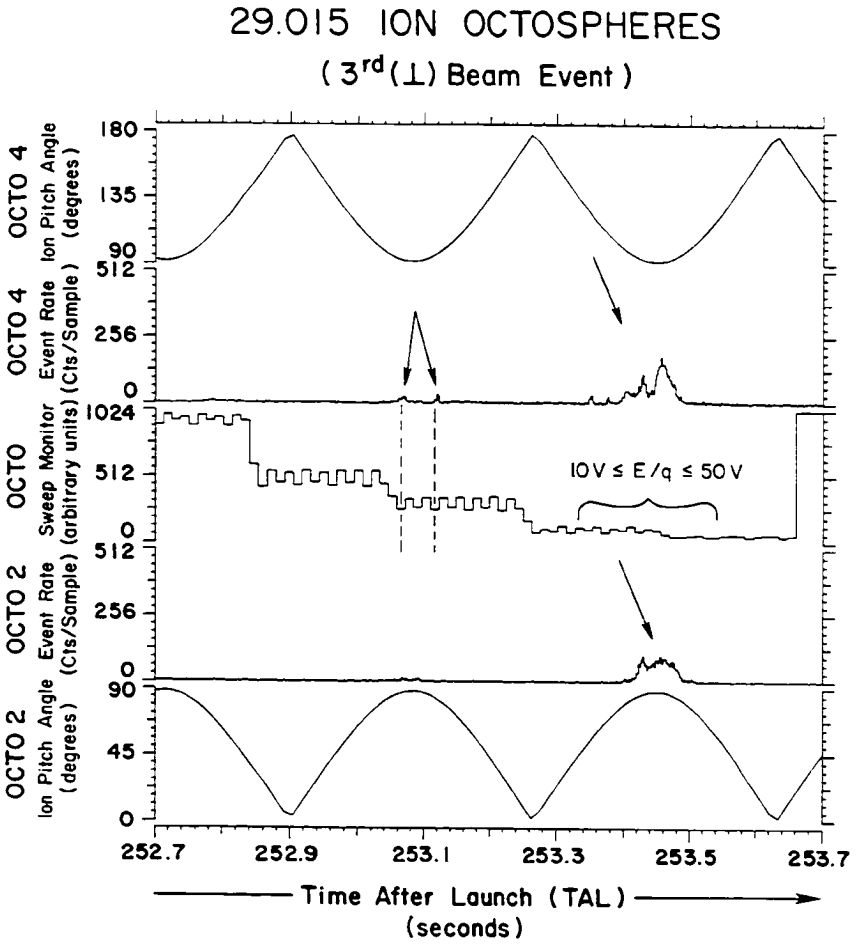

Figure 2-30

As a final example, in Figure 2-31 we show octosphere ion flux measurements carried out during the 6th (⊥) beam event. The three count rate peaks seen in the OCTO-2 signal between 410.3 and 410.4 seconds TAL are due to positive ion fluxes near 90° magnetic pitch angle and are clearly modulated by the sweep toggling, indicating the presence of strong fluxes near 125 eV/q, but not near 160 eV/q. The particles giving rise to these peaks are the same as those seen in the HEEPS data shown in Figure B-6. This is a particularly clear example of the corroboration between the octosphere results and the HEEPS results. The reason for the presence of these events in the OCTO 2 data and not in the OCTO 4 data is that these two analyzers were sensitive to particles moving at different magnetic azimuths when viewing 90° pitch angles. In particular, when viewing 90° pitch angle, OCTO 2 was sensitive to ions moving toward the magnetic north, while OCTO 4 was sensitive to particles moving toward magnetic south. Thus, the Octospheres lend support to the HEEPS observation that, late in the flight, ~100 eV/q ion fluxes near 90° magnetic pitch angle are anisotropic with respect to magnetic azimuth, favoring southward moving directions. An in depth analysis of the Octosphere ion observations, in the context of Ar^+ ion trajectory modelling is underway at the University of New Hampshire and will be the subject of another Dissertation (Keyung Tang, 1987).

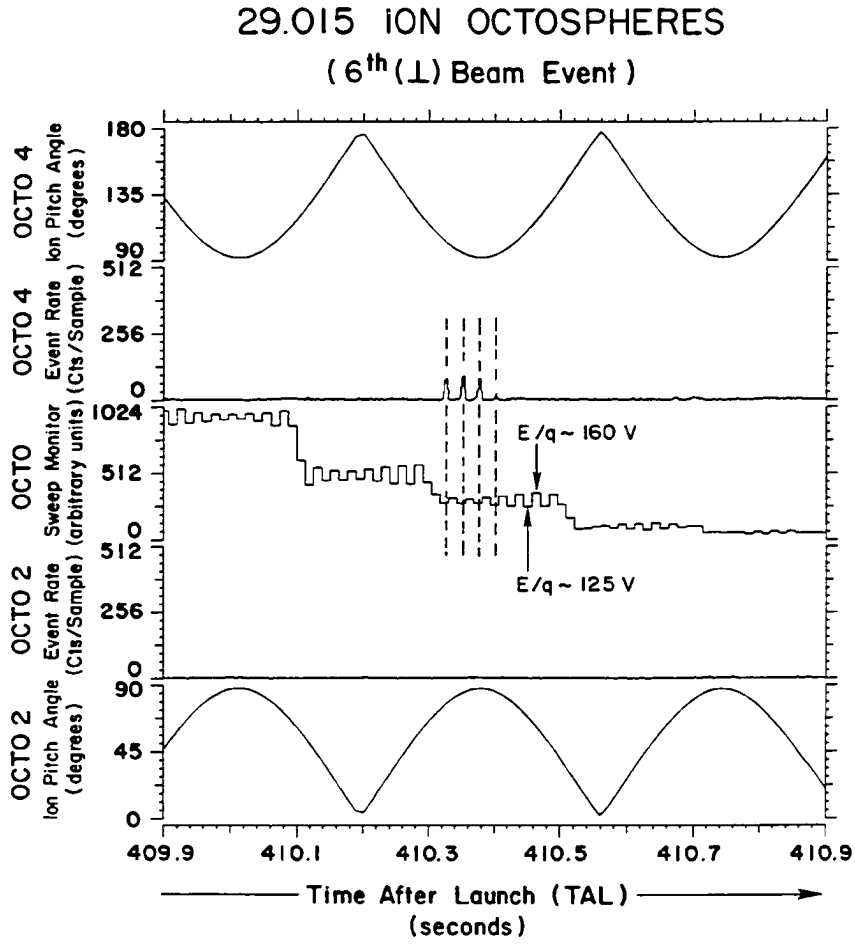

Figure 2-31

Field Observations And Other Data

Electric and Magnetic Fields.

The determination of the convective electric field during flight in a high latitude sounding rocket experiment is important in itself due to the importance of large scale ionospheric convective motions to the global magnetospheric physics. In experiments such as the heavy ion beam injections carried out on board flight 29.015, the importance of complete electric field measurements cannot be overemphasized, especially where measurements can be carried out in the 'near zone', close to the beam source.

A single pair of Weitzmann **E** field booms was deployed for the measurement of DC electric fields on NASA flight 29.015 (see Figure 2-12). Commonly, the boom measurement is employed in combination with the assumption that any steady **E** fields are such that $\mathbf{B} \cdot \mathbf{E} = 0$, where **B** and **E** are the geomagnetic field and the electric field, respectively. Given the orientation and directed velocity of the booms with respect to a geomagnetic reference frame, then, the two components of the 'strictly transverse' electric field may be computed in that reference frame from the boom measurements. That analysis has been carried out, but there still exists some uncertainty as to the resulting **E** field azimuth. Figure 2-32 shows the envelope of the Electric field in the moving main payload frame of reference plotted versus time for most of the duration of the flight. The instrument is saturated during the 1st ($\perp$) event. Large, spiky field enhancements are then associated with ACS neutral gas injections until about 165 seconds. The termination of the 2nd ($\perp$) beam event near 206 secs (TAL) and the operation of the 3rd ($\perp$) event near 250 seconds TAL are evident in the data from the large amplitude of the electric field envelope. Since this data is plotted as an envelope, signal enhancements may be due to steady electric fields or to electric field fluctuations. After the 3rd ($\perp$) beam event, the field gradually increased

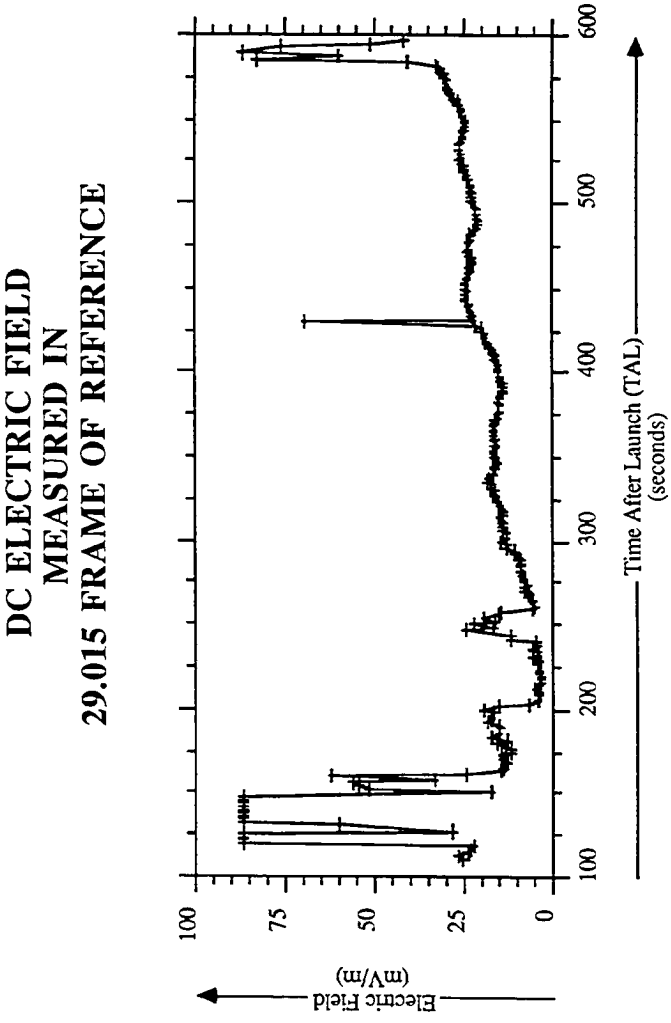

Figure 2-32

through the rest of the flight, but remained below 25 mV per meter, corresponding to plasma drifts of 250 m/sec, until very late on the downleg.

The DC magnetic field was measured by the use of a 3-axis magnetometer mounted near the nose of the sub payload. Figure 2-33 shows the total measured field intensity plotted versus time, every two seconds for the duration of the flight. This information is shown along with a simple model field intensity, given by:

$$|B|_{mod} = 0.53 \times \left(\frac{r}{r_0}\right)^3 \quad \text{(Gauss)},$$

where r is the geocentric radial distance to the point of observation and r_0 is the geocentric radial distance to a reference altitude of 300 km above Sondre Stromfjord, Greenland. It can be seen that through most the flight the measured total magnetic intensity varied according to the model, although with a steady ~0.03 Gauss offset, representing an deviation in the measured quantity of ~6%.

During the time when the sub payload was attached to the main payload, the magnetometer was surrounded by magnetic materials. Furthermore, ion beam operation involved the flow of sometimes large currents in the sub payload circuitry, which was located in immediate proxitmity to the magnetometer. For these reasons, the magnetometer data collected before sub payload separation is of little use. The large transient field perturbation near 134 seconds was created by the ejection of the stainless steel sub payload, which had shrouded the magnetometer until this time. After sub payload separation, this data may be used for carrying out aspect analysis. However, higher time resolution plots of this magnetometer data show the field magnitude to be varying with spin frequency, indicating inaccuracies in the mutual alignment or gains of the 3 sensor axes. For this reason, we have used the gyroscope data to carry out payload aspect analysis whenever possible. Late in the flight, after 536 seconds TAL, the gyroscope data is not available, so the aspect analysis must be carried out using the magnetometer data.

VARIATION OF GEOMAGNETIC FIELD DURING FLIGHT (29.015)

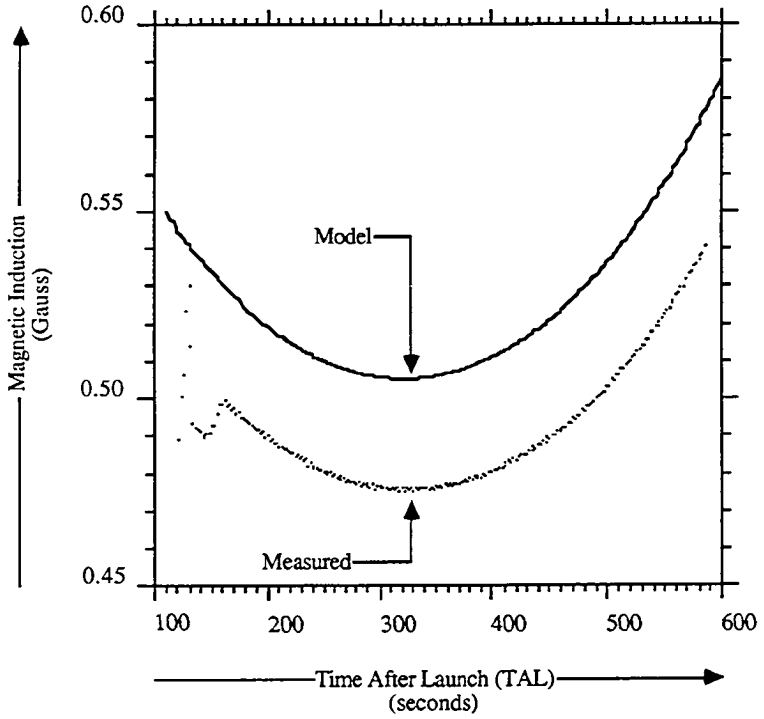

Figure 2-33

It is natural to look for magnetic signatures of currents flowing in the beam plasma environment. In particlular, a field aligned current is thought to flow to the sub payload during ($\perp$) beam events. Such a current would give rise to a solenoidal magnetic field perturbation whose magnitude is given by Ampere's law to be

$$|\Delta B| = \frac{2\mu_0 I}{r}$$

$$= \frac{20}{r} \text{ nT},$$

assuming a line current of 100 mA, and where r is given as the distance (in meters) from the current line. Since the best sensitivity we can hope for from the 3-axis magnetometer is around 7.5 nT, a 100 mA line current would not be detectable by this instrument for r greater than about 3 meters.

29.015 Plasma Wave Observations.

Extensive high and low frequency plasma wave observations were obtained during the 29.015 rocket experiment. The spherical electrical potential probes and cylindrical Langmuir probes deployed on the 3 meter Weitzmann booms were used to detect electric field and plasma electron density fluctuations, respectively. These signals were fed into various wave receivers which featured bandpass filtration and automatic gain control electronics. Extensive analyses of the results of a large portion of the electric field fluctuation measurements have been reported by R. E. Erlandson (1986) in his Ph.D Dissertation. An initial report of the entire experiment (Erlandson et al., 1987), which provides many details of the wave observations has appeared recently in the refereed literature. Only the major aspects of these observations will be summarized here.

In Figure 2-34, we show the inverse of the gain states of the AC-E electric field receiver, which was flown by the University of Minnesota, plotted versus time during most of the flight. Electric field fluctuations in the frequency ranges 0-1 kHz and 1-10 kHz induce the reciever gain variations shown in the 0-1 kHz (bottom) and the 1-10 kHz (top)

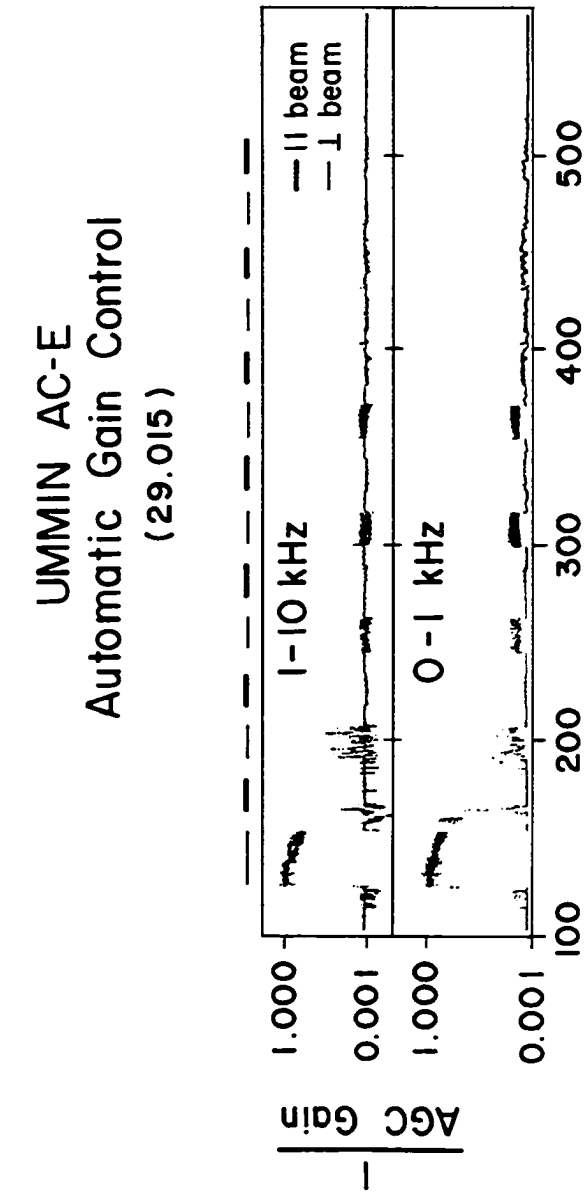

Figure 2-34

receiver channels. Gain decreases correspond to electric field wave power increases in the given frequency pass band, so that the sense of the signals plotted in Figure 2-34 is directly indicative of the measured amplitude of the fluctuations. Indications have been provided as to which beam is on at a given time in the figure, which was provided by of R. E. Erlandson. The plasma wave emissions observed on board flight 29.015 were characterized by field amplitudes measured at near 100 mV/m during the 1st (⊥) beam event and which ranged down to less than 0.1 mV/m late in the flight.

It can be seen that very strong response in the gain signals in both passbands was induced during the 1st (⊥) beam event, with moderate responses in the subsequent (⊥) events, through the 5th. Large amplitude response in the wave reciever gains can be seen during the early part of the 2nd (||) beam exercise, although only small amplitude response can be discerned later in the event. The large amplitude gain response seen early in the 2nd (||) event are associated with the expulsion of neutral Argon gas by the attitude control system in re-aligning the main payload after sub payload ejection. The gain response amplitude is very small (although often discernable) for all subsequent (||) events.

As in the cases of previous experiments of this type, the electric field fluctuations measured in the 0 to 1 and 1 to 10 kHz passbands exhibited extensive structure in the wave frequency domain. Most of this structure, especially in the cases of perpendicular beam events, was seen to exist at harmonics of various ion gyrofrequencies. However, the fluctuations are often seen to exhibit structure at frequencies characteristic of the lower hybrid frequency, especially during (||) beam injections.

As an example, we show in Figure 2-35 (from Erlandson, 1986) the measured electric field spectral density plotted versus the fluctuation frequency for an interval during the 2nd (⊥) beam event. The 13 arrows mark locations of the various H^+ cyclotron harmonics in the ambient geomagnetic field. The ordering of the wave power with respect to the H^+ cyclotron frequency is clear. In fact, extensive ordering of the low frequency electric field wave power near ion gyrofrequency harmonics is generally associated with

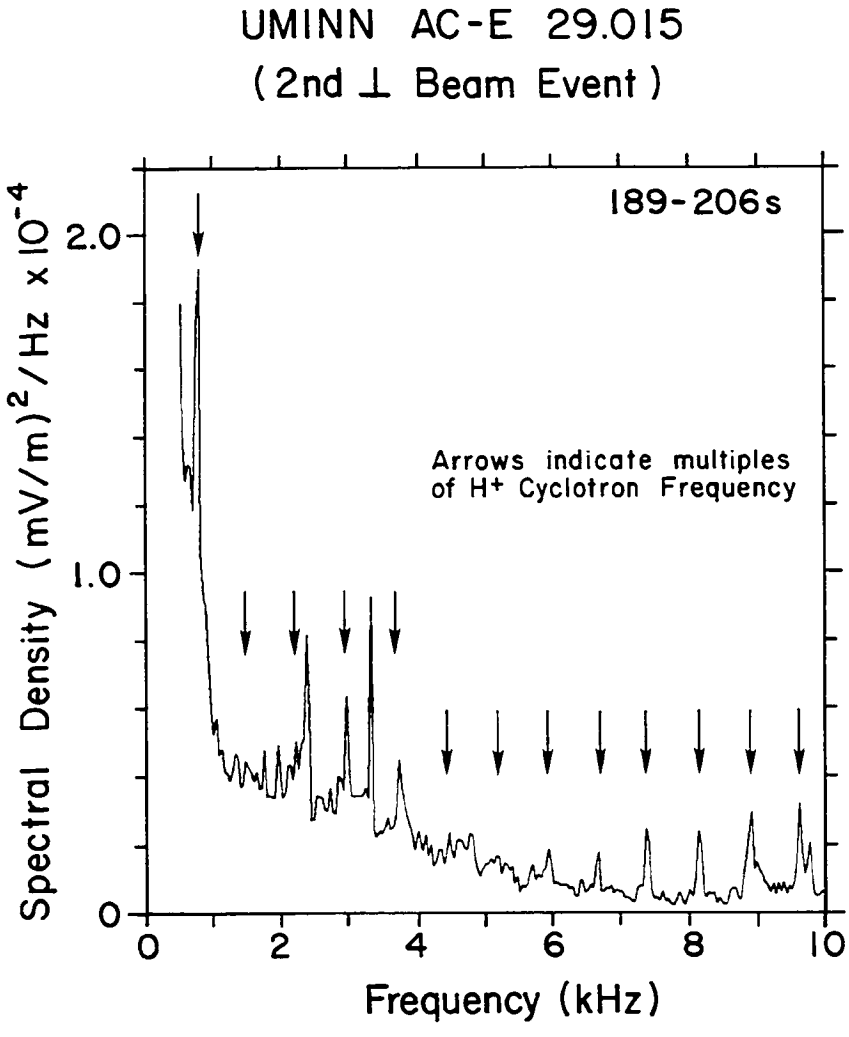

Figure 2-35

(⊥) beam events, although this ordering varies in detail from event to event and disappears late in the flight. The multiple emissions near harmonics of the H^+ cyclotron frequency during the 2nd (||) beam event have been seen before, during the Porcupine experiment, and have been identified by Kintner and Kelly (1983) as Hydrogen Bernstein waves driven by the gyrating ion beam. The growth of waves in a plasma which contains an ion component which is streaming across magnetic field lines with respect to the other plasma species has been studied by a number of authors (Hudson & Roth, 1984; Kintner & Kelley, 1983; Roth et al., 1983; Seiler et al, 1976 and Walker et al., 1986;) through the use of analytical linear Vlasov theory, numerical Vlasov theory, numerical simulation and in the laboatory. These studies have predicted wave growth which feeds on the energy of the streaming ion species and which is ordered by both the relavent ion cyclotron frequencies and the lower hybrid frequency. In turn, these waves are often found to contribute to transverse heating of the non-streaming ion components and parallel heating of the ambient electrons. Wave power during (||) beam events is often observed in the vicinity of the lower hybrid frequency, with several peaks in the power spectral density appearing in the vicinity of 6 kHz. The spacing of these peaks is seen to be near the H^+ cyclotron frequency.

Observations Carried Out From The Sub Payload.

The two instruments operated from the sub payload which may contribute to our understanding of the processes under study during these experiments are the calibrated auroral photometer and the Langmuir probe. The photometer look direction was antiparallel to the sub payload spin axis, so that it looked upward, toward the main payload and would not be expected to be sensitive to auroral emissions which may have been taking place below, near 100 km altitude. The geometry shown in Figure 2-6 indicates that this photometer would be looking almost directly into the (||) beam when it was operating, but this is not the case with regard to the (⊥) beam, which was fired out the side of the sub payload.

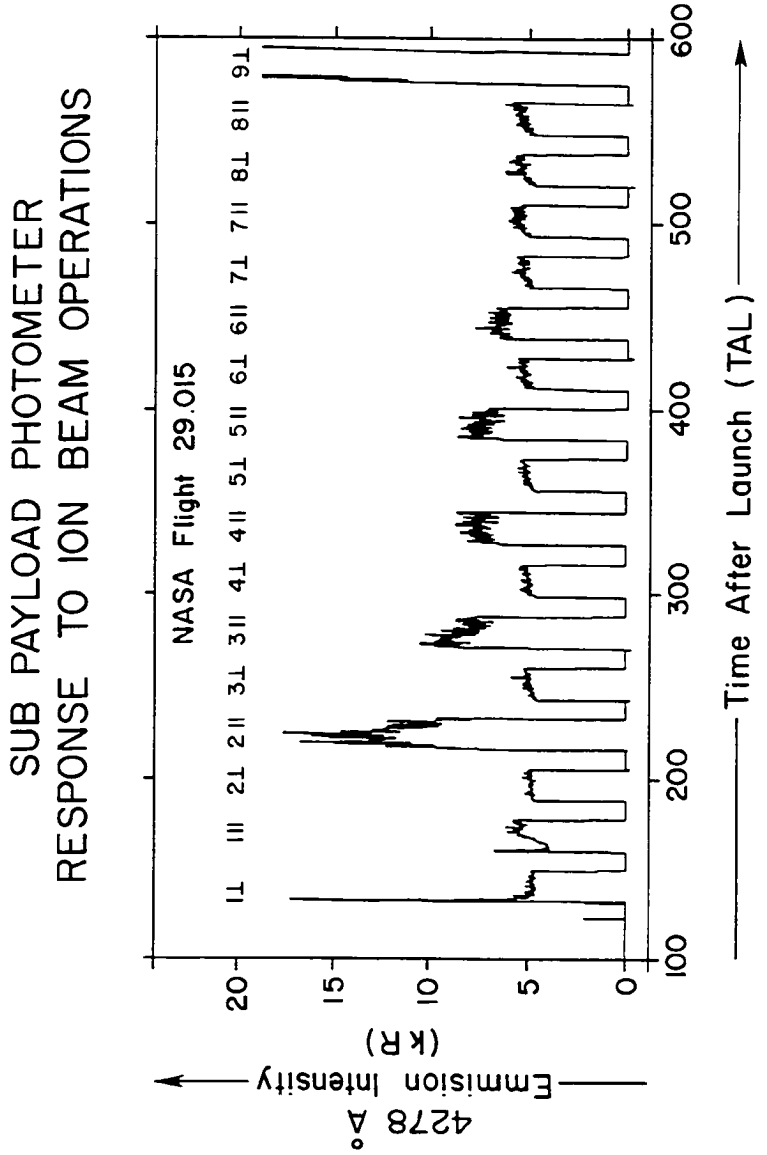

Figure 2-36

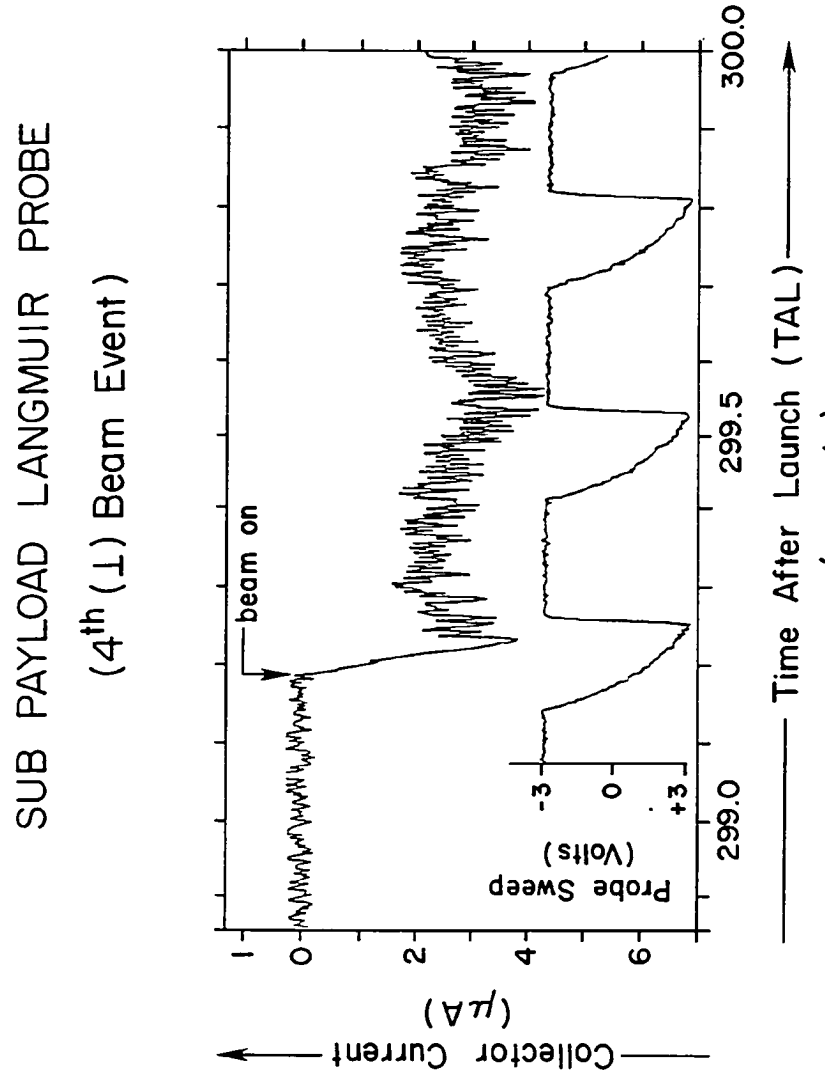

Figure 2-37

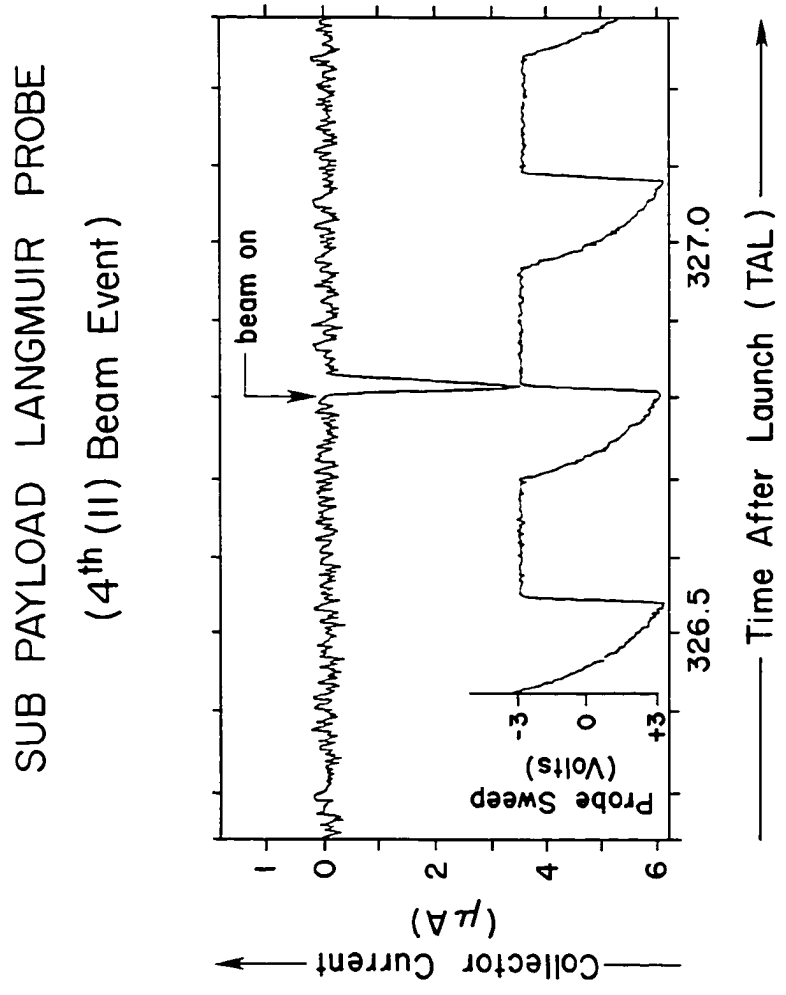

Figure 2-38

Figure 2-36 shows the response of the photometer as a function of flight time for most of the flight, as well as indications as to the times that various beam operations took place. The photometer response to Ar^+ beam injections is readily apparent in this figure, beginning near 134 seconds, when the sub payload was ejected, uncovering the photometer viewing aperture. With the exception of a large amplitude (~17 kR) leading edge effect seen at sub payload separation, the photometer response varies little from the 1st through the 8th ($\perp$) events, with a uniform emission intensity of near 5 kR being observed during each event. The comparatively very large response seen during the 9th ($\perp$) event is probably associated with the much larger neutral particle density encountered at this time, as the payloads were re-entering the atmosphere. The nature of the photometer response is quite different during ($\parallel$) beam injections and exhibits significant temporal structrue over a wide range of time scales. The 1st ($\parallel$) event is characterized by a response whose amplitude increases from ~4 to ~6 kR during the event, while the 2nd ($\parallel$) event gives rise to more intense light emissions, ranging between 10 and 15 kR. The emission intensity then decreases from event to event, in the ($\parallel$) cases and by the time of the 7th ($\parallel$) event, is at the same level as that observed during ($\perp$) beam events, at ~5 kR. The observed photo-emission taking place in the plasma near the sub payload during parallel and perpendicular beam events is indicative that significant electron heating is probably taking place and that these hot electrons are, in turn, collisionally exciting the ambient neutrals and causing them to radiate.

As mentioned earlier, the 29.015 sub payload also carried a crude Langmuir probe which was biased by a sweeping voltage signal which ranged from -3 Volts up to +3 Volts. In Figures 2-37 and 2-38, we show the probe current and the applied probe bias as functions of time for short periods of time during the 4th ($\perp$) and 4th ($\parallel$) events, respectively. These cases are typical of the responses seen in the Langmuir probe to ($\perp$) and ($\parallel$) events during this flight. It can be seen by comparison of these two figures that the Langmuir probe response to ($\perp$) and ($\parallel$) beam injections differed markedly, with ion current

collection during (||) events being limited to a transient (~20 ms) leading edge effect at the time the beam was turned on, while a steady ion current was collected during ($\perp$) events. This steady ion current was not seen to be modulated by the Langmuir probe sweep, indicating a negative charge state on the sub payload during ($\perp$) beam events of at least 3 Volts in magnitude. The low frequency modulation in the probe current shown in Figure 2-38 is related to the sub payload spin period, rather than to the sweeping probe bias.

Discussion

The structure evident in the positive ion flux observations carried out using the capped hemisphere HEEPS ion analyzer on board NASA flight 29.015 presents a series of difficult and important questions regarding the environment of the beam emitting sub payload. It is an understatement to say that the observations don't correspond to what one might anticipate, based on a simple free particle trajectory picture of the beam as we understand it. In fact, several aspects of the observations are no less than dramatic, in my opinion, because of their strength in the system, their strong repeatability and their defiance of explanation. On the other hand, there is at least some correspondence of the observations with simple expectations, which, along with the corroborative Octosphere ion data, gives confidence in the quality of the major aspects of the HEEPS ion results. The data set itself is quite complex, representing an intimate mixture of effects which are due to the characteristics of the instrument and those which are due to real variations in the ion flux. This was the first time a HEEPS instrument had been flown by researchers at UNH and, although the results of careful calibrations have been presented earlier in Section 1, the differences between the controlled, low flux environment of the calibration laboratory and the multidirectional high flux conditions encountered in space on the spinning rocket payload are extreme. The reader may already be aware that heavy saturation of the HEEPS instrument was common throughout much of the flight, with peak event rates of over 100 kHz encountered in every $\perp$ beam event through the 4^{th}, although there was substantial nonsaturated operation in addition. At the other end of the event rate scale, the HEEPS instrument was subject to a large background of > ~3 kHz throughout the flight. These two factors combined to impose severe limits on the dynamic range of the instrument in terms of particle flux intensity. For these reasons, we feel that highly quantitative conclusions based on certain aspects of the HEEPS data would be unwarranted at this time.

This point applies more directly to the quality of the angular imaging under high event rate conditions, with the quality of the electrostatic energy analysis remaining reasonably reliable to event rates (not count rates) of on the order of 1 Mhz, with the application of an appropriate saturation model. Since the event rates were generally much larger during ($\perp$) beam operations than during ($\parallel$) beam operations, the HEEPS data will be found to be more quanititative during ($\parallel$) beam operations.

However, it is the premise of this work that there exist several central aspects of the data which stand out as fundamental elements of the ion flux environment surrounding the beam emitting sub payload and are not subject to significant uncertainty as to their reality or basic characteristics. It is the purpose of this section to reiterate these central aspects of the observations and to examine them in light of our understanding of the experiment parameters and the beam-plasma system itself.

Single Particle Motion. The most simple picture of the evolution of the beam (in the ($\parallel$) or ($\perp$) case) calls for the beam particles to move away from the sub payload as free particles, gyrating up (or down) geomagnetic field lines along trajectories which, for a given species, are determined solely by their initial velocities and the ambient magnetic and electric fields and, ultimately, being lost to the system. In the absence of diffusive processes, an Ar^+ ion emitted at the sub payload ($\mathbf{r \equiv 0}$) with energy ε (we will assume single charge states) and magnetic pitch angle α will move along the field line at a velocity

$$v_{\parallel} = \sqrt{\frac{2\,\varepsilon}{m}}\,\cos(\alpha) = 2.2 \times 10^3 \sqrt{\varepsilon}\,\cos(\alpha)\,\left(\frac{m}{sec}\right), \qquad \text{Eq. 2-13}$$

where ε is given in Volts and m is the Ar^+ ion mass (equal to ~40 proton masses). During a single gyro period (~ 50 msecs), a 200 eV Ar^+ ion moving at a magnetic pitch angle of 180° will have moved 1.5 km up the field line, while a 150° ion will have moved 1.3 km up the field line. Furthermore, an Ar^+ ion injected at a given energy, pitch angle and magnetic azimuth (ψ) will gyrate about a guiding center, the location of which is given by

$$\mathbf{r}_g = -\,r_g \sin(\psi)\hat{x} \;-\; r_g \cos(\psi)\,\hat{y}, \qquad \text{Eq. 2-14}$$

where r_g is the radius of gyration, given for an Ar^+ ion in the Earth's magnetic field at the location of this experiment to be

$$r_g = 17\sqrt{\varepsilon}\,\sin(\alpha) \quad \text{meters.} \qquad \text{Eq. 2-15}$$

The coordinate system in use here is a local geomagnetic system, with x, y, and z axes pointing along the geomagnetic field and toward geomagnetic east and south, respectively, and with the origin at the beam-emitting sub payload. At any position (z) along the field line, the position of the Ar^+ ion in the radial (x-y) plane is given as

$$\mathbf{r}(z, \alpha, \varepsilon) = \mathbf{r}_g\left(1-\cos\left(\frac{z\tan(\alpha)}{r_g}\right)\right) + (\mathbf{r}_g \times \hat{z})\sin\left(\frac{z\tan(\alpha)}{r_g}\right) + \frac{z\tan(\alpha)}{\omega_g r_g}\frac{\mathbf{E}\times\mathbf{B}}{B^2}, \qquad \text{Eq. 2-16}$$

where ω_g is the Ar^+ cyclotron frequency, given as ω_g = 127 rad/sec in the Earth's 0.53 Gauss field. The last term in Eq. 2-16 represents the effect of guiding center drift in the presence of a transverse electric field. This drift amounts to 10^3 m/sec in the presence of a 50 mV/m transverse field in the 0.53 G geomagnetic field. Figure 2-32 shows that the measured electric field is less ~25 mV/m during most of the flight, amounting to transverse guiding center drift velocities of less than 500 m/sec or less than ~25 meters per Ar^+ gyro-period (~ 50 msec). This term could be important in considering beam focusing properties, or the trajectories of particles with pitch angles near 90°, which will undergo many more gyrations for a given distance travelled along the magnetic field line than particles with pitch angles closer to 0° or 180°.

Neglecting the convection field, **E**, we find that r, the magnitude of the transverse displacement may be written as a function of ε, α and z as

$$r(z, \alpha, \varepsilon) = 24\sin(\alpha)\sqrt{\varepsilon\left(1-\cos\left(\frac{z\tan(\alpha)}{r_g}\right)\right)} \quad \text{meters.} \qquad \text{Eq. 2-17}$$

This is an oscillating function of z, with an amplitude of $24\sin(\alpha)\sqrt{\varepsilon}$ meters. For parallel beam events, when particles are thought to be injected at all azimuths ($0° \le \psi \le 360°$) and at all pitch angles between roughly 150° and 180° we expect a sausage link shaped volume to

be filled with upgoing Ar^+ ions, as pictured in Figure 2-39. This figure illustrates the limiting trajectories of 150°, 200 eV/q Ar^+ ions, along with the nominal trajectory of the main payload (see Appendix A), with respect to the sub payload, in the r-z plane. Also indicated in Figure 2-39 are the geomagnetic field, the location of the sub paylaod (at the origin), the nominal locations of the main payload at the end of the 6th and 8th parallel beam events, the applicable length scale and a reference indicator as to geomagnetic azimuth. This figure illustrates an aspect of the data which is somewhat difficult to understand. That is, based on the illustration in Figure 2-39, we should have observed roughly anti-parallel beam ions throughout the experiment. Instead, such ions disappeared from the observatons after the 6th (II) beam event (compare Figures B-13 & B-14), at the position marked by the unfilled square, well inside the region thought to be filled with upgoing Ar^+ plasma.

In this case of parallel beam injections, we expect to observe upgoing 200 eV/q ions at the main payload, whose pitch angles should be strongly peaked at values given by solutions to the transcendental equation

$$r_{mp} = 24 \sin(\alpha) \sqrt{\varepsilon \left(1 - \cos\left(\frac{z_{mp}\tan(\alpha)}{r_g}\right)\right)}, \qquad \text{Eq. 2-18}$$

where r_{mp} and z_{mp} are the radial and axial positions, respectively, of the main payload with respect to the sub payload at a given time. There are an infinite number of solutions (for α) to this equation, for a given r_{mp} and z_{mp}, with the density of solutions diverging near $\alpha = 90°$. However, for all values of r_{mp} and z_{mp} thought to be encountered during the 29.015 experiment, only a single solution exists in the pitch angle range (150° - 180°) in which Ar^+ ions were injected at the sub payload. Figure 2-40 shows solutions to equation 2-18 plotted versus time (marked as model 1), at the times of the 1st through the 6th (II) beam events. Model 1 is based on the deployment geometry described in Appendix A. That is, the vector from the main payload is assumed to form an angle of 7.5° with the local geomagnetic field and to increase linearly in magnitude with time, based on a 2.2 m/sec

ANTI-PARALLEL BEAM INJECTION GEOMETRY

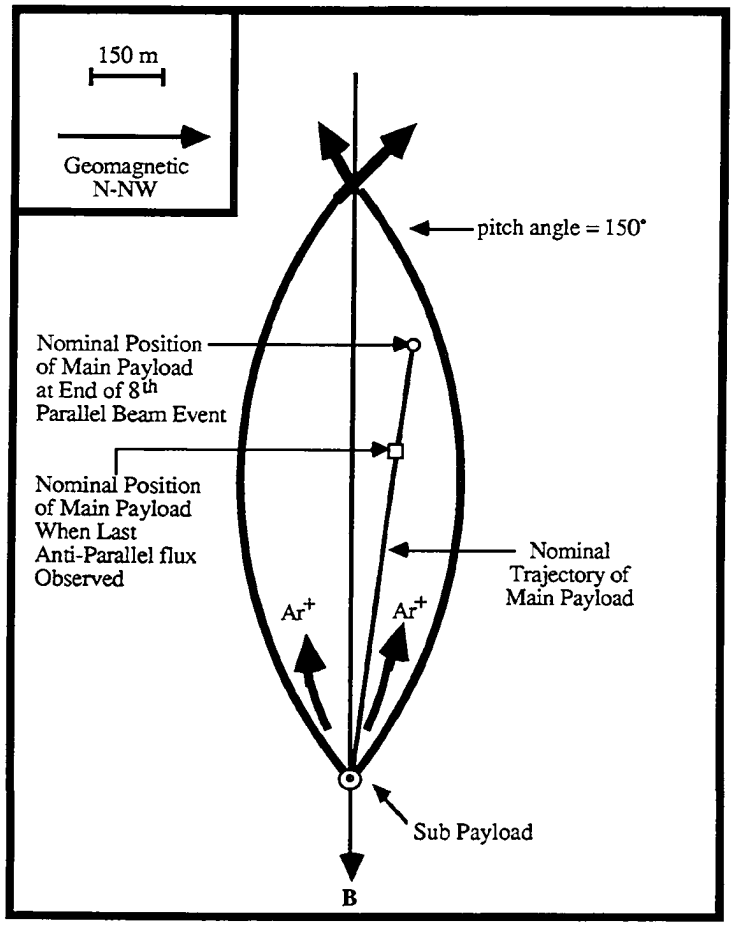

Figure 2-39

UPCOMING BEAM PARTICLES (PARALLEL EVENTS)

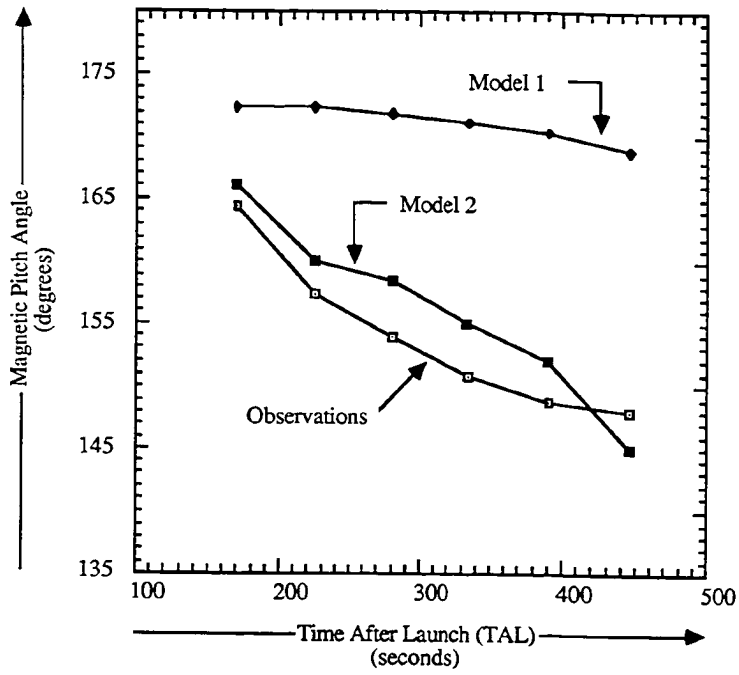

Figure 2-40

separation velocity. The curve marked model 2 also shows solutions to Eq. 2-18, above, based on another separation model which is probably more accurate than the simple uniform velocity model descibed above. The reader will recall that after the sub payload was ejected down the geomagnetic field line, the main payload was rotated as illustrated in Figure 2-16, so that it became oriented with its spin axis at 135° to the magnetic field. This maneuver was accomplished through the operation of a single high pressure ACS gas nozzle, applying a torque to the main payload about its center of mass. Since this was a single nozzle and not a pair, which would form a torque couple, a net force will unavoidably have been applied to the payload center of mass during the operation. We have therefore hypothesized that an additional transverse velocity was imparted to the main payload by the operation of the attitude control system during the period between roughly 140 and 170 seconds flight time. Specifically, in model 2, we have assumed that the parallel separation between the two payloads is nominal (based on the separation geometry) and that the transverse velocity of the main payload with respect to the sub payload is given as 0.29 m/sec, for t<155 sec and as 0.9 m/sec, for $t \geq 155$ sec. Thus, we have assumed that the ACS operation has imparted a transverse velocity of ~0.6m/sec, impulsively, at 155 seconds TAL to the main payload. In addition to data generated with models 1 & 2, we have reproduced, in this illustration, the data from Figure 2-26, showing the measured mean values of the pitch angle associated with the upcoming beam particles seen during the 1^{st} through the 6^{th} (II) beam events (see Figures B-9 through B-15). These mean values, derived from the data, are represented by open squares. It can be seen that there is a large discrepancy between the data obtained through particle measurements and that generated with model 1, wheras there is reasonable agreement between the measurements and results derived using model 2.

Figure 2-41 shows the radial position, given by Eq. 2-18, of a 200 eV/q Ar^+ ion at two distinct axial locations (parts a and b) as a function of magnetic pitch angle. The two axial positions are given as 680 and 800 meters in parts 'a' at the top and 'b' at the bottom,

DYNAMICS OF 200 EV AR+ IONS IN GEOMAGNETIC FIELD

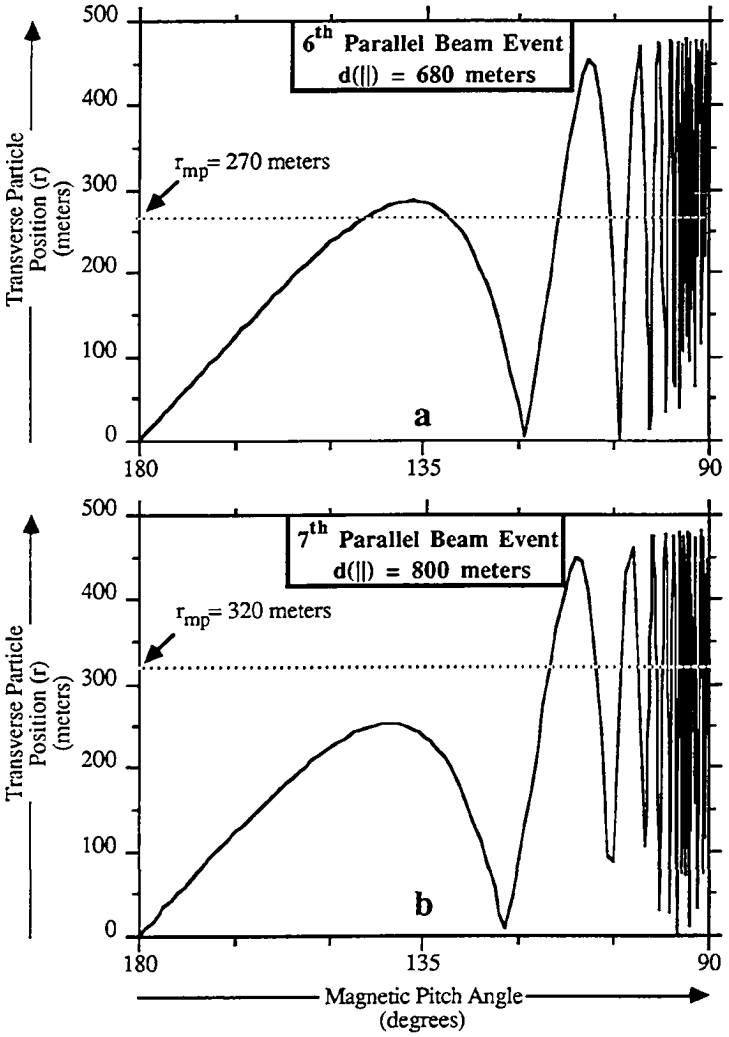

Figure 2-41

respectively, and correspond to the axial positions of the main payload with respect to the sub payload at the times of the 6th and 7th (ll) beam events. The horizontal dotted line in each case represents the transverse location of the main payload with respect to the sub payload, at the times of these beam events, as derived using the separation scenario described above as model 2. This figure illustrates two characteristics of the particle trajectories which have heretofore been difficult to understand. First, we see that at a given axial and transverse position, particles from the sub payload will reach the main payload only if they have certain pitch angles, regardless of the fact that these particles may be injected at any azimuth. For example, a detector located 680 meters above the sub payload and 100 meters across field lines from it will observe particles at near ~165° and at many pitch angles between ~120° and 90° , but will observe none at pitch angles between ~165° and ~120°. This gives some insight into the consistent observation during (ll) beam events (#1-#6) of a peak at large pitch angles and one at pitch angles near 90°, coupled with the absence of observed flux at intermediate pitch angles, and leads to the conclusion that the beam is much more isotropic at the sub payload than we have previously believed. It is to be emphasized that this isotopization must occur very local to the sub payload, for a distributed isotropic source would not produce the distinct pitch angle peaks seen near 200 eV/q in Figures B-9 though B-14. At this point, we can put forward no plausible mechanism which would isotropize these particles over such short distances, while not degrading them in energy. Secondly, Figure 2-41 illustrates the cause of the disappearance of the upgoing particles between the 6th and 7th parallel beam events, while the transverse particles near 200 eV/q continue to be observed. In Figure 2-41b, no particles with pitch angles greater than ~120 degrees have access to the (hpyothesized) radial location of the main payload.

In the case of (⊥) beam injections, the single particle picture is quite different, with strong anisotropy in magnetic azimuth expected in the Ar^+ ion fluxes. Figure 2-42 illustrates the perpendicular injection of plasma over a 60° range in magnetic azimuth. This

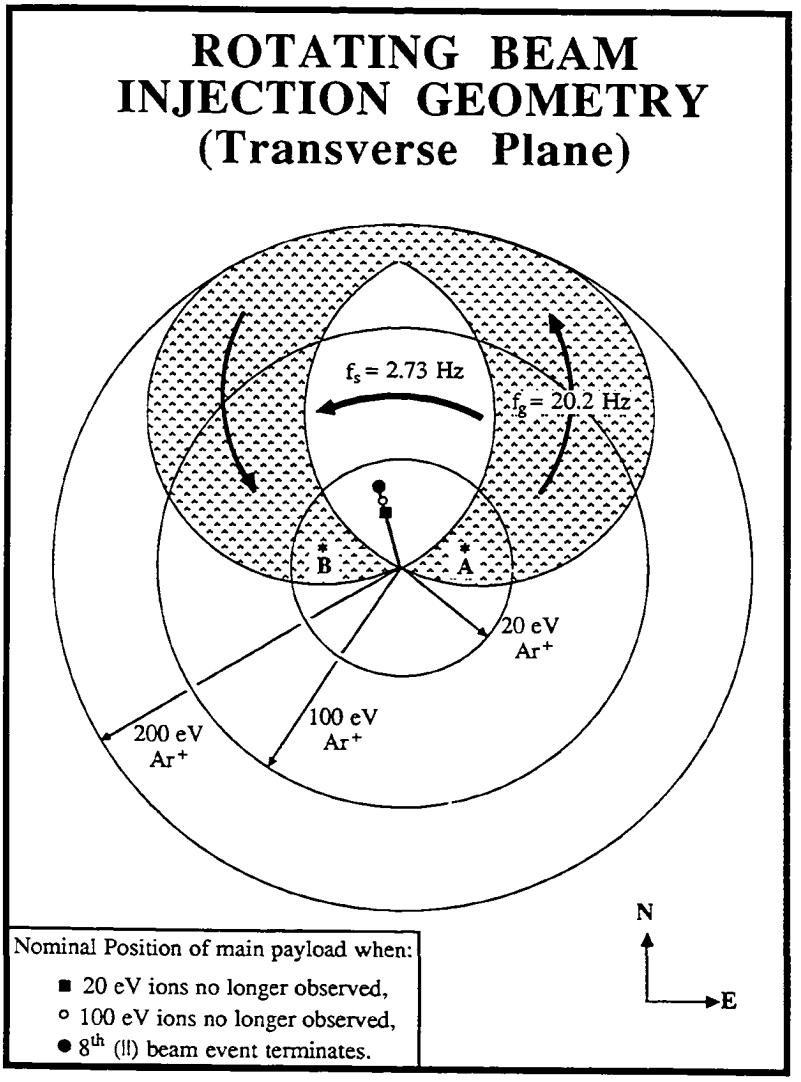

Figure 2-42

illustration shows a projection, onto the transverse plane containing the beam-emitting sub payload, of the trajectories of 200 eV/q Ar^+ ions injected at pitch angles near 90° and at azimuths within ±30° of magnetic east. The shaded region is the region filled with gyrating Ar^+ ions. As noted, the Ar^+ ions gyrate at ~20 Hz, wheras the entire shaded region rotates at 2.73 Hz, as the beam-emitting sub payload spins on its axis. The apparent symmetry in this illustration is somewhat misleading. The (geomagnetic) field aligned expansion of the beam plasma results in far larger Ar^+ fluxes at point A, near the sub payload, than at point B, where extensive field aligned expansion has taken place during the gyration period. Also shown projected onto this transverse plane is the nominal trajectory of the main payload in the sub payload frame of reference (see Appendix A), with indicators as to the location of the main payload, as derived from the nominal payload separation geometry, when the 20 eV/q and 100 eV/q 90° flux peaks disappeared from the data and at the end of the 8^{th} (||) beam event. The concentric circles show the radial limits on where we expect to observe Ar^+ ion flux at the indicated energies per charge. Again, as in the case of parallel injections (Figure 2-39), a gross discrepency exists between expectations and observations, with Ar^+ ion fluxes disappearing much earlier than predicted by the simple single particle dynamics and the nominal relative positions of the main and sub payloads, based on the nominal separation geometry described in Appendix A. On the other hand, Figure 2-43 is identical to Figure 2-42, except that the projection of the main payload trajectory onto the transverse plane is based on separation model 2, described above. This figure illustrates that, to a reasonable degree, the payload separation dynamics embodied in model 2 account for the disappearance of 100 eV/q transverse Ar^+ ions at the time of the end of the 7^{th} ($\perp$) beam event.

It is extremely difficult to account for the discrepencies between the measured Ar^+ fluxes and the predictions of the simple single particle model, without resorting to the notion that the position of the main payload with respect to that of the sub paylaod is not given simply by consideration of the payload separation geometry. The fact that we

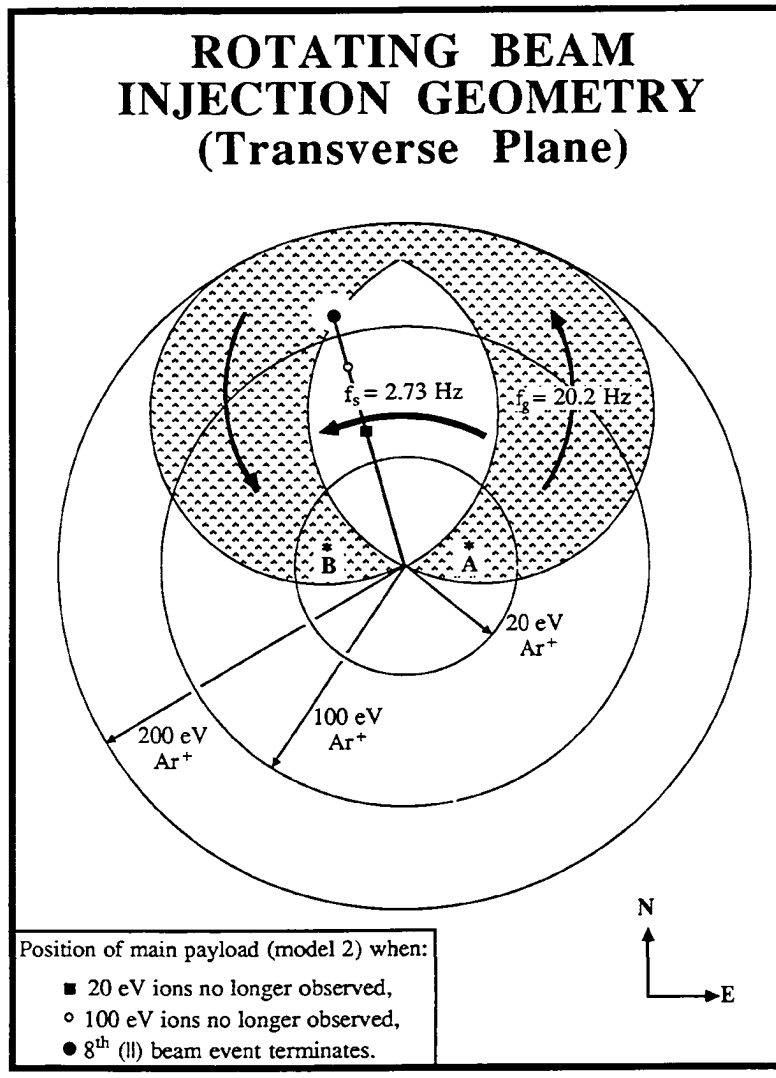

Figure 2-43

observe a given population of particles requires these particles to occupy a circular transverse region of space, whose diameter is equal to twice the gyro-radius of the observed particles. In the case of near perpendicular injections, the idea has been put forward that perhaps the system is localized along the magnetic field line, and that fluxes are no longer observed when the main payload moves through the top of this contained volume of space. For 100 eV/q Ar^+ ions injected at 120° magnetic pitch angle, accounting for the disappearance of these particles during the 7^{th} ($\perp$) beam event requires the loss of ~25 eV energy over a parallel distance of ~750 meters. If this energy loss were due to the presence of a parallel electric field, an average field of some 33 mV/m would be required. Furthermore, this field would be required to fill a cylindrical region of space of the order of 1/2 km in diameter and 1 km in length. The existence of such a field is highly unlikely in view of the normally large electrical conductivity along magnetic field lines and the measured electric field data shown in Figure 2-32. On the other hand, we feel quite confident that the measured geometry of the sub payload deployment is accurate. Therefore, the picture of the main payload being pushed aside by the operation of the attitude control system is probably correct.

The ~100 eV 90° Peak ($\perp$Events). Figures B-1 through B-8 show the existence of a population of positive ions distributed near 90° magnetic pitch angle and near energies per charge of ~100 V during ($\perp$) beam injection events (barely discernable during the 8th ($\perp$) event). These particles are interpreted as being Ar^+ beam ions, although their localization to energies per charge of on the order of 1/2 the expected beam energy is poorly understood. The contrast between the ($\perp$) beam ions, seen at ~100 eV/q and the ($\parallel$) beam ions seen at ~200 eV/q indicates that the retardation is directly related to the perpendicular injection geometry, rather than to some cause characteristic of the beam generators, or to some error in the interpretation of the HEEPS electrostatic energy analysis. It is likely that what we are observing here is a slowing of the beam, due to negative charging of the sub payload during ($\perp$) beam emission. This charging would result from the inability of the

sub payload to collect enough ion current or emit enough electron current to offset the 100 mA Ar^+ beam current emitted by the plasma generator. In the (||) injection cases, this would not be a problem, since low energy electrons emitted by the beam generator could move with the ions along **B**, unimpeded. This is not the case for ($\perp$) injections, however, because the electrons are prohibited from travelling across **B** field lines by the Lorentz force. The escape of gun electrons may be strongly influenced by the merging geometry between the magnetic field produced by the solenoid winding of the beam generator (see Figure 2-7) and the geomagnetic field. If these two fields are aligned roughly parallel at, say, the mouth of the beam generator, then electron escape would be facilitated. On the other hand, if these fields are unaligned or anti-aligned, the escape of the low energy electrons from the immediate vicinity of the beam generator would be more problematical.

The presence of a transverse polarization electric field would permit electron transport across magnetic field lines, but it is likely that the ionospheric plasma would largely short out any such polarization field. In the case of the Porcupine experiment, the measured polarization field was found to be only ~10% as large as would be required to permit current free beam propagation. Further, the electric current carried by the beam ions was in fact observed during the Porcupine experiments, through the measurement of the associated magnetic field perturbations (Häusler et. al., 1986). The Porcupine beam carried 40 times the current as the 29.015 beam, at ~1/2 the velocity, resulting in beam densities at a given distance from the emitter of on the order of 10^2 those at the same distance associated with the 29.015 beam. Since more dense beams are better able to sustain a transverse polarization electric field in the presence of the ambient ionospheric plasma, we see that it is even less likely that the 29.015 beam could have supported such fields. We have other evidence that the 29.015 sub payload is charging negatively during perpendicular beam injections, in the form of the University of Minnesota Langmuir probe data presented in Figure 2-37. This figure shows that the Langmuir probe continuously collects ion current during the ($\perp$) event shown, beginning at the commencement of the

event. The same behavior was seen in the other (⊥) beam events. This current collection is independent of the 3 Volt probe bias sweep, indicating the existence of a DC charge state of at least 3 Volts negative on the sub payuload during (⊥) beam operations. This situation is to be contrasted with the case of (||) beam injections (Figure 2-38), where only a transient (~20 ms) pulse of ion current is drawn at the beginning of beam operations, with no steady state charging indicated.

The Low Energy 90° peak (⊥and || Events). Data in Figures B-1 through B-6 and B-9 through B-12 show the existence of a low (compared to the beam generator anode bias) energy ion population extending from ~5 eV/q to 60 eV/q. These ions are located near 90 degrees magnetic pitch angle and are commonly observed during both || and ⊥ beam injections. The very existence of this population of particles was totally unanticipated and is unexplained at this time. A very simple explanation presents itself in the possibility that the main payload, on which these particles are measured is charging up to some ~5 Volts negative in the presence of a hot (~ 50 eV) ion plasma. This may be expected to produce an ion distribution similar to that shown, with the low energy cut-off providing a measure of the payload potential. However, we have no reason to believe that the main payload should charge up in this manner. We do expect that a conducter immersed in a warm plama should aquire a small ($\sim kT_e$) negative payload potential due to the high mobility of the electrons in the plasma as compared to the ions. However this picture calls for the observed population to be composed of the ambient thermals around the main payload, which have been accelerated through the payload Debye sheath. This could be the case, but probably is not, which can be argued based on the following two points.

First, the evolution of the fluxes, in time, is not what we might expect if the above scenario is correct. As the main payload moves away from the beam source, we would be more likely to see variations in the energy distribution of this low energy peak, which is dependent on beam processes, than in the intensity of the peak which would be dependent on the ambient density. We see the intensity of these particles decrease through apogee,

and, finally disappear on the downleg, not showing the monotonic dependence upon altitude expected for ambient densities. Meanwhile, we see only few thermal events throughout most of the flight until downleg. In both cases, the thermals increase in intensity and the 'low energy 90°' ions decrease in intensity without the appearance of an evolution from one to the other energy distribution. This is well illustrated in Figure 2-22f where the measured particle flux is plotted against the measuered energy during the 6th $\perp$ beam exercise. At this time, the thermal events have risen above background, while the 'low energy 90°' ions are still discernable above background. These two populations are clearly shown to be distinct in this figure.

Secondly, if ions were accelerated to the HEEPS aperture through a Debye sheath surrounding the payload, we would expect to see strong isotropy in the fluxes, with respect to the magnetic field. This is because the potential drop would be localized within a Debye sheath whose dimensions are of the order of the thermal electron gyro-radius, so that that the sheath structure would not be strongly effected by the magnetic field. That the low energy ion fluxes are strongly anisotropic is evident in the data that has been presented, with the stong peaking at 90° pitch angle illustrated in Figures B-2 through B-5 and B-10 through B-12 and the azimuthal structure shown in Figure 2-27 serving as examples.

In the paragraphs above, we have argued that the observed 'low energy 90°' ion peak is not composed of ambient thermal ions and that the observed energy distribution of these particles does not result from acceleration of thermal particles through some potential drop associated with electrostatic charging of the main payload. The absence of such an accumulated charge on the main payload is probably the more certain of these two assertions. Indeed, Cornell University's Langmuir probe data shows no systematic variation in the plasma density through the conduct of the experiment, indicating that the absence of thermal ion events in the HEEPS instrument was not related to the absence of thermal fluxes in the sampled plasma. If the main payload were to become charged to ~+1 Volt, this would account for the absence of thermal events in the HEEPS instrument.

Wayne Scales of Cornell University is modelling wave growth and ion heating in the presence of (⊥) beam events through numerical solution of the Vlasov equation and through electrostatic particle simulations. He has found strong transverse ion heating in these systems and his approach holds some promise for understanding the origin of these low energy particles.

Another possibility, suggested by Professor R. Kaufmann (personal communication), is that these low energy ions may be ambient O^+ ions which have been accelerated in steady transverse electrostatic fields associated with beam operations. Possible sources for such fields include negative electrostatic charging of the beam-emitting sub payload and electric polarization of the beam itself, near the sub payload, as envisioned by Peter & Rostoker (1982), and illustrated in Figure 2-3. Negative charging of the sub payload would not be likely to account for the observations. Such charging would result in an electrostatic potential well which would tend to attract ambient ions. How such a well might result in the presence of energetic ions at distant locations is not known. With regard to beam polarization fields, Porcupine observations (Häusler et al., 1986) show that the strength of these are limited to ~ 10% of that predicted, based on the beam drift velocity. Such polarization fields are an attractive alternative, however, in that they are transverse (to **B**), possibly accounting for the localization of these ~20 eV particles near 90° magnetic pitch angle. These points illustrate the importance of carrying out 3-dimensional electric field measurements in the vicinity of the beam-emitting payload in future experiments.

The ion beam as the source for these particles is another possiblity which should be considered. If this is the case, the mechanism by which particles have been removed from the beam to populate this low energy band near 90° magnetic pitch angle is unclear. If the beam is driving plasma waves which modify the ion distribution in a quasi-linear fashion such diffusion of beam particles to lower energy would be expected. Figure 2-44 shows the positive ion phase space density (assuming Ar^+, Figure 2-44a) and differential directional flux (Figure 2-44b) plotted versus energy during the 3rd (⊥) beam event.

ION FLUX AND PHASE SPACE DENSITY (3rd PERPENDICULAR EVENT)

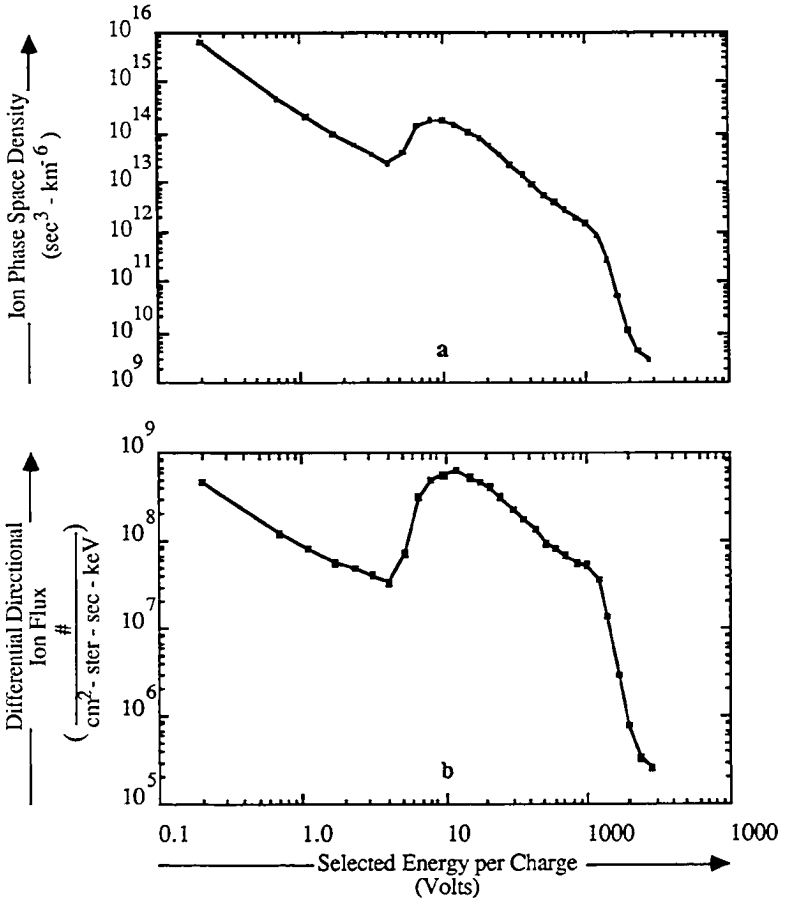

Figure 2-44

Indeed, this data is suggestive of quasi-linear processes stabilizing the ~100 eV ions. However, this particle distribution is peaked in phase space. It is not understood how diffusive processes might account for the creation of such a peaked particle distribution. As can be seen by inspection of Figure 2-32, the ambient electric field was at a minimum at this time, so that the loss of ions due to convection was the least consequential during this 3rd (⊥) event. It is during this event that the low energy ~90° ions were most prominent, dominating the higher energy ions in terms of total flux. This is made evident through a comparison of frame 'c' with the other frames in Figure 2-22. I have therefore chosen to show data associated with this 3rd (⊥) event in Figure 2-44 because it may represent the most highly evolved example of the ion distributions under discussion.

The High Energy 90° Peak (|| Events). Finally, as can be seen by inspection of Figures B-10 through B-15, we observe positive ion fluxes near 200 eV/q and broadly distributed near 90° magnetic pitch angle during the 2nd through the 7th (||) beam events. The origin of these particles is not fully understood, although, it is true that the distribution of ion flux with pitch angle would be qualitatively similar to that observed if there were an isotropic source of 200 eV/q Ar^+ ions located in the immediate vicinity of the sub payload. This is true because of the helical trajectories followed by charged particles in the geomagnetic field. This point has been discussed earlier and illustrated in Figure 2-41. Of course, an obstacle to our understanding the observations in these terms is our understanding that the beam should be only ~60° wide, and not include particles near 90° pitch angle at all. The fact that we observe these particles with large transverse velocity components implies that some process is scattering beam particles in pitch angle, while not significantly scattering them in energy. That the scattering is taking place near the sub payload is also implied by the observations. Such a process might involve the collision of Ar^+ ions with neutral Ar atoms or other Ar^+ ions in the immediate vicinity of the beam generator, although this is unlikely because significant energy transfer would be expected to take place between the particles involved in such collisions, resulting in the observation

of a highly degraded energy distribution in the scattered particles. The fact that the energy distributions are not observed to be degraded points to scattering off of magnetic fields or some massive scattering center. A ~25 Gauss magnetic field is known to exist within the beam generator. However this field falls off very quickly ($\sim r^{-3}$) with distance from the generator and is miniscule compared to the 0.53 Gauss geomagnetic field at a distance of 5 meters, which is the gyroradius of a singly ionized 200 eV Ar+ ion in a 25 Gauss field. These numbers do not support the notion that the observed pitch angle deflection results from a simple gyro-deflection in the magnetic field of the ion beam generator, since the angular deflection of such a particle would be 1 radian ($< \pi/2$) over a path length of 5 meters in a *uniform* magnetic field of 25 Gauss. The average solenoid field over the first 5 meters traversed by a beam ion is much less than 25 Gauss, producing an angular deflection of much less than 1 radian.

Conclusions

We have seen in the foregoing subsections that the 29.015 heavy ion beam experiment has added greatly to our observational knowledge of these type of beam plasma systems, although the argument can be made that the data obtained with the HEEPS instrument has presented more questions than answers. The combination of expected and unexpected ion results from the HEEPS analyzer, in addition to the corroboration of these results by the Octosphere analyzer measurements presents a complex picture of the beam-plasma system which is far from the undistorted single particle trajectory picture that we expected to see before launch. Based on the results of the Porcupine experiment (Häusler et al., 1986), in which the emitted Xe^+ beam was observed to move away from the payload in nearly a free particle fashion and the 29.014 experiment in which such striking effects were observed in the electron particle distributions (Moore et al., 1982; Kaufmann et al., 1985), one might have been led to believe that most of the interesting physics, in terms of the redistribution of particles in phase space, involved the electrons. The 29.015 ion observations indicate that this is not the case, with large scale redistribution and strong ordering of positive ions in phase space being the observational common denominator during both parallel and perpendicular events. It should be emphasized in comparing the 29.015 experiment with those that have preceeded it that similar effects to those observed in the ions on 29.015 may have been present in association with the preceeding experiments and, yet, not been observable. In the case of both of these earlier experiments, the instrumentation for carrying out detailed ion flux measurements in the superthermal energy range of interest was not present.

It is worthwhile at this point to reiterate the major observational findings resulting from the HEEPS positive ion measurements carried out on NASA flight 29.015. They are:

1) During both (||) (1st - 4th) and (⊥) (1st - 6th) Ar^+ beam injections, a population of low energy ions are observed to be present and localized near 90° magnetic pitch angle. These particles extend in energy per charge from ~5 V to ~50 V, with the cutoff at low energy being very sharp. The origin of these particles is unknown, as is their species. They may be beam particles which have been moved to this location in phase space by some unknown mechanism, or they may be ambients which have been energized by interaction with steady state electric fields associated with beam operations or by beam associated plasma turbulence.

2) During (⊥) beam injections (1^{st} - 7^{th}), a population of ~100 eV/q ions is observed to be localized near 90° magnetic pitch angle, though extension to larger pitch angles is often observed in the distributions. These ions are interpreted as being beam Ar^+ ions, although their localization to energies near 1/2 the expected beam energy was not fully anticipated. This effect is probably indicative that the beam-emitting sub payload is becoming negatively charged to a level of ~100 Volts during (⊥) beam events, due to the inability of the electrons to follow the more massive ions across magnetic lines of force. This idea is supported by the Langmuir probe data shown in Fig. 2-37 and is consistent with the modelling carried out by Peter & Rostoker (1982) and Treumann et al. (1983) who predicted beam slowing of up to 50% in association with cross-field injection geometries. In our case, the beam is observed to have been slowed by ~30%.

3) During (||) beam events, positive ions were consistently observed at energies per charge near 200 Volts, the expected beam energy. These ions were observed to be bi-modal with respect to magnetic pitch angle, with a broad peak appearing at pitch angles near and somewhat above 90° and a second, narrower peak appearing closer to 180°. These particles are interpreted as being beam Ar^+ ions, although the existence of the component near 90° is poorly understood. The 90° component implies that scattering of the beam ions is taking place near the beam-emitting sub

payload, although the fact that they are not observed to be degraded in energy places significant constraints on the scattering mechanism involved.

4) In general, beam related effects are seen to disappear much earlier than one would expect, based on our understanding of the nominal sub-main payload separation geometry and the trajectories of the particles involved in the geomagnetic field. This is well illustrated in Figures 2-39 and 2-42. It is probably true that this is at least partly accounted by the operation of the Attitude Control System shortly after sub payload separation, which rotated the main payload through 135 degrees about its pitch axis, with a single high pressure gas nozzle. This system must have imparted an additional transverse (across field lines) velocity to the main payload, with respect to the sub payload. Such an additional velocity of only ~0.6 m/sec could account for several features of the observations. This aspect of the operation of the ACS system has not been analyzed in detail, but this analysis will be carried out in the near future. Closer attention should be paid to this problem before launching future experiments with similar geometry.

5) Finally, the near total absence of HEEPS ion events in the thermal energy range during much of the 29.015 flight is not understood, although the possibility must be admitted that this absence is associated with beam operations. This is especially true in view of the fact that an identical HEEPS instrument was in flight on board NASA flight 35.012 at the same time, in the same region of space and recorded large event rates in the thermal energy range throughout most of the flight. However, this dearth of 29.015 thermal events was observed to extend through the 10 second time intervals between beam operations, an interminable length of time on ionospheric plasma time scales. This fact points to an instrumental explanation for the absence of thermal events, but, again, we have no satisfactory instrumental explanation at this time. The source of this phenomenon remains an open question.

The conclusions listed above summarize the results of the HEEPS measurements of the positive ion fluxes in the vicinity of the Ar^+ ion beam emitting sub payload during the 29.015 active sounding rocket experiment. In considering the contributions of this experiment to our understanding of the interaction of injected heavy ion beams with the ionospheric plasma, these ion observations should be considered in concert with the extensive plasma wave observations carried out on flight 29.015 by the University of Minnesota and reported as the subject of another PhD. dissertation (Erlandson, 1986) and with their comparison with detailed ion trajectory calculations carried out by Keyun Tang at UNH, under the direction of Professor R. L. Kaufmann, which will be reported in full at a later date (Tang, 1987).

Future Directions. Naturally, we want to repeat the experiment. The value of the observations reported in this work would be enhanced manyfold if they could be shown to be repeatable. In a future experiment of this type we should become more quantitative in our measurement of the positive ion fluxes during beam injections, particularly with regard to the angular imaging of these fluxes, the quality of which suffered greatly due to the instrument saturation commonly encountered during the flight. For this reason, high priority should be placed on the devolopment of future generation HEEPS instruments, which don't suffer the limited dynamic range characteristic of the instrument flown on 29.015. The important thing here is to decouple the quality of the HEEPS imaging from the instrument event rate. In the absence of HEEPS type analyzers with significantly enhanced dynamic range, a pair of instruments could be flown, with a small geometry factor instrument operating at small main-sub payload separations, where the heaviest fluxes will be encountered and more sensitive instruments turned on only at larger separations, after the fluxes have become less intense. Another large improvement in the ion flux measurements could be obtained by flying two identical HEEPS instruments, with their axes oriented perpendicular to each other to provide more complete angular coverage, and a measure of redundancy at the same time. While it is true that the capped heimisphere

concept greatly enhances the obtainable field of view compared to more conventional electrostatic analyzers, there were still some directions in which the 29.015 HEEPS instrument never looked, because of the 3 instrument blind spots. Deployment of two such instruments simultaneously would eliminate that problem, providing full 3 dimensional coverage.

In addition, the importance, on future missions of this type, of 3-dimensional electric field measurements, especially in the immediate vicinity of the beam-emitting sub payload cannot be over emphasized. The same is true of the measurement of positive ion species through the use of magnetic mass spectrometers. Either of these measurements could have had critical bearing on the question of the origin of the ~20 eV/q 90° ions observed with the HEEPS instrument on board flight 29.015. Finally, every effort should be made to carry out electron flux measurements with as complete angular coverage as possible and down to as low energy as possible on future missions. Detailed beam related electron flux measurements have yet to be carried out from a platform which is separated from the beam emitting sub payload. One or two HEEPS type instruments which are sensitive to electrons would be ideal for this purpose.

APPENDIX A

29.015 ASPECT AND SUB PAYLOAD EJECTION GEOMETRY

The data obtained from a given particle, photon or field detection experiment on board a space platform will give information about the measured quantity in the frame of reference of the given platform. In order to relate this information to a reference frame of physical interest, we must determine the relationship between the reference frame of interest and that of the platform in question. Hence, the problem of determining the physical orientation, or aspect, and position of the experimental package arises. In the case of geophysical sounding rockets carrying plasma experiments, the orientation and position of the package in a reference frame fixed with respect to the earth is required. This information permits measurements to be interpreted in terms of the (fixed) geomagnetic field, the (vertically) stratified ionospheric plasma and, often, in terms of some localized ionospheric feature, such as an auroral arc, the target region of a ground-based ionospheric modification device, or the magnetic footprint of some magnetospheric feature or instrumented satellite.

In the case of NASA flight 29.015, the position of the instrumented package with respect to the earth is secondary to the questions of the relative positions of the instrumented main payload and the sub payload which carried the ion beam generators and of the orientations of these two payloads in a geomagnetic frame of reference. The physical positions of these two payloads is of interest, however, in order to provide a zeroeth order context for the conduct of the experiments. The trajectory of the 29.015 main payload is provided by NASA as the result of radar tracking carried out from the launch site. Figure A-1 provides plots of the geodetic altitude and the geographic latitude and longitude,

respectively, in parts a, b & c, as functions of flight time for the 29.015 payload, as provided by the NASA radar measurements. The flight took place shortly after local magnetic midnight, and the vehicle trajectory remained within the nominal magnetospheric polar cap, approaching the statistical auroral oval from magnetic north.The position of the sub payload is, to the resolution of Figure A-1, identical to that of the main payload. The relative position of these payloads will be discussed further below.

The orientation of the instrumented main payload may be determined using data from either a (Develco #7200-C) 3-axis fluxgate aspect magnetometer, or a (Space Vector Corporation) 3-axis inertial gyroscope system. The aspect magnetometer provides a measure of the vector magnetic field in the reference frame of the rocket. This measurement provides the capability for carrying out pitch angle analysis on collected charged particle data, with the particle pitch angle given as:

$$\cos(\alpha) = (\mathbf{v} \cdot \mathbf{B}) / |\mathbf{B}|, \qquad \text{Eq. A-1}$$

where **v** and **B** are the unit direction of particle motion and the magnetic induction vector, respectively, both of which are measured in the rocket frame of reference. Use of the vector magnetometer does not provide full 3-dimensional aspect, however, because the measurement is invarient under rotation of the rocket payload about the magnetic vector.

The gyroscope provides vehicle aspect data in the form of yaw (y), pitch (p) and roll (r) angles with respect to the orientation of the rocket payload at the time (shortly before launch) that the gyroscope was uncaged. When combined with a knowledge of the payload orientation, in a geographic or geomagnetic frame of reference, at the time of uncaging, this data provides the full 3-dimensional orientation of the payload in the geophysical frame of reference as a function of the time of flight.

The convention we have used for carrying out rotational reference frame transformations has been the **xyz** convention (Goldstein, 1980), whereby a given (unprimed) coordinate system undergoes 3 elementary rotations in sequence, to bring it into alignment with a new (primed) coordinate system. The unprimed system first undergoes a

VEHICLE TRAJECTORY
(Flight 29.015)

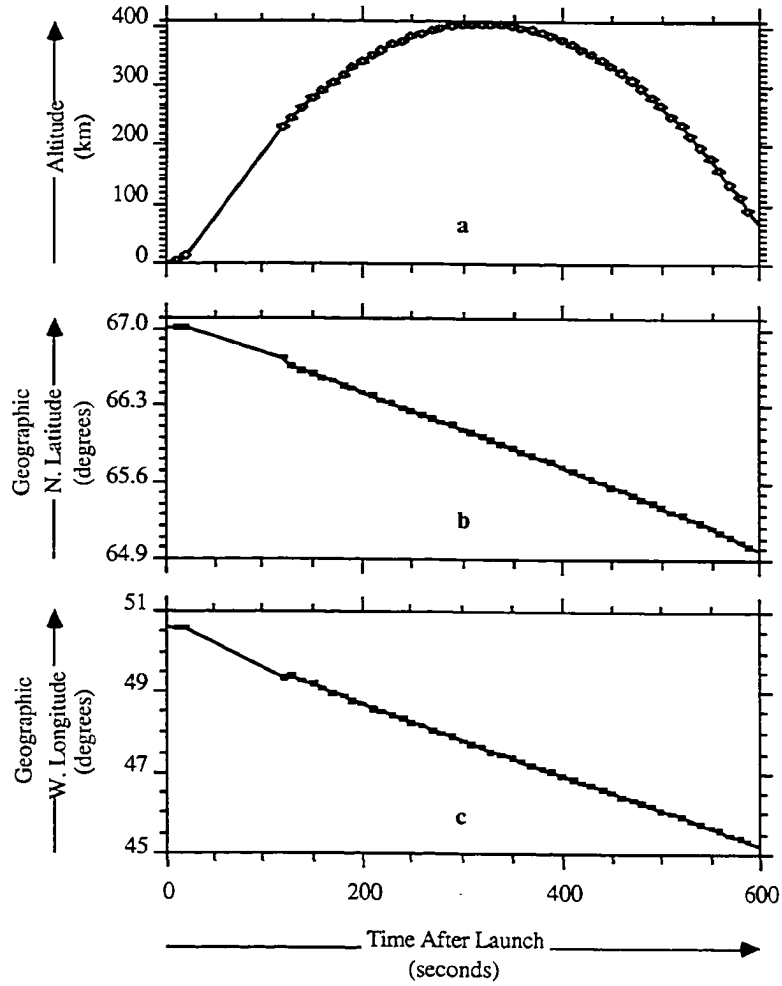

Figure A-1

yaw ($-90 \leq y \leq 90$) rotation about its z-axis, followed by a pitch ($-180 \leq p \leq 180$) rotation about an intermediate y-axis and finally undergoes a roll ($0° \leq r \leq 360°$) rotation about the (final) x-axis. The coordinate transformation may be expressed analytically by the use of a rotational transformation matrix $\underline{\mathbf{M}}$, such that a vector **A** in the original sytem is represented in the new system by the vector **A'**, given as:

$$\mathbf{A}' = \underline{\mathbf{M}} \bullet \mathbf{A}\,, \qquad \text{Eq. A-2}$$

where $\underline{\mathbf{M}}$ is given in terms of y, p and r as:

$$\underline{\mathbf{M}} = \begin{pmatrix} \cos(p)\cos(y) & \cos(p)\sin(y) & -\sin(p) \\ \sin(r)\sin(p)\cos(y) - \cos(r)\sin(y) & \sin(r)\sin(p)\sin(y) + \cos(r)\cos(y) & \cos(p)\sin(r) \\ \cos(r)\sin(p)\cos(y) + \sin(r)\sin(y) & \cos(r)\sin(p)\sin(y) - \sin(r)\cos(y) & \cos(p)\cos(r) \end{pmatrix}.$$

Eq. A-3

Specific gyroscopic aspect for flight 29.015 was determined on the basis of the following considerations. We begin with a geographic coordinate system fixed with respect to the earth and defined at the location of SondreStrom Fjord, Greenland such that x points horizontally toward geographic east, y points horizontally toward geographic north and z, obtained by the use ot the right hand rule, points vertically upward. We refer to this system as 'Launch Cartesian Coordinates', or 'LCC', and and illustrate it in Figure A-2, below.

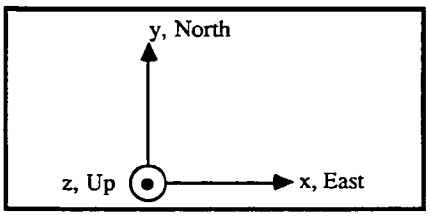

Figure A-2: Launch Cartesian Coordinates (LCC)

The most interesting geophysical frame of reference in which to express the results of particle and field measurements, as well as the relative positions of the main and sub

payloads is a geomagnetic frame of reference. We therefore define a local system of Magnetic Cartesian Coordinates (MCC). This coordinate system has its z-axis along the local magnetic induction field, **B** (assumed to be uniform and constant), given at 300 km altitude above the launch site by data obtained aboard the MagSat satellite (L. Zanetti, private communication), in LCC, as:

$$\mathbf{B}_{LCC} = (-0.0598, 0.0686, -0.527) \text{ Gauss,} \qquad \text{Eq. A-4}$$

yielding

$$\mathbf{z}(MCC)_{LCC} = (-0.112, 0.128, -0.985). \qquad \text{Eq. A-5}$$

This vector points generally downward, with small components to the geographic north and west. The x-axis of the MCC system is defined to be perpendicular to the geomagnetic meridian plane, which contains both the induction vector given above, and the Earth's magnetic dipole. A horizontal line in this geomagnetic meridian plane deviates from magnetic north, and at SondreStrom Fjord, lies approximately 27° west of geographic north (Wickwar et al, GRL, 9/84). This MCC x-axis is expressed in LCC as:

$$\mathbf{x}(MCC)_{LCC} = (0.891, 0.454, -0.391) \qquad \text{Eq. A-6}$$

and points generally geographically eastward, with smaller northward and downward components. Finally, the MCC y-axis is obtained from the MCC x and z-axes through the use of the right hand rule. It is given in LCC as

$$\mathbf{y}(MCC)_{LCC} = (0.442, -0.882, -0.164). \qquad \text{Eq. A-7}$$

It can be seen that $\mathbf{y}_{MCC}$ points generally toward the geographic south, with smaller eastward and downward components. A rotational transformation matrix, denoted as $\underline{\mathbf{M}}_1$, may be used to re-express a vector, given in LCC, in terms of MCC. This matrix is given as:

$$\underline{\mathbf{M}}_1 = \begin{pmatrix} 0.891 & 0.454 & -0.391 \\ 0.442 & -0.882 & -0.164 \\ -0.112 & 0.128 & -0.985 \end{pmatrix}. \qquad \text{Eq. A-8}$$

Next, we define a set of coordinates fixed in the rocket and based on the gyroscope axes, which we refer to as Gyroscope Rocket Coordinates (GRC). This system is defined such that the x-axis points along the rocket spin axis from the tail toward the nose, the y-axis points from the rocket spin axis through the 270° payload raceway and the z-axis, obtained by the use of the right hand rule, points from the rocket spin axis through the 0° payload raceway (See Figure 2-12). The GRC system is illustrated in Figure A-3, below.

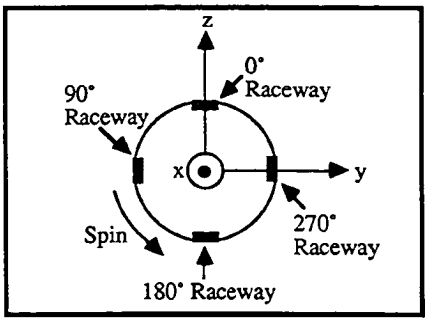

Figure A-3: Gyroscope Rocket Coordinates (GRC)

Based on information provided by NASA personnel on the night of the 29.015 flight, the relation between the LCC and the GRC systems at the time that the gyroscope was uncaged is specified by yaw, pitch and roll angles of -46°, -84.2° and 0°, respectively, which will rotate the LCC system into the uncaging orientation of the GRC system. The rotation matrix for this operation will be denoted as $\underline{\mathbf{M}}_2$. The inverse of $\underline{\mathbf{M}}_2$, denoted as $\underline{\mathbf{M}}_2^{-1}$, is required for data analysis and is given by the transpose of $\underline{\mathbf{M}}_2$ as:

$$\underline{\mathbf{M}}_2^{-1} = \begin{pmatrix} 0.0702 & 0.719 & -0.691 \\ -0.0727 & 0.695 & 0.716 \\ 0.995 & 0 & 0.101 \end{pmatrix}.$$

Eq. A-9

As mentioned above, at any time in flight, yaw, pitch and roll angles (y(t), p(t) and r(t)), given in the gyroscope data stream, specify the orientation of the main payload with respect

to its orientation at the time of gyroscope uncaging. This relationship may be represented in terms of a 3rd rotational transformation matrix ($\underline{M}_3$) according the the formulation of eq. A-3. Finally, using the ordered product of $\underline{M}_1$, $\underline{M}_2^{-1}$ and $\underline{M}_3$, a vector given in the rocket frame (GRC) may be re-expressed in terms of Magnetic Cartesian Coordinates as:

$$A_{MCC} = \underline{M}_1 \bullet \underline{M}_2^{-1} \bullet \underline{M}_3(t) \bullet A_{GRC} \qquad \text{Eq. A-11}$$

At the origin of a set of spherical coordinates which conventionally compliment the MCC system, the direction of motion of a given charged particle is specified by a pair of polar (α) and azimuthal (ψ) angles, where the polar angle α corresponds identically to the particle magnetic pitch angle. Having measured particle velocity vectors (v_{GRC}) (or other directed quantities) in the rocket (GRC) frame, then, these may be re-expressed in the local magnetic system as described above, and the magnetic pitch angle and azimuth determined as:

$$\text{mag pitch} = \text{COT}^{-1}\left\{\frac{v_z}{\sqrt{v_x^2 + v_y^2}}\right\}, \quad (0^\circ \le \text{mag pitch} \le 180^\circ)$$

Eq. A-12

and

$$\text{mag az} = \text{COT}^{-1}\left\{\frac{v_x}{v_y}\right\}, \quad (0^\circ \le \text{mag az} \le 360^\circ),$$

Eq. A-13

where all velocity components are expressed in the MCC system. Note, for the sake of electrostatic analyzer measurements, that the arguments of the COT^{-1} functions are independent of particle mass and charge.

An example of the use these formulations is provided in the determination of the orientation of the main payload spin axis as a function of time during the flight. Figure A-4 illustrates this orientation, showing, in parts a and b, the payload spin axes' magnetic azimuth and pitch as functions of time throughout the flight, as derived by use of the gyroscope data, while in Figure A-4c, the magnetic pitch of the spin axis, as derived

29.015
MAIN PAYLOAD ASPECT
(Geomagnetic)

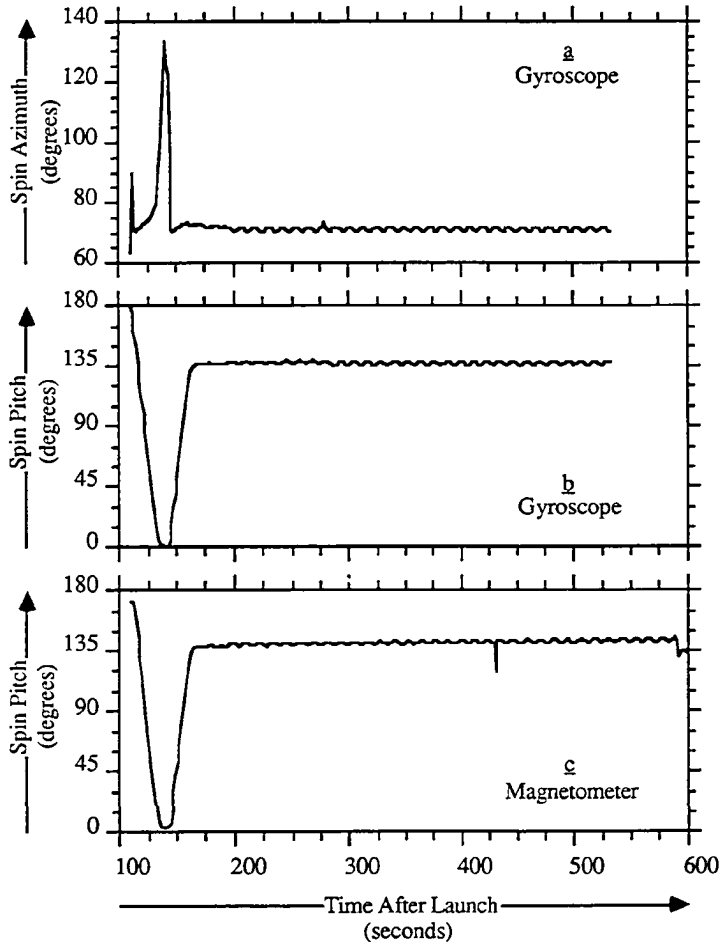

Figure A-4

through the use of the 3-axis magnetometer data is shown. The large changes in magnetic pitch of the spin axis between ~110 and 160 seconds flight time show the results of Attitude Control System (ACS) maneuvers executed for the purpose of ejecting the sub payload downward along the geomagnetic field line. The large deviation of the magnetic azimuth of the spin axis near 140 seconds reflects small changes in the actual orientation of the payload which result in large azimuthal deviations, due to the small value of the magnetic pitch at this time (recall that azimuth becomes undefined for perfect polar alignment or anti-alignment). The data shown here has been averaged to provide a temporal resolution of 1 second. The determined azimuth is very noisy due to this effect near 140 seconds flight time and oscillates with an amplitude of ~90 degrees. Note the small (~3° amplitude) degree of payload coning, as indicated by the (~0.1 Hz) oscillation which sets in shortly before 200 seconds flight time.

Figure A-5 shows the same data, in higher time resolution, as that shown in Figure A-4. Using this data, the spin axis orientation may be determined at the moment that the sub payload was ejected down the geomagnetic field line. This ejection is determined to have taken place at 133.35 seconds flight time. The large transient deflection in the magnetometer-based data, as well as the large (~15°) amplitude oscillation of the resulting pitch at the payload spin frequency is thought to be due to the presence of magnetic materials in the sub payload. As indicated in the figure, both the gyroscope data and the aspect magnetometer data allow the conclusion that the sub payload was ejected in a direction characterized by a magnetic pitch of near 7.5°, with an uncertainty of $\pm$ ~2° in the case of the gyroscope data and somewhat more in the case of the magnetometer data. Similarly, the magnetic azimuth of sub payload separation, as determined from the gyroscope data, is given as 76° (south of magnetic east), with an uncertainty of (somewhat pessimistically) $\pm$ ~10°, corresponding roughly to the magnitude of the azimuth noise level immediately prior to 134 seconds flight time. The sub payload was ejected with a measured separation velocity of 2.2 ± 0.1 m sec^{-1} (Erlandson Ph.D. Thesis) and is known,

29.015 SUB PAYLOAD DEPLOYMENT GEOMETRY

(Geomagnetic)

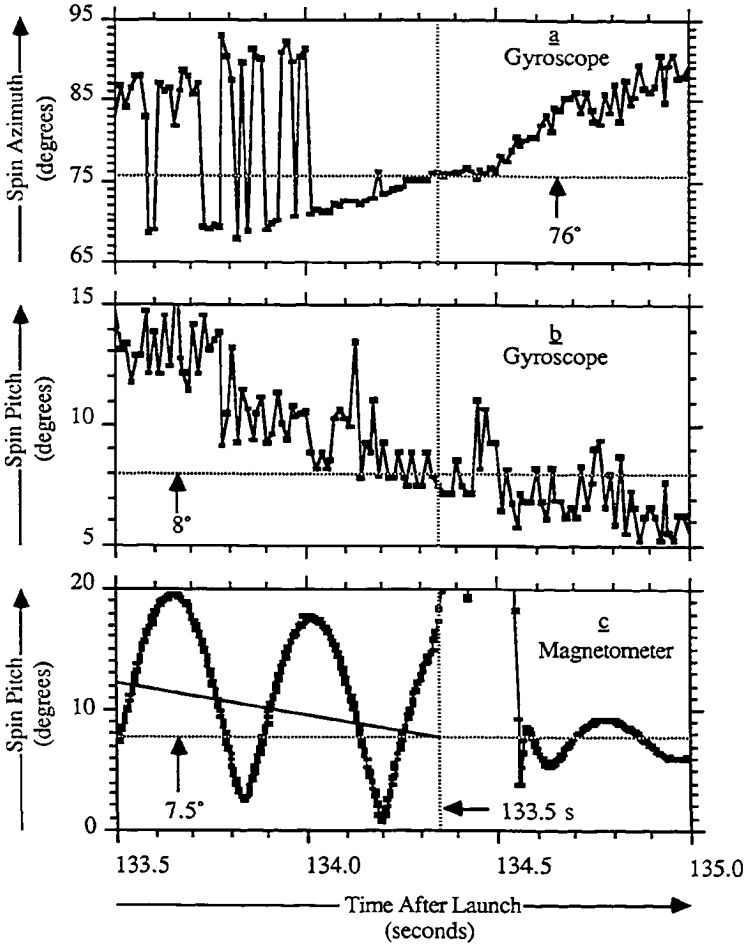

Figure A-5

by virtue of an on-board single axis magnetometer, to have maintained a stable trajectory with a uniform spin rate of 2.73, and a small (< 2°) coning at ~0.1 Hz. As a result, we conclude that the vector pointing from the sub to the main payload is characterized by a magnetic pitch of (180 - 7.5)° = 172.5°, a magnetic azimuth of (360 - 76)° = 284°, both of which remain constant with time, and by parallel and perpendicular (to **B**) components whose magnitudes are shown as functions of time in Figure 2-17. This sub payload ejection geometry is illustrated with sketches in Figure 2-16.

APPENDIX B

HEEPS DATA REDUCTION AND RESULTING ENERGY-PITCH ANGLE FLUX SPECTRA

As described in Section 1, the HEEPS ion data consisted of a 'HEEPS Total Counts' (HTC) signal which consisted of a 10-bit word delivered in the telemetry stream every 1.6 ms, and 'HEEPS Serial Data' (HSD) which consisted of 64 10-bit words delivered in the telemetry stream every 12.8 ms (see Figure 1-24). The HTC signal contained the value read from a counter which was incremented every time an event stimulated a charge pulse large enough so that the resulting voltage pulse (A+B) exceeded the voltage threshold set on the lower level discriminator shown in Figure 1-23. This signal is interpreted as the total number of valid ion events (0-1023) to have occurred during the 1.6 ms accumulation interval. The HTC counter was reset each time it was read out. On the other hand, the HSD signal provided the HEEPS image data, with one 10-bit word delivered for each of the 64 angular imaging bins. The valid portion of each of these 10-bit words included only bit 1 through bit 8, with bits 0 and 9 being garbage bits. Each of these valid 8 bit words represented the number of events to be recorded in the given imaging bin during the *previous* 12.8 ms accumulation period, the data having been buffered for one 12.8 ms period. The sum of the events in the 64 bins, then, represents the number of events during the 12.8 ms accumulatioin period giving rise to voltage pulses (A+B) such that the threshold set on the lower level discriminator is exceeded, while that set on the upper level discrimminator is not (see Figure 1-23). In addition to these signals in the telemetry stream, HEEPS Sweep (HSwp) data and gyroscopic yaw, pitch and roll data, giving the state of the periodic voltage sweep and the vehicle aspect, as described in Appendix A, were delivered every 12.8 ms. Note that the 12.8 ms image and aspect data

periods, combined with the 2.73 Hz payload spin frequency combine to yield an uncertainty of ±6.5° in the payload aspect at which the image data was collected.

Figure B-0 shows, in block diagram form, the sequence of analyses to which this data was subjected. The rectangular boxes represent Pascal computer programs in all cases except 'MASK', which was a subroutine written in the C programming language, and 'GRAPHICS ROUTINES' which represent a package of C and Pascal programs. The data reduction sequence represented in Figure B-0 was quite straight forward, with only simple procedures carried out at every step.

Program 'RINTER' called subroutine 'MASK' which masked off the 0th and 9th bits in the 10-bit HSD image words and produced the file 'HEEPSilv', which contained a series of 64 element arrays, each of which represented a single complete 64 bin angular image.

File 'HEEPSilv' was combined with the HTC data, HSwp data and sensitivity calibration data, as inputs to the the Pascal program 'HPS_CTS_ADJ'. The results of the sensitivity calibration consisted of an individual geometry factor for each of the 64 angular imaging bins. These results and the details of their derivation have been presented in Section 1. Program 'HPS_CTS_ADJ' performed several functions, ultimately producing a file containing a time series of 32x64 arrays of the derived differential directional positive ion energy flux, with each array corresponding to a 32x64 energy-angle flux spectrum. The HTC event rates were corrected according to a non-paralyzable saturation model (see Section 1), incorporating a dead time of 2.6 μsecs. Noise subtraction was carried out on the 64 bin image data by uniformly subtracting 0.63 events from the events in each bin during each 12.8 ms accumulation period. This noise subtraction was based on the measurement of event rates at times in the flight when the instrument was apparently recording only background events. The (dead time) corrected HTC event rates were used to normalize the sum of the events in the 64 angular imaging bins. That is, the event rate in each bin was multiplied by the ratio of the sum of the counts in the bins to the average of

29.015 HEEPS DATA REDUCTION

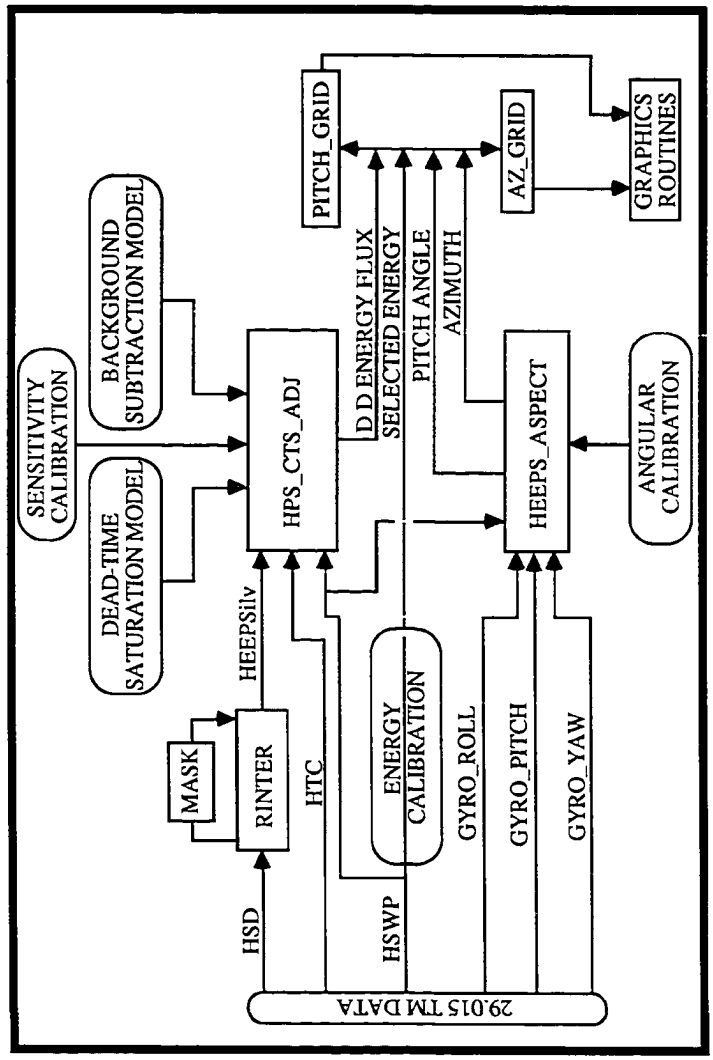

Figure B-0

the corrected HTC event rate taken over the appropriate 12.8 msec period. The HSwp signal was used within 'HPS_CTS_ADJ' strictly for data syncronization purposes. The differential directional energy flux was then derived from the data by use of the equation

$$\{EJ'\}_{i,j} = \frac{C_{i,j}}{G_{oi}}, \quad 0 \le i \le 63, \quad 0 \le j \le 31, \qquad \text{Eq. B-1}$$

where $\{EJ'\}_{i,j}$ and $C_{i,j}$ are the differential directional energy flux and the corrected bin event rate associated with angular imaging bin i and energy selection state j, respectively, and $G_{0,i}$ is the bin geometry factor associated with angular imaging bin i.

The Pascal program 'HEEPS_ASPECT' used gyroscopic aspect data to determine the orientation of the 29.015 payload in a fixed geomagnetic frame of reference, as described in Appendix A. This information was combined with HEEPS angular calibration data and a knowledge of the physical orientation of the HEEPS instrument within the 29.015 payload (See Figure 2-12), to derive the magnetic pitch angle and azimuth of a particle exciting response in each of the 64 bins every 12.8 ms. The results of this determination were written to files 'HEEPS_PITCH' and 'HEEPS_AZ', which contained a time series of 32x64 values of the particle pitch and magnetic azimuth. This program also used the HSwp signal for temporal syncronization.

Finally, synchronized files containing the ion energy flux, magnetic pitch angle and azimuth were given as inputs to the Pascal programs 'PITCH_GRID' or 'AZ_GRID', which simply binned the derived energy flux according to the energy index ($0 \le j \le 31$) and magnetic pitch angle or azimuth, producing time series of 32x40 element arrays of energy flux vs energy index and pitch angle or azimuth, suitable for input to the various plotting routines. In the case of program 'AZ_GRID', facility existed for the specification a range of pitch angles to be included in the binned data, with data at other pitch angles being discarded. In the case of the data shown in this appendix and in Figures 2-27 and 2-28, some 39 of these 2-dimensional arrays were averaged together for each figure, to present a highly statistically significant picture of the entire beam event in question.

In Figures B-1 through B-16, displayed on the following pages, we show positive ion energy flux plotted, from three points of view, against the measured magnetic pitch angle and a measure of the selected energy per charge, which was derived, as described above, from the HEEPS data during the 1st through the 8th perpendicular (Figures B-1 through B-8) and parallel (Figures B-9 through B-16) Ar^+ ion injection events to be carried out during the 29.015 active ion beam experiment. These figures make clear the central observational characteristics of the positive ion flux environment of the main payload, associated with the operation the the two Ar^+ ion beams from on board the separated sub payload. The flux characteristics shown in these figures are described and discussed in Section 2 of this Dissertation.

HEEPS ION MEASUREMENTS
(1 st ⊥ Beam Event)

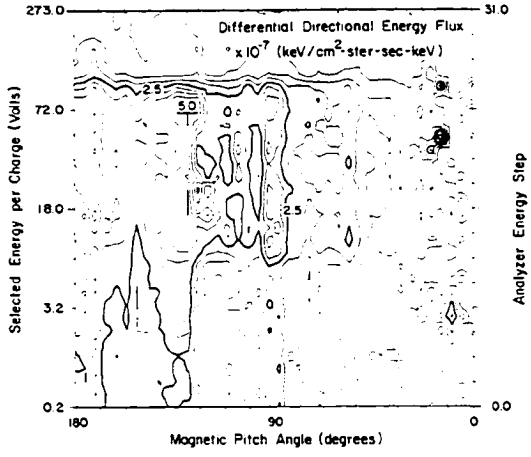

a)

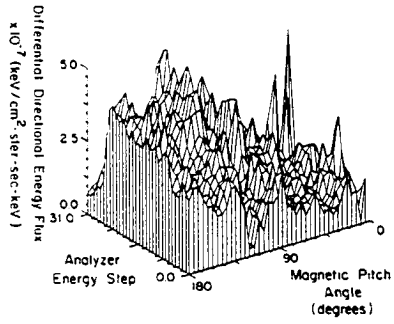

b)

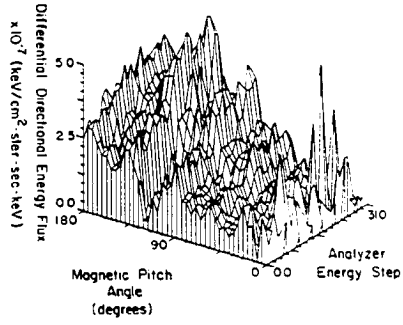

c)

Fig. B-1

HEEPS ION MEASUREMENTS
(2 nd ⊥ Beam Event)

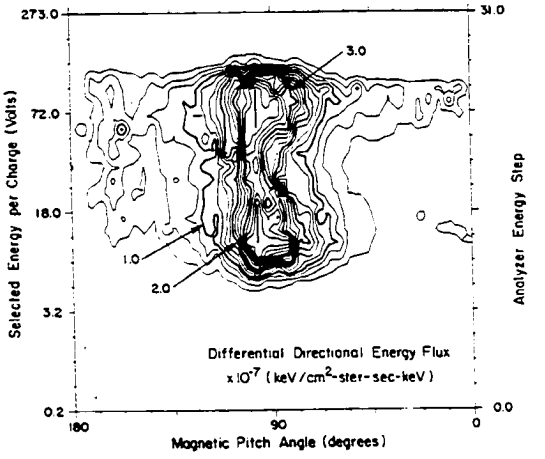

a)

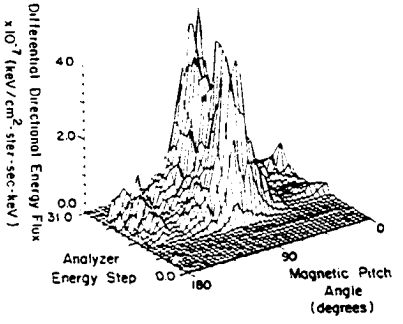

b)

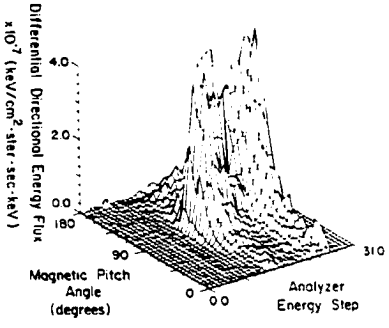

c)

Fig. B-2

HEEPS ION MEASUREMENTS
(3rd ⊥ Beam Event)

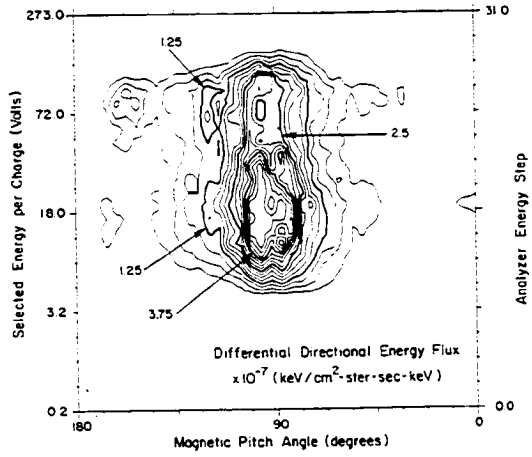

a)

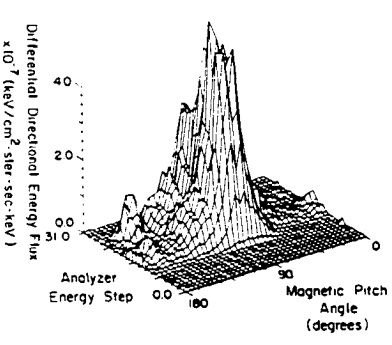

b)

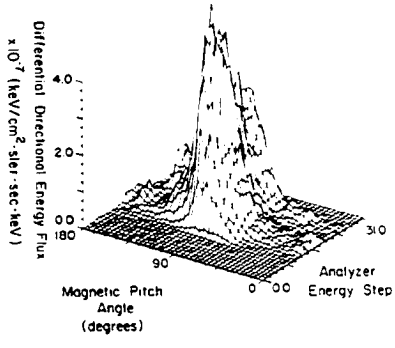

c)

Fig. B-3

HEEPS ION MEASUREMENTS
(4 th ⊥ Beam Event)

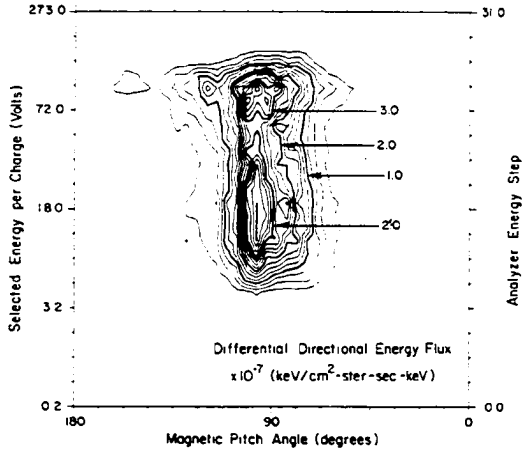

a)

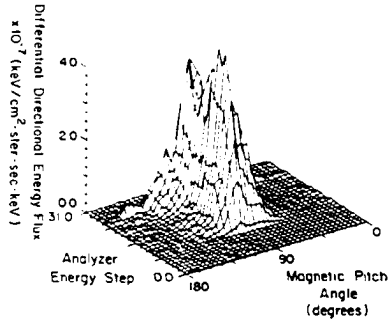

b)

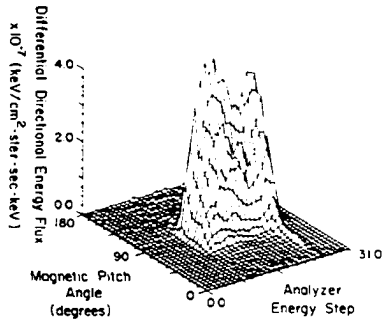

c)

Fig. B-4

HEEPS ION MEASUREMENTS
(5 th ⊥ Beam Event)

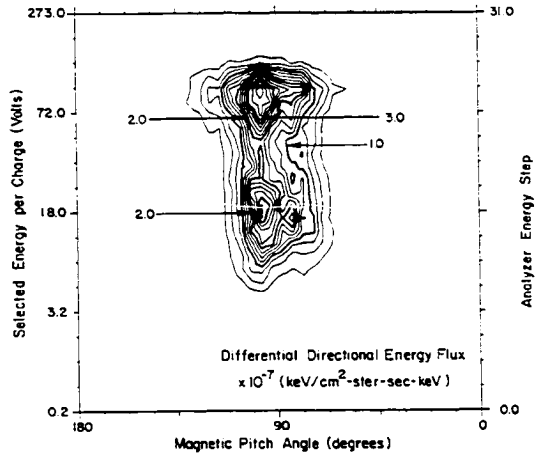

a)

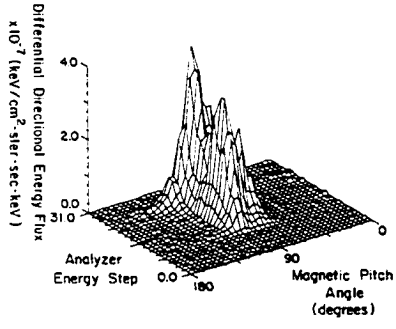

b)

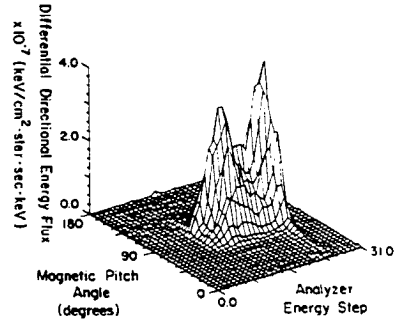

c)

Fig. B-5

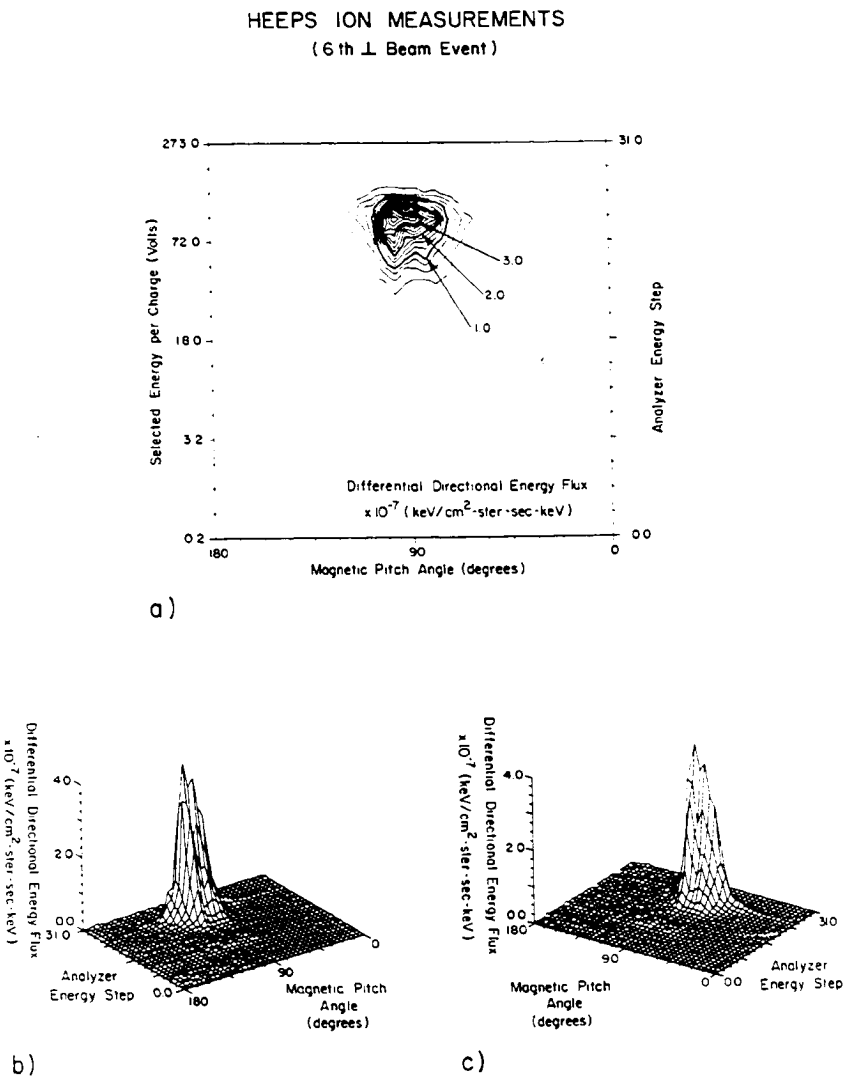

Fig. B-6

HEEPS ION MEASUREMENTS
(7th ⊥ Beam Event)

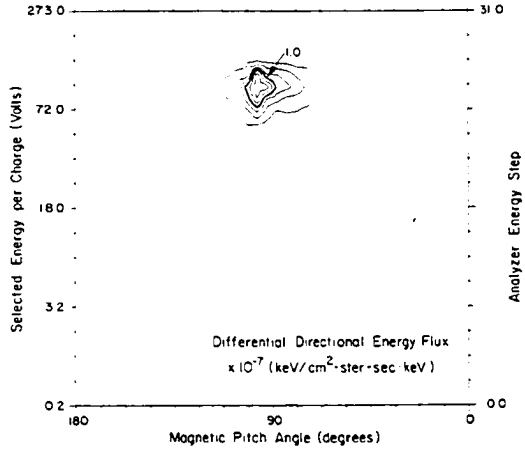

a)

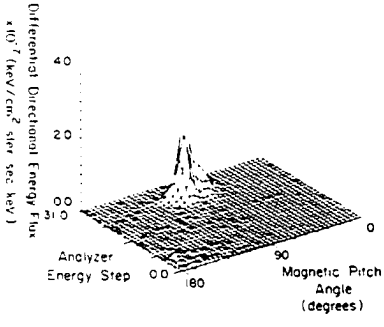

b)

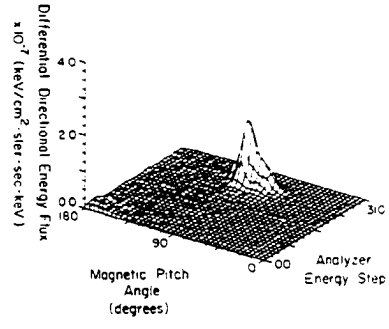

c)

Fig. B-7

HEEPS ION MEASUREMENTS
(8 th ⊥ Beam Event)

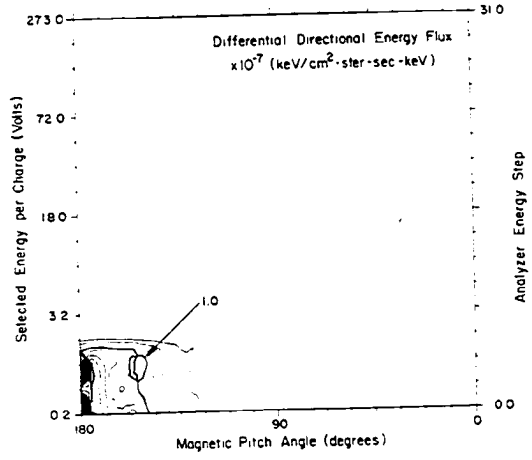

a)

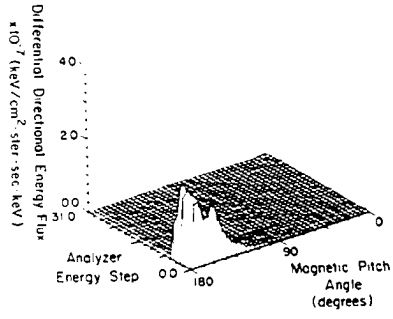

b)

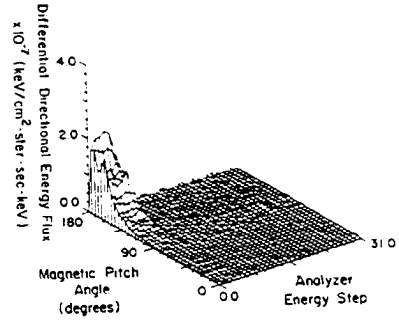

c)

Fig. B-8

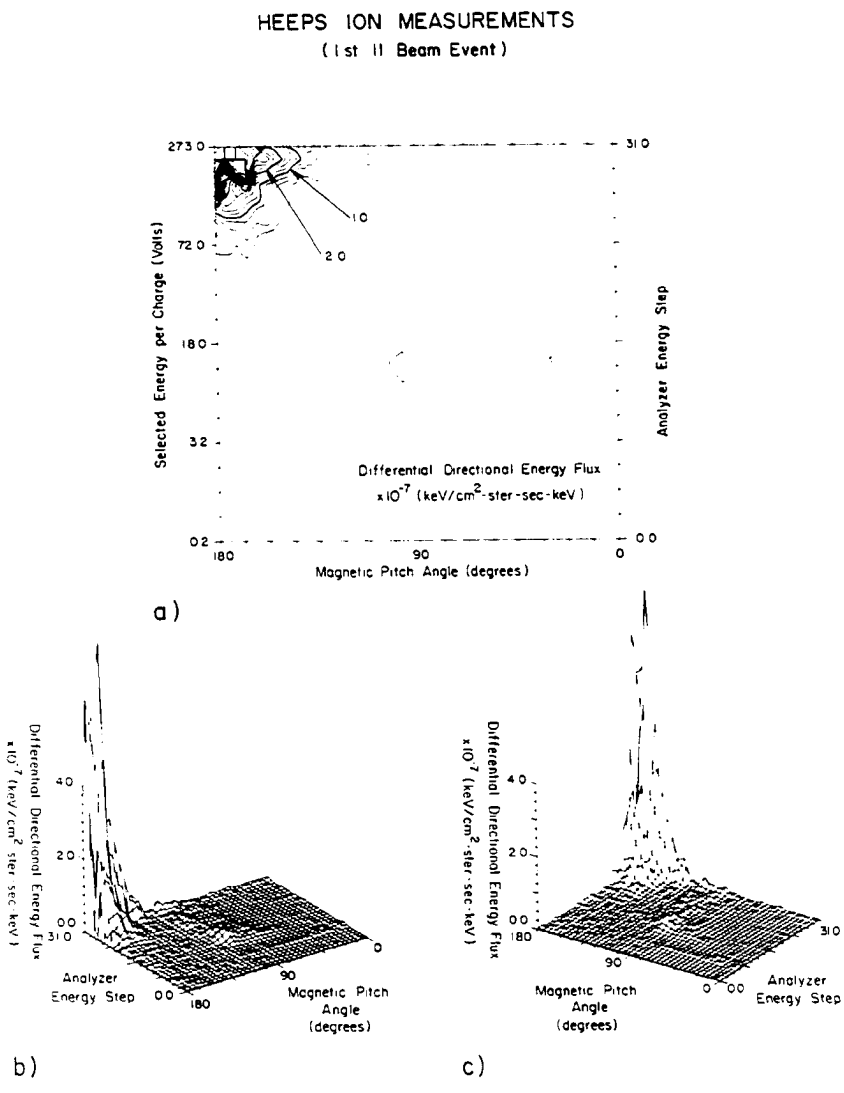

Fig. B-9

HEEPS ION MEASUREMENTS
(2nd II Beam Event)

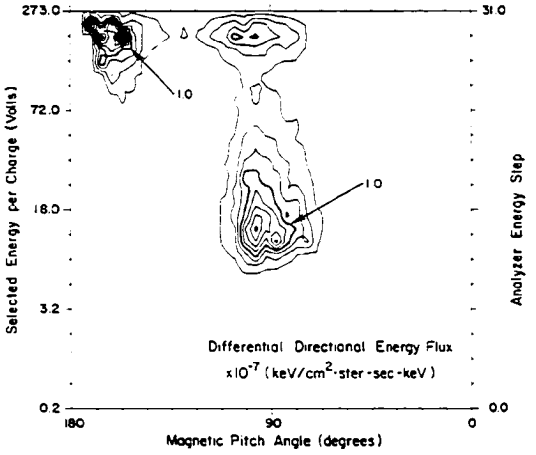

a)

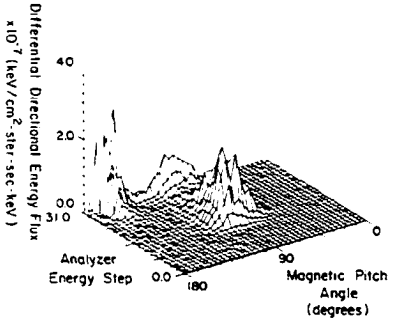

b)

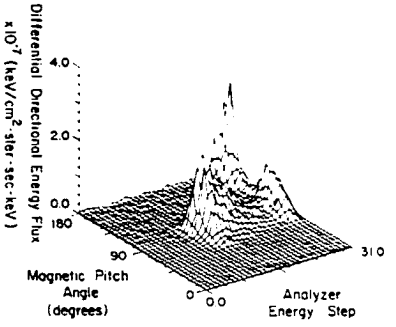

c)

Fig. B-10

HEEPS ION MEASUREMENTS
(3rd II Beam Event)

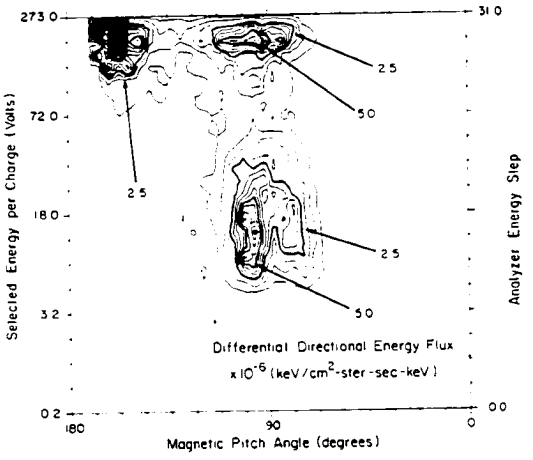

a)

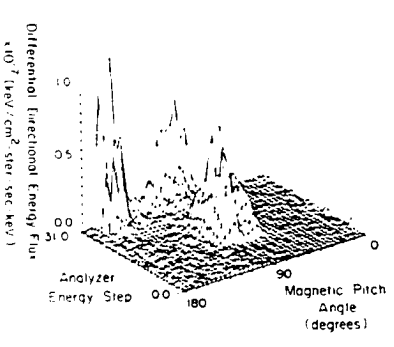

b)

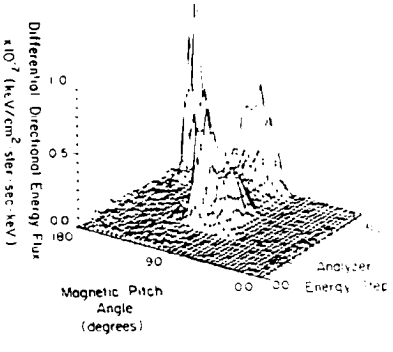

c)

Fig. B-11

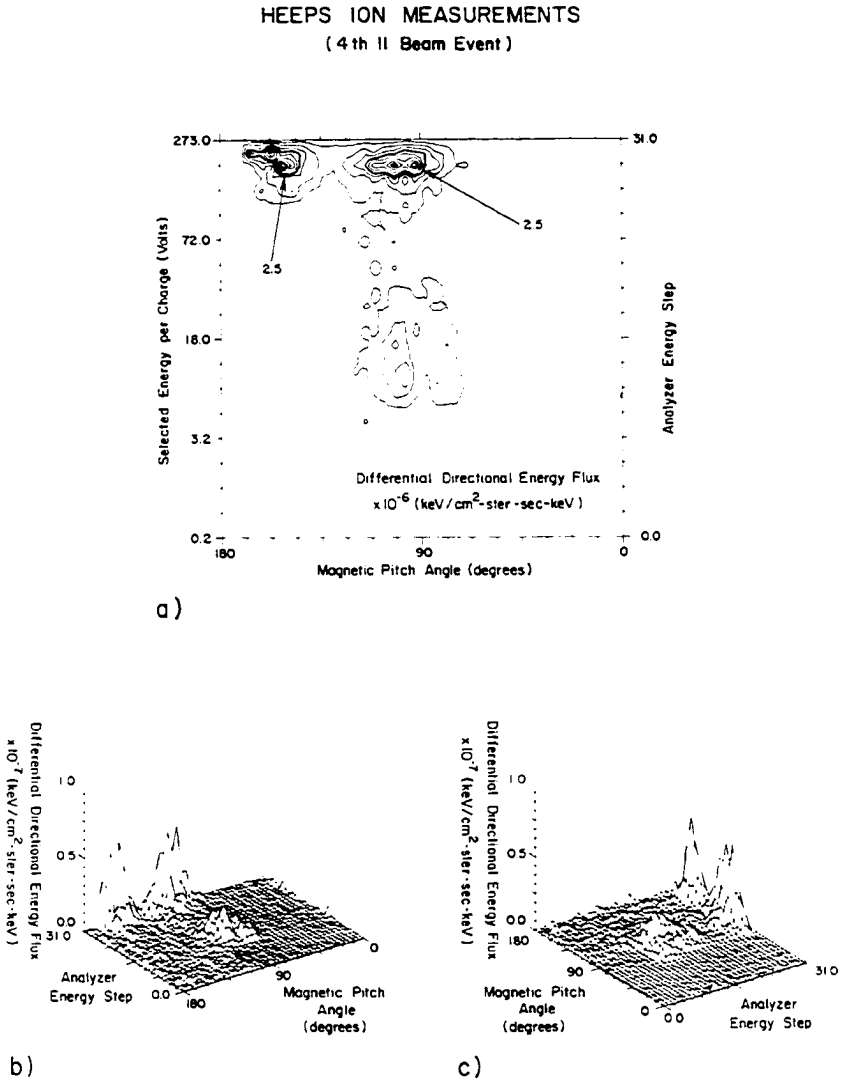

Fig. B-12

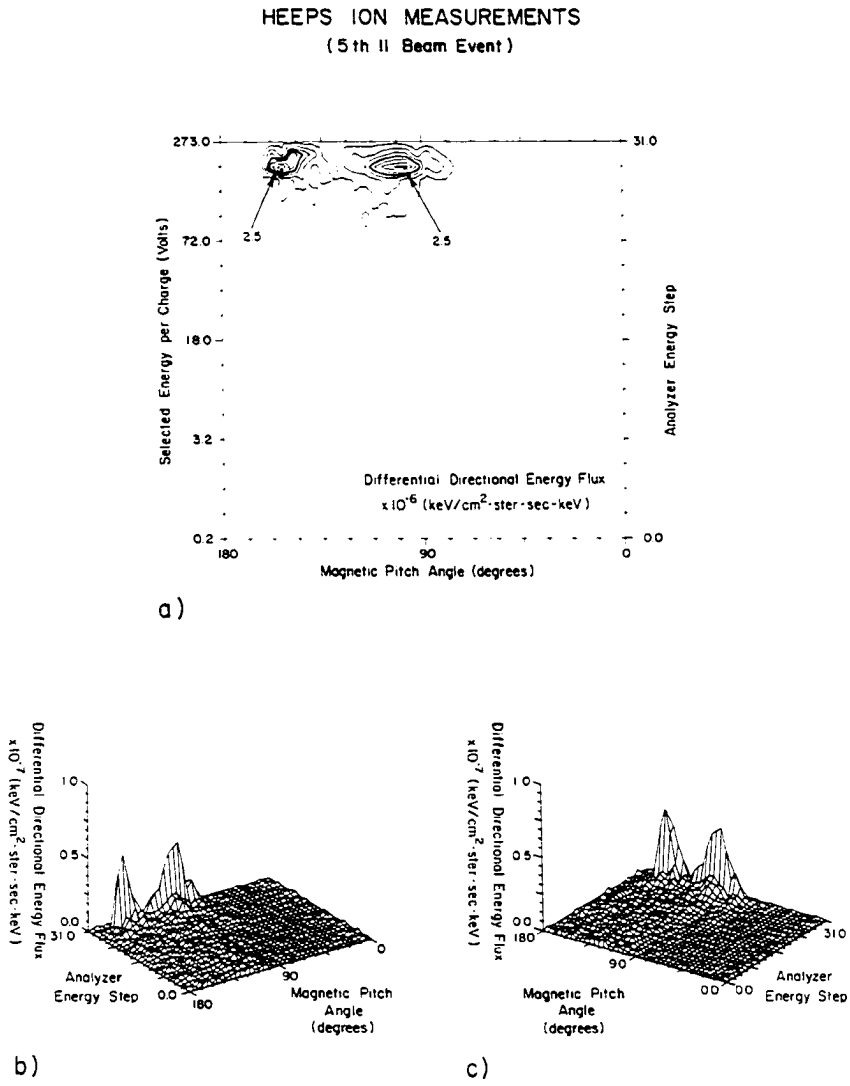

Fig. B-13

HEEPS ION MEASUREMENTS
(6th II Beam Event)

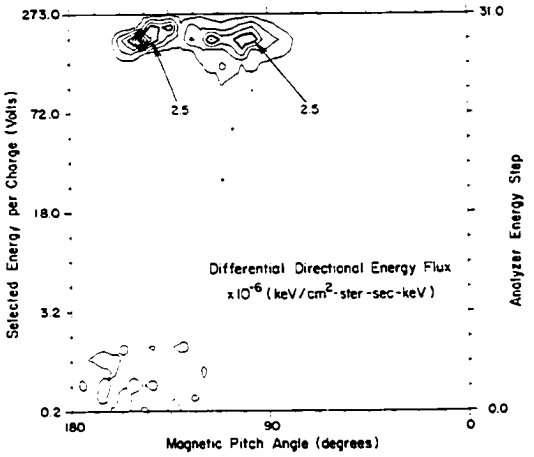

a)

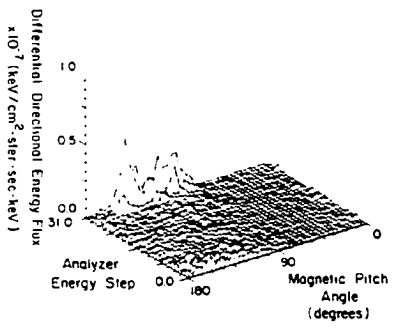

b)

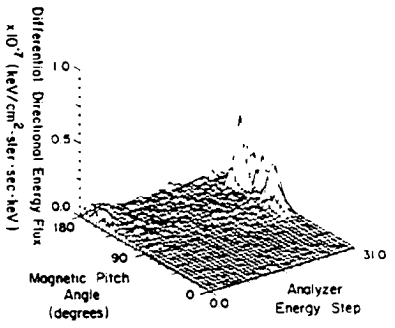

c)

Fig. B-14

HEEPS ION MEASUREMENTS
(7 th II Beam Event)

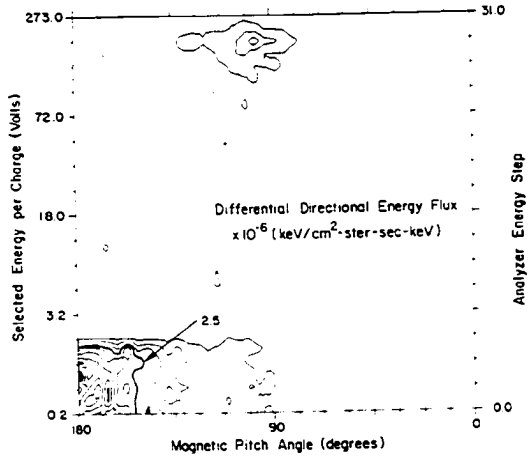

a)

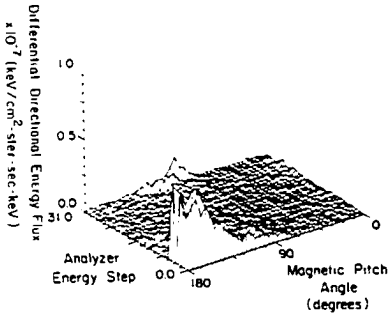

b)

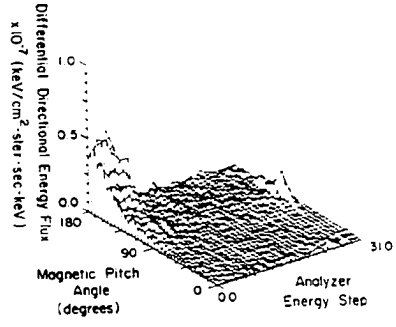

c)

Fig. B-15

HEEPS ION MEASUREMENTS
(8 th II Beam Event)

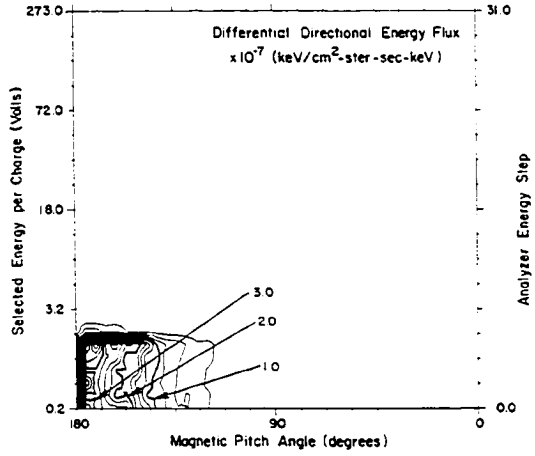

a)

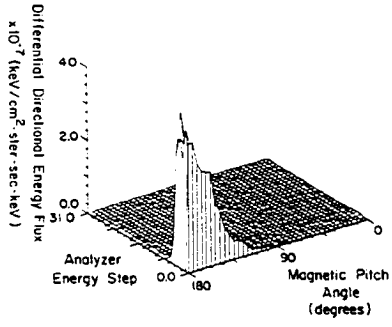

b)

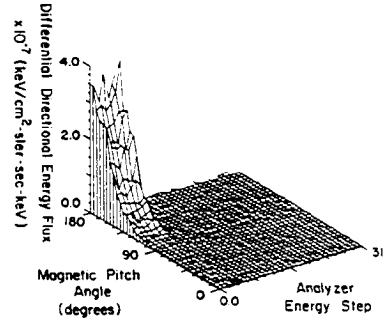

c)

Fig. B-16

REFERENCES

Alfven, H., *On the Origin of the Solar System*, Oxford University Press, 1954.

Arnoldy, R. L., C. J. Pollock and J. R. Winckler, The Energization of Electrons and Ions by Electron Beams Injected in the Ionosphere, *J. Geophys. Res.*, **90**, 5197, 1985.

Arnoldy R.L., T. E. Moore and L. J. Cahill, Jr., Low-Altitude Field-Aligned Electrons, *J. Geophys. Res.*, **90**, 8445, 1985.

Biddle, A. P., J. M. Reynolds, W. L. Chisholm, Jr. and R. D. Hunt, The Marshall Space Flight Center Low-Energy Ion Facility - A Preliminary Report, *NASA Technical Memorandum, NASA TM - 82559*, 1983.

Campbell, W. A., Jr., R. S. Marriot and J. J. Park, Outgassing Data for Selecting Spacecraft Materials, *NASA Reference Publication 1124*, 1984.

Carlson, C. W., D. W. Curtis, G. Paschmann and W. Michael, An Instrument for Rapidly Measuring Plasma Distribution Functions with High Resolution, *Adv. Space Res.*, **2**, 67, 1983.

Chapman, S. and V. C. A. Ferraro, A New Theory of Magnetic Storms, *Terr. Mag. Atmos. Elec.*, **35**, 77, 171, 1931.

Chapman, S. and V. C. A. Ferraro, A New Theory of Magnetic Storms, *Terr. Mag. Atmos. Elec.*, **37**, 147, 421, 1932.

Chapman, S. and V. C. A. Ferraro, A New Theory of Magnetic Storms, *Terr. Mag. Atmos. Elec.*, **38**, 79, 1933.

Chappell, C. R., T. E. Moore and J. H. Waite, Jr., The Ionosphere as a Fully Adequate Source of Plasma for the Earth's Magnetosphere, *J. Geophys. Res.*, **92**, 5896, 1987.

Chen, F. F., *Introduction to Plasma Physics*, Plenum Press, New York, 1974.

Cohen, H. A. and S. Lai, Discharging the P78.2 Satellite Using Ions and Electrons, Presented at the 20th Aerospace Sciences Meeting of the American Institute of Aeronautics and Astronautics, January 11-14, 1982, Orlando, Florida.

Eastman, T. E., L. A. Frank and C. Y. Huang, The Boundary Layers as the Primary Transport Regions of the Earth's Magnetotail, *J. Geophys. Res.*, **90**, 9541, 1985.

Egeland, A., O. Holter and A. Omholt, (Ed.), *Cosmical Geophysics*, Scandinavian University Books, Oslo, Norway, 1973.

Elmore, W. C., Transient Response of Damped Linear Networks with Particular Regard to Wideband Amplifiers, *J. Appl. Phys.*, **19**, 55, 1948.

Erlandson, R. E., M. S. Thesis, University Of Minnesota, 1984.

Erlandson, R. E., Ph. D. Thesis, University Of Minnesota, 1986.

Erlandson, R. E., L. J. Cahill, Jr., C. J. Pollock, R. L. Arnoldy, W. A. Scales and P. M. Kintner, Initial Results from the Operation of Two Argon Ion Generators in the Auroral Ionosphere, *J. Geophys. Res.*, **92**, 4601, 1987.

Evans, R. D., *The Atomic Nucleus*, McGraw-Hill, New York, 1955.

Goldstein, H., *Classical Mechanics*, Addison-Wesley, Reading, Mass., 1980.

Häusler, B., R. A. Treuman, O. H. Bauer, G. Haerendel, R. Bush, C. W. Carlson, B. Theile, M. C. Kelley, V. S. Dokukin and Yu Ya Ruzhin, Observations of the Artificially Injected Porcupine Xenon Ion Beam in the Ionosphere, *J. Geophys. Res.*, **91**, 287, 1986.

Holmes, J. C. and E. P. Szuszczewicz, A Versatile Plasma Probe, *Rev. Sci. Instrum.*, **46**, 592, 1975.

Hudson, M. K and I. Roth, Thermal Fluctuations from an Artificial Ion Beam Injection into the Ionosphere, *J. Geophys. Res.*, **89**, 9812, 1984.

Humphries, S. Jr., Intense Pulsed Ion Beams for Fusion Applications, *Nucl. Fus.*, **20**, Page 1549, 1980.

Kalbitzer, S. and W. Melzer, On the Charge Dividing Mechanism in Position Sensitive Detectors, *Nucl. Instr. and Meth.*, **56**, Page 301, 1967.

Kaufmann, R. L., R. L. Arnoldy, T. E. Moore, P. M. Kintner, L. J. Cahill, Jr. and D. N. Walker, Heavy Ion Beam-Ionosphere Interactions: Electron Acceleration, *J. Geophys. Res.*, **90**, 9595, 1985.

Kaufmann, R. L., D. N. Walker, C. J. Pollock, R. L. Arnoldy and L. J. Cahill, Jr., Heavy Ion Beam-Ionosphere Interactions: Charging and Neutralizing the Payload, In Preparation, 1987.

Kintner, P. M. and M. C. Kelley, Ion Beam Produced Plasma Waves Observed by the $\delta n/n$ Plasma Wave Receiver During the Porcupine Experiment, *Adv. Space Res.*, **1**, 107, 1981.

Kintner, P. M. and M. C. Kelley, A Perpendicular Ion Beam Instability: Solutions to the Linear Dispersion Relation, *J. Geophys. Res.*, **88**, 357, 1983.

Klumpar, D. M., Transversely Accelerated Ions: An Ionospheric Source of Hot Magnetospheric Ions, *J. Geophys. Res.*, **84**, 4229, 1979.

Lebreton, J. P., R. Pottelette, O. H. Bauer, J. M. Illiano, R. Treumann and D. Jones, Observation of Waves Induced by an Artificial Ion Beam in the Ionosphere, *Eur. Space Agency Spec. Publ.*, Active Experiments in Space *ESA-195*, 35, 1983.

Longmire, C. L. *Elementary Plasma Physics*, Interscience, New York, 1963.

Martin, C., P. Jelinsky, M. Lampton, R. F. Malina and H. O. Anger, Wedge-and-Strip Anodes for Centroid-Finding Position-Sensitive Photon and Particle Detectors, Rev. Sci. Instrum., **15**, 1067, 1981.

McBride, J. B., E. Ott, J. P. Boris and J. H. Orens, Theory and Simulation of Turbulent Heating by the Modified Two-Stream Instability, *Phys. Fluids*, **15**, 2367, 1972.

Moore, T. E., R. L. Arnoldy, R. L. Kaufmann, L. J. Cahill, Jr., P. M. Kintner and D. N. Walker, Anomalous Auroral Electron Distributions Due to an Atificial Ion Beam in the Ionosphere, *J. Geophys. Res.*, **87**, 7569, 1982.

Moore, T. E., R. L. Arnoldy, L. J. Cahill, Jr. and P. M. Kintner, Plasma Jet Effects on the Ionospheric Plasma, *Eur. Space Agency Spec. Publ.*, Active Experiments in Space, *ESA SP-195*, 197, 1983.

Olsen, R. C., Modification of Spacecraft Potentials by Plasma Emission, *Journal of Spacecraft and Rockets*, **18**, 462, 1981a.

Olsen, R. C., Modification of Spacecraft Potentials by Thermal Electron Emission on ATS-5, *Journal of Spacecraft and Rockets*, **18**, 527, 1981b.

Olsen, R. C., Experiments in Charge Control at Geosynchronous Orbit - ATS-5 and ATS-6, *Journal of Spacecraft and Rockets*, **22**, 254, 1985.

Ott, E. and W. M. Manheimer, Cross-field Injection, Propagation, and Energy Deposition of Intense Ion Beams with Application to Tokamak Plasma Heating, *Nucl. Fus.*, **17**, 1057, 1977.

Peter, W. and N. Rostoker, Theory of Plasma Injection into a Magnetic Field, *Phys. Fluids*, **25**, 730, 1982.

Pottelette, R., J. M. Illiano, O. H. Bauer and R. Treumann, Observation of High-Frequency Turbulence Induced by an Artificial Ion Beam in the Ionosphere, *J. Geophys. Res.*, **89**, 2324, 1984.

Roth, I., C. W. Carlson, M. K. Hudson and R. L. Lysak, Simulations of Beam Excited Minor Species Gyroharmonics in the Porcupine Experiment, *J. Geophys. Res.*, **88**, 8115, 1983.

Rowland, H. L., P. J. Palmadesso and K. Papadopoulos, One-Dimensional Direct Current Reisistivity Due to Strong Turbulence, *Phys. Fluids*, **24**, 832, 1981a.

Rowland, H. L., P. J. Palmadesso and K. Papadopoulos, Anomalous Resistivity on Auroral Field Lines', *Geophys. Res. Lett.*, **8**, 1257, 1981b.

Rowland, H. L. and P. J. Palmadesso, 'Anomalous Resisitivity Due to Low-Frequency Turbulence, *J. Geophys. Res.*, **88**, 7997, 1983.

Schmidt, G., Plasma Motion Across Magnetic Fields, *Phys. Fluids*, **3**, 961, 1960.

Schmidt, R., H. Arends and N. Nikolaizig, Ion Emission to actively Control the Floating Potential of a Spacecraft, Presented at the 26th Plenary Meeting of the Committee on Space Research (COSPAR), June 30 - July 11, 1986, Toulouse, France.

Seiler, S., M. Yamada, and H. Ikezi, Lower Hybrid Instability Driven by a Spiraling Ion Beam, *Phys. Rev. Lett.*, **37**, 700, 1976.

Sharp, R. D., R. G. Johnson and E. G. Shelley, Observations of an Ionospheric Acceleration Mechanism Producing Energetic (keV) Ions Primarily Normal to the Geomagnetic Field Direction, *J. Geophys Res.*, **82**, 3324, 1977.

Shelley, E. G., R. D. Sharp and R. G. Johnson, Satellite Observations of an Ionospheric Acceleration Mechanism, *Geophys. Res. Lett.*, **3**, 654, 1976.

Tang, K., Ph. D. Thesis, University Of New Hampshire, In Preparation, 1987.

Timothy, J. G., Preliminary Results With Saturable Microchannel Array Plates, *Rev. Sci. Instr.*, 45, **6**, 834, 1974.

Timothy J. G. and R. L. Bybee, One Dimensional Photon-Counting Detector Array for Use at EUV and Soft X-ray Wavelengths, *Appl. Opt.*, **14**, 1632, 1975.

Timothy, J. G., Curved-channel Microchannel Array Plates, *Rev. Sci. Instrum.*, **52**, 1131, 1981.

Timothy, J. G., Electronic Readout Systems for Microchannel Plates, *IEEE Trans. Nucl. Sci. NS*-**32**, 427, 1985.

Treumann, R., O. H. Bauer, G. Haerendel and B. Häusler, Dynamics of Quasineutral Beams, *Eur. Space Agency Spec. Publ.*, Active Experiments in Space, *ESA SP-195*, 197, 1983.

Treumann, R. A. and B. Häusler, The Propagation of a Dense Quasi-Neutral Ion Beam Across a Magnetized Plasma', *Astrophys. & Space Sci.*, **110**, 371, 1984.

Walker, D. N., J. C. Holmes and E. P. Szuszczewicz, 'Auroral Electrodynamics I, 1, Preliminary Electron Density Profile, *NRL Memo. Rep.*, NRL-MR-4229, 1980a.

Walker, D. N. J. C. Holmes and E. P. Szuszczewicz, Auroral Electrodynamics I, 2, Vehicle Potential Changes During an Active Experiment, *NRL Memo. Rep.*, NRL-MR-4229, 1980b.

Walker, D. N., Perpendicular Ion Beam-Driven Instability in a Multicomponent Plasma: Effects of Varying Ion Composition on Linear Flute Mode Oscillarions, *J. Geophys. Res.*, **91**, 3305, 1986.

Wetstone, D. M., M. P. Ehrlich and D. Finkelstein, Experiments on Plasmoid Motion Along Magnetic Fields, *Phys. Fluids*, **3**, 617, 1960.

Whalen, B. A., W. Bernstein and P. W. Daly, Low Altitude Acceleration of Ionospheric Ions, *Geophys. Res. Lett.*, **5**, 55, 1978.

Wiza, J. L., The Microchannel Plate: A Shift to III and New Terrain, *Optical Spectra*, April, 1981.

Yau, A. W., B. A. Whalen, A. G. McNamara, P. J. Kellogg and W. Bernstein, Particle and Wave Observations of Low-Altitude Ionospheric Ion Acceleration Events, *J. Geophys. Res.*, **88**, 341, 1983.

Yau, A. W., E. G. Shelley, W. K. Peterson and L. Lenchyshyn, Energetic Auroral and Polar Ion Outflow at DE 1 Altitudes: Magnitude, Composition, Magnetic Activity Dependence, and Long-Term Variations, *J. Geophys. Res.*, **90**, 8417, 1985.